An Approach towards Organic Thin Film Conductivity Measurements under Ultra-High Vacuum Conditions

Andreas Spielhofer

Physics Department

McGill University, Montréal

Canada

A thesis submitted to McGill University in partial fulfillment

of the requirements of the degree of

Doctor of Philosophy

©Andreas Spielhofer, Montréal 2018

Acknowledgement

"Finally, from so little sleeping and so much reading, his brain dried up and he went completely out of his mind."

— Miguel de Cervantes, *Don Quixote*

It has been a long way from where I started four years ago and it has been another long journey from when the cursor repeatedly blinked on my empty thesis, page one. The cursor on my screen was watching me, mocking me, laughing at my inability to get words out. But I finally made it this far at least, and as far I am aware, I can successfully report that my brain has not dried up. I am indubitably thankful for finally handing in a written version of my work and would like to take this moment to thank everybody who supported me during my Ph.D. in the past few years.

First, I would like to express my gratitude to my supervisor Peter Grütter. Peter, I would like to thank you for the opportunity working with you for these past few years and for your mentorship, insight and patience. I would like to especially highlight the intellectual freedom and trust you gave me in designing all the scientific instruments and it was truly satisfying to see everything coming to life bit by bit. I also would like to thank you the weekly group lunches and the annual fondue, raclette and summer-cottage events that are filled with so many good memories. Nothing makes a student more happy than free food!

I would also like to thank Dr. Yoichi Miyahara for supporting me during daily research, for the many discussions and for always helping me finding the devil in the itty-bitty details. Thanks to you, electronics has become accessible to me and it has become a joy for me to open, modify and fix electronic instruments. I'm very thankful for this gained confidence and your feedback and support have been absolutely invaluable. Thank you so much Yoichi!

I also would like to thank you Dr. Zeno Schumacher and Dr. Ann-Lauriene Haag for the support and encouragement, particularly when things got meta and I enjoyed the numerous

discussions over beers, the many events and activities we shared together so much. Zeno, thanks a lot for taking me under your wing at the beginning and introducing me to the world of UHV science, for the great teamwork and for all the support you gave me in acquiring, building and setting up my system. Without your help, most of the acquired parts would still be in boxes.

I further would like to thank the whole research group of David Cooke and Carlos Silva for the great teamwork and collaboration I encountered. Working with both of you was a great experience for me and your research group members are truly exceptional! In that sense, would like to especially thank Dr. David Valverde, Ben Dringoli and Yang Lan from the Cooke THz group and Dr. Ajay Ram Srimath Kandada, Elizabeth Gutierrez and Laura-Isabelle Dijon-Bertrand from the Silva group for the tremendous work, the night-shifts and for the various lab meetings.

A further thank goes to the machine shop supervisor Pascal Boursequin who not only looked over my designs and machined an endless amount of parts for me, but also was always approachable and allowed me to take several machine shop trainings under his supervision. I've learned a lot about machining and would like to thank you for sharing your knowledge with me and teaching me!

Further, I would like to thank John Smeros, Robert Gagnon and Richard Talbot for all the technical support and Dr. Adam Gilbert for helping me with designing and processing PCB boards.

Thanks to my fellow lab-mates Ann-Lauriene, Zeno, Antoine, Oscar, Tyler, Matthew, Aaron, Ying, Madeleine, Rasa, Megan, Connor and Rikke who helped me in countless efforts on the way and without whom my time at McGill would have been nearly as enjoyable. We are truly the coolest group in the physics department!

To my former roommates Matt, Gordon, Maximilian, Siobhan, Kyle, Andrea and Matthew for becoming such close friends and making me miss Montreal. To my parents Margrit and Franz and my brothers Markus, Peter, Fred and Christian for guiding me through life and

for the good time I always have with all of you. And to Nadia for always having an open ear, for the many laughter, the good time and the strong shoulder to lean on.
I also would like to thank the Canada Foundation for Innovation (CFI) and Natural Sciences and Engineering Research Council of Canada (NSERC) for the funding of this project. Without your financial support, this project would still only exist as a CAD file on my computer. I also want to thank the Swiss National Science Foundation (SNF) for the Doc.Mobility fellowship that was awarded to me for 18 months.
And finally, I would like to thank everyone for the little things that truly made this time unforgettable. Walking with me to Tim Horton's during my obligatory afternoon coffee breaks, exploring numerous microbreweries, watching and playing hockey, having a midnight-Poutine and Pogos at Chez Claudette, ice-skating on the Canal, going for a run on Mont-Royal, climbing all 46 high peaks of the Adirondacks, hosting Halloween parties where your costumes were truly stunning and a blast, and occasionally setting the barbecue on fire on our terrace: Je me souviens! Thanks everyone for keeping my brain hydrated, you are the true Sancho Panzas out there!

“"What giants?" asked Sancho Panza. (...)
"Those over there are not giants but windmills. Those things that seem to be their arms are sails which, when they are whirled around by the wind, turn the millstone."“

— Miguel de Cervantes, *Don Quixote*

Contribution of Authors

All the results presented in this Thesis were performed by the author, with the exception of the following contributions:

- The terahertz measurments that are shown in the Results and Discussion section 5 were performed by Dr. David Valverde, Ph.D. Candidate Yang Lan and Ph.D. Candidate Benjamin Dringoli from the Cooke research group at McGill university.

- The sample preparation of the graphene flakes on the diamond sample, as well as the Raman spectroscopy and mapping that are shown in the Results and Discussion section 5 were performed by Ph.D. Candidate Eric Whiteway from the Hilke research group at McGill university.

- The epitaxial graphene samples grown on semi-insulating 6H−SiC substrate that were used in this work were prepared and provided to us by the Ozaki group at INRS.

- The Atomic Force Microscopy measurements on the epitaxial graphene samples grown on semi-insulating 6H−SiC substrate, as shown and discussed in the Results and Discussion section 5 were performed under the guidance of Dr. Zeno Schumacher and measured by Ph.D. Candidate Rasa Rejali, Ph.D. Candiate Megan Cowie and Ph.D. Candidate Rikke Plougmann from the Grutter research group at McGill university.

Abstract

An ultra-high vacuum system was built that can produce molecular films for organic photovolatics applications. A UHV compatible cantilever based four-point probe system was built, implemented and critically analyzed in order to measure the resistivity of thin films during the evaporation. A transportable ultra-high vacuum system, specifically built for an optical-pump terahertz-probe was set up that allows to transport and keep the samples under UHV conditions at all times. Special diamond windows were designed that allow ultra-broadband transmission and a home-built two axis piezo stage was implemented that allows to fine position the sample inside the suitcase. The suitcase allows to record the pressure, to monitor the rest gases inside the suitcase and to controllably leak gases inside the suitcase. Preliminary measurements on epitaxially grown graphene on a 6H-SiC sample show that the suitcase can be used for time-resolved terahertz measurements.

Résumé

Une chambre à ultravide a été construite qui permet de produire des couches minces de molécules pour des applications en photovoltaïque organique. Un système avec une sonde consistant de quatre micro-leviers servant de pointes de contact a été conçu et implémenté dans cet environnement ultravide pour mesurer la résistivité des couches minces lors de l'évaporation. Un système à ultravide portatif, sous forme de valise, a été spécifiquement construit pour réaliser des expériences de pompage optique dans le régime térahertz. Celle-ci permet de transporter et de garder les échantillons dans un ultravide à tout moment. Ses fenêtres en diamant spécialisé ont été conçues pour permettre une transmission optique sur une large plage de fréquence et une plate-forme avec deux axes actués par des éléments piézoélectriques a été implémentée pour permettre un fin positionnement de l'échantillon à l'intérieur de la valise. Le système mesure et enregistre la pression ce qui permet de surveiller la prèsence de gaz à l'intérieur de la valise et de contrôler précisément son niveau de pression. Des mesures préliminaires sur des films de graphène préparés par croissance épitaxiale sur une surface de $6\,\mathrm{H}-\mathrm{SiC}$ montrent que la valise permet de réaliser des mesures térahertz résolues dans le temps.

Contents

1. Introduction **1**

1.1. Aim of this Work 9

2. Ultra-high Vacuum System Overview **12**

2.1. Sample Transfer 18

2.2. Water Cooling 19

2.3. Bake-out Tent 20

3. Ultra-High Vacuum in-situ Four-point Probe Method for Electrical Characterization of Thin-film Materials **22**

3.1. Introduction 22

3.2. Micromanipulator Implementation 27

3.2.1. Mapping the Local Conductivity of Thin Films 33

3.3. Surface Detection 39

3.4. Electrical Contact Verification with Multiplexer Board 42

3.5. Probes and Limitations 49

3.5.1. Micro Four-Point Probes 49

3.5.2. Other Cantilever Based Probes 55

3.5.3. Spring-Loaded Test Pins and the Force Limit of the Micromanipulator 59

3.5.4. Platinum-Iridium Wire Chip 61

3.6. Conclusion and Outlook 63

4. Ultra-High Vacuum Suitcase **67**

4.1. Introduction 67

4.2. Compact Non-evaporable Getter and Ion Pump 71

4.3. Optical Windows for Optical Pump Terahertz Probe Experiments 76
4.3.1. Design Restrictions and Criteria 78
4.4. Two Axis Piezo Stage 82
4.4.1. Description 84
4.4.2. Implementation 87
4.4.3. Electronics 91
4.4.4. Outgassing 95

5. Results and Discussion **97**
5.1. Probing Thin Film Organic Molecular Systems 97
5.2. Probing Single-Layer Deposition Graphene 102
5.3. Probing Epitaxial Grown Graphene 106

6. Conclusion and Outlook **115**

7. References **119**

A. Technical Drawings **131**
A.1. Vacuum Suitcase 131
A.1.1. Two-Axis Piezostage 135
A.1.2. Vacuum Suitcase - Diamond Windows 150
A.2. UHV Four Point-Probe 152
A.3. JEOL Sample Holder - Modifications 162
A.4. Ultra-high Vacuum Preparation Chamber Design 165
A.5. Vertical Sampletransfer - Modifications 167

B. Electronics **171**
B.1. Four-Point Probe Multiplexer Board 171

B.2. Data Logger 174

C. Serial Communication **177**

C.1. Description 177

C.2. Kleindiek MM3A Micromanipulator 179

C.3. Keithley SourceMeter 2400LV 185

C.4. Arduino Multiplexer Board 190

C.5. MKS 937B Pressure Controller 193

D. Specification Sheets **195**

E. Manuals **211**

E.1. Electrical Shutdown - How to turn the UHV System off and on again 211

E.1.1. Before Shutdown - How to turn the System off 211

E.1.2. After Shutdown - How to turn the System on 213

E.2. Bake-out 215

E.2.1. Preparation 215

E.2.2. During Bake-out 217

E.2.3. Post Bake-out 218

E.3. UHV Four-Point Probe Software - Quick Guide 219

E.3.1. Start-up 219

E.3.2. Overview 220

E.3.3. Connecting to Controllers 223

E.3.4. Micromanipulator Control and Approach Mechanism 223

E.3.5. Four-Point Probe Measurement 225

E.4. UHV Suitcase PiezoStage - Quick Guide 228

E.4.1. Components 228

E.4.2. Connection and Operation 229
E.4.3. Problem Solving 230
E.5. Granville Phillips 835 Vacuum Quality Monitor - Quick Guide 232
E.5.1. Important Notes 232
E.5.2. Components 233
E.5.3. Initial Startup 233

1. Introduction

As a consequence of progressive industrialization, the worldwide power consumption increases every year. The growth of global primary energy consumption has been strikingly stable since 1850 ($2.40 \pm 0.08\,\%/\,\text{year}$) and there are no signs that the growth will slow down [1]. Even without this increase, an energy transition from non-renewable sources such as oil, coal and natural gas towards renewable sources that can be naturally replenished is inevitable, as today's energy sources show signs of being depleted in the near future. Also considering the environmental impact of fossil fuel use with its rapid increase of CO_2 level in the atmosphere [2, 3], new ways to reduce emissions have gained great attention.

Solar energy is by far the largest energy resource on Earth. The amount of energy that the reaches the surface on Earth in one hour ($4.3 \times 10^{20}\,\text{J}$) is more than the energy consumption of humans in one year ($4.1 \times 10^{20}\,\text{J}$). Regarding the potential that solar energy has, combined with the fact that it is nonhazardous, decentralized and an unlimited natural resource, it is hoped that the contribution of solar electricity will increase from $0.01\,\%$ worldwide to an import energy source in the future [4].

Over the last two decades, π-conjugated polymer-based heterojunctions have attracted considerable attention due to their various potential applications in electronic- and optoelectronic applications such as photovoltaic cells [5], light-emitting diodes [6] and field-effect transistors [7]. Plastic solar cells, where the active semiconducting material are conjugated polymers, are interesting alternatives to inorganic semiconducting devices due to their low cost, and fast energy payback time. In terms of materials and device processing, substantial effort has been put into understanding the correlation and interplay between the morphology on a nanometer to micrometer scale and the fundamental physical parameters leading to high power conversion efficiencies. Nowadays, the findings have led to devices of blends of semiconducting polymers and fullerene derivatives that produce power conversion efficiencies exceeding $10\,\%$

under standard solar illumination [8]. As a high conversion efficiency ultimately relies on the conductive and photoconductive properties of the materials, it is important to understand the physical mechanisms of charge generation, transport, trapping and recombination [9, 10]. Although design rules for the chemical structure of materials that lead to a high conversion efficiency were proposed as early as in 2006 [11], not all materials following these rules turn out to be good candidates. The reasons for this are the excitonic and molecular nature of the material that lead to challenges in both experimentally revealing intrinsic properties of the material as well as finding ideal growth conditions for molecular films. Unlike inorganic silicon-based photovoltaic devices, where free carriers are directly generated from the absorption of a photon, organic materials do not screen charges efficiently due to their known low dielectric constant. Instead, extra steps need to be introduced. In these materials, the absorption of a photon leads to the formation of an exciton (bound electron-hole pair located on the same molecule where the net-charge is zero), which then must be split into free carriers before it can decay back to its ground-state. The currently proposed scheme is that the generated excitons migrate to the donor-acceptor interface where they dissociate to a Coulomb bound charge transfer state (CT state). In these CT states, the electron and the hole occupy adjacent molecules and unlike excitons, they display a static electric dipole moment. A large number of groups have observed CT exciton signatures with representative small molecule organic photovoltaic devices [12, 13]. From there, a CT state can dissociate into free charges (polarons) by overcoming the attractive Coulomb barrier, which then can drift to the collecting electrodes. From Coulombs Law, with given molecular dimensions and dielectric constants,

$$E = \frac{1}{4\pi\epsilon\epsilon_0}\frac{q_1 q_2}{r} \tag{1}$$

where ϵ is the relative- and ϵ_0 the vacuum permittivity, q_1 and q_2 are the charges on the particles an r the distance between the point charges, one can estimate an interfacial CT

exciton binding energy of a few hundred meV (assuming a radius $r = 1\,\text{nm}$ and relative dielectric constant $\epsilon = 5$ [14, 15]). How these CT states overcome this Coulomb barrier which is at least an order of magnitude higher than the kinetic energy at room temperature (25 meV) is still under debate. One theory involves hot processes, so called hot charge-transfer states that have an excess amount of energy and can directly convert into free charges [8, 16, 17]. In figure 1, a schematic of exciton generation and charge dissociation is shown that was proposed by Grancini et al. [16]. The time constants at which exciton formation and charge dissociation in organic films happen are in the femtosecond ($10^{-15}\,\text{s}$) range and dissipate within the picosecond ($10^{-12}\,\text{s}$) time regime. In order to temporally resolve the dynamics of charge creation in organic films, ultrafast pump-probe spectroscopy is required.

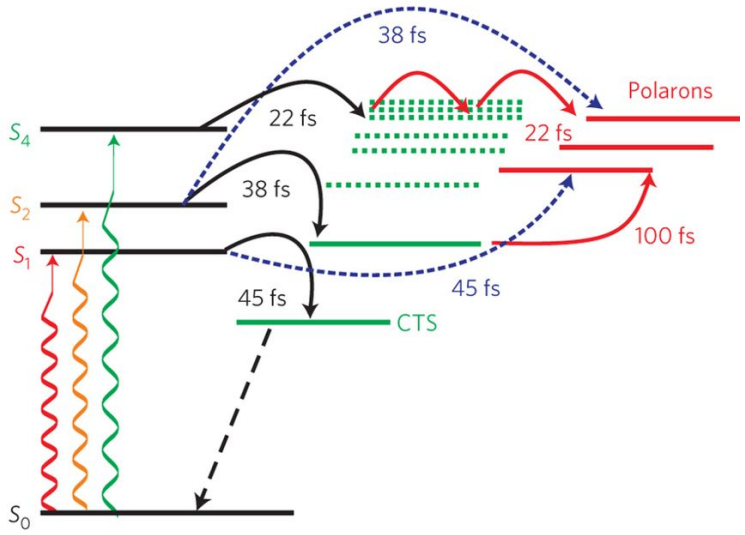

Figure 1: Schematic of exciton generation and charge dissociation in a PCPDTBT/$PC_{60}BM$ molecular film blend. After singlet exciton states are formed (black lines), the excitons can dissociate into the CTS manifold (green lines). From there, the CT states can dissociate into free polarons (red lines). The blue dashed arrows indicate exciton quenching into free polarons. The time constants at which these processes happen are ultrafast (in the femtosecond regime). In order to follow the dynamics of creation, relaxation and decay of low energy excitations in such materials, ultrafast pump-probe laser spectroscopy techniques are required. Figure taken from Grancini et al. [16], figure 5a, page 32.

From a fabrication point of view, in order to efficiently drive free carrier formation and separation, interfaces and architectures need to be controllably designed to energetically favor such charge transfers. Although it is commonly accepted that this exciton scission process works best at a donor/acceptor interface of two constituent materials with energy offsets between their energy levels, the challenge is to find the right packing and dispersion of the molecules, if they are layered or intimately mixed, that provide the best continuous pathways for both the excitons to reach the interface and the electron and holes to traverse toward the electrodes. Theoretical studies have indicated that charge transport properties in such crystalline organic materials depend sensitively on the molecular packing motifs which control the strength of intermolecular coupling either directly due to the overlap of molecular orbitals or indirectly via vibrational mediated coupling. These intermolecular overlaps of directional π-orbitals are responsible for transport whether it is band-like or hopping type. Thus one can design materials with favorable optical properties, but slight variations in their packaging give subsequently different charge transfer properties such as diffusion lengths, drift direction and charge mobility [18, 19].

Besides having the difficulty of controlling intrinsic properties of the material, many applications proposed thin-film geometries. In terms of thin film materials that are normally thinner than 1 µm, the properties of a material are dominated by the surface. In the extreme condition where the film only consists of one monolayer of material, the system is completely reduced to two dimensions (2D) and is all surface. A reduction in film thickness can provide a rich playground for new phenomena and can serve as a sensitive system to explore quantum theory, however, in terms of experimental science, the reduction of film thickness needs special precautions in both sample production and performing measurements that have to be addressed. Generally, surface atoms are significantly affected by adsorbates and cleaning, controlling and characterizing surfaces is challenging. As surfaces are in direct physical and

chemical contact with its surrounding, extrinsic properties such as disorder can easily be introduced to the system. The interaction with surface contaminants thus can completely dominate the underpinning electronic and optical property of the material and mask its intrinsic properties. The adsorbates often act as doping- as well as scattering centers and thus change the material response. In organic photovoltaic systems, such degradation processes can affect the limited exciton lifetime and the limited diffusion length that ultimately will favor charge recombination. It is not surprising that experimental observations are often not in agreement with theoretical models and predicted phenomena as experimental systems are often far from ideal. This draws a lot of challenges into the methods of material purification and device fabrication.

To preserve surfaces that are sensitive to ambient air for analysis, it is usually necessary to handle them under ultra-high vacuum (UHV) conditions. The UHV regime is characterized by pressures lower than 10^{-9} mbar and requires the use of unusual materials for equipment. To reach UHV conditions, a leak-tight chamber typically made of stainless steel and different stages of pumping are necessary. The first stage of pumping is normally achieved by a roughing pump that works in the usual gas flow regime (down to 10^{-3} mbar), followed by a turbo-molecular pump that which is efficient at low pressure (down to 10^{-8} mbar) and gives its exhaust gases to the roughing pump. Although turbo pumps can technically reach UHV conditions, ion pumps and getter pumps are used that are easier to maintain and pump large loads at low pressures. These pumps only work at low pressure in the range of 10^{-6}–10^{-11} mbar and trap rest gases. Additionally, baking the system at high temperatures at various times is required to remove adsorbed molecules such as water from the walls. Other methods to preserve surfaces that would include subsequent encapsulation or inert gas environment after fabrication may open many technical challenges, change the physical properties of the films, are less accessible for surface analysis methods such as surface sensitive Scanning

Probe Microscopy techniques and potentially have the problem of cross contamination.

One of the crucial factors in determining how long a surface can be maintained clean is the number of gas molecules impacting on the surface from the gas phase. From the ideal gas law, the gas density ρ can be estimated,

$$\rho = \frac{N}{V} = \frac{P}{k_B T} \tag{2}$$

where P is the pressure, V is the volume, N is the total number of molecules of the gas, k_B is the Boltzmann constant and T the temperature. Reducing the pressure from ambient air to UHV is already an effective way to reduce the interaction of surfaces with surrounding particles as ρ linearly decreases with pressure. The flux F now can be related the above mentioned gas density by

$$F = \frac{1}{4}\rho\bar{v} \tag{3}$$

where $\bar{v}$ is the mean velocity. The mean molecular velocity can be derived from Maxwell-Boltzmann distribution of gas velocities and is denoted as

$$\bar{v} = \sqrt{\frac{8k_B T}{m\pi}} \tag{4}$$

where m is the molecular mass. Combining the equations 2 and 4, the flux leads to the also known Hertz-Knudsen expression

$$F = \frac{P}{\sqrt{2\pi m k_B T}}. \tag{5}$$

Expressed in SI units, the flux denotes the number of molecules impacting with the surface per square meter per second. The number of atoms on the surface is typically on the order $10^{19}/\mathrm{m}^2$ and if we assume that every gas particle that impacts the surface is directly absorbed

by the surface, the time to form a monolayer of contaminants as a function of pressure can be estimated. This relationship is shown in figure 2. A general guideline that is used for UHV work is that a pressure of 10^{-6} mbar a crystal surface will be contaminated with a monolayer of gas in one second. Every order of magnitude drop in pressure will result in an order of magnitude increase in time it takes to contaminate the crystal with a monolayer of material. Organic materials however are normally not that reactive and ion pumps, getter-pumps and titanium sublimation pumps that are necessary to reach UHV pump chemically reactive (H_2O, O_2) very efficiently. The majority of the residual gases remaining in a UHV chamber (e.g. H_2, CH_4, N_2) are non-reactive and thus the surface of a material prepared under UHV conditions can normally be kept clean for much longer time presented in figure 2. Thus, the need for good UHV conditions is inevitable to maintain a clean surface, especially when experiments are involved that can run for hours or even days.

To preserve samples from exposure to air, it is important as well to already start with the fabrication process under UHV. Thin films can be grown under UHV condition by using thin-film deposition techniques. Thermal evaporators that are nowadays commercially available increase the vapor pressure of a source material through resistive heating. The source material is evaporated and can condense back on a target object. The evaporation rate can be monitored by a quartz crystal micro-balance allowing to grow thin films with sub-angstrom to nanometer per second growth rates. The target object (substrate) can be brought under UHV conditions over a high-vacuum load-lock and cleaving, heating and annealing of the substrate allows to remove surface impurities from the target object. By controlling the substrate temperature, evaporation temperature and growth rate, films from sub-monolayer to micrometer thicknesses can be grown in a systematic manner.

Although there are still a lot of new papers being released every week about new molecules that have the potential to break a new barrier for higher efficiencies, research on organic

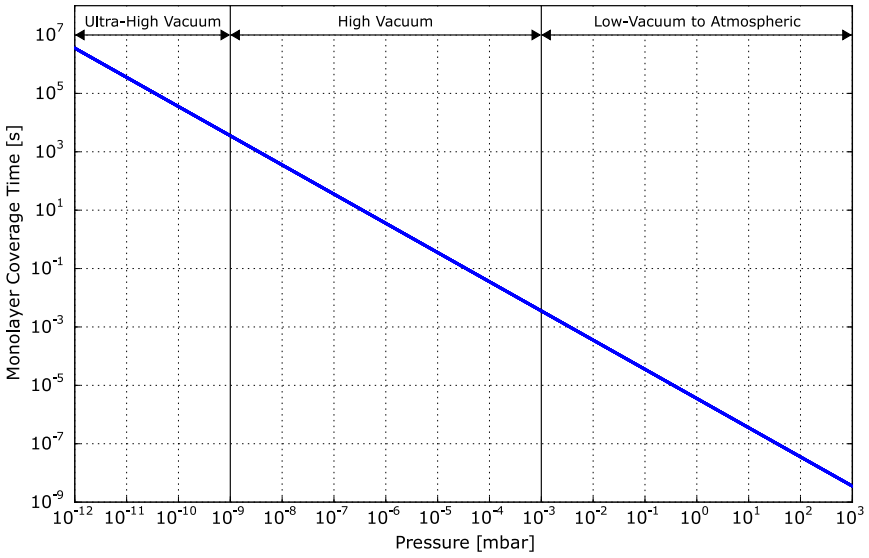

Figure 2: Time needed to form a monolayer of surfactants as a function of pressure at room temperature. Here, the assumption is made that the number of atoms on the surface is in the order of $10^{19}/\mathrm{m}^2$, that every particle that impacts the surface is absorbed and that the average density of the rest gases (around 29 g/mol) does not change. A guideline is that it takes about 1 s at 10^{-6} mbar, and with every order of magnitude lower, the time increases by a magnitude. Under UHV conditions (lower than 10^{-9} mbar), surfaces can be maintained clean for long enough to perform experiments.

photovoltaics has also shifted from finding new materials to understanding the fundamental processes during charge generation and transport. The development of suitable cleaning protocols and finding the right growth conditions is often a lengthy process and must be aided by characterization tools. Low-Energy Electron Diffraction (LEED) for global characterization [20], X-ray Photoelectron Spectroscopy for energy level determination [19, 21] and Atomic Force Microscopy [22, 23] are common techniques to reveal the crystal structure and packing of the molecules within the films.

1.1. Aim of this Work

Since organic films suffer from degradation processes due to exposure to ambient air, it is often challenging to measure the same sample in different laboratories under the same conditions that are necessary to investigate the processes leading to charge generation and separation in organic films. The long-term goal is thus to establish a facility that allows the systematic investigation of organic systems under well-defined UHV conditions. The vision is to apply various characterization tools that are traditionally not performed in UHV, ideally on the same samples, to achieve a comprehensive understanding of the charge generation and separation in model systems. This includes determining the effect of ambient contamination such as H_2O and O_2 on intrinsic properties. To achieve this, a new UHV system needed to be built that allows to controllably grow organic molecular films on various substrates by thermal evaporation technique. This chamber will be equipped with a four-point probe setup that allows to directly measure the DC conductivity of the produced films. Since the four-point probe setup will be directly implemented in this evaporation chamber, it can be used to directly measure the electrical conductivity of the films during the bottom-up layer-by-layer sample production, where growth parameters can directly be adjusted and optimized in order to produce conductive films.

From there, an UHV suitcase that can be attached to the evaporation system will be used to transport the samples under UHV at all times allowing to further multidisciplinary investigation. The goal is to use surface characterization tools in the Grutter SPM group such as Atomic Force Microscopy (AFM) and Kelvin Probe Microscopy (KPFM) that allows to map the work function and gives information about the composition and electronic state of the local structures on the surface of the material [24, 25]. These characterization tools are implemented in the JEOL UHV chamber and the suitcase will be used to transport the samples from one UHV system to the other. Further, to gain better understanding in the

fundamental processes during charge generation and transport in OPV devices at the molecular scale, a collaboration with Prof. Carlos Silva's Ultrafast Spectroscopy Lab, formerly at Université de Montréal and now at Georgia Tech University, and Prof. David Cooke's Time-Resolved Terahertz Lab at McGill University was started. Since laser setups are normally in air, the suitcase will be equipped with special windows that make ultra-broadband transmission possible. This way, the suitcase can be placed directly into the beam line of various laser spectroscopy setups allowing to directly probe the samples under UHV conditions. Time-resolved optical spectroscopy with temperature-dependent photoluminescence (PL) can be used to characterize the energy of luminescent charge-transfer excitons relative to bulk excitons in the material. This will give information about the energy migration as well as dissociation of the exciton and can determine the lifetime and the diffusion radius of the created excitons. To investigate the picosecond conductivity dynamics of the materials, time-resolved terahertz spectroscopy (TRTS) that is sensitive to mobile carriers with a sub-100 fs resolution can be used. The long-term goal was to use the available techniques to directly resolve the creation of mobile charges in polymer films, while using scanning probe techniques to bringing together a vision of designing and characterizing molecular- and electronic structure, with optical and electrical characterization tools.

In this thesis, the main focus is the design concepts and the implementation of the new hardware and software that needed to be set up to achieve this goal. Chapter 2 will give an overview of the UHV hardware that was set up, chapter 3 will go in detail about the four-point probe setup, and will give a broader insight into its challenges and limitations, especially in terms of measuring organic materials with high resistivity and thin films in general. Chapter 4 will give an overview on the requirements that the suitcase had to fulfill, how these requirements have guided the design and will show the capability of this unique system. In chapter 5, preliminary proof-of-principle results on organic evaporated films and graphene

will be presented, and in chapter 6, an outlook for further experiments will be made. The project can be considered as a work in progress and it is hoped that this thesis will guide and assist future students to take over the project and to directly jump in where this thesis ends. To enable this, deeper details about the system, all technical drawings, information about the home-built electronic boards, the most important serial communication implementations, as well as specification sheets and manuals for operation are presented in the appendix.

2. Ultra-high Vacuum System Overview

The instruments that are fundamental to this thesis are a unique combination of an UHV sample preparation chamber that is capable of producing both organic and metal films, can measure the direct-current conductivity of the samples by a four-point probe approach and allows samples to be transported to various spectroscopy laboratories while maintaining UHV conditions. Although there were other UHV systems already available and set up in the research group (see figure 3), a new sample preparation chamber was designed. The already existing UHV systems in the research groups use very special sample holders, unique transfer tools and have a layout that was adjusted, modified and modified over years. Adding additional functionality to an existing chamber thus can be problematic as it can interrupt and conflict the setup's functionality.

In our case, if we want to implement additional evaporators for thick film production through

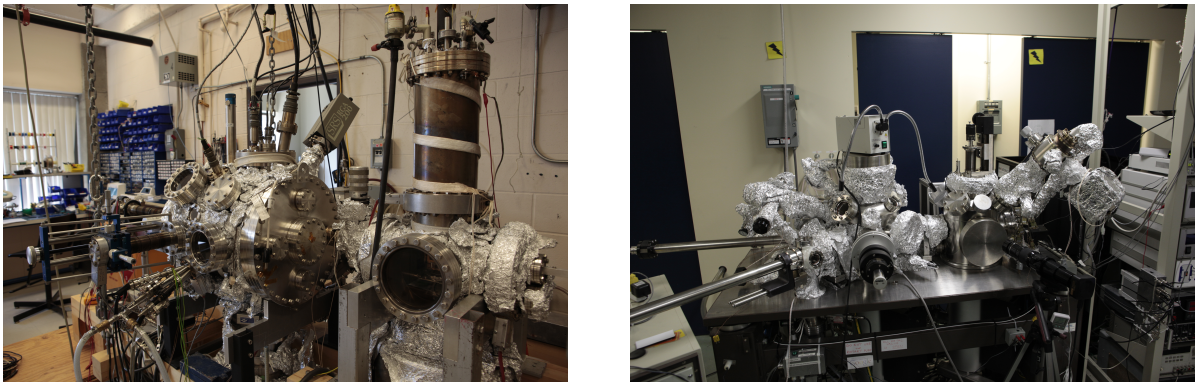

Figure 3: Two UHV systems available in the Grutter research group with separated preparation and measurement chamber. Left: Field-Ion Microscope in the Rutherford physics building, right: JEOL 4500A Atomic Force Microscope in the basement of the Wong building.

evaporation, the shape and outline of the preparation chamber plays a crucial role. Since the existing chambers have cylindrical- and hemispherical outline with additional sensors and equipment at the focal points of the chamber, adding additional thick film evaporators would cover and damage the sensitive equipment that is in the evaporation path of the newly added

evaporators. Namely LEED detectors, ion gauges, sputter guns, sample storages, cleaving stages and ion pumps would be at risk to suffer from damage. Thus it was inevitable to design and set up a new chamber.

In this part, all the equipment and outline of the chamber will be listed. The new ultra-high vacuum chamber can be separated in four compartments that are connected by gate valves. The gate valves allow independent venting, baking and repairing of the system.

1. **Load Lock:** A conflat (CF) 6-way cross is the main body of this chamber. A CF 4.5 inch viewport on one side can be removed to load samples and can be used to observe sample transfer inside the chamber. Disposable copper UHV gaskets are used to seal the detachable viewport. The load lock is pumped by a Pfeiffer HiPace 300 turbomolecular pump (260 L/s N_2 pumping speed, 1×10^{-7} mbar ultimate pressure) backed by an Adixen Pascal rotary vane pump (1×10^{-3} mbar maximum fore-vacuum). The pressure is read by an MKS 345 Pirani (atmospheric to 1×10^{-3} mbar) and an MKS 421 Cold Cathode (1×10^{-3} mbar to 1×10^{-11} mbar) gauge. A pressure of below 5×10^{-6} mbar can normally be achieved in less than 45 min. When a new sample is loaded to the system, the load lock is typically baked for 6 h at 120 °C over night to remove water and oxygen sufficiently. The load lock is directly connected to the preparation chamber and the UHV suitcase. A UHV Design Powerprobe transfer arm is used for horizontal sample transfer to the preparation chamber and a modified UHV Design Pincer Grip (see appendix A.5) is used for vertical transfer to the suitcase. Figure 4 shows a picture of the implementation.

2. **Preparation Chamber:** This chamber facilitates all of the parts that are needed for sample preparation and measurement. Most UHV systems are normally divided in two completely separated chambers where one part is used for sample preparation and the other chamber is used for measurements. This way, sensitive measurement equipment

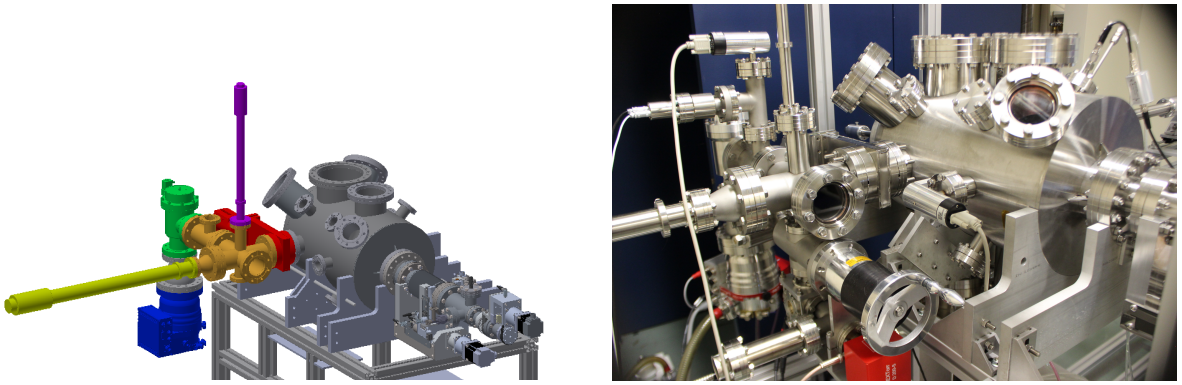

Figure 4: Schematics and implementation of the Load Lock. Left: Main body with viewport for sample exchange (orange), horizontal transfer arm (yellow) for sample exchange towards preparation chamber and modified pincer grip transfer arm (violet) for vertical transfer towards vacuum suitcase, manual gate valve (red) and pneumatic gate valve (green) to isolate the load lock from the preparation chamber and the turbo pump (blue). Right: Picture of the implementation.

is not contaminated during sputtering and evaporation processes and the vacuum in the separated measurement chamber can be kept clean. In our case, only one chamber body is used. Instead, the chamber is set up in a horizontal plane and two vertical planes and a total of 19 flanges are arranged in these planes (technical drawing in appendix A.4). In the horizontal plane, sample alignment and transfer are arranged and the vertical planes are used to separate sample preparation and measurement from each other. This way, the chamber design can be kept small, less pumps and vacuum parts are required and bake-out time can be reduced significantly. In figure 5, a cross-sectional view through the main chamber is shown. The chamber is pumped with a Gamma Vacuum T300 ion pump (300 L/s N_2 pumping speed, 1×10^{-11} mbar ultimate pressure), with an integrated titanium sublimation- and cryo-pump. No roughing- and turbo pump are connected to the main chamber as the pre-vacuum is achieved by pumping through the load-lock. The pressure is measured with same mentioned MKS 345 Pirani and MKS 421 Cold Cathode gauge and is typically $\sim 1 \times 10^{-9}$ mbar. The chamber is equipped with a Creaphys three-pocket organic molecular evaporator (3x 2 cm^3 shuttered ceramic

pockets, temperature range 50–800 °C, typical deposition rates 1–5 Å/s, focal point at 180 mm) and an Oxford Applied Research EGCO4 four-pocket e-beam metal evaporator (maximum filament current 6.5 A at 8 V, typical deposition rates ≤5 nm/min). An Inficon bakeable quartz-crystal microbalance is used to monitor the deposition rate of the films. A UHV Design multimotion sample manipulator that is capable to cool and heat the sample (−196–800 °C), and to translate and rotate the sample (250 mm z-travel, 25 mm x- and y-travel, 360° primary and secondary rotation). A stationary support structure on the other side of the chamber is used as a docking station to bring the four-point probe system and the multimotion sample manipulator together. The chamber can be separated from the load lock and the four-point probe exchange chamber with gate valves to avoid large quantities of gas during sample transfer, venting or baking.

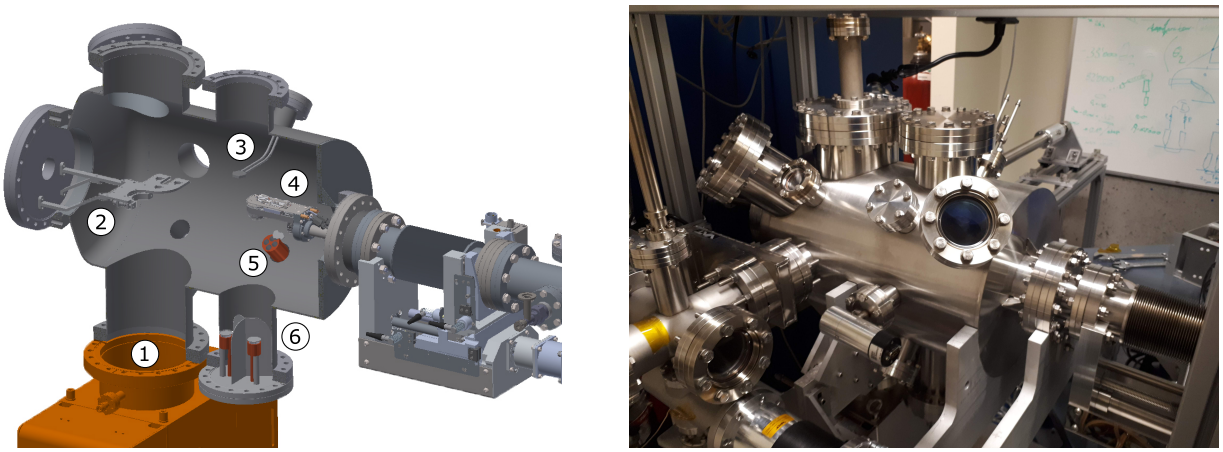

Figure 5: Left: Cross-sectional view through the main chamber. 1) Ion pump, 2) stationary support structure for the four-point probe, 3) quartz-crystal microbalance, 4) multimotion sample manipulator, 5) four-pocket mini e-beam evaporator and 6) three-pocket organic molecular evaporator. Right: Final implementation of the chamber.

3. **Four-point Probe Chip Exchange Chamber:** The chip exchange chamber hosts a Kleindiek MM3A micromanipulator that can be used to bring micro-fabricated four-

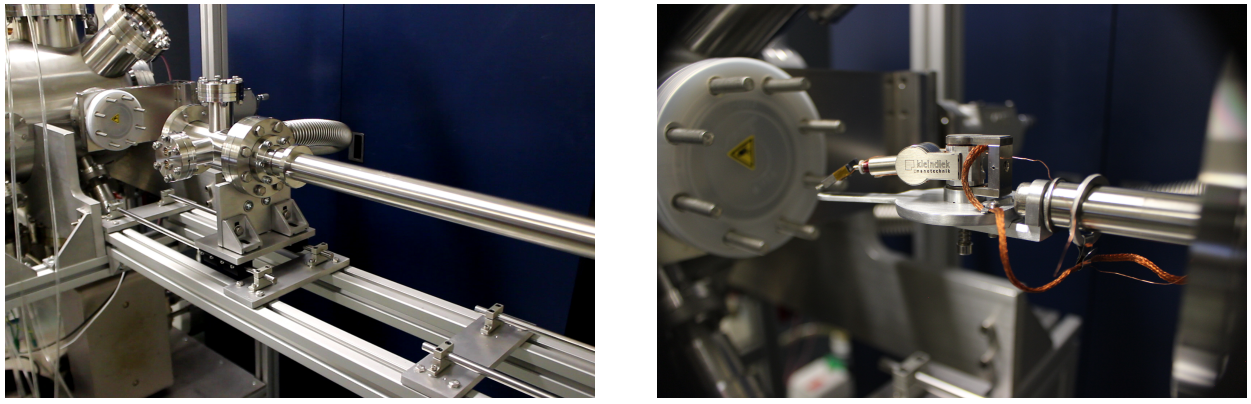

Figure 6: Four-point probe setup. Left: Exchange chamber, right: Kleindiek MM3A micromanipulator with mounted four-point probe chips outside the exchange chamber.

point probe chips in contact with the sample. The four-point probe setup is mounted on a linear transfer arm and can be transferred into the preparation chamber and docked on the stationary support structure inside the preparation chamber. The idea behind this design is to be able to separate the setup from the preparation chamber in order to keep the measurement tools clean when sample degassing and preparation procedures are carried out and to be able to vent the exchange chamber independently when four-point probes need to be exchanged. The exchange chamber is differentially pumped through the load lock and thus no additional pumps are required. When the fragile four-point probe chips need to be replaced, the micromanipulator can be retracted from the preparation chamber, and after independent venting the exchange chamber can be slided open through a linear slider mechanism. Figure 6 shows the implementation. The working principle of the four-point probe setup will be discussed in full detail in section 3.

4. **Ultra-high Vacuum Suitcase:** The UHV suitcase can be mounted underneath the load lock, samples can be transferred vertically into the suitcase and it can be completely detached from system without the loss of UHV. This makes it possible to trans-

port samples to other laboratories and systems. A non-evaporable getter pump (NEG) with integrated ion pump (NexTorr D200-5, 80 L/s N_2 pumping speed, 1×10^{-11} mbar ultimate pressure) is attached to the suitcase that allows to maintain UHV conditions without the need of a power supply. The suitcase has an all-metal gate valve for long durability (VAT All-metal Gate Valve, 482 Series) and hosts a home-built two-axis piezo stage for sample positioning. Special designed and brazed diamond windows to copper on a CF 2.75 inch flange with leak-rates below 10^{-10} mbar l/s allow ultra-broadband transmission while maintaining full UHV compatibility. Further, a Residual Gas Analyzer (Granville-Phillips, Series 835 Vacuum Quality Monitor) and a leak valve (VAT Variable Leak Valve, Series 590) allow to monitor the quality of the UHV and allows the additional possibility to controllably leaking gases into the system. Figure 7 shows the implementation. The design choice and working principle of the UHV suitcase will be discussed in full detail in section 4.

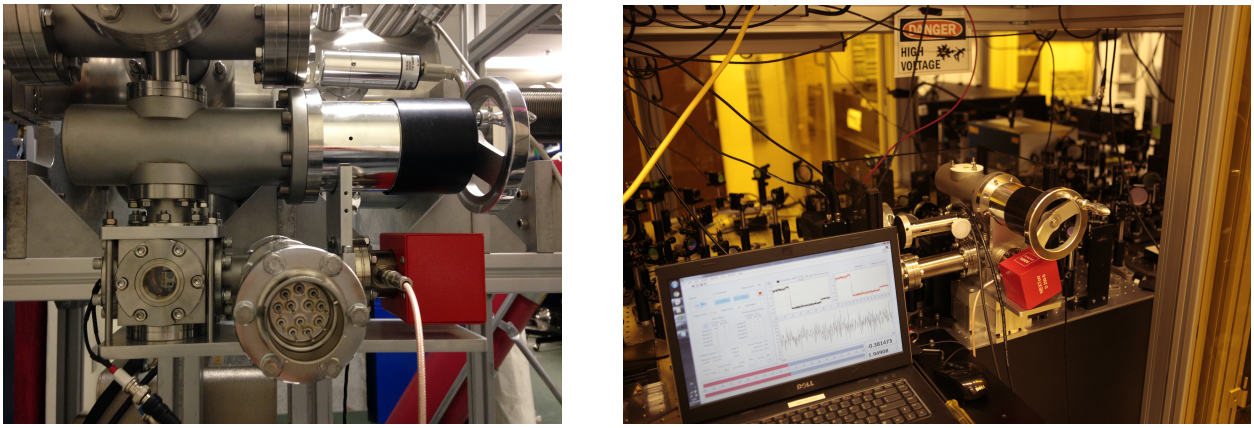

Figure 7: Ultra-high Vacuum Suitcase. Left: Attached to the load lock of the preparation chamber. Right: Transported and installed on the optical table of the ultrafast terahertz setup in the Cooke laboratory at McGill University.

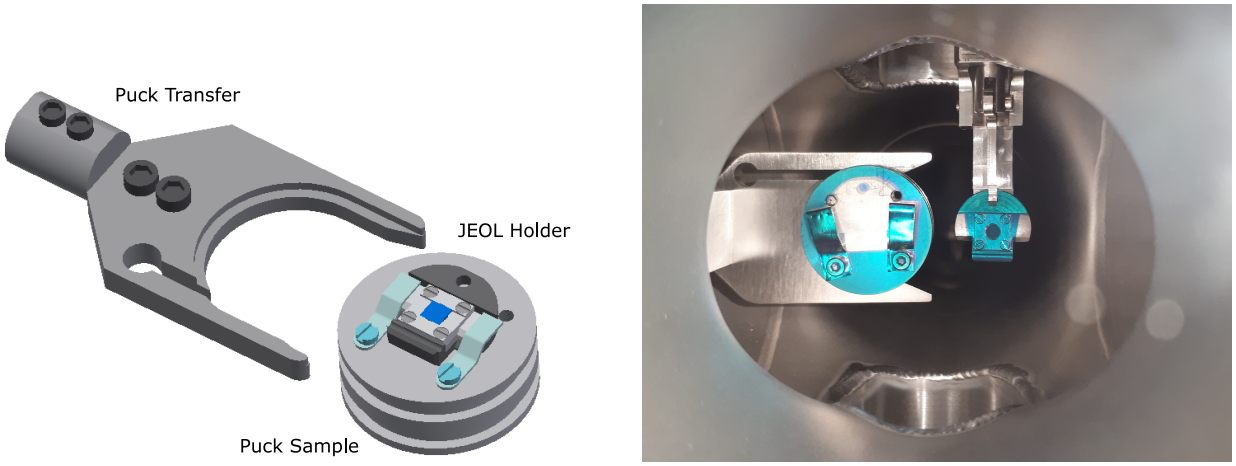

Figure 8: Left: Schematics of the sample puck with the JEOL holder on top. Right: View through the load lock. The puck is mounted on a linear transfer arm for horizontal transfer and the JEOL holder can be grabbed by a modified micro-grabber in order to transfer the JEOL holder vertically towards the suitcase. This picture was taken after an evaporation cycle where the blue color is due to a 1 µm thick film of TIPS-pentacene.

2.1. Sample Transfer

In order to transfer samples from the load lock to the preparation chamber and the vacuum suitcase, a puck style sample design was chosen. Unlike other sample designs such as the flag style (Omicron) and rotate to lock and release sample holders (JEOL), the puck style design offers a simpler transfer because a successful transfer is less dependent on the orientation of the puck. Further, the relatively large top surface of the puck (1 inch diameter) offers enough space for potential future modifications. The puck itself is made of molybdenum that allows sample heating above 1000 °C. However, molybdenum can be tricky to machine because it is considerably more abrasive than steel and has the tendency to chip while being machined. In our case, we added four holes with threads to the puck to be able to mount clamps on top of the puck. I used low drilling speeds and carbide graded taps to achieve good results. On top of the sample puck, a JEOL sample holder can be mounted. This holder was chosen because the UHV AFM system in the Wong laboratory only allows to measure samples that

are mounted to this specific holder geometry. In our case, the JEOL holder was modified to hold a 3 mm × 3 mm diamond wafer and has a hole behind the crystal in order to be able to perform transmission spectroscopy experiments. The JEOL holder can be vertically transferred to the suitcase by a modified pincer grip (see appendix A.3). In figure 8, the sample puck configuration with the JEOL sample holder is shown.

2.2. Water Cooling

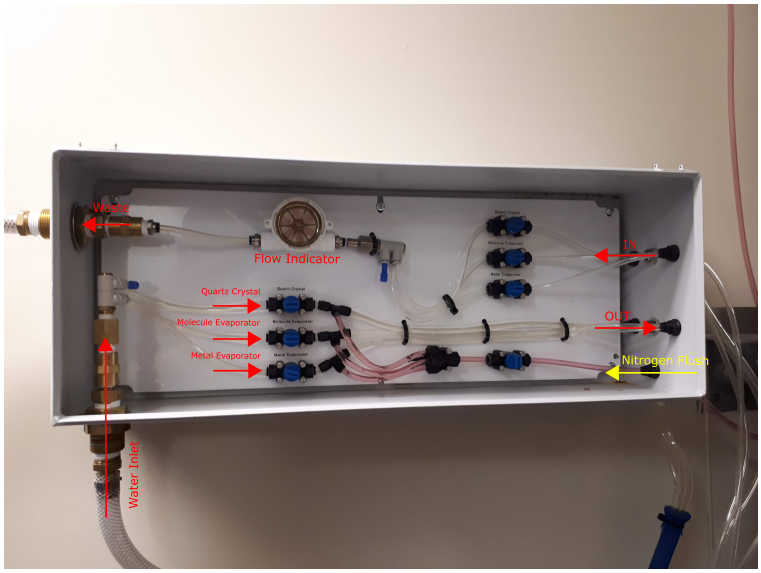

Figure 9: Water cooling line for the molecule evaporator, metal evaporator and quartz crystal microbalance.

The organic molecular evaporator, the e-beam metal evaporator and the quartz-crystal microbalance that are installed in the preparation chamber need water cooling in order to use the full potential of the PID temperature controllers and to get necessary frequency stability on the quartz crystal for precise film thickness readout. Figure 9 shows the panel to control the water flow and to flush all lines with nitrogen. The water is filtered (McMaster Carr, Plastic Filter Housing, 4448K36) and then passes through the panel. On/Off valves control the water to the two evaporators and the quartz microbalance (McMaster Carr,

Push-to-Connect Water Valves, 4764K46). A flow indicator is used to observe the water flow (McMaster Carr, Flow Transmitters for Water, 9687K11). To prevent contamination sites throughout the piping and to remove the water lines from the evaporators and microbalance after use, an additional nitrogen line allows to flush the water lines.

Be aware that lot of different piping standards exist (NPT/BSPT/BSPP, imperial/metric, inserts/ferrules/push-to-connect). In order to keep the waterline connections uniform through out the system and to avoid headaches, all lines were adapted to 6 mm outer diameter tubing and 6 mm push-to-connect fittings. For low-pressure room-temperature applications, push-to-connect connectors came in handy because it is very adaptive and no tools are needed to connect and disconnect the lines.

2.3. Bake-out Tent

In order to remove absorbed impurities from the walls of an UHV system, the system is uniformly heated at high temperatures while pumping. Since ion pumps have a finite gas capturing capacity, a bake-out into the turbo pump is recommended in order to prevent high gas loads into the ion pump. Generally, stainless steel systems are baked at around 120 °C to remove water efficiently and at higher temperatures in the range of 150–200 °C to degas most of the common hydrocarbons. There are many methods to bake out metal systems and most common ones are heating tapes, infrared radiation heaters, clamp-on band heaters, heating fans and internal light-bulb heaters. In order to insulate the system during a bake-out and to achieve an even heat distribution on the system, the system can be either covered with aluminum foil or with an insulating heating tent.

In our system, silicone rubber encapsulated heating tapes with incorporated percentage controller (Omega HTWC Series) are used to heat the system. In hindsight, non-rubberized heating tapes would have been a better choice as they tend to leave an oil-like residue behind

after a bake-out, the silicone rubber dries out and starts to become brittle after a while. The system has an aluminum frame so that a heat tent can be set up in a very simple manner. Figure 10 shows the setup of the bake-out tent. In appendix E.2 a step-by-step manual can be found how to set up a bake-out of the system. In appendix B.2, a home-built data logger is shown that allows to both record pressure and temperature of the system. The data logger runs a web application that always makes the data accessible from any computer connected to the internet.

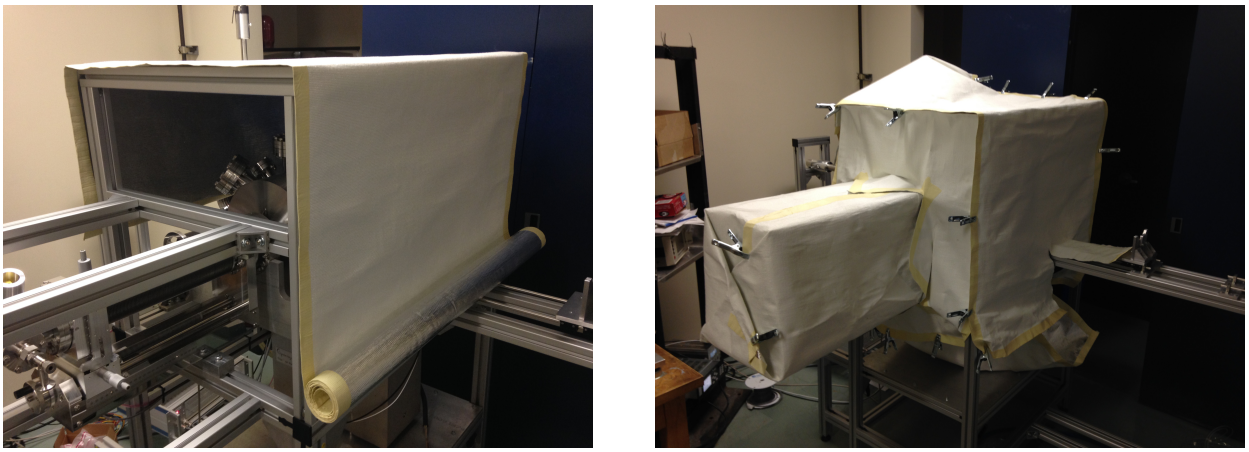

Figure 10: Left: Preparation of the bake-out tent. A permanent aluminum frame around the whole system was set up in order to use it as a bake-out tent. Heat-deflecting fiberglass fabric with one-sided aluminum coating is ideal to insulate the system while baking. Right: System covered with the fabric and ready for a bake-out. All-metal clamps hold the sheets in place.

3. Ultra-High Vacuum in-situ Four-point Probe Method for Electrical Characterization of Thin-film Materials

3.1. Introduction

The specific electrical resistivity ρ of a solid represents an important fundamental property as it influences the series resistance, threshold voltage, capacitance and other important parameters of electronic device structures. From a fundamental point of view, a current is drawn when an electric field is applied to a material. The resistivity ρ of an isotropic material then is defined as the ratio between the electric field E and the current density J:

$$\rho = \frac{E}{J} \tag{6}$$

The resistivity of the material is measured in $\Omega\,\mathrm{cm}$, the electric field in V/cm and the current density in $\mathrm{A/cm^2}$. Experimentally, the resistance R is derived from the ratio of an applied voltage V and current I. The resistance R however is intrinsically geometry dependent and sensitive to the set-up such as electrode position and limiting boundary conditions. For example, determining the resistance R between two electrodes by applying a defined current and measuring the voltage drop between them is usually incorrect, as it includes the contact resistances R_C at the positions of the probes, which are in series with the resistance of the sample. This problem was addressed the first time in 1915 by Wenner [26] while trying to measure the soil resistivity of the Earth. An in-line four-point probe setup with equidistant spacing was proposed, where a current is applied through the outer two probes while measuring the voltage drop through the two inner probes. If the impedance of the voltage probes is infinitely high, no current is flowing through the inner probes and thus the

ratio of V/I is a measure of only the sample resistance R. The contact resistance R_C thus can be eliminated, irrespective of whether the probe contacts are ohmic or Schottky type. In 1954, the four-point probe geometry was used by Valdes [27] to measure the resistivity ρ of a semiconducting Germanium wafer and since the early 1970s, this method has become the acknowledged method procedure for testing materials throughout the semiconductor industry [28, 29].

In the in-line four-point probe setup where the probes are aligned in an array, the effect of limited geometries applied to completely arbitrary shapes is important to consider. How to accurately derive the intrinsic material's resistivity ρ from the measured resistance R can be a challenging task as inhomogeneities of the sample as well as geometrical effects affect the paths of current flow and are often not obvious. The bulk resistivity of a sample is generally expressed as

$$\rho = F\frac{V}{I} \tag{7}$$

where F is a geometric correction factor which is divided into other factors related i.e. to the finite thickness of the sample, the alignment of the electrodes relative to the sample edge and the finite lateral width of the sample [30]. Many theoretical studies have been triggered to accurately determine the correction factors for the different configurations over the last decades. As this work is focusing on an experimental implementation technique to measure the resistivity of a thin film material, the inclusion of a sophisticated view of all aspects would exceed the scope of this work. The interested reader is referred to Smits [28] and Vaughan [31] for mathematical theory on isotropic, circular samples and Schroeder [32] and Guise et al. [33] for technical aspects of implementation.

Fast forward, we want to combine the theoretical and practical findings to our specific implementation and research topic and find an idealized way to get around the issue with determining correction factors. To remind the reader again, the goal is to measure thin or-

ganic films, with thicknesses of 100–1000 nm. The films can be controllably grown in our UHV chamber with growth rates of 1–10 Å/s. The substrate will be a 3 mm × 3 mm, 0.3 mm thick diamond crystal and thus the underlying substrate will be insulating. Diamond as a substrate is necessary for optical-pump THz-probe and will be explained in detail in section 4.3. In the following part, simplified equations will be presented on how we can extract ρ from a measurement. Please note that ρ, ρ_{3D}^{line} and ρ_{2D}^{line} in the following part will be one and the same material property, where the upper cases will denote the type of measurement technique (in-line four-point probe) and the lower cases will denote if a 3D bulk or 2D sheet system is assumed.

From the given boundaries from our sample, we can have a look at the relations that are derived for an infinite 3D bulk system and a 2D sheet system as shown in figure 11.

For the ideal case of a 3D semi-infinite material with the four electrodes equally spaced and

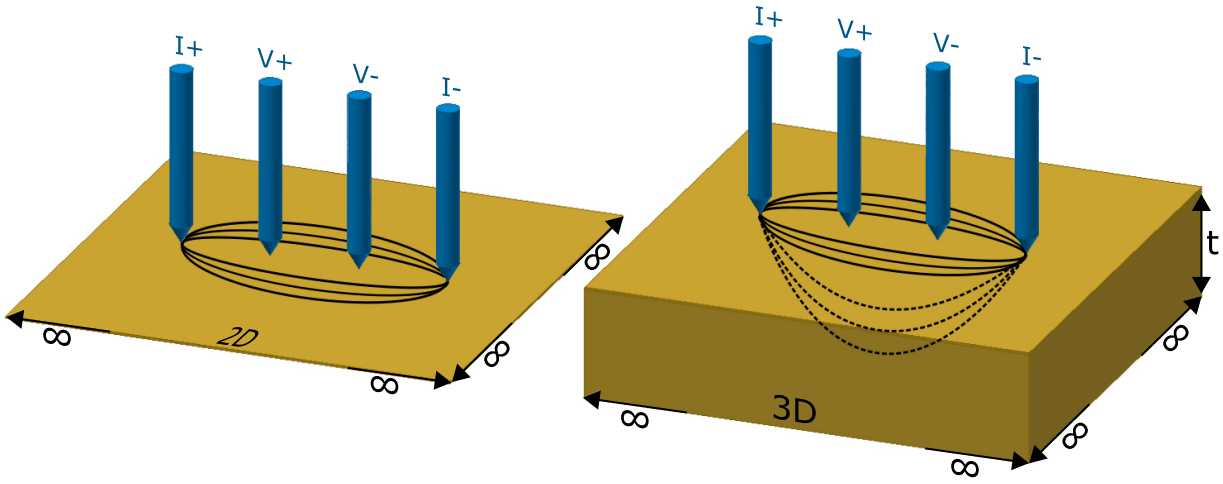

Figure 11: Comparison of the current flow in an infinite 2D sheet and a semi-infinite 3D material in a linear arrangement of the probes. When the thickness of the material becomes relatively small compared to the probe spacing, the system can be considered as a two-dimensional entity where the current implied to the system is along the plane of the sheet, not perpendicular to it.

aligned in a line, the material resistivity is given by

$$\rho_{3D}^{line} = 2\pi s \frac{V}{I} \tag{8}$$

where s is the probe spacing, V is the measured voltage drop between the two inner probes and I is the current flowing through the outer pair of probes. In the theoretical models to calculate the resistivity of thin films with an underlying non-conducting substrate, it was shown that if the probes are aligned collinear and with equidistant spacing and the conducting film thickness is less than half of the spacing of the probes s and the edges of the sample are more than four times the spacing distance from the measurement point, the resistivity of a sample can be expressed as

$$\rho_{2D}^{line} = \frac{2\pi}{ln(2)} t \frac{V}{I} = 4.53t \frac{V}{I} \tag{9}$$

where t is the thickness of the sample. Thin layers are often characterized by their sheet resistance R_{sh} expressed in units of $\Omega/\,\mathrm{sq}$. The sheet resistance of a uniformly doped sample is given by

$$R_{sh} = \frac{\rho_{2D}^{line}}{t} = 4.53 \frac{V}{I} \tag{10}$$

with the condition that $t \leq s/2$ [32]. The sheet resistance is invariable under scaling of the film contact and therefore is often used to compare the uniformity of the electrical properties of devices that are significantly different in size. The four-point probe technique does not directly measure the thickness of thin films, but from the equations 9 and 10, one can see that if two of the following three characteristics for a given sample are known, a four-point probe can be used to determine the third characteristic: 1) the bulk resistivity in $\Omega\,\mathrm{cm}$, 2) the sheet resistance in $\Omega/\,\mathrm{sq}$, 3) the sample thickness. Since the resistivity is often unknown for organic materials, it is important to measure t by means of AFM or another profilometry technique to extract ρ.

At this point, it is important to note that from the equations given above, ρ can be extracted relatively simple for conductors that follow Ohm's law, which means conductors that have a linear current-voltage curve. In these materials, either a DC or low-frequency AC lock-in metrology module can be used to extract ρ. However, many materials do not obey Ohm's law, and especially semiconducting materials show a rather diodic current-voltage behavior. Thus, the current needs to be swept so that the current-voltage characteristic curve of the material can be obtained. Further, since the electrical conductivity of a semiconducting material can be changed by the absorption of light, it is important to do measurements in the dark and compare it to its photoconductive properties.

Further, standard four-point probes that are widely used and commercially available normally use tips that are relatively large and the spacings between the probes are often in millimeter range. Since we are using a small CVD single crystal diamond as a substrate, correction factors for boundary conditions would have to be considered again and proper extraction of ρ would thus be complicated. Such macroscopic probes would also easily damage the relatively soft organic films since large contact forces are exerted to those sensitive surfaces. Commercially available systems, such as the Unisoku SPM USM1200, the Kleindiek Prober Shuttle, the Omicron Nanoprobe and the mProbe Multi-Tip SPM use macroscopic tips. To address these limitations, cantilever-based microscopic four-point probe chips have been developed earlier and are commercially available [34–36]. By reducing the electrode pitch significantly compared to macroscopic point probes, thin films can be measured accurately and benefit from an increased sensitivity to the surface conductance. Approaches towards reducing the pitch were made by using micro-fabricated cantilever arrays, where current lithography processes allow to reduce the pitch below 1 µm [37, 38]. Compared to the previously mentioned commercially available techniques, placing the micro-cantilevers in an array on one chip allows to use only one positioning manipulator instead of four independent

manipulators. Further, fixed and precise cantilever spacing leads to a more accurate measurement and the down-scaling allows a possible direct mapping of the micro-conductivity of the sample when used in combination with a high precision positioning stage [35]. Also, the spring-constant of cantilevers can directly be controlled during the manufacturing process and can be reduced significantly compared to macroscopic probes. Thus, it allows a less destructive approach towards soft and thin films where the probes penetrate less through the layer of interest revealing the very local in-plane conductivity on a micrometer scale.

3.2. Micromanipulator Implementation

In order to position the four-point probes on the sample and to bring them in electrical contact with the sample under UHV conditions, a commercially available Kleindiek three degree of freedom micromanipulator with revolute-revolute-prismatic (RRP) actuator structure was implemented to the system (see figure 12). Unlike linear nanostages which normally only provide a couple of micrometers working range, the micromanipulator provides a wide range of action. Both revolute actuators can independently move by 240° and the prismatic actuator can move by 12 mm using piezoelectric motors. Unlike other electric motors, piezoelectric motors are ideal for the UHV science environment due to its low outgassing, absence of grease, high temperature tolerance and low source of vibration and noise.

In the Kleindiek micromanipulator, the motors consist of a stator and a slider. These motors can be moved in a *fine* and *coarse* mode. In the fine mode, the stator deflects in extremely small steps. A voltage between ±80 V can be applied through a 12-bit DAC, allowing 4096 step sizes. The prismatic actuator has a total deflection range of about 1 µm, thus each step corresponds to roughly 0.25 nm and the revolute actuators have a fine range of about 20 µm thus corresponding to about 5 nm step size. The software has three fine mode speeds available

(f01, f08, f64), where the numbers represent the numbers of fine steps executed each time the controller receives a command to move. This fine mode actuation is purely piezoelectrically, as the slider touches the stator and thus is held in place by friction during deflection. In the coarse mode, momentum is used to push the stator forward ('stick-slip' principle). In stick-slip motion, the frictional force between stator and slider is exceeded during a fast movement of the actuation piezo. The slider thus moves relative to the stator ('slip' phase) until friction stops it. A slow piezo movement then resets the stator extension ('stick' phase). This way, infinite motion in either direction is theoretically possible and is normally only limited by its geometry. The software has three coarse mode speeds available (c01, c08, c64) where the number corresponds to the number of coarse steps executed each time a command is received. Due to the large operation range and small step size resolution in combination with the possibility to operate it under UHV conditions, the manipulator offers a low cost and ready to use solution. The manipulator can be equipped with a four-point probe holder that will be used to perform electrical conductivity measurements on various samples. The manipulator's interface can be used to implement an automatic approach mechanism to get in electrical contact with the sample. Figure 12 shows the Kleindiek micromanipulator with the chip holder implementation that will be used to perform four-point probe measurements.

Over the last few years, the Kleindiek micromanipulator has especially found its implementations in the field of Electron Microscopy. It has been employed in a wide spectrum of SEM, FIB and other microscopes. The main modes of operation are mostly high-vacuum (HV), where the main issue is minimizing scattering of the electron beam before reaching the specimen. Unlike UHV chambers, HV chambers can be pumped from ambient air to a sufficient 10^{-6} mbar range in less than 30 min and often a further bake-out is not required. A roughing- and turbomolecular pump are generally sufficient enough to reach these pressure levels. In these HV systems, the main chamber can be vented each time a sample needs to

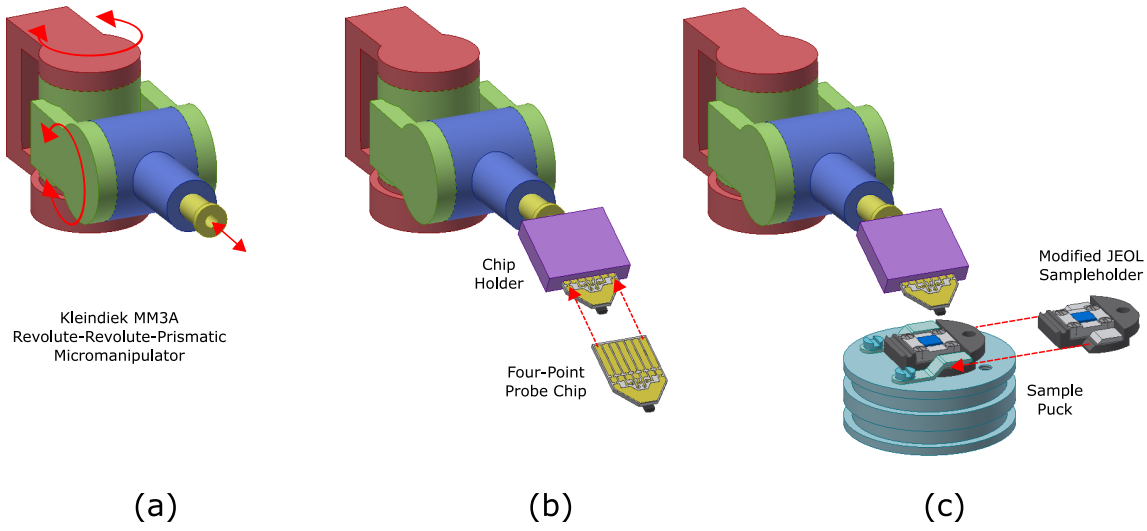

Figure 12: Representation of the revolute-revolute-prismatic (RRP) micromanipulator with its implementation. a) Commercially available Kleindiek MM3A manipulator with its RRP actuator structure. b) The micromanipulator is equipped with a special chip holder that allows to exchange four-point probe chips. c) The micromanipulator will be used to position the four-point probes on the sample. The sample is mounted on a modified JEOL sample holder which in turn can be slid to the sample puck inside the UHV system.

be replaced and the four-point probes need to be exchanged and aligned. In our case, the micro-manipulator should not be permanently fixed in the main chamber, as it would require a complete venting of our system each time the fragile four-point probes have to be replaced. Probes need to be handled with care and the micromanipulator needs to be held in place as improper stress to the micromanipulator can damage the piezo-ceramic material which leads to a failure of operation. Figure 13 shows a normal procedure how a chip must be replaced. From a practical point of view, it would be a challenging task to replace the chips inside the UHV chamber with conventional manipulator arms and to make reliable contact between chip and the external source-meter. Further, to reach ultra-high vacuum conditions in the main chamber, a proper bake-out procedure is required that can take several days. Further, the ion pumps attached to the main chamber should not be vented on a regular basis as the pumping speed will decrease significantly over time. The Kleindiek micromanipulator with

the chip holder however should still be incorporated to the main chamber, as the combination with the Multicentre sample manipulator allows to cool, to heat and to rotate the sample, which is ideal for our case.

To address the above mentioned issues, the decision was made to build a tip exchange

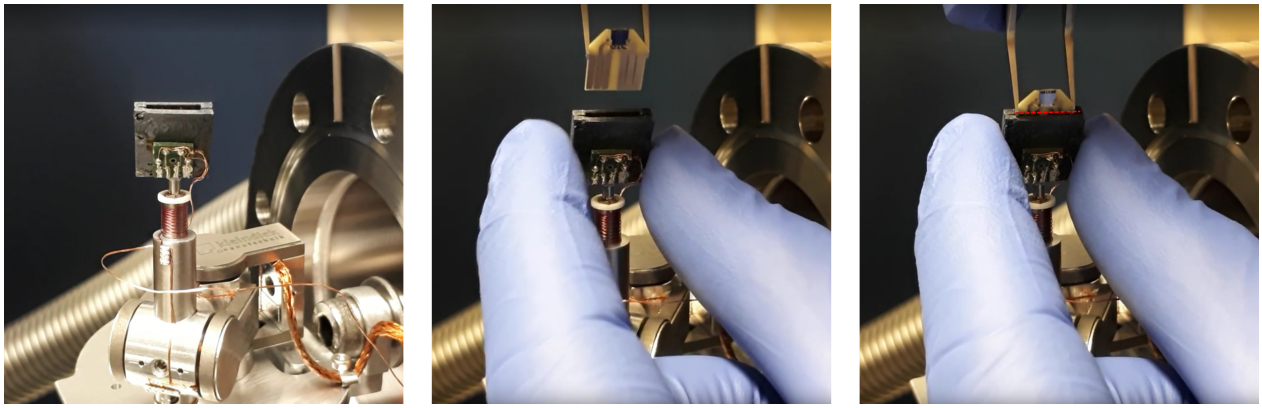

Figure 13: Chip replacement procedure: The manipulator is placed in an upright position. With special tweezers, the chip can be comfortably held at the very end and by gently holding the probe holder, the chip can be inserted. The motion should be linear, and the probe should be properly aligned (red line).

chamber that accommodates the four-point probe setup and is separated through an all-metal gate valve from the main chamber. This setup allows to independently vent the tip exchange chamber, allowing to exchange the chips without interfering the UHV condition in the main chamber. Figure 14 shows the final implementation of the exchange chamber. The main design idea was to mount the chamber on linear motion carriages that allows one to open the exchange chamber by sliding away from the main chamber. Self-lubricating PTFE-lined aluminum bearings were used because they can still be baked up to 190 °C.

In order to incorporate the four-point probe inside the main chamber, the micromanipulator setup was mounted on a transfer arm inside the exchange chamber allowing to bring transfer the whole setup into the main chamber. Figure 15 shows the schematic idea of the setup inside the main chamber. Inside the main chamber, a stationary base was designed where the micro-manipulator can be slid on and locked in place. Since both sample and

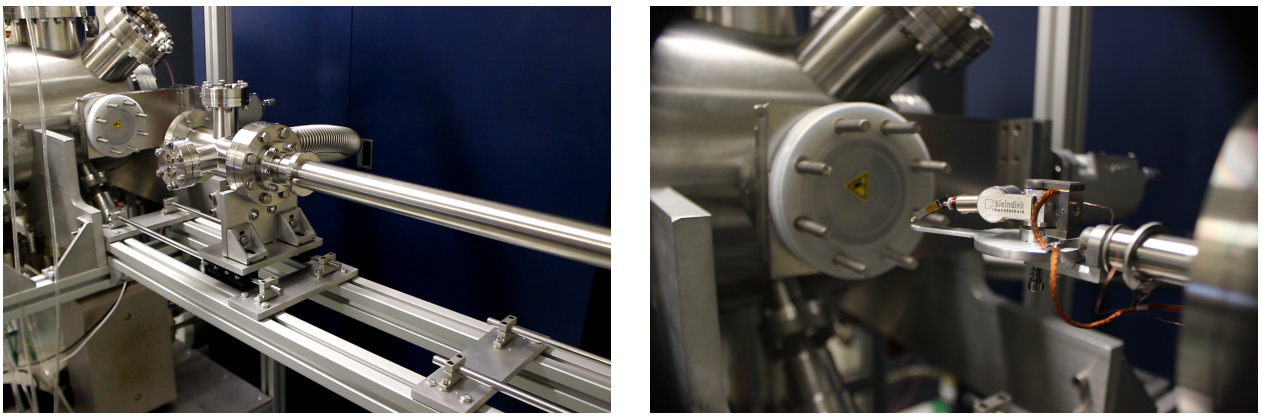

Figure 14: Tip exchange chamber.

micromanipulator are sitting on two long and separated transfer arms, the stationary base is needed to reduce vibrations and to mechanically couple the two arms. In order to place the micromanipulator precisely on the stationary base and to avoid misalignment of the probes relatively to the sample, a kinematic design with three point contacts was designed. Kinematic couplings are useful in machine design because they are a cheap, precise, and robust manner of ensuring that two parts sit at the same relative position every time they meet, which is crucial for future probe alignment. The kinematic counter-part on the transfer arm is held in place by a spring, which allows to slide the four-point probe on top of three special hardened stainless steel balls and prevents bending the transfer arm. In order to use the full capability of the sample manipulator, a spring-loaded counterpart was designed and mounted to the stationary base that allows to lock the sample manipulator arm in place. Since the torus of the sample manipulator can not be easily taken apart and is made of molybdenum, which is much more abrasive than stainless steel and tends to chip while being machined, the spring loader design with a soft aluminum counterpart allows to hold the sample manipulator in place while still offering full 360° sample rotation and sample heating. In order to visibly observe the transfer and to visibly observe the approach mechanism, three optical viewports were considered in the main chamber design allowing optimal visible access to the setup,

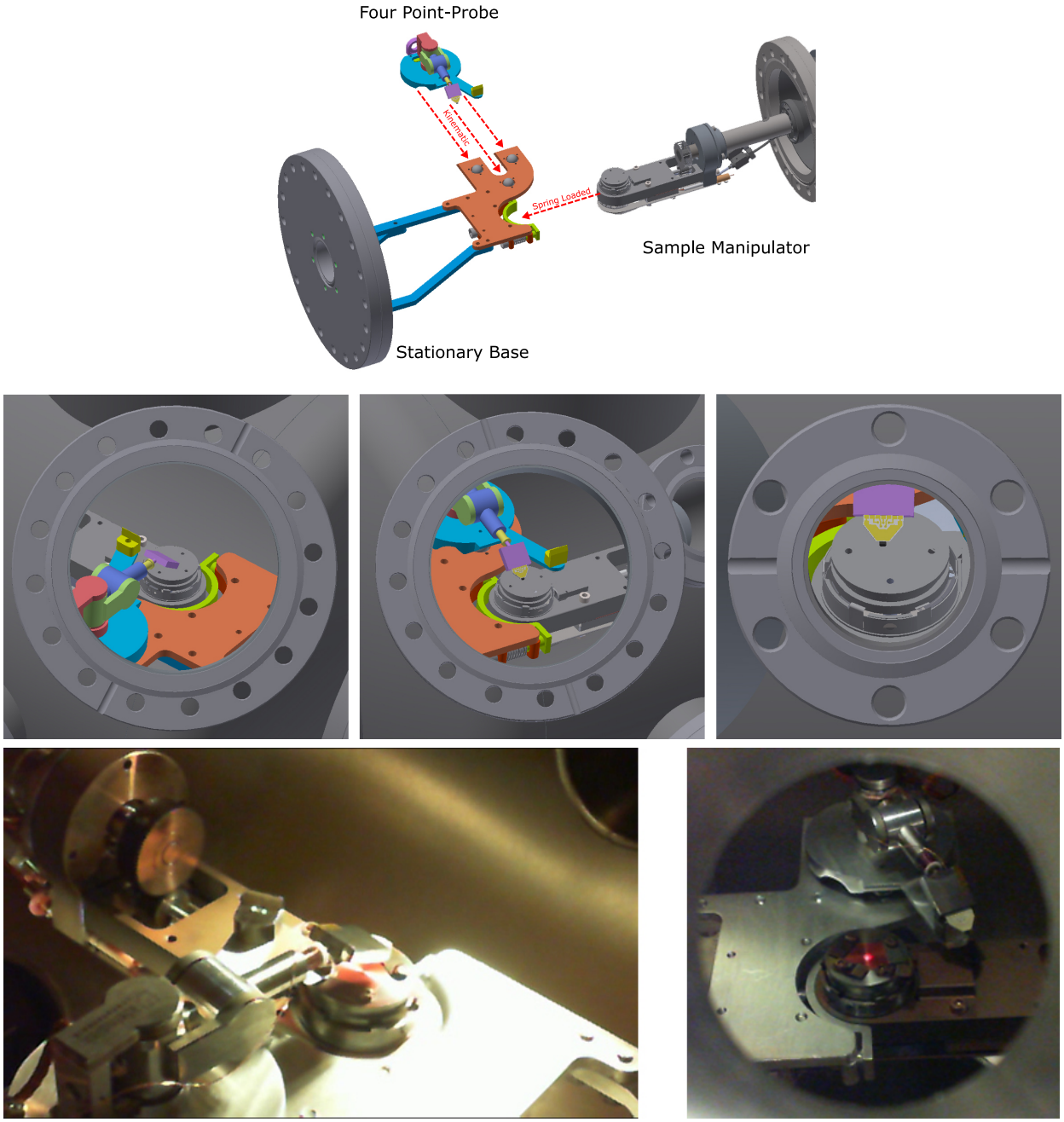

Figure 15: Top: Situation inside the main chamber. A stationary base structure was built that connects both the four-point probe setup with the sample manipulator. The four-point probe sits on a transfer arm and can be brought into the system from the tip exchange chamber. A kinematic connector principle guarantees precise positioning of the four-point probe setup which is crucial for probe alignment. The sample manipulator can be pushed towards a spring-loader that locks the manipulator in place. The setup still allows sample heating, cooling and sample rotation. Middle: View through the three viewports that provide visible access to the setup. Bottom: Pictures of the final implementation.

which is also shown in figure 15. For further details, the technical drawings of the whole setup can be found in appendix A.2.

3.2.1. Mapping the Local Conductivity of Thin Films

The electronic performance of a sample depends on the mobility of charge carriers, which intimately depends on the structure and morphology of the film. It is of paramount importance to both understand and control the processes that influence the molecules to form disordered and semi-ordered films. To determine the relationship the in-plane conductivity of the samples that can be extracted by four-point probe technique with its local film morphology, a mechanism needs to be found that allows spatially resolved mapping on a micrometer scale. Since the films we want to investigate are thin, a spatially mapped four-point probe measurement can be directly related to its local surface conductivity.

Unlike linear nanostages which only provide a couple of micrometers working range, the Kleindiek manipulator provides a much wider range of action. Both the coarse mode of the manipulator and fine mode could potentially be used to bring the manipulator arm in close distance to the sample, from where an automated approach mechanism can be used to detect the surface of the sample. Since both coarse- and fine mode allow high precision positioning from nanometers up to micrometers, the Kleindiek manipulator can possibly be used for local conductivity mapping of the sample.

In order to effectively control the Kleindiek micromanipulator, an attempt was made to automate the driving principle that would be necessary to move the manipulator and scan the sample. For this, both direct and inverse kinematics as well as the operable space needs to be defined. Due to the special construction of the micromanipulator and its RRP structure, this problem is a non-trivial task. Fortunately, similar RRP robotic manipulator arms have already been mathematically described earlier [39, 40]. The so called Denavit-Hartenberg

representation [41] is a known mathematical framework that is often used in robotics to obtain the direct and inverse kinematics of motion of a manipulator where the assumption must be given that the joints of the manipulator are decoupled from each other. This framework can be adapted to the Kleindiek manipulator and in a first step, an open-loop control algorithm can be implemented to test the practicability of the manipulator for further control- and mapping implementations [42, 43]. In figure 16, the dimensions of the micromanipulator are shown that are necessary for a static solution of the framework.

First, the forward kinematics of only the Kleindiek micromanipulator (without the addi-

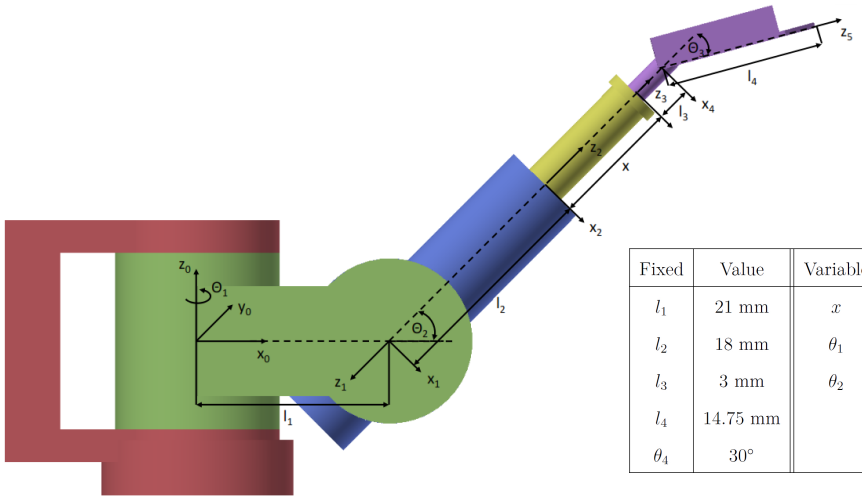

Fixed	Value	Variable	Value
l_1	21 mm	x	0...12 mm
l_2	18 mm	θ_1	-120...120°
l_3	3 mm	θ_2	-120...120°
l_4	14.75 mm		
θ_4	30°		

Figure 16: Model of the Kleindiek micromanipulator that is used to define the mathematical framework for the operation. The manipulator has two revolute (θ_1 and θ_2) and a prismatic (x) joint. The violet part is the additional chip-holder that can be placed at the end-effector of the micromanipulator.

tional chip holder) is described. The forward kinematics gives us the Cartesian (X,Y,Z) values of the end effector of the micromanipulator, where θ_1, θ_2 and x are the given parameters [42]:

$$\begin{bmatrix} X \\ Y \\ Z \end{bmatrix} = \begin{bmatrix} l_1 cos(\theta_1) + (l_2 + x) cos(\theta_1) cos(\theta_2) \\ l_1 sin(\theta_1) + (l_2 + x) sin(\theta_1) cos(\theta_2) \\ (l_2 + x) sin(\theta_2) \end{bmatrix} \tag{11}$$

If the Cartesian values (X,Y,Z) are given, inverse kinematics equation can be used to determine the joint parameters (θ_1, θ_2, x) that provide a desired position of the end-effector:

$$\begin{bmatrix} \theta_1 \\ \theta_2 \\ x \end{bmatrix} = \begin{bmatrix} atan(\frac{Y}{X}) \\ atan(\frac{Z}{(X^2+Y^2)^{0.5}-l_1}) \\ (Z^2 + ((X^2 + Y^2)^{0.5} - l_1)^2)^{0.5} - l_2 \end{bmatrix} \tag{12}$$

We now add the four-point probe chip holder on front of the MM3A manipulator. This adds an additional vector to the end of the effector and the position of the four-point probes can be calculated, if the additional dimensions l_3, l_4 and θ_3 are known (see figure 16). The forward kinematics for (X,Y,Z) the micromanipulator with the chip add-on are then:

$$\begin{bmatrix} X \\ Y \\ Z \end{bmatrix} = \begin{bmatrix} l_1 cos(\theta_1) + (l_2 + l_3 cos(\theta_3) + x) cos(\theta_1) cos(\theta_2 - atan(\frac{l_3 sin(\theta_3)}{l_2 + x + l_3 cos(\theta_3)})) \\ l_1 sin(\theta_1) + (l_2 + l_3 cos(\theta_3) + x) sin(\theta_1) cos(\theta_2 - atan(\frac{l_3 sin(\theta_3)}{l_2 + x + l_3 cos(\theta_3)})) \\ (l_2 + l_3 cos(\theta_3) + x) sin(\theta_2 - atan(\frac{l_3 sin(\theta_3)}{l_2 + x + l_3 cos(\theta_3)})) \end{bmatrix} \tag{13}$$

From this, the inverse kinematics can be calculated by the same approach as before and leads to the following expressions for the joint parameters (θ_1, θ_2, x):

$$\begin{bmatrix} \theta_1 \\ \theta_2 \\ x \end{bmatrix} = \begin{bmatrix} atan(\frac{Y}{X}) \\ atan(\frac{l_3 sin(\theta_3)}{(sqrt(X^2+Y^2)-l_1) sqrt(\frac{Z^2}{l_1 - sqrt(X^2+Y^2)}^2 + 1)}) + atan(\frac{Z}{sqrt(X^2+Y^2)-l_1}) \\ \frac{Z}{sin(\theta_1) cos(atan(\frac{Z}{(X^2+Y^2)^{0.5}-l_1}))} - l_2 - l_3 cos(\theta_3) \end{bmatrix} \tag{14}$$

Knowing both forward and inverse kinematics of the manipulator, the space of the possible operation can be represented and is shown in figure 17. Since the setup was built from scratch, knowing the possible operation space of the micromanipulator was useful to find the best sample position so that the movement of the manipulator covers as much of the sample as possible. Further, it allows to aim for the optimal approaching angle of the chip holder to the sample which should be at an inclination angle of about 30° relative to the sample surface.

So far, the mathematical framework presented is static. To effectively control the manipulator, dynamic equations of motion need to be introduced as well. Unlike typical macroscale manipulator models and controllers, the controller development is not trivial due to potential nanoscale movement, coupled with unmodeled dynamics, nonlinear structural dynamics and mainly the absence of position sensors and velocity feedback in this particular micromanipulator. Unlike other motors such as stepper motors, a prediction of the step sizes can not simply be made. As piezo actuated stick slip motors rely on friction, the step size is not a fixed number and it has been found that variables such as the load on the manipulator, ambient conditions (and quality of the bake-out), as well as local variances in the contact of stator and actuator cause variances in the stick-slip movement. An implementation at this stage is only possible in an open-loop predictive manner. Saeidpourazar et al. [42] have intensively worked on modelling the kinematics of the Kleindiek manipulator and have noted similar difficulties. A memory-based adaptive controller was suggested that can track the manipulator step size to overcome these difficulties. Utilizing pure vision feedback to acquire tip position has limited capabilities in achieving the desired control accuracy.

In order to test the idea of sample mapping, a resolution test target with optical line grating patterns of known spacing of 10 µm was placed inside the chamber to test the repeatability of the movement. Using a serial communication protocol with the microcontroller (see appendix

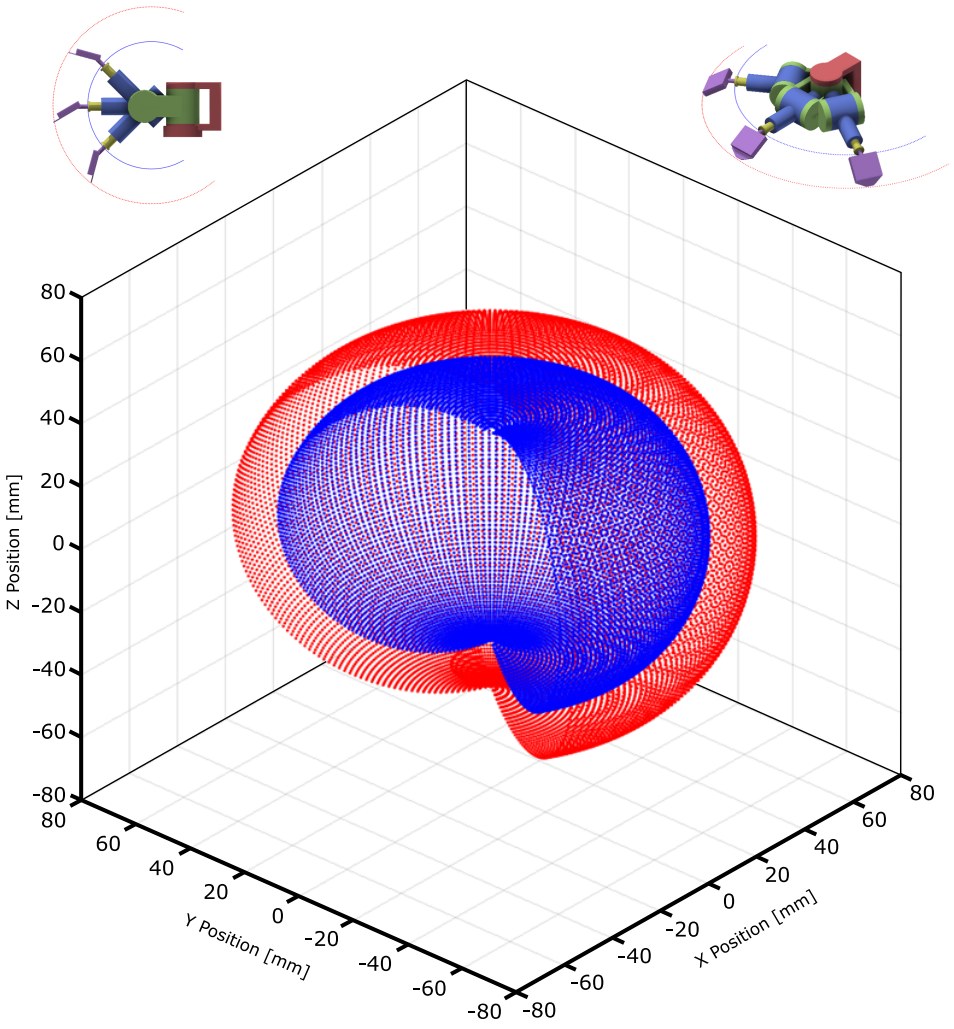

Figure 17: Representation of the operation space of the micromanipulator. The manipulator spans a doughnut-shaped room. Blue shows the operation space of the end-effector of the Kleindiek manipulator and red shows the end-position of the additional chip holder. For simplification, the prismatic joint x was constant at 6 mm.

C for details), an attempt was made to calibrate each movement direction. In conclusion, we found that the slip-stick coarse mode is too unpredictable for further modelling. I found that the different coarse mode speeds available (c01, c08, c64) have very different movement variances, e.g. one step in the smallest speed available has been found very unreliable for certain movements (such as the up movement), as it seems to sometimes gets stuck and does

not move at all. This specific issue indicated that both amplitude and frequency must be reset correctly for reliable, consistent and high-resolution functionality in coarse mode. The frequency affects the speed of the manipulation and the amplitude determines the size of the coarse step. Further, it was found that different number of steps have different acceleration and deceleration characteristics that makes the movement hard to predict. This means doing a burst of 10 steps is not the same as doing 10 separate steps with otherwise the same parameters. The number of steps needed to move the effector by a distance of 100 µm along the sample surface can easily vary by 20 %. Thus we wanted to know if we could use the fine mode of the micromanipulator instead as a mapping tool. Since the actuator does not slip in the fine mode, and the revolute actuators have a fine range of about 20 µm with about 5 nm step size, it should be easier to implement.

Having a closer look at the operation principle of the controller unit, we realized that the controller is only designed to control one stator at the time in fine mode. In fine mode, the voltage on the stator must be applied constantly in order to keep the manipulator at the desired fine position. If we switch to another stator, the constant voltage on the stator will be discharged and the manipulator will move to an unpredictable position. Since the needed movement for mapping involves all axis to be switched, it would mean that every time would switch the axis to go to a new position, the position of the other axis moves back to its 0 V position. Having this in mind, we realized that we can only overcome this issue by designing our own controller, which let us withdraw from the idea of mapping the sample as there were many other prioritized issues related to this project. We first want to focus on an approach mechanism that allows to detect the surface of the sample reliably before we want to implement a possible mapping. This will be now explained in the next chapter.

3.3. Surface Detection

To successfully make a four-point probe measurement, all four probes need to be brought in electrical contact with the sample. Since thin films such as conjugated semiconducting polymers are often soft and easy to scratch and micro-fabricated cantilevers are fragile, an automated mechanism needed to be implemented that minimizes potential for damage to the sample surface and avoids cantilever fracture and probe crash.

Commonly used surface detection modes are either done optically, electrically or by force detection. Optical detection, where either the deflection of the cantilever can be visibly seen through optical patterns such as a change in reflection or shadowing, needs to be done manually and relies on proper illumination and magnification of the sample and probe. As image recognition methods are challenging to implement, this method was not considered as the main method for automation. An additional camera however is still a valuable tool to watch the probes closely while an approach and measurement is performed. In force detection, the detection of the surface is independent of its conductivity. Similar to atomic force microscopy, laser beam detection reflecting off the back of the cantilever can be used to record the cantilever displacement as the cantilever approaches the surface. This method for micro four-point probes has been implemented elsewhere [44], however, this was not considered for our setup. The reason for not considering this option is due to the wide operation range of the Kleindiek micromanipulator. Proper laser alignment to the relatively short cantilevers (30 µm) would be challenging and since the cantilever to laser position is not fixed, both laser and detector would need to be aligned again when the manipulator changes its position. Other force detection modes such as using piezoelectric thin layers evaporated on the cantilevers and where the displacement is read through strain [45–47] is an interesting alternative and might be considered for future cantilever designs for our setup.

The most commonly used surface detection method to date is electrical detection. It relies

on the conductivity of the sample where a two-point resistance is measured continuously between the two outer probes until a resistance drop or sudden conductivity upon contact is detected. Two different electrical approach mechanisms can be used and are represented in figure 18. In the first method, a constant current is applied, and a voltage drop upon contact with the sample is detected. In the second method, a constant voltage is applied and the current upon contact with the sample is detected. The first mechanism, where a voltage drop

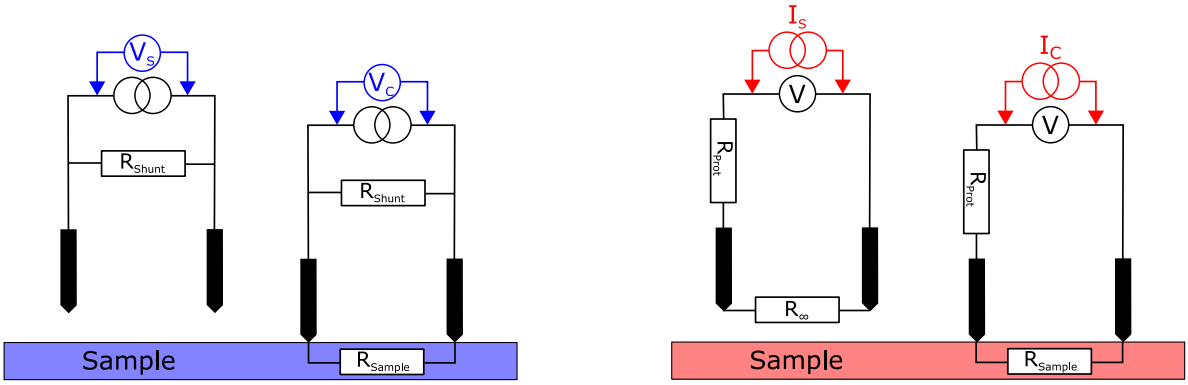

Figure 18: Schematics of two electrical surface detection methods. Left: A constant current is applied to a shunt resistor that is in parallel to the sample and a sensed voltage through the resistor is measured (V_{Sense}). Upon contact, the voltage drops and can be used as a detection mode. Right: A constant voltage is applied to the outer probes. When not in contact, the controller applies almost no current to the probes (I_{Sense}). When in contact, a sudden flow of current can be used as a detection mode. R_{Prot} is needed to limit the amount of current upon contact to prevent probe damage.

is detected, a shunt resistor R_{Shunt} needs to be coupled between the two outer electrodes and a current is applied. When the electrodes are not touching the surface, the current is driven only through R_{Shunt} and the reference voltage (V_{Sense}) is equal to

$$V_{Sense} = IR_{Shunt} \tag{15}$$

When the probes come in contact with the surface, the additional sample resistance R_{Sample} is in parallel to R_{Shunt} and leads to a voltage drop which can be used as a detection method:

$$V_{Contact} = I(\frac{1}{R_{Shunt}} + \frac{1}{R_{Sample}})^{-1} \tag{16}$$

In practice, values of I are in the order of 1 µA and should not exceed over 1 mA in order to protect the probes from sudden electrical discharge and failure, and an R_{Shunt} of 1 MΩ gives a high surface sensitivity. Since R_{Shunt} will be in parallel with R_{Sample}, this method only works reliably if R_{Shunt} is orders of magnitudes larger than R_{Sample}. If samples become more resistive, the change in voltage upon contact decreases significantly. In our case, this is of concern because organic molecules have a high resistance and other materials that surfaces with an oxide layer might not be detected properly. In order to perform measurements, R_{Shunt} needs to be disconnected from the circuit.

The second mechanism is to use a current protection resistor R_{Prot} that is in series with R_{Sample}. In this method, a constant voltage of about 1 V is applied to the probe and the current is recorded. When the probes are not in contact with the sample, the resistance between the probes will be infinitely high. The current then is

$$I_{Sense} = \frac{V}{R_{Prot} + R_{\infty}} = \frac{V}{R_{\infty}} \approx 0 \tag{17}$$

Real source-meters however have a finite input resistance (normally R_{∞} in the order of GΩ) and thus a small leakage current in the order of pA to nA from the controller will be measured at 1 V. When the probes are touching the surface, the resistance becomes finite and a current can flow:

$$I_{Contact} = \frac{V}{R_{Prot} + R_{Sample}} \tag{18}$$

Since we want to limit the current applied to the sample in order to protect the probes, R_{Prot} is used as a current protection resistor. It should be chosen in a manner so that the current is limited to 1 mA upon contact. From equation 17 and 18, the surface is only detectable if the sample has a much smaller resistance than the input resistance of the controller ($R_{Sample} \ll R_{\infty}$). Since organic samples are very resistive, it is advisable to keep the leakage current as small as possible to gain from a high sensitivity and to keep the spacing between the probes as small as possible (since we are detecting a resistance R, which is geometry dependent and increases with distance). Since we want to optimize the system for micro four-point probes with small spacings, the sample resistance should be much smaller than the input resistance of the controller and should thus be detectable. In our case, we use a Keithley 2400LV source-meter that can measure a current in the range of pA to A and its high input resistance of $>10\,\mathrm{G\Omega}$ leads to a leakage current below 100 pA that will define the detection limit of our setup. The source-meter has an inbuilt R_{Prot} that allows to set a current protection limit automatically so that the applied current does not overshoot. Since both the Kleindiek MM3A micromanipulator and the Keithley 2400LV source-meter allow serial communication, a user interface was made that that includes an automated approach mechanism. First, a reference measurement is made and then the manipulator moves towards the surface until an applied current is detected. For the sake of completeness, appendix C includes the drivers for the Kleindiek MM3A and the Keithley 2400LV controller and appendix E.3 includes a manual how to operate the user interface and the approach mechanism.

3.4. Electrical Contact Verification with Multiplexer Board

Since we are using collinear four-point probe arrays where the electrodes are aligned equally in one line and microfabrication processes nowadays allow to produce cantilevers with very precise dimensions, the assumption can be made that when using the two outer probes to

detect a surface, the two inner probes should be close upon contact when a surface has been detected. In case of the samples that were tried to measure, it turned out that this assumption was far from being true. A fundamental problem in micro four-point probe measurements is the electrical- and mechanical contact between the electrode tips and the surface to be measured. Measurements could normally not be stabilized from the beginning on. There was either a bad connection between the sample and one or several probes, the probe was not aligned well enough, the probes are worn or broken, the sample was very rough, or the sample was just not conductive. Since reliable measurements depend on proper contacts to all probes, a method needed to be found to check if all probes are in physical- and electrical contact with the surface to be measured and not only the two outer probes. Since we do not want to introduce vibrations to the system, this should not be done by manually switching the controller's output to the different probes. A better version is to build a multiplexer board and a user interface that allows to switch between probes and check every contact by making two-point measurements with the probe.

To see if every probe is in contact, electrical switches can be used to check if every probe is in contact with the sample. Switches have an input for the common signal (COM) and a normally-open (NO) and normally-closed (NC) for the outgoing signal. Upon a logic input, the output switches and a current can be applied to a different probe. Mechanical relays could technically be used, however, they are not ideal in our case. Mechanical switches require relatively high power to switch, and as relays rely upon mechanical contact, formed oxide layers on the contacts can lead to unwanted resistance making it harder to pass small currents to the probes. Compared to mechanical relays, CMOS analog switches such as the MAX4679 are better and ideal for our case. These CMOS switches have four independent analog switches, require little board space and low power and are more reliable than mechanical relays. When operated, the switches have a maximum of $1.6\,\Omega$ contact resistance and at

room-temperature and the off-leakage current is as low as 0.1 nA. The CMOS feature separate logic supply inputs for each switch and operates from 2.7 V up to the supply voltage of the CMOS. One CMOS chip per source-meter in- and output is needed to be able to switch between all probes. In appendix B.1, the schematics of the board and the PCB layout can be found, in appendix C.4, the serial communication protocol with the Arduino is shown.
In figure 19, the advantage of the multiplexer board is now shown. Since the multiplexer board now allows all probes to be chosen as current pin or voltage pin, one can verify if the contacts are good or not. Figure 19 shows a typical measurement of a bad contact and how a four-point probe measurement looks like upon bad contact. In figure 19A), pin 2 has improper contact, which can be spotted in the current-voltage curve when measuring the contact through pin 1 and pin 2. From these measurements, it is simple to find the mistake. However, without contact check, it is non-obvious to spot the issue, depending on your sample under investigation. In figure 19B), a four-point probe measurement is shown upon bad contact. In this case, pin 2 is not in contact and thus the measurement only shows a controller internal measurement, and not the sample itself. Since one would expect a small resistance R from a conductive sample such as Au, it is important to have a closer look at the lower boundaries of the source-meter to spot the problem. At voltage measurements below 2 V, the source-meter has a temperature-dependent accuracy specification of

$$V_\alpha = \pm(0.012\% + 45)\mu V/^\circ C \tag{19}$$

where V_α is the temperature coefficient in V/°C. In figure 19B), both the voltage offset at 0 A of about 20 µV and the linear behavior can be explained due to heating (about 0.5 °C internal heating). To avoid this confusion, it is generally advised to adjust the current source in such manner that the voltage readout is on the order of mV to V. However, as figure 19B), indicates, gold has a very small resistivity and since we want to limit the maximum applied

current, the measured voltage for conductive samples will most likely always be in the µV regime.

In figure 20, a proper measurement on a 150 nm Au sample is shown where the electrical connection of each pin to the sample was verified. Since the resistivity of Au is reported ($2.44 \times 10^{-8}\,\Omega\,\mathrm{m}$ at room temperature [48]), the thickness of the sample can be calculated from the four-point probe measurement (see equation 9 in chapter 3.1). The measurement reveals a sample thickness of 164 nm ± 35 nm, which agrees with the measured 150 nm sample thickness from the quartz-crystal readout during evaporation.

The additional multiplexer board adds the advantage to check the electrical contact of each pin, which helps preventing mistakes in taking real measurements. However, since we add CMOS devices in series to the application, there are a couple of disadvantages that need to be mentioned as well. First, CMOS devices need proper power-supply sequencing and absolute maximum ratings need to be kept in mind to prevent permanent damage to the devices. For the multiplexer board shown in appendix B.1, it is of paramount important to always sequence $V+$ first, then $V-$, then V_L, followed by the logic inputs (NO, NC or COM). Since V_L is powered through the Arduino, one must remember to unplug the board from the USB connection when $V+$ and $V-$ are disconnected or turned off. Since proper power-supply sequencing might get forgotten, it would have been a better design to add two small signal diodes (D1/D2) in series with the supply pins as shown in figure 21. An additional Schottky diode between $V+$ and V_L would further add overvoltage protection. The additional diodes would reduce the analog signal range by one diode drop below $V+$ and above $V-$, but do not affect the devices performance in terms of leakage characteristics and switch resistance.

A limitation that needs to be considered during measurement is that the logic input signals (NO,NC and COM) can not exceed the supply voltages $V+$ and $V-$, which should not exceed ±5.5 V. Signals on the logic inputs that are exceeding the supply voltages are clamped

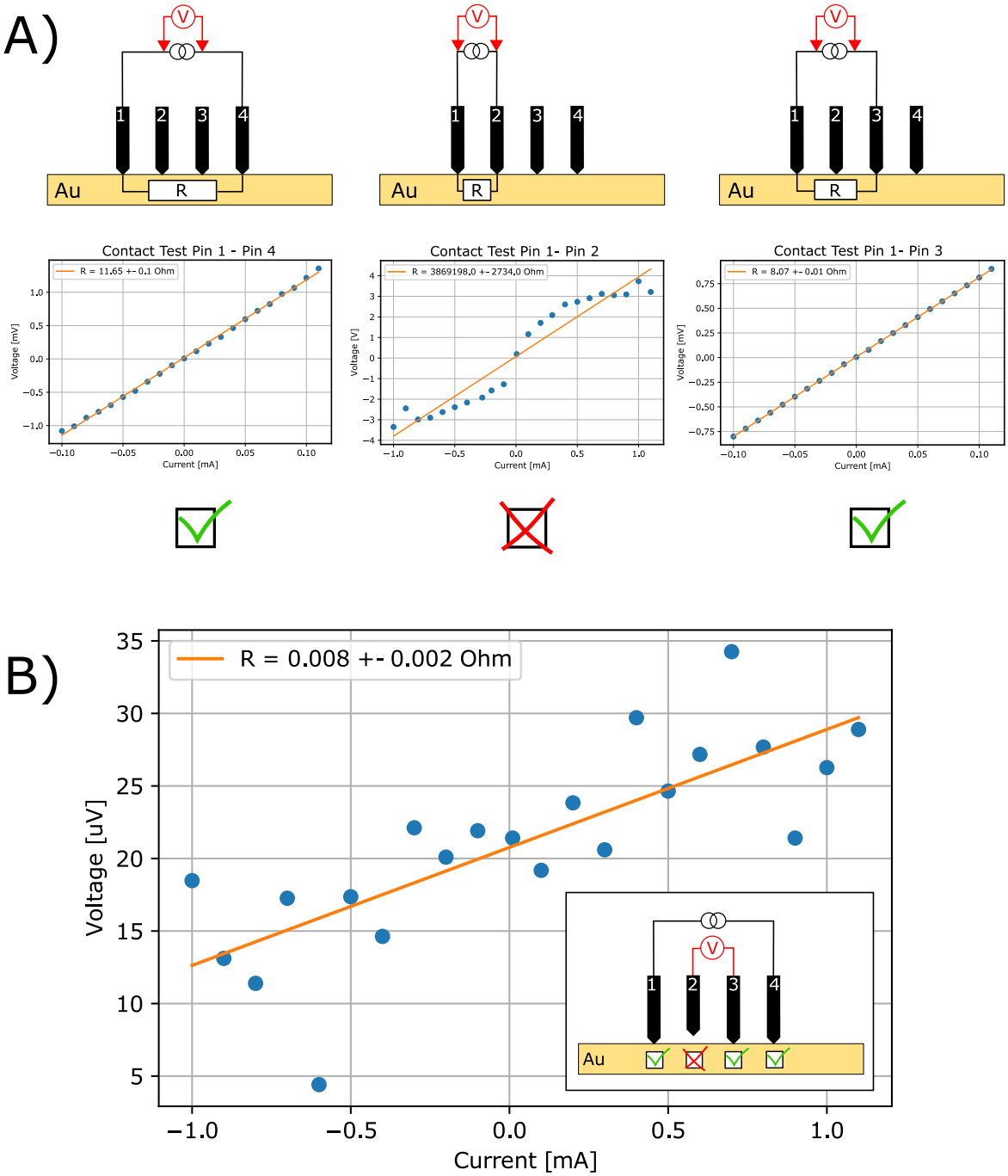

Figure 19: Example for an improper contact measurement on a 150 nm thick gold (Au) sample. A) The multiplexer board allows to switch between all probes to be chosen as current- or voltage pin. In this measurement, pin 2 is not properly in contact with the sample and an IV-measurement reveals a very high resistance in the GΩ range. B) Four-point probe measurement with an improper contact. Since pin 2 is not in contact with the sample, a voltage measurement only reveals the controller's internal thermoelectric effect and not the IV-characteristics of the sample. This can be misleading because such a small resistance on a conductive sample such as Au is expected.

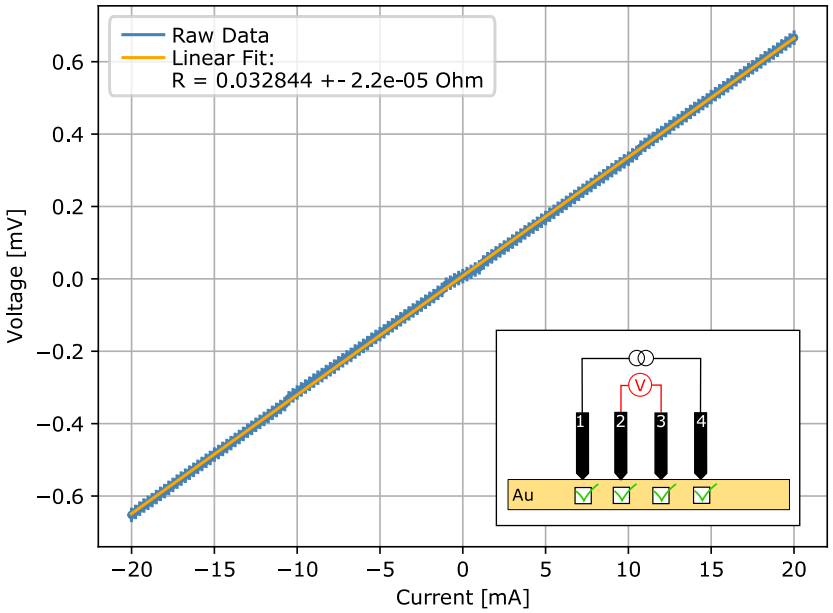

Figure 20: Successful four-point probe measurement on a 150 nm thick Au sample.

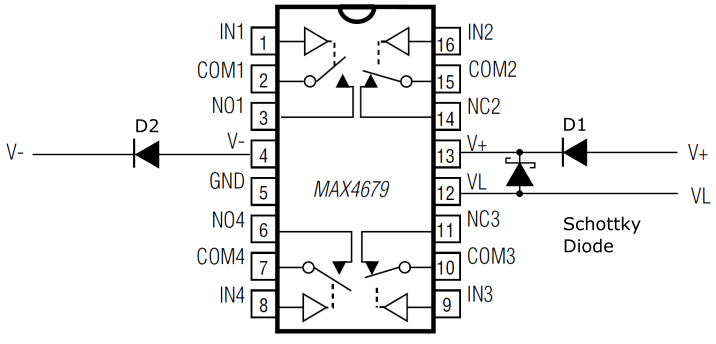

Figure 21: Overvoltage protection using external blocking diodes.

by internal diodes and will lead to a wrong four-point probe measurement. This can be prevented by setting the voltage protection limit of the Keithley 2400LV source-meter below 5 V. The maximum current rating of 50 mA to any terminal of the CMOS sensor was never encountered as problematic since the current-protection limit of the source-meter should be limited to 1 mA in general to prevent micro-cantilever probe failure from electromigration and probe heating [37].

Another issue that needs to be kept in mind is the on and off leakage current of 0.1 nA per switch at room temperature. For a four-point probe measurement, it is important to measure with a high enough current in order to keep the error on the measurement small and normally should not be an issue. However, the leakage current might influence the surface sensitivity when a surface needs to be detected. In figure 22 a comparison between a surface approach with the multiplexer board and without the multiplexer board is shown. From this comparison, it can be seen that the leakage current with the multiplexer board is at around 1.6 nA (16 times 0.1 nA for every switch) and is two orders of magnitudes higher than the Keithley 2400LV. Since we are doing a two-terminal measurement and we are limited to ± 5 V approach voltage due to the CMOS sensors, the maximum resistance we can detect is in the 100 to GΩ range. Since organic molecules are known to have high resistivity, it is important to reduce the spacing between the probes. Since the measured resistance in a two-terminal measurement directly correlates with spacing,

$$R = \rho \frac{l}{A} \tag{20}$$

where l is the length of a conductor (or in this case the spacing between the probes) and A the conductor's cross section, the detected resistance R of the sample can be reduced by reducing the spacing of the probes. In the next section, different probes were used to perform measurements on organic thin films and its limitations will be discussed.

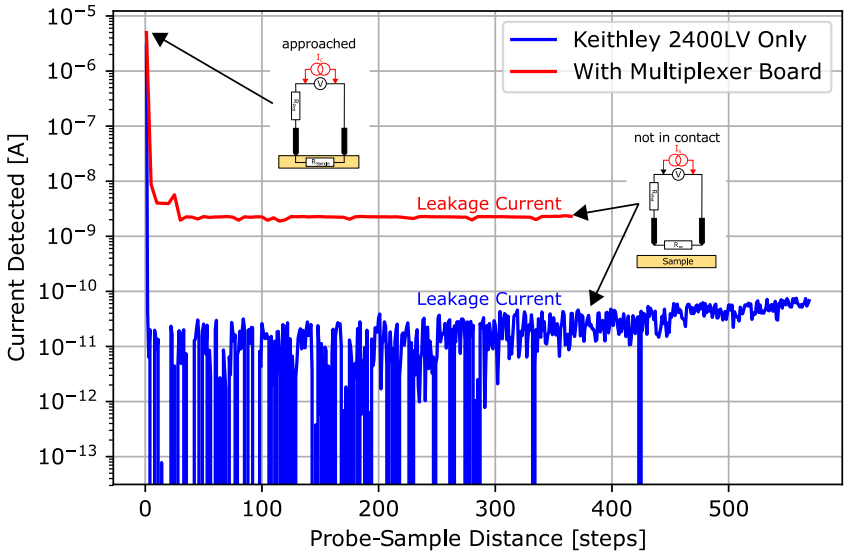

Figure 22: Comparison of the current detection approach mechanism with and without the multiplexer board.

3.5. Probes and Limitations

During the period of this project, different probes were used to perform measurement on molecular thin films. The main idea was to use micro four-point probes (such as probes from Capres A/S), however in our case, in combination with the Kleindiek MM3A micromanipulator and the direct implementation into UHV with limited visual access, it was not found very user friendly and useful. In this section, the choices of different probes are discussed. Reliable surface detection as well as mechanical stability, lifetime and restricted commercial availability of the probes were the main reasons why different probes had to be tested.

3.5.1. Micro Four-Point Probes

Micro four-point probes manufactured by Capres A/S have become a preferred tool for surface conductivity characterization. They are widely used in SEM four-point probe measurement systems in combination with the Kleindiek system. Using silicon-based micro-fabrication

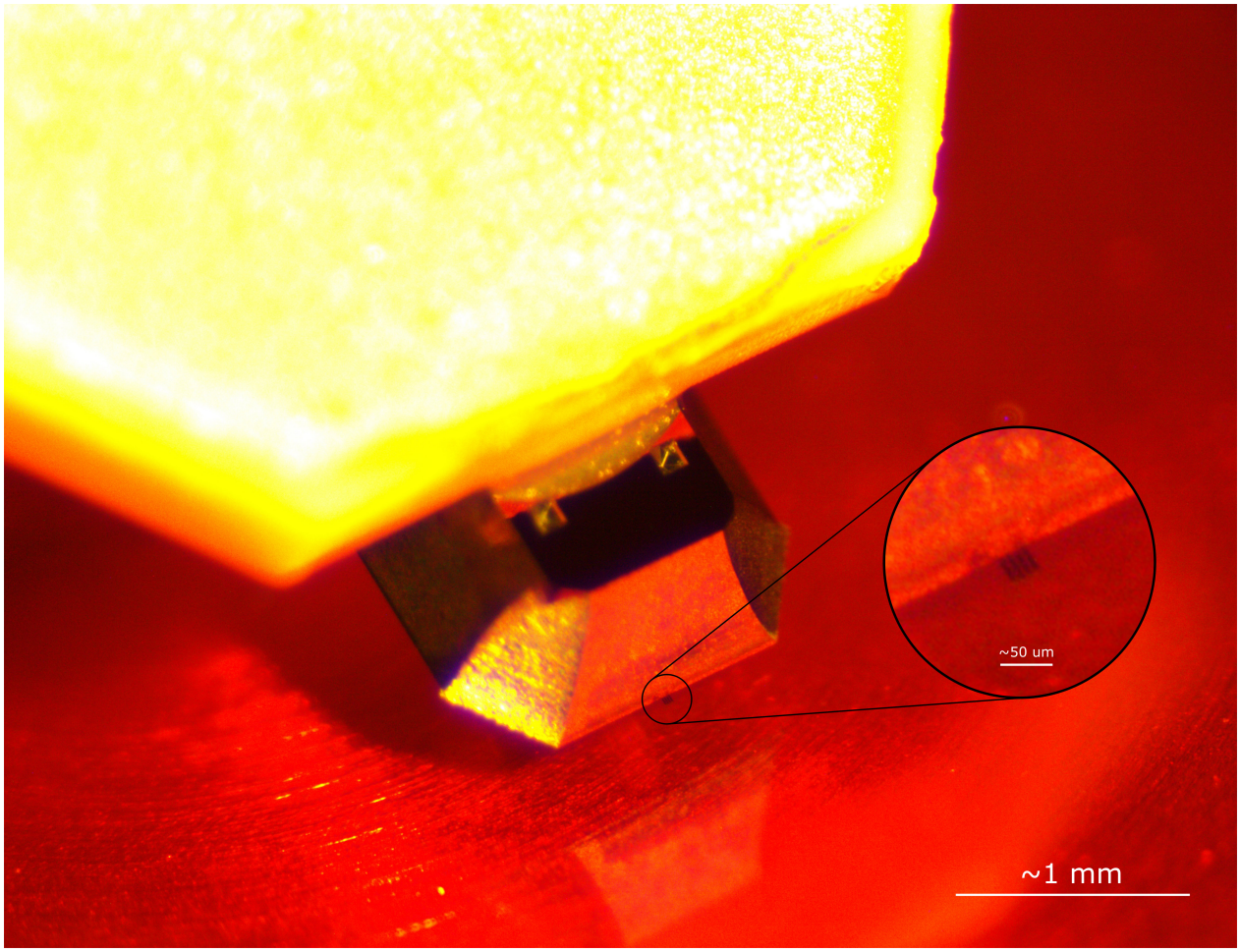

Figure 23: Optical view on the Capres micro four-point probes inside the UHV chamber. A long-distance microscope is used to achieve good optical visibility. The red background is a 1 µm Rubrene film that was evaporated on a glass slide substrate.

technology, the microscopic four-point probes have electrode spacings can be reduced by three order of magnitude compared to conventional four-point probes systems. The probe electrodes consist of 1 µm thick SiO_2 cantilevers with a conducting 25 nm Ti adhesion layer and a 100 nm conducting Au layer. The cantilevers are normally 30 µm long, 3–6 µm wide and electrode spacings of 5–30 µm are available. The cantilever spring constants are typically between 5–50 N/m. The silicon chip containing the electrode structure is bonded to a ceramic chip plate. This ceramic support plate has plated Au electrodes that are connected to the integrated electrode structure of the chip through Au wires. The ceramic support allows simpler probe handling as it can be held safely by tweezers without the risk of damaging the chip. Further, the chip can be pushed into the probe holder on the micromanipulator where the Au plated electrodes of the ceramic chip make contact to metal springs that are connected to the exterior by wires. Since optical visibility of the probes helps preventing probe misalignment to avoid cantilever fracture and probe crash, and since the viewports on the UHV chamber that allow optical visibility are about 20–25 cm away from the sample, a long-distance microscope (Infinity K2 DistaMax, working distance of 228–388 mm, 4–6 µm resolution, 4 mm field of view) was purchased and implemented. In figure 23, one of these chips implemented in our system with 10 µm pitch size together with the optical visibility of the small probes is shown. In appendix A.2, further details about the dimensions of both the ceramic- and silicon chip are shown.

During the time when micro four-point probes were used, the problem of chip alignment relative to the sample surface was often encountered. The situation is shown in figure 24. The probes are normally approached to the surface at an inclination angle of about $\alpha = 30°$ relative to the sample surface. In this case, since the cantilevers are only 30 µm long, the gap between the chip wafer body and the sample surface is only 15 µm. The edge of the silicon support holding the cantilevers however has a length of the order of 1 mm. If the

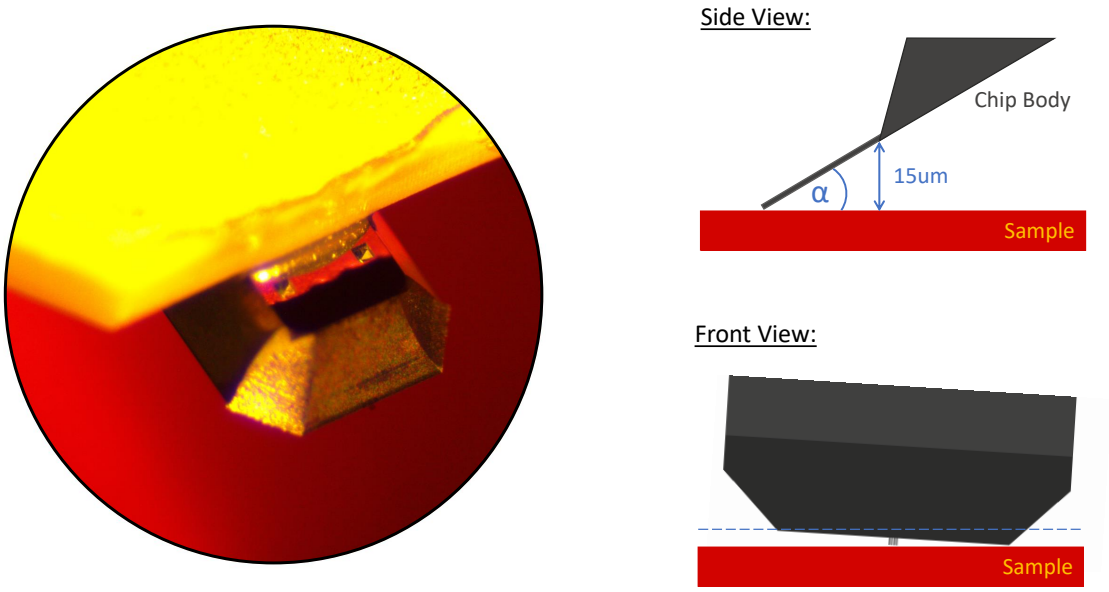

Figure 24: Micro four-point probe. Left: Image of the probes taken with the long-distance microscope (Infinity K2 DistaMax). Good light conditions are needed to optically resolve the micro probes. Right: Schematic of the issue with the small cantilevers. Due to the long edge of the silicon support of 1 mm, and the approach inclination of SI30, proper alignment is needed in order to get in contact with all probes.

misalignment of the electrode probes and the surfaces is larger than 1.5°, not all probes can get in physical contact with the sample as the edge of the silicon support will start to touch the sample surface first. Technically, a better alignment than 1.5° sounds doable, however, since the gap between the chip and surface is only 15 µm, the alignment must be much better because the cantilevers also need to apply force and bend. Proper alignment in our setup is difficult because there are some intrinsic problems in our setup. First, there is no mechanism implemented to the system that allows to rotate the chip holder to correct for misalignment relative to the sample surface. Since the chip holder needs to be aligned outside of the system by hand relative to the sample that is always kept inside the chamber, a mechanism needed to be found that allows prior repeatable good alignment. The solution to this problem was to use the kinematic coupling that was explained earlier and was implemented in the system. Since kinematic coupling allows to exactly constrain the four-point probe setup inside the chamber while providing precision and certainty of location, a sharp knife edge alignment tool was directly added to the setup that allows to align the probes. With this technique that is shown in figure 25, the misalignment can be reduced to below 0.5°. If the misalignment is still an issue once under UHV, the edge of the alignment tool can be used to slightly push the chip-holder into a rotation which can lead to better alignment.

Another issue with the micro four-point probes is the optical visibility when the probes are close to being approached to the surface. On samples that have a metallic shining appearance, the mirror image on the sample and shadows from the cantilever body can be used to visibly track the approach to the sample and to check for misalignment. In our case, we want to evaporate and measure organic molecules on a transparent diamond substrate and there, the contrast is often very weak. Since there are only a limited number of viewports on the system, both the light source and optical view is limited. Such a scenario is shown in figure 26, where a micro four-point probe is almost in contact with the sample surface.

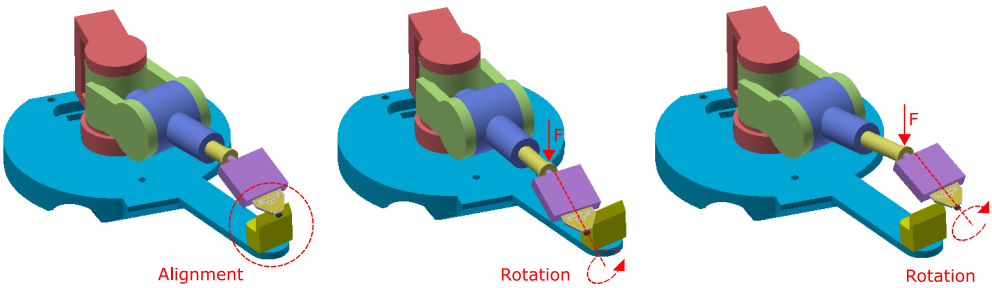

Figure 25: Alignment position and positions to correct for misalignment. A knife edge alignment tool was machined that allows to align the chip by hand before the exchange chamber is pumped to UHV conditions. The alignment tool was revised until a misalignment of below 0.5° was achieved. If the misalignment is still an issue, the edge of the alignment tool can be used to push the chipholder into a rotation that sometimes can help to reduce the misalignment.

Due to the relatively small length of the cantilevers, the issue with the relative long silicon

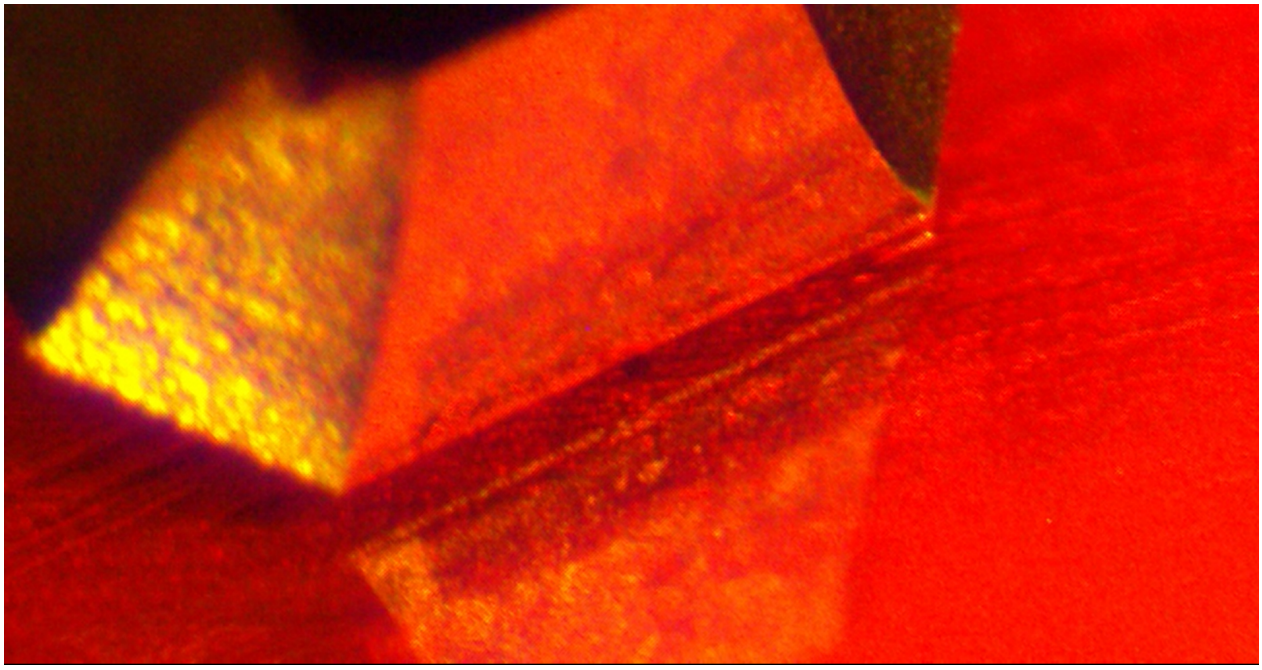

Figure 26: Almost approached to the substrate using micro four-point probes. On transparent substrates with a thin organic molecular film on top, the contrast of the mirror images and shadows on the sample are often very weak to validate if the alignment is good enough.

support edge, the limitations in aligning the probes and visible restrictions, the conclusion was made that other electrode designs need to be tested in order to overcome these limita-

tions. Some ideas to overcome these issues such as etching the relative long support edge or use focused ion beam were considered but validated as impractical. Single-handedly post-processing cantilever chips that are already fixed on a ceramic plate is time- and cost intensive and the problem that these probes are still too short would remain problematic.

3.5.2. Other Cantilever Based Probes

In order to test the functionality of the setup, the idea was to use other cantilever based four-point probes that are commercially available. The goal was to find probes that can be simply modified for our purpose in order to cut costs and lead time. Ideally, these probes would have four or more cantilevers that are equally long and equally spaced, an insulating layer (e.g. >100 nm thick SiO_2) or are completely made of SiO_2 that allows electrical cantilever isolation and possibly come with a metallic coating. As a metallic coating, different materials with relative high work function (above 5 eV) would work, e.g. Al, Au, Pt and Ni. Ni has shown to have very low contact resistance on graphene and due to its mechanical stability (not as soft as Au, only forms one monolayer of oxide), it would be a very promising electrode material [49]. Either masking (pre-processing) or focused ion beam (post-processing) could be used to produce metallic electrode structures.

Although many companies exist that produce microfabricated cantilever chips e.g. for Atomic Force Microscopes and chemical sensing applications [50, 51], not many companies were found that offer array sensors that can be easily modified. In most cantilever sensor applications, the cantilevers do not need to be electrically isolated from each other what means that most sensors do not need an insulating layer as a base material. Rather a highly doped base is often desired for these kinds of application in order to dissipate static charge and to still be chemically inert. Further from a micro-fabrication point of view, it was shown that highly doped (n- and p-type) Si exhibits a much higher etching rate than undoped Si [52] and

in terms of SiO_2, hydrofluoric acid (HF) is the wet-chemical medium with which SiO_2 can be isotropically etched at a reasonable rate [53]. Thus the base material of commercially available cantilevers often is doped Si. It is possible to thermally oxidize Si or to deposit SiO_2 on top, however at this point, a simpler solution had to be found.
Promising commercially available cantilever arrays that were found were the following (in order or practicability):

- *Micromotive*: Type Octosensis Chip, 8 tipless undoped cantilevers per array, 500–1000 µm long, 250 µm spacing, spring constant of 0.003–0.023 N/m.

- *Cantisens*: Type CLA-500, 8 tipless p-doped cantilevers per array, 500 µm long, 250 µm spacing, available with plain silicon surface or with a 20 nm Au coating, spring constant in the order of 0.001 N/m.

- *NanoWorld*: Type TL-8, 8 tipless and highly p-doped cantilevers with triangular free end, 500 µm long, 250 µm spacing, spring constant of about 0.03 N/m.

- *NanoInk*: Type 2D nano PrintArray, up to 500 silicon nitride tips in a row, 60 µm long, 20 µm spacing, spring constant of 0.2 N/m.

- *SmartTip*: Type CIPT, 12 tipless cantilevers per array, 10 µm long, uneven spacing ranging from 1.5–59 µm, Au covered and electrically separated, spring constant >50 N/m.

Most arrays have much wider spacing (normally around 250 m) and have a much smaller spring constant than the micro four-point probes from Capres (5–50 N/m). The wider spacing is troubling because this means that during the approach mechanism (2-point measurement), the resistance will be much higher as the current has to pass a longer distance through the sample. Thus, if the sample is very resistive, a smaller current flow needs to be detected. A

smaller spring constant can be beneficial to reduce the risk of damaging the fragile films, but could also be troubling because this means that less force can be applied to get in contact with the material if the surface is passivated. In figure 27, a comparison is shown how a chip with eight cantilevers of 500 µm length and 250 µm spacing would look like. In combination with the Infinity K2 long-distance microscope, the cantilevers could be optically resolved very well. Since most of the issues with the previous micro four-point probes were due to alignment issues, longer cantilevers could be tracked optically during the approach to a surface.

Reaching out to Micromotive, they fortunately had a couple of Octosensis Chips that they

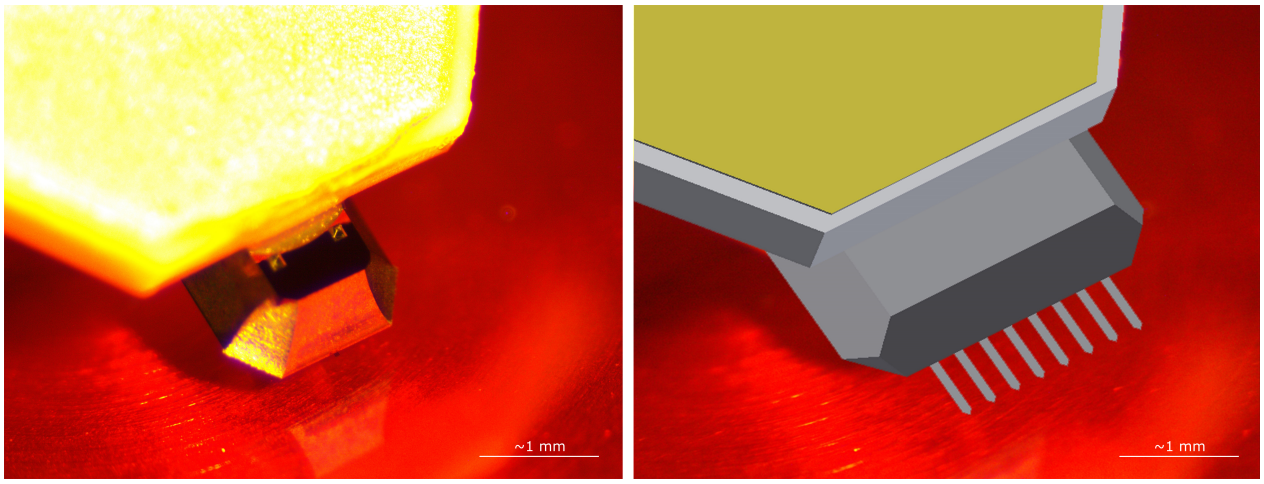

Figure 27: Comparison of short micro four-point probes and other 500 µm long cantilevers (e.g. Arrow TL-8 from NanoWorld). The short cantilevers do not allow to optically track them during the approach mechanism, whereas longer cantilevers (drawing, right) could benefit from it.

could send us. In figure 28a), the sensors are shown that they generously made available to us. The normal configuration of the Octosensis Chips is normally without metal pads, however they had 4 remaining chips from a former customer requests available that have 100–200 nm thick Au patterns on a 1 µm thick SiO_2 layer. The only issue with these probes were that it was unknown how long they were stored before, if they were used or not and the Au coating on the chips had residues on it. After arrival of the chips, the wafers were cleaned with acetone, ethanol, isopropyl alcohol, treated with UV-O_3 and later oxygen plasma cleaned to

remove the residues and to make a fresh Au surface. The chips were glued (Epo-Tek, H22) and wire bonded (10–20 µm thick Al wire) to a PCB chip that allows to mount the probes to the Kleindiek micromanipulator. Figure 28b) shows the final probes that were produced.

The four produced Micromotive cantilever chips were tested on a 150 nm thick Au substrate,

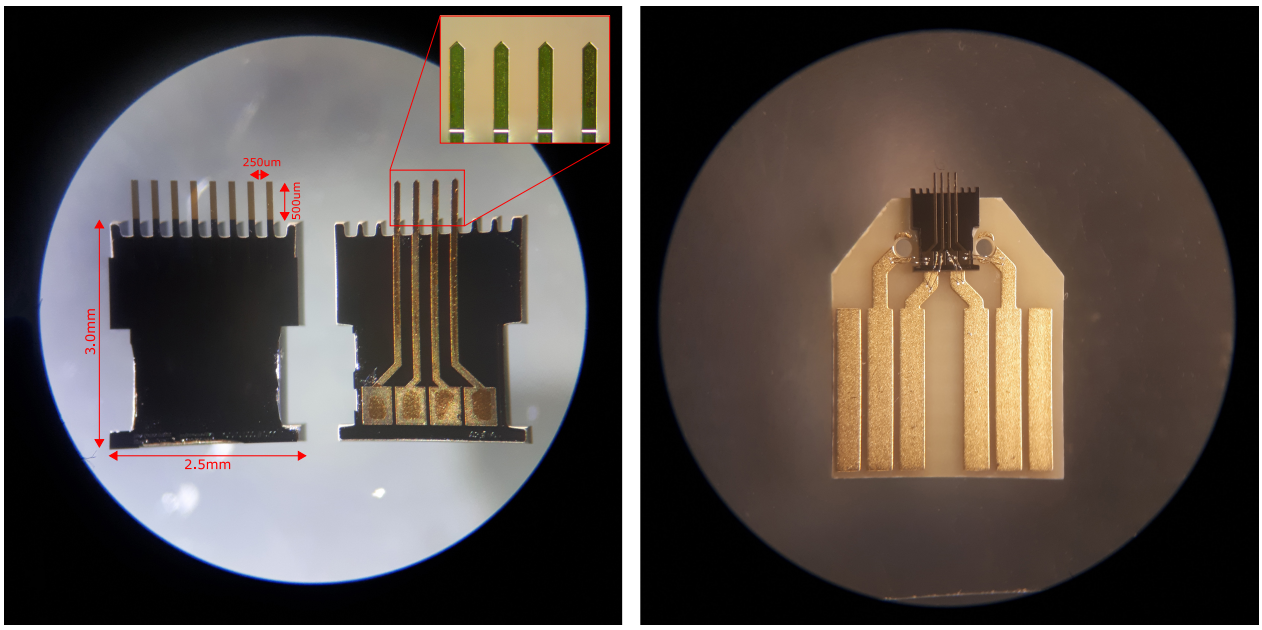

Figure 28: Micromotive Micro Cantilever Arrays. Left: Uncoated commercial Octosensis chips and Octosensis chips coated with SiO_2 and Au electrodes. Right: The chips were glued and wire-bonded to a PCB board that allows to mount the probes to the Kleindiek micromanipulator.

however, no four-point probe contact could be established to the sample. At this point, it was not clear if the spring constant in the order of µN/m is too low to apply enough pressure to break through thin native-oxide layers and debris on the cantilevers or if the contact pads were not good anymore. The wire-bonds were not the issue as the contacts were tested by macroscopic probe-tips. All four chips were tested and in combination with the multiplexer board, only a couple of two-point contacts could be made which was not satisfying. Since several reasons could be the problem that these chips did not work (old and dirty Au pads, low spring constant, broken electrical pads, misalignment), another approach had to be made in order to test the setup. At this point, the microscopic probes had to be given up and due

to limited accessibility, macroscopic probe chips had to be designed and to be tested.

3.5.3. Spring-Loaded Test Pins and the Force Limit of the Micromanipulator

Macroscopic probes are the most common probe types that are implemented in combination with four-point probe tools. Often, the samples are handled in air and measurements are done in air, thus it is often unavoidable to penetrate through non-conducting oxide layers in order to test the material underneath it.

Only a handful of spring-loaded test pins were considered as useful for our implementations. The challenge was to find small probes with small diameter in order to keep the separation between them as small as possible, no electrical discontinuity upon mechanical vibration, contact resistance in the mΩ range and UHV compatible material and coating (lead free). The following test pin was found:

- *Harwin* P13-0123 with Spear Head (Digikey), 16.65 mm total length, 0.68 mm diameter, 2.65 mm full travel, spring constant of 488 N/m at 2/3 travel.

In figure 29, the test pin in comparison with standard probe pin and the built in-line four-point probe chip are shown. A special PCB was produced that allows to glue these probes in an appropriate holder. A gold sample was used to test the pins with the Kleindiek manipulator, however no contact could be made because a new issue was found that was not encountered before. Since the probes are aligned by eye, they need to be compressed in order to allow every probe to get in contact with the sample. Since the spring constant of the probes is high (488 N/m at 2/3 travel), which is much higher than the microscopic four-point probes from Capres (5–50 N/m), more force needs to be applied to compress the pins. I was able to align the probes with offsets of 50 µm, however, not all probes could get in contact with the sample. Thus, the maximum force that can be applied and held by the Kleindiek manipulator was measured by using a scale and the maximum force that can be

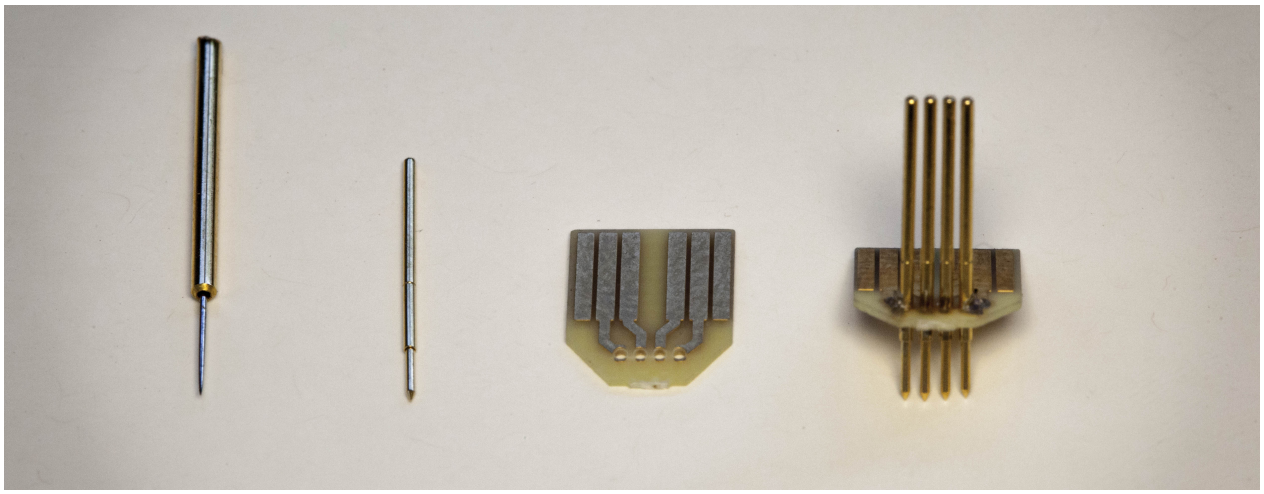

Figure 29: Macroscopic spring contacts and probe assembly. Left) Standard spring-loaded test pins are often large and contain lead which is not ideal for our case. Left, center) A small 0.68 mm diameter test pin was found as ideal. Right, center) A PCB was produced and assembled using conductive silver epoxy (right).

applied is 0.12 ± 0.01 N when the piezos actively push the probes into the sample. When the piezos are at rest, the springs relax and the maximum force settles at around 0.04 ± 0.01 N within 15 s. Since we have four probes to compress, the maximum force per probe that can be applied is thus in the order of 0.01 N.

From Hooke's law, we thus can calculate the maximum compression of each probe,

$$F = kx \tag{21}$$

where F is the force, k the spring constant and x the distance of compression. With the given values, each probe can only compress by about 20 µm before the maximum applicable force is reached. This is too small to guarantee proper contact with each probe. In order to make probes that allow to test the setup, the idea of using macroscopic spring contacts was thus aborted and instead, thin and flexible wires will be used to produce a four-point probe chip that will be explained in the next part.

3.5.4. Platinum-Iridium Wire Chip

In order to be able to test the setup, a step back from microfabricated cantilevers was made and instead, thin wires were used to make in-line array four-point probes. Ideally, the four electrodes are collinear with an equidistant electrode pitch s. Since the electrodes on the chips will be aligned by hand, the real positions of the electrode contacts may in practical measurements differ from the ideal positions and in order to extract ρ, the measurements need to be corrected for the variations of the effective spatial tip positions [54]. At this stage of the project however, this is less of a concern since still an electrode design had to be found that allows to approach and to test the setup.

In order to get the spring constant of the Pt/Ir in the right order of magnitude, the wires can be modelled as clamped-free beams, where the spring constant k in can be simplified as:

$$k = \frac{3EI}{L^3} \tag{22}$$

where E is the Young's modulus of the material, I the moment of inertia of beam, and L the length of the beam. The moment of inertia of a rectangular beam and of a cylinder are given by

$$I = \frac{1}{12} W H^3 \quad \text{and} \quad I = \frac{1}{6} R^4 \tag{23}$$

where W is the width and H is the height of the rectangle and R is the radius of the cylinder. Pt has a low Young's modulus which makes pure platinum wires bend too easily. Thus Ir is added which by itself is very difficult to pull into small diameter wires. Typical Pt/Ir alloy proportions are 90/10 to 70/30 where the alloys have the chemical stability of Pt, but increased hardness from the Ir. (GoodFellow, PT025110, Pt:Ir 90:10, diameter of 125 µm, E-value 160–200 GPa). If we want to bend each wire by $x_{min} = 50\,\mu\text{m}$ in order to get in electrical contact with the sample, and the maximum force being applied per wire is given

by the micromanipulator ($F_{max} = 0.01\,\mathrm{N}$), we can calculate k_{max}:

$$F = kx \tag{24}$$

where k_{max} would be $200\,\mathrm{N/m}$. From equation 22 and 23, the Pt/Ir thus must be at least $1.9\,\mathrm{mm}$ long, otherwise the wires are too stiff in order to bend by at least a distance of $x_{min} = 50\,\mu\mathrm{m}$. At a length of $2.5\,\mathrm{mm}$, the spring constant of a wire is in the range of 80–$100\,\mathrm{N/m}$. In order to align the Pt/Ir wires, fiber optic v-groove arrays made of SiO_2 with $250\,\mu\mathrm{m}$ fiber spacing were used to guide the wires. The wires were glued to the array (Torr Seal, low vapor pressure epoxy), connected to the electrodes of the PCB board using conductive silver epoxy (Epo-Tek, H22), and the wires were etched in order to have smooth rounded ends.

In Scanning Tunneling Microscopy, electrochemical procedures to etch Pt/Ir wires are widely

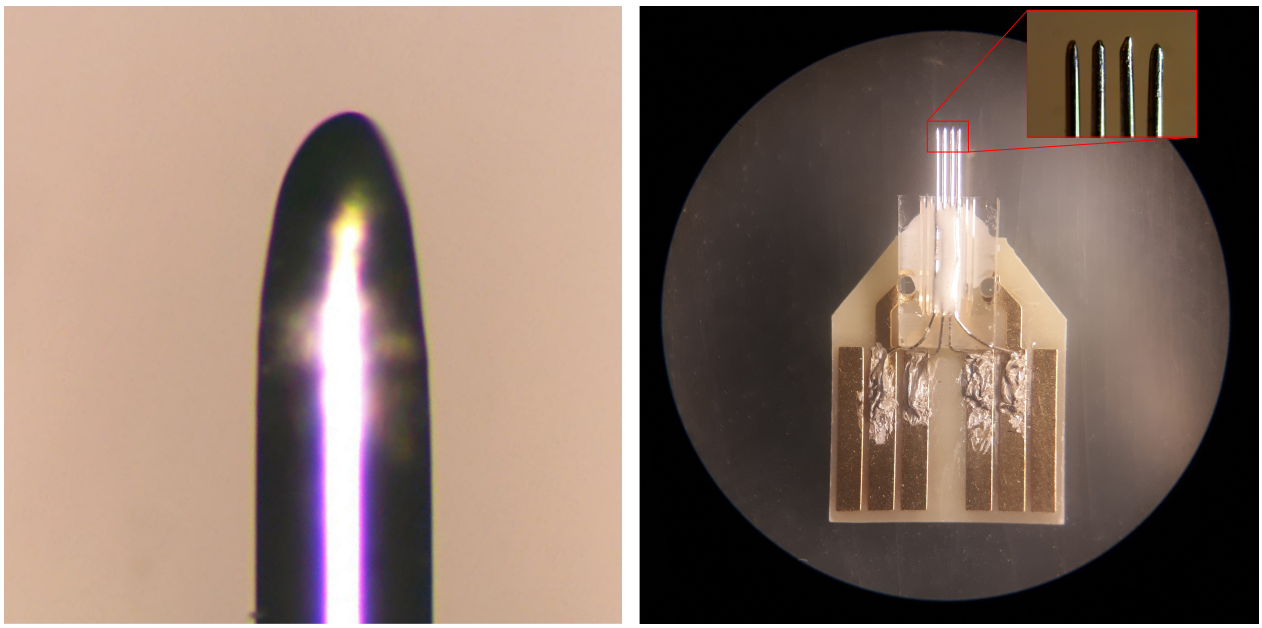

Figure 30: Pt/Ir wire chip assembly. Left) The $125\,\mu\mathrm{m}$ thick Pt/Ir 90/10 wires were etched in order to obtain a smooth and round tip. Right) The chip consists of four $2.5\,\mathrm{mm}$ long and $250\,\mu\mathrm{m}$ equally spaced wires. The estimated spring constant per wire is in the order of 80–$100\,\mathrm{N/m}$.

established to obtain very reproducible tip geometries that are necessary for both high stabil-

ity and well-defined tunnel currents [55–57]. By etching the tip, the head can be rounded and a smooth surface can be achieved. The goal is not to make the tip too sharp, as sharp ends and high contact pressure can easily damage the films. The electrochemical etching can be done in 20 mL distilled water with 20 mL acetone and 7 g $CaCl_2$ solution [55]. The solution was over-saturated with acetone in order to create a thin film of acetone swimming on top of the etching solution. The wires were dipped 1 mm into the solution. The thin acetone film helps to control the gas bubble formation during the etching process, as bubble streams can disturb the smooth etching process [58]. A graphite rod was used as a counter electrode and a 40 Hz 20 V_{pp} sinusoidal voltage was applied. The etching had to be stopped when a current below 10 mA was detected in order to create a round tip. Details about the setup for wire-etching can be found in [57]. During the etching process, PtCl is formed that appears as black precipitate that adheres to graphite. The PtCl can influence the etching process and thus the graphite needs to be flushed with distilled water and the solution needs to be replaced completely after 10 to 20 etchings. In figure 30 the final assembly and rounded tips of the Pt/Ir chip are shown.

3.6. Conclusion and Outlook

During the period of this thesis, only a handful of successful measurements could be done on Au substrates (see measurement shown earlier in figure 20 on a 150 nm thick Au sample). As shown in this figure, when all four probes are in contact, ρ can be extracted successfully. Besides Au, several materials were tried to be measured: 1–2 µm thick Rubrene-, Pentacene-, TIPS-Pentacene-, C_{60}-film and an inorganic electride material ($Ca_{24}Al_{28}O_{64}$, [59, 60]). The target diamond substrate was baked at 200 °C for >30 min and the substrate temperature was set to 85 °C during evaporation as an increased substrate temperature for pentacene-like

molecules yields larger crystal domains and exhibits improved photoconductive properties compared to substrate temperatures at room-temperature [61]. Due to the low charge transport abilities of organic materials, and due to the large pitch between the probes of 250 µm that unfortunately could not be minimized in a feasible way, it is believed that the system at this stage is not capable to measure high resistive materials. With such a large pitch size, and the restrictions from the multiplexer board and source-meter, the following restrictions are given:

- The maximum voltage rating for both approach mechanism and measurements is ±5.0 V. Higher voltages will damage the multiplexer board.
- The maximum current rating is ±1.0 mA. Higher currents will damage the probes.
- The applied current must be larger than 1.6 nA due to the leakage current from the multiplexer board.
- The source-meter has an input resistance in the order of 10 GΩ. The readout of sample resistances in the order of GΩ or higher will lead to a corruption of the measurement.

With a total pitch size of 750 µm for the current electrodes, the distance is too large to apply a current without reaching the compliance voltage. Even with a two point-probe measurement, no current could be applied through the material. With the larger and stiffer wires and pin probes, special attention had to be taken in order to prevent scratches on the samples. With other samples, such as an inorganic electride material ($Ca_{24}Al_{28}O_{64}$) that was prepared outside of the UHV chamber with a mechanically polished surface, the force limitation of the manipulator was often reached. Although the papers mention a conductance of around 800 S/cm (translates to a resistivity of $1.25 \times 10^{-5}\,\Omega\,\mathrm{m}$) [59, 60] and such a high conductivity should be measured in principle with our four-point probe. However, samples that are not prepared under UHV often suffer from native oxide layers and thus the probes need to

penetrate through these oxide layers. The sample was measured by using the Micromotive cantilevers and the Pt/Ir wire chips but no successful measurement could be made. Since the manipulator can only apply forces up to 0.04 N in total, this manipulator has been found as too weak in these cases. Other commercial four-point probe setups (e.g. from mProbes) that are also piezo-driven can apply 0.3 N per wire and still might be suffer from not being able to penetrate through hard native oxide layers.

In summary, the goal was to build an automated system that allows to easily contact a sample, to measure the conductivity of the sample and be able to map the surface. Although the electrical detection method technically allows to detect samples with resistivity up to MΩ, and together with the multiplexer board explained in section 3.4 allows to verify the contact to each probe, it has been found that the electrical detection method is still not very reliable on high-resistive samples and does not consistently work on semiconductor surfaces. Since the goal was to use cantilever-based electrodes, the issue remains that the cantilevers will always crash and break as soon as no electrical contact to the sample can be made. It is thus recommended to implement another surface detection method in the future, if an application towards automated sample-approach and sample-mapping is still of interest.

A mapping by using the RRP micro-manipulator arm will remain challenging. The non-obvious dynamic equations of motion of the RRP structure, in combination with the unpredictable slip-stick motion of the piezo-motors did not allow to progress further at this stage. Absolute tracking of the position of the four-point probe would be recommended.

In conclusion, both the commercial probes and micromanipulator might be great products that are worth to be considered for many applications, however, in our case where we have tried to combine both products, implement them in a UHV chamber, with optical access only through a long-distance optical microscope, with limited possibilities to rotate the probes relative to the sample surface, being able to both automatically detect the surface and scan

them in order to measure highly resistive semiconducting thin films, the application is not good. Since we are operating the four-point probe under UHV, solving the problems while maintaining UHV conditions are time consuming. At this stage, it might be the best solution to either micro-fabricate four-point probes that meet our needs and to only do single-point probe measurements, or to completely give up the combination of the micromanipulator and the probes. The work on an ultra-high vacuum chamber is slow and tedious, and in order to keep motivation high and frustration low, a reliable measurement tool should set the foundation for further measurements that are planned on this system.

4. Ultra-High Vacuum Suitcase

4.1. Introduction

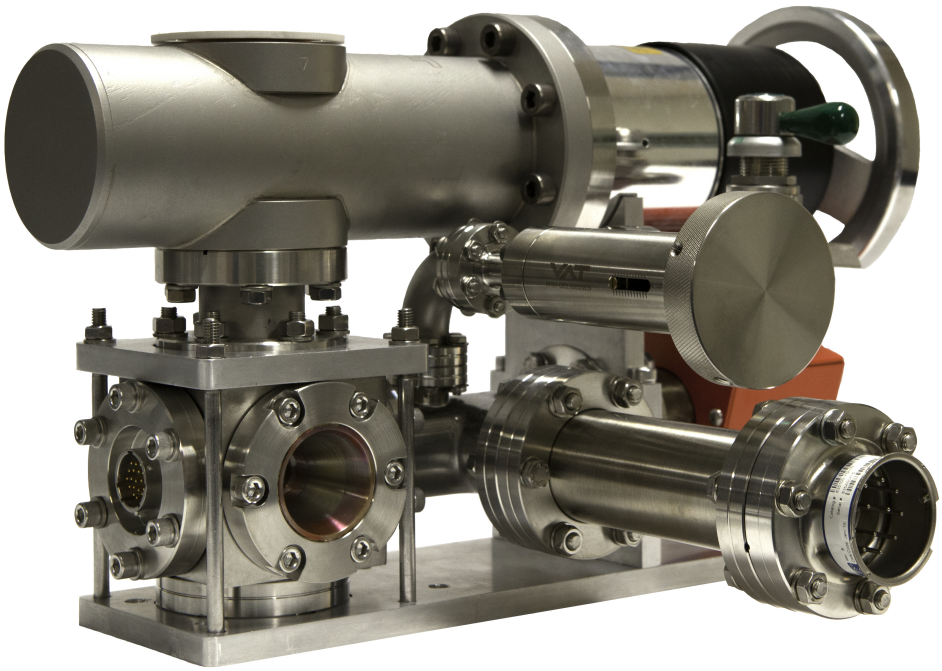

Figure 31: Home-built ultra-high vacuum suitcase. The suitcase allows to transport samples while maintaining pressures at 10^{-10} mbar. A non-evaporable getter- and ion pump sufficiently remove chemically active gases and thus keep samples clean at any given time. The suitcase is equipped with an all-metal gate-valve for sample transferring, consists of a home-built piezostage that allows to fine position samples very accurately with sub-micrometer precision and is equipped with two custom-made diamond windows that allow ultra-broadband transmission spectroscopy. Further, a residual gas analyzer allows to monitor the quality of the vacuum and a leak valve allows to controllably leak gases inside the chamber to monitor its effect on the physical properties of the sample.

Many interesting active materials suffer from the problem of degradation through various physical and chemical process pathways. It is often difficult to impossible to transfer samples with a potentially interesting surface condition to an analysis chamber or to another

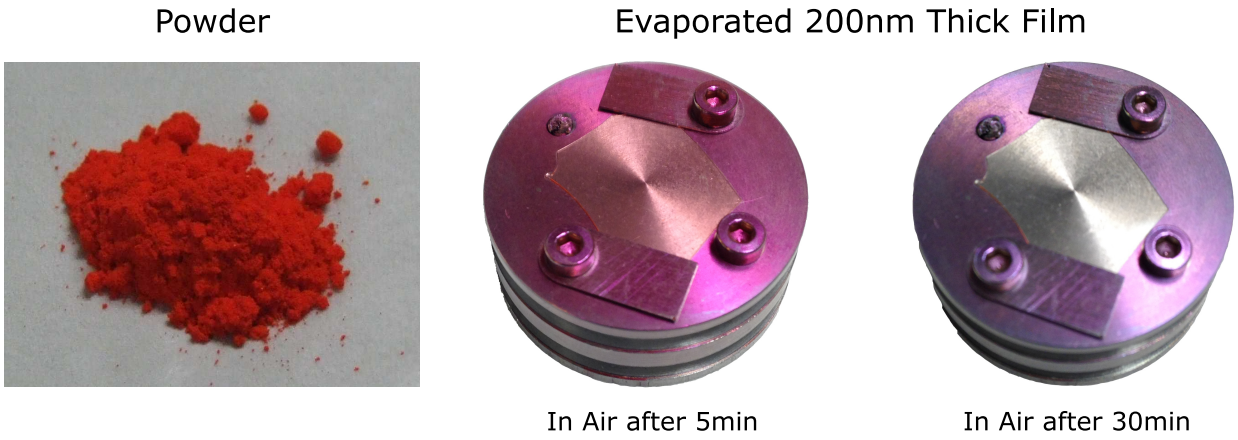

Figure 32: Discoloration of Rubrene. Left) The pristine Rubrene powder appears in a bright orange color (left). The oxidation of thin film rubrene films can be monitored visually as the film changes from red to pink (center)to pink-violet. When the oxidation process is finished, the films appear to be colorless as seen on the glass as substrate (right).

research facility without contaminating the samples to the point where useful information can be obtained. In terms of organic semiconducting materials, several studies observed that environmental exposure causes material degradation mainly due to oxygen and water [62–65]. For example, the oxidation of rubrene ($C_{42}H_{28}$) can be monitored visually as the molecules change from red to colorless, which is shown in figure 32. In this example, a 200 nm thick rubrene film was evaporated in the UHV chamber on a glass slide. Within 5 min in ambient air, a discolorations from orange to pink can be seen, and after 30 min the molecules appear transparent on the glass slide and remain pink-violet on the Mo sample holder. The mechanism behind the discoloration has been explained by Sinha et al. [62] and Ly et al. [66], where an oxygen induced chemical reaction forms rubrene-epoxide and rubrene-endoperoxide that completely destroys the delocalized nature of the electron distribution in the tetracene backbone of rubrene. This contamination affects the optical properties of the films and the results are relevant to the performance and reliability of rubrene based devices.

If we want to gain deeper understanding of the charge-carrier formation and separation processes in such model systems, it is of key interest that samples can thus be transported

and always kept under clean conditions and can be measured under the same conditions over a long period. A promising solution is the installation of a small UHV transfer chamber that can transport samples from the preparation chamber to other research facilities in a different geographic location. Further, it is of interest to be able to controllably leak gases to the sample, allowing us to ultimately study the effects and processes happening when contaminants are introduced to the system.

The idea of a portable UHV systems that is capable of transporting samples without the loss of UHV conditions is not new. Various types of home-built specialized systems and commercially available systems have been developed and reported [67–73]. Their chamber design and transfer system of the reported portable UHV systems are all unique for their usage and function. So far, no design has been reported that would allow to transport a sample under UHV conditions, maintaining a pressure at or even below 10^{-10} mbar and is capable of ultra-broadband pump-probe laser spectroscopy.

The word *suitcase* has been adapted due to common needs: It must be small, compact, lightweight and needs to be able to be transported. The UHV suitcase is enclosed and must have the ability to maintain pressures in the UHV regime at all times. Ideally, there is no or minimal power requirement during the operation and during the transport. Since we especially want to keep the samples away from water and oxygen, the pump attached to the suitcase must have a large pumping capacity for active gases. To keep the suitcase small and lightweight, sample-transfer and -manipulation as well as pre-vacuum pumps to reach UHV should be mounted to the attaching load-lock and not be a direct part of the suitcase.

We don't only want to transport the sample under UHV but also monitor the quality of UHV and have the possibility to leak gases into the chamber. Thus, a leak valve should be attached to controllably expose the sample to oxygen and water and a residual gas analyzer should be mounted to the system to monitor the quality of the environment at all time. Further, for

optical pump and THz probe spectroscopy measurements that are performed by the Cooke THz research group, the sample must be optically accessible by windows that cover a wide spectral range. The suitcase must fit between two parabolic mirrors on an optical table and thus the window-to-window width of the suitcase must be smaller than 10 cm.

A CF275 6-way cube as the central body part for the suitcase is thus ideal for our application and together with the attached window flanges, leaves a couple of millimeters of clearance to just slide the suitcase between the mirrors. All parts used must be vibration free, thus mechanical pumps can not be used, and the sample must sit and be held in position properly. Further for spectroscopy, we need a sample holder that allows us to position the sample precisely on a long-range millimeter motion scale with sub-micrometer resolution, ideally with the possibility to scan the sample.

Since we do not only want to perform transmission spectroscopy experiments on the sample but also want to have the ability to transfer the sample to the UHV JEOL Atomic Force Microscope Setup, a sample holder needed to be designed that fits into the UHV JEOL Setup, allows optical transmission through the sample, can be transferred inside the evaporation chamber and can be transferred and mounted properly in the UHV suitcase. This will allow different types of optical spectroscopies as well as AFM experiments on the same sample.

On top of that, all components used must be bakeable to at least 150 °C to efficiently remove adsorbed gases during a bake-out and only low outgassing materials should be used. Finally, to cut costs and machining and build time, the parts should be built up from standard available UHV parts as far as possible.

In this chapter, a solution for all the technical challenges of building such an ultra-high vacuum transport suitcase will be presented and discussed. In section 4.2, the choice of pump will be explained that ultimately makes it possible to keep the suitcase under UHV conditions. In section 4.4, a solution will be presented to fine position samples inside the

suitcase that is necessary for proper laser alignment and section 4.3 will discuss the technical challenges and implementation that were encountered to make ultra-broadband transmission possible. In figure 31, the final implementation from all the findings of every section of the suitcase is shown. For the sake of completeness, all the technical drawings, details about the home-built parts, as well as electronics, software implementation and manuals for operation can be found in the appendix.

4.2. Compact Non-evaporable Getter and Ion Pump

In earlier published transport suitcase versions, the vacuum inside the suitcase was often obtained by using battery powered ion pumps and reached pressures in the order of 10^{-9} mbar. In newer designs, non-evaporable getter pumps (NEGs) have become a practical tool to maintain low pressure in such suitcases. The main element of this pump consists of a porous getter material with a large surface area that chemically adsorbs gases and a heater element to activate the material. Once activated, the NEG element is a highly efficient capture pump which chemically pumps almost all active gases that are usually present in vacuum (H_2, H_2O, CO_2, N_2 and O_2). Since the pump does not require a continuous power supply, is compact, lightweight, vibration free, simple to use and affordable at low cost, this pump is ideal for our suitcase.

Nowadays, NEG pumps are commercially available and often come suited with an additional compact ion pump. The additional ion pump removes noble gases such as Ar, Ne and He that is not efficiently pumped by the getter material and removes additional methane that is generated by the NEG element [74]. The additional integrated ion pump thus enhances the pumping performance when powered. When the ion pump is powered, the current applied to the pump exponentially decreases with the pressure inside the chamber. The pump current

readout thus directly provides a pressure reading.

In our case, we use the NexTorr D200-5 pump. During normal UHV operation, the NEG element sorbs gases without the need of external power and only the ion pump needs to be turned on. After the pump has sorbed a significant amount of gases or is being vented, the surface of the NEG element will become saturated mainly by a passivation layer of carbides and oxides. To activate and restore the pumping speed, the getter cartridge needs to be heated at high temperatures. During the activation process, the suitcase should be connected to the load-lock of the main chamber so that released gases can be pumped and removed from the system by a turbo pump. Before activating, a pressure below 10^{-5} mbar should be achieved. To ease degassing, a bake-out of the ion element and of the entire suitcase is in general advisable and will result in better final pressure. Standard heating tapes (Omega HTWC101, 576 W) and fiber-glass sheets (McMaster-Carr, 40 inch wide, Al-backed) are used to heat and insulate the system from its surrounding. Baking temperatures of 150 °C have been found efficient to remove adsorbed gases such as H_2O and O_2. During the chamber and ion element bake-out, the magnets of the ion pump need to be removed and the pump to be turned off. This process will degas the ion pump. To activate the NEG filament and degas the pump and to reduce gas evolution, the internal getter cartridge heater can be used during the last hours of the bake-out to activate the NEG element. The internal heater reaches activation temperatures around 450 °C and the chamber wall will act as a thermal shield for such high activation temperatures. During the activation, a current of 4.8 A (60 W) should be applied for 1 h, where it is advisable to not exceed pressures above 10^{-3} mbar to avoid corrosion. The controller comes with an inbuilt *Timed Activation* process where the cartridge is heated by successive steps, allowing to prevent high gas loads. Once the getter element has been activated, the ion pump can be turned on and the pump will develop its full speed, removing both inert and active gases from the suitcase.

In order to show the operational capability of maintaining UHV conditions at all times, the

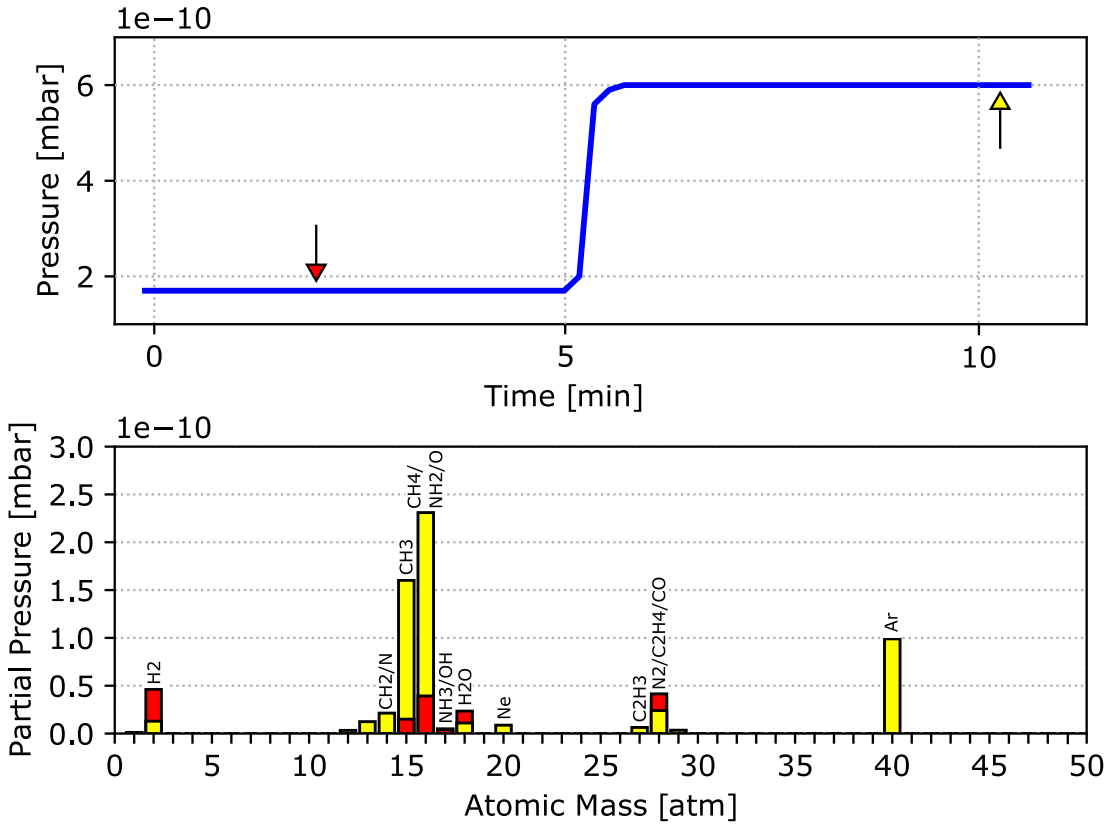

Figure 33: Pressure and rest gas comparison when the ion pump is turned on and off. Top: From t = 0–5 min, the ion pump is on and the base pressure is at 1.7×10^{-10} mbar. At t = 5 min, the active ion element is turned off and the pressure quickly raises up to 6×10^{-10} mbar but still remains in the UHV regime. Bottom: The residual gas analyzer is used to monitor the quality of the vacuum. When the pump is on (red), main gases in the UHV are H_2, CH_4, N_2/C_2H_4 and H_2O. When the pump is turned off (yellow), noble gases (Ar and Ne) as well as CH_4 can not be pumped efficiently anymore which are the main components that lead to a pressure increase.

evolution of the pressure was recorded when the power-operated ion pump is turned off. For this experiment, an additional gauge needed to be added to the suitcase due to two reasons: First, since the pressure of the suitcase can only be read when the ion element of the ion getter pump is powered, the temporary additional gauge (MKS 421 Cold Cathode) is needed to be able to monitor the pressure even if the ion pump is turned off. Second, the residual gas analyzer (Granville-Phillips 835 VQM) mounted to the suitcase can accurately measure

the gases present in the suitcase, however, the monitor is ratiometric, meaning that it only determines the ratio of each gas to other gases in a vacuum chamber. To calculate the partial pressures of each gas, the RGA needs to be coupled with a total pressure gauge. In figure 33 both the pressure evolution and outgassing of the ion getter pump was tested when switched from on (normal operation) to off (transport). When the ion pump is on, a pressure low as 1.7×10^{-10} mbar was recorded. The main components shown in the RGA histogram in red are H_2, CH_4 and N_2/C_2H_4, and shows a H_2O peak. When the ion pump is turned off (during transport), the pressure increases rapidly to 6×10^{-10} mbar but stays in the UHV range at that pressure for a long time. When the ion pump is off, the increased pumping efficiency for CH_4 and noble gases such as Ar and Ne falls away and the partial pressures for these gases increase (yellow peaks in histogram). Since the getter pump has a high pumping capacity for oxygen, neither mode has a detectable amount of O_2. Interestingly, the partial pressure for H_2O decreases when the ion pump is turned off and can be explained with the operation principle of the ion pump. Gases flowing into an ion pump are being negatively ionized and accelerated towards the positive cathode of the ion pump by a high voltage and a high magnetic field. The ions that hit the cathode chemically and physically react with the cathode material being expelled through the impact. The bombardment of the ions leads to reorganization of the cathode surface, that can also lead to releasing gases from the ion element during operation. In case of H_2O, this seems to happen. This back-streaming effect is known and was considered in the pump geometry [72, 75]. By placing the NEG element in front of the ion pump, the element can sorb these back-streaming gases very efficiently and only a small fraction is released to the chamber. In case of H_2O, this can generally be fixed by baking the system above 120 °C as baking removes water very efficiently. Also, the ion pump should be turned on at the last stage of a bake-out for a couple of hours to remove water from the underlying reactive cathode material.

Next, the ultimate pressure inside the suitcase has been monitored for one and a half

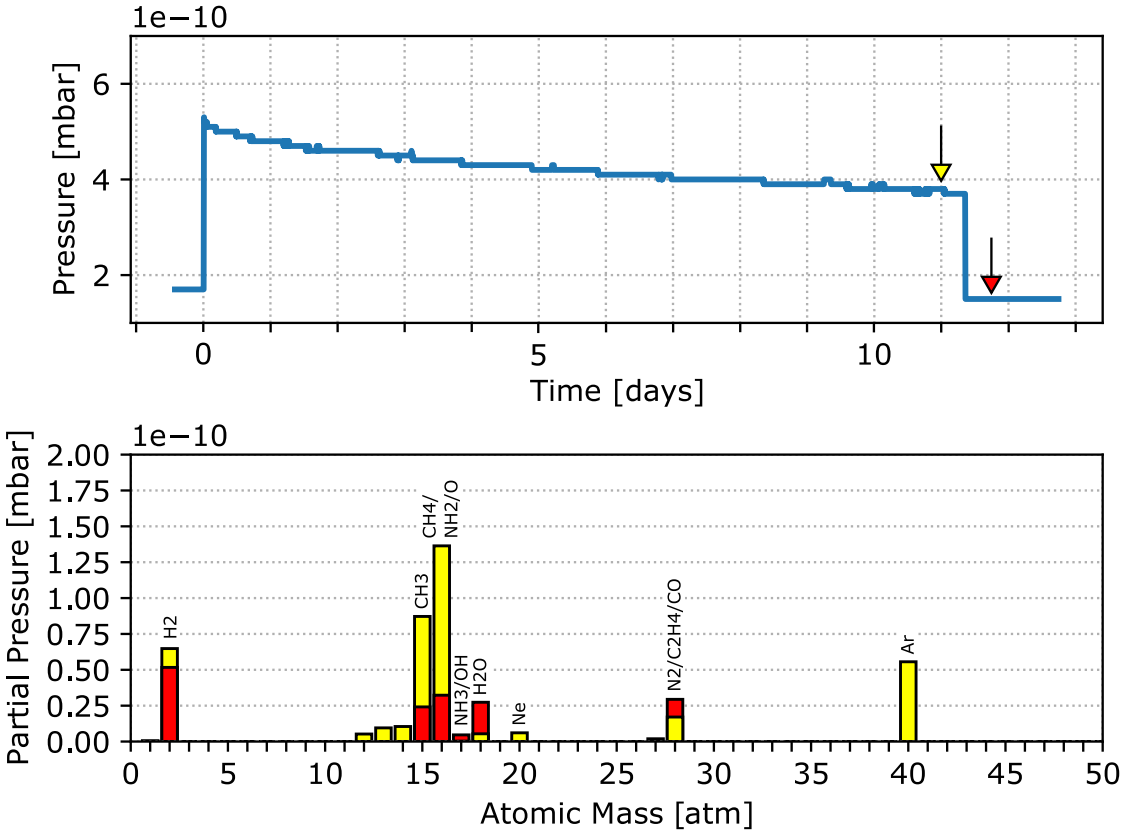

Figure 34: Pressure and rest gas evolution when the ion pump is turned off for 11 days. This scenario simulates a long transport in case the suitcase has to be shipped or sent to another facility that is far away. Top: At t = 0 days, the ion element is turned off and remains off for 11 days. The pressure increases upon turning the pump off (5×10^{-10} mbar), but will slowly decrease again because both the getter and inactive ion pump still actively sorb residual gases. Bottom: The residual gas analyzer is used to monitor the quality of the vacuum after 11 days with the ion pump turned off (yellow) and on (red) again. When the pump is turned on again, noble gases (Ar and Ne) as well as CH_4 will be pumped efficiently again and the pressure decreases quickly back to its original state (1.5×10^{-10} mbar).

weeks in static condition with the ion pump being turned off and the pressure evolution is shown in figure 34. As discussed before, once the pump is turned off, the pressure increases immediately but there is no observable increase of pressure even over a time period of one and a half weeks. The pressure decreases over the time, indicating that the getter pump actively sorbs residual gases. After eleven days of inactive pumping (yellow arrow and histogram),

the main rest gases are still CH_4 and its residues, H_2 and Ar. By turning the ion pump on again, CH_4 and noble gases are being actively pumped again and the pressure drops back to its original state (1.5×10^{-10} mbar).

4.3. Optical Windows for Optical Pump Terahertz Probe Experiments

To perform pump-probe experiments on our sample, the sample must be optically accessible through UHV graded windows. For optical pump and terahertz probe experiments, two broad transmission spectra are required; the visible regime from sub-400–800 nm and 300–12 µm (or 1–25 THz). Normally, a multitude of different windows each spanning a small wavelength range is used for such a broad transmission spectrum. In our case, the optical pump and the THz probe waveguide are collinear and thus must be transmitted through the same window. For illustration purposes, figure 35 shows the transmission spectra of some materials with known transmission in the given range that can be bought as UHV graded windows. The most common window materials in UHV science are fused silica and sapphire due to their high transmission in the optical regime and due to their low costs. However, in figure 35, one can already clearly see that both materials have a cutoff at frequencies above 10 µm and are not a good choice for a window material as they do not allow THz transmission beyond 2–3 THz at room temperature. A good alternative would be z-cut quartz with an absorption coefficient of around 0.3/cm at 1.5 THz at room temperature. However, quartz is dispersive, birefringent and cuts off THz frequencies above 6 THz. Since we want to measure organic molecular films like Rubrene, we would cut off the higher frequencies where a much higher ac conductive response is expected. In this regime, the conductive response increases linear to quadratic with increasing frequency. The cutoff above 6 THz thus would defeat the purpose of the suitcase. Other materials like dispersionless high resistivity silicon or high-density

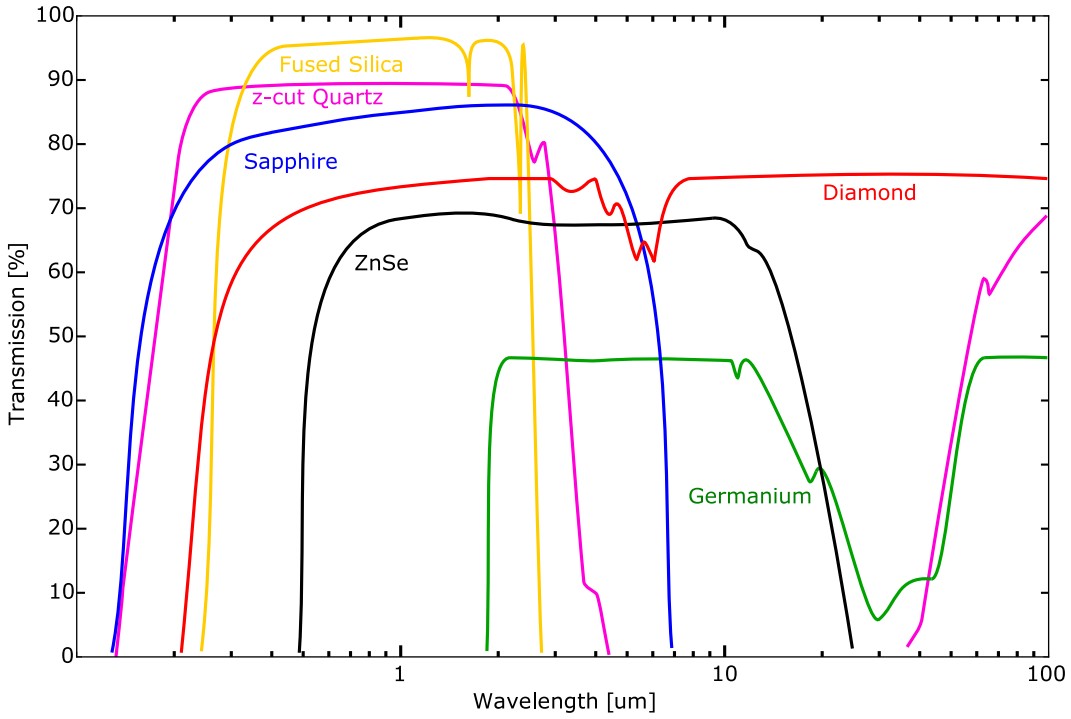

Figure 35: Transmission spectra of considerable materials used as UHV windows. Redrawn from technical notes of UHV graded window components that are commercially available, Newport [76], Rayotek [77], Diamond Materials [78] and Del Mar Photonics [79]. Compared to other window graded materials and coatings, high-quality diamond transmits in the entire spectral range from the visible at 225 nm over the infrared-, the terahertz range and even up to radar frequencies.

polymers that are good for THz transmission cannot be considered because they are either not optically transparent or cannot be considered for UHV graded windows. The only known material left that provides such a broadband transmission window and suits our demands is thus diamond.

Diamond exhibits a variety of extraordinary properties that make it an ideal material for optical applications. Only high-quality diamond wafers are known to transmit in the entire spectral range from the visible at 225 nm over the infrared- and terahertz range and even up to radar frequencies, which is ideal for our application. Apart from a weak absorption peak at around 5 µm, no further absorption affects the transmission in the given range. Furthermore,

diamond is isotropic and dispersionless and thus ideal for time-domain pulse sampling. Unlike most electrical insulators, diamond is a good heat conductor due to the strong covalent bonding and low photon scattering which makes it a good choice of material for high power density laser applications [80]. Important for UHV window designs, diamond is also very robust and can withstand the pressure difference between ambient air and UHV. Diamond thicknesses low as 1.5–2 % of the free aperture diameter are recommended for mechanical and thermal stability. Industrialized chemical vapor deposition method (CVD) nowadays allows to synthetically grow diamond on areas greater than 100 cm^2. Impressive 96 mm free aperture 2.23 mm thick diamond windows for high-vacuum systems were achieved and implemented already earlier [81]. With diamond as the chosen material, the implementation and design as a UHV graded window with its restrictions needs to be discussed.

4.3.1. Design Restrictions and Criteria

In the THz setup, both the visible pump and THz probe waveguide are collinearly aligned using parabolic mirrors with a hole parallel to the focused beam. Figure 36A) illustrates the THz setup. The beam aperture of the pump can be kept below 1 mm and does not give further restrictions to the design of the windows for the suitcase. The THz beam propagation on the other hand is very special and needs to be considered. The collimated THz beam is reflected from parabolic mirrors with a diameter of 2 inch (50.8 mm) and is focused on the sample with a focal length of 4 inch. The transmitted beam is then collimated by same mirrors on the other side and propagated to the detector. In figure 36B) the UHV suitcase is put in between the setup. If we assume that the collimated THz beam covers the whole area of 2 inch mirror before it is focused, the THz beam has roughly a beam aperture diameter of 32 mm when it hits the window flange of the suitcase. Thus we cut 45 % of the outer area of the propagating field away if we would use standard UHV windows with standard window

diameter. Both Mueckstein et al. [82] and He et al. [83] have mapped the evolution of a generated THz pulse produced by a two-color laser plasma, as in the Cooke laboratory and have observed that the intensity of the THz wave outside of the Rayleigh range shows an annular, doughnut-like shape where most of the energy is in a ring at the periphery. Two-color laser plasmas are generally not the normal mode of generating THz pulses, however it is the way how the ultra-broadband pulse is generated in the Cooke laboratory. By cutting off the outer 45 % of the area, the major part of the pulse would not propagate into the chamber. We thus need a much wider opening as the loss of the majority of the intensity would defeat the purpose of the suitcase.

Reaching out to different companies that nowadays industrially produce high quality dia-

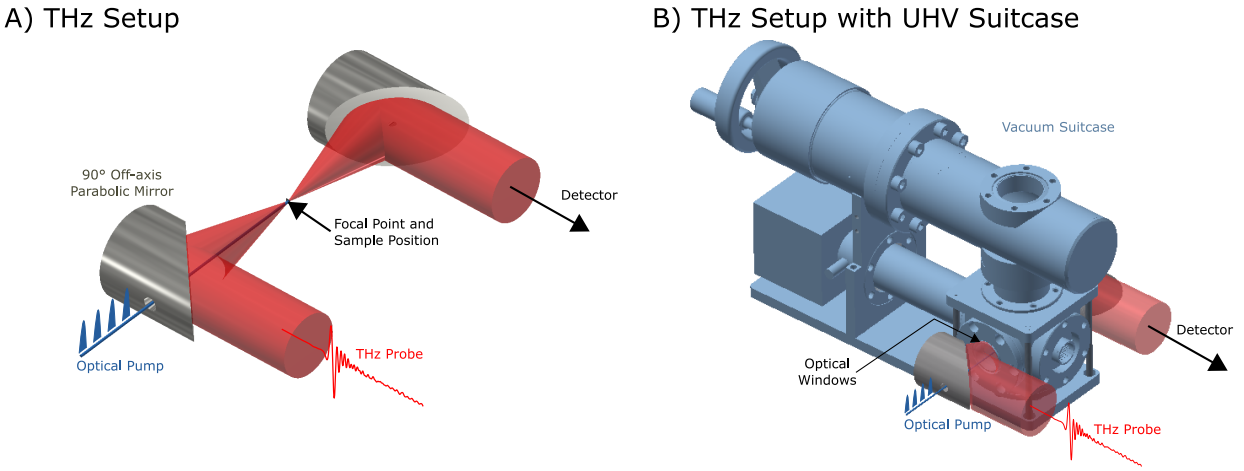

Figure 36: THz Setup. A) Beam path of the optical pump and THz probe on the optical table. The collimated THz beam is reflected from parabolic mirrors with a diameter of 2 inch and is being focused together with the collinearly aligned optical pump to the sample with a focal length of 4 inch. B) Suitcase placed in the beam path of the THz setup. The free aperture of a standard UHV window is much smaller than the aperture of the THz beam on the same spot and thus a big portion of the THz is cut away and can not reach the sample.

mond wafers, we realized that further adjustments need to be done, since a solution had to be found how to seal the wafer to the flange. In figure 37, an evolution of the window design is presented. The idea of using a 33 mm free aperture window and custom build a knife-edge

sealing window with detachable windows failed due to geometrical restrictions since we cannot further extend the suitcase (figure 37a). The suitcase otherwise would not fit between the two parabolic mirrors. Important to note, it was of main interest to reduce the diameter of the diamond wafer due to financial restrictions. The price per window roughly scales with the area of the diamond wafer and we not only want one window but need two windows for optical transmission experiments. By reducing the free aperture of the diamond wafer from 33 mm to sub-15 mm, both the cost and the thickness of the diamond wafer can be reduced significantly. This can be achieved by placing the diamond wafer closer to the inside and use a conical extension to mount it to the flange.

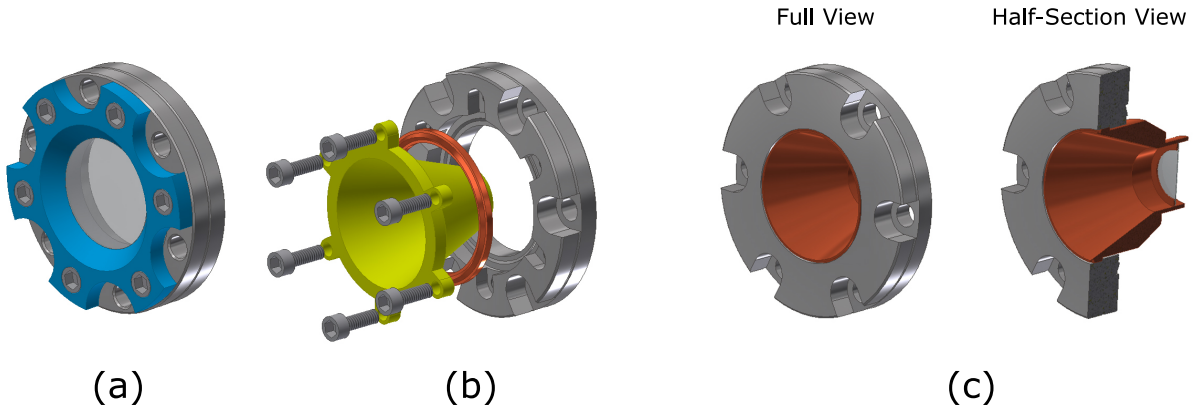

Figure 37: Evolution of the window design. Different designs were elaborated where the window material is a) clamped, b) knife-edge sealed and/or glued and c) directly brazed to the flange.

As we know the rough design of the windows now, a method needs to be found how to seal the diamond wafer to the flange. Several groups have made their own UHV windows and have worked on finding ideal designs and sealing methods how to make a UHV window leak-tight. Common sealing methods are clamping by using elastomers or soft metals [84–87], gluing by using UHV compatible adhesives [88], welding [89] and brazing [90]. Each technique has advantages and disadvantages that highly depend on the operating conditions

such as pressure and temperature, the design architecture of the window and the contacting materials that need to form a seal. In our case, clamping was considered but withdrawn because clamping needs space that is not available in our configuration and because time-intensive machining would be involved (figure 37b). Gluing is the most cost-effective solution and has almost no sterical restrictions to our design. Adhesive epoxies and UV curable systems that have low outgassing for use in vacuum environments and are stable to the bake-out temperature were considered as bonding materials. To mention some adhesives that resist high temperatures and chemicals, have low outgassing and bond to various materials, Epo-Tek 353ND , Master Bond EP42HT-2LO and Loctite 9492 are good candidates to be considered. However, gluing is a delicate process where right bonding conditions must be found, and virtual leaks must be avoided. Once the adhesive is cured, little can be done to change the bonding conditions. Further, information about long-term mechanical- and thermal stability is often not available and ideal adhesion conditions for diamond has not been reported. In industry, brazing diamond wavers to copper has become a common technique as a sealing method with leak-rates below $10^{-10}\,\mathrm{mbar\,l/s}$. Since diamond is often used for high power density laser applications and diamond is a good heat conductor (thermal conductivity $>1000\,\mathrm{W/mK}$), brazing it to copper is a popular choice because the high thermal conductivity of copper (about $400\,\mathrm{W/mK}$) allows heat to pass through it quickly and can also be actively cooled efficiently. This option was the best choice as it offers the best durability and stability for our suitcase.

A window design that passes all of our needs was elaborated and Diamond Materials GmBH in Germany industrially manufactured our design for us. In figure 38, a half-section view through the suitcase is shown in order to visualize the propagation of the optical pump and THz probe through the sample. The conical design of the windows allows full propagation of

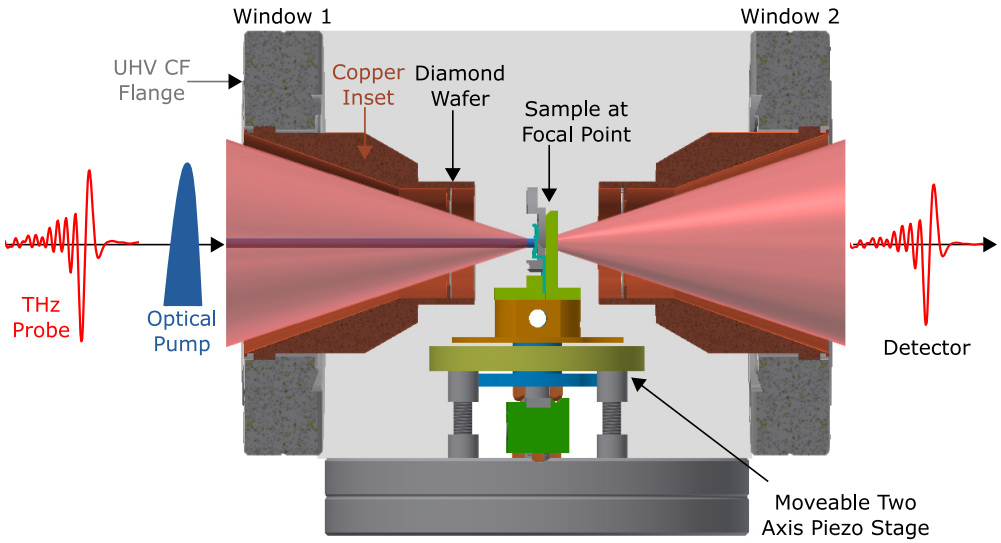

Figure 38: Cross-sectional view through the suitcase. Both the optical- and THz beam can fully propagate through the window and reach the sample and be collected by the detector. A two axis piezo stage allows to fine position the sample to the focal point of the beam.

the THz probe. The final windows that were produced are shown in figure 39. The assembly consists of the copper inset tube bonded to the CVD diamond using diffusion Ag-(Cu)-brazing technology [81, 91, 92]. This assembly left a useable free aperture of the diamond window of 14 mm. For more information, Appendix A.1.2 shows the detailed technical drawings and the specifications of the final diamond windows.

4.4. Two Axis Piezo Stage

To optimize optical measurements, the sample inside the suitcase needs to be placed in focus of the optical laser setup. Normally, the laser beam setup is fixed, and the sample must be brought into the focal point of the setup. Normally, samples are mounted on a translational stage that allows to precisely align the sample. In our case, the suitcase that contains the sample is heavy (about 10 kg) and the width of the suitcase has just a couple of millimeter clearance to fit between the mirrors and lenses. If the sample would be mounted stationary

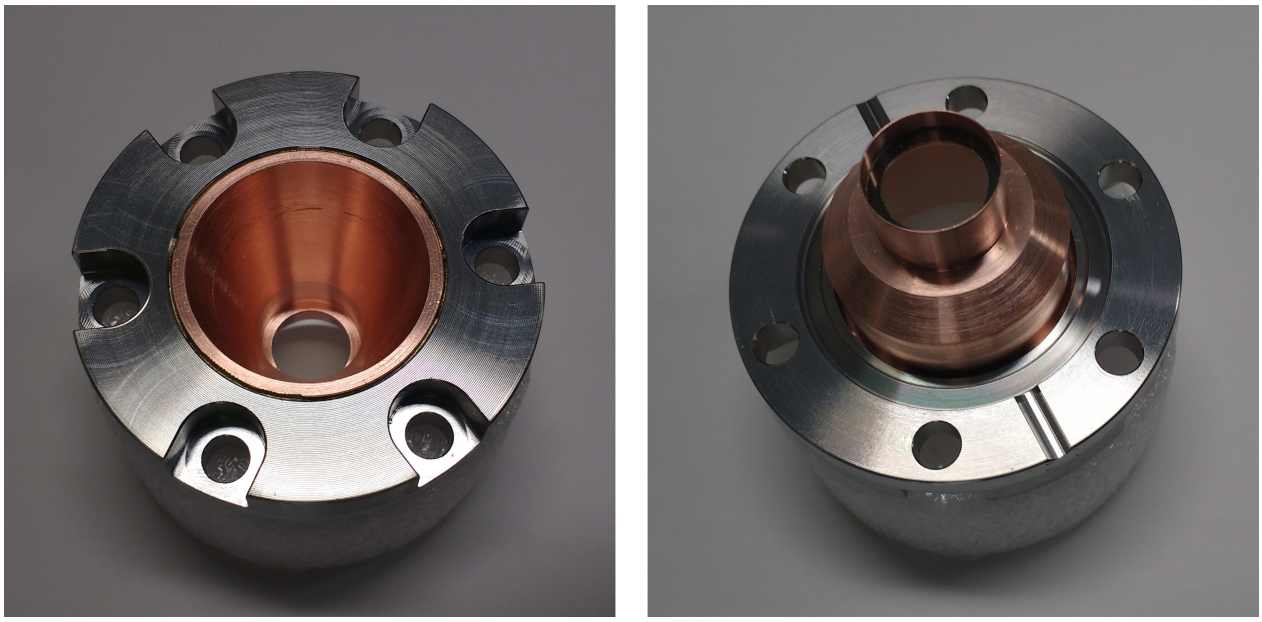

Figure 39: Air side view (left) and vacuum side view (right) of the implementation of the diamond window. This design allowed to reduce the diameter of the diamond wafer drastically while still maintaining a large enough opening to allow maximum THz beam propagation through the window.

within the suitcase, finding the right sample position by hand would thus be hard. Further, once the suitcase is roughly aligned and the laser propagates through the suitcase with the windows, the position of the suitcase should be fixed and only the sample in the suitcase should be fine-aligned and remotely be scanned.

An elegant way to meet our requirements of long-range millimeter motion with sub-micrometer resolution, stability, low noise and versatility is offered using a so-called piezoelectric stepping motor. A similar principle of operation is used by the Kleindiek micromanipulator that was explained in section 3.2. These stepping motors work under extreme environmental conditions such as low temperature, high inert gas load and UHV condition and have been widely used and described [93–97]. Although many different piezo stages are commercially available nowadays, it was difficult to find a product that satisfied all our needs due to several reasons. First, piezo stages have a very wide scope of application. This means that not all commercially available stages are UHV compatible because either the component materials

outgas or cannot be heated to sufficiently high temperatures which is necessary to remove absorbed rest gases to reach UHV conditions. Second, the compact design of the suitcase also requires a restricted design of the piezo stage. Most stages do not fit inside the CF275 6-way cube or are too tall to sufficiently mount the sample at the right height so that the sample is in the center position of the windows. And fourth, disassembling, modifying and reassembling existing piezo stages can lead to damaging the piezo material or to a general loss in performance and warranty. Thus, for the reasons mentioned, it was necessary to make a home-built version of a piezo stage that satisfies all of our needs.

4.4.1. Description

Piezoelectric materials generate a linear internal mechanical stress if an electric field is applied to the material. The range of the maximum mechanical stress generated on the piezoelectric element is very small, normally in the order of micrometers and can be little as angstroms. This small induced mechanical stress is key for obtaining high precision positioning in the order of nanometers.

In combination with a schematic representation of the principle shown in figure 40, the mechanism of motion will be discussed now. The common drive mechanism is to use piezoelectric actuators to push a stator. By periodically deform the actuator and using asymmetric accelerations, a one-dimensional motion can be provided. In the first step, the actuator is slowly deformed in one direction. During this slow period, the stator can follow the deformation due to friction. In a second step, the actuator immediately jumps back in the opposite direction. During this fast period, the stator cannot follow the actuator due to its inertia. By repeating the steps, the stator can be pushed in one direction and the total travel is only limited by the geometry of the moving parts. As thin sheets of piezoelectric materials normally have nominal displacement in the order of nm/V, high driving voltages and high

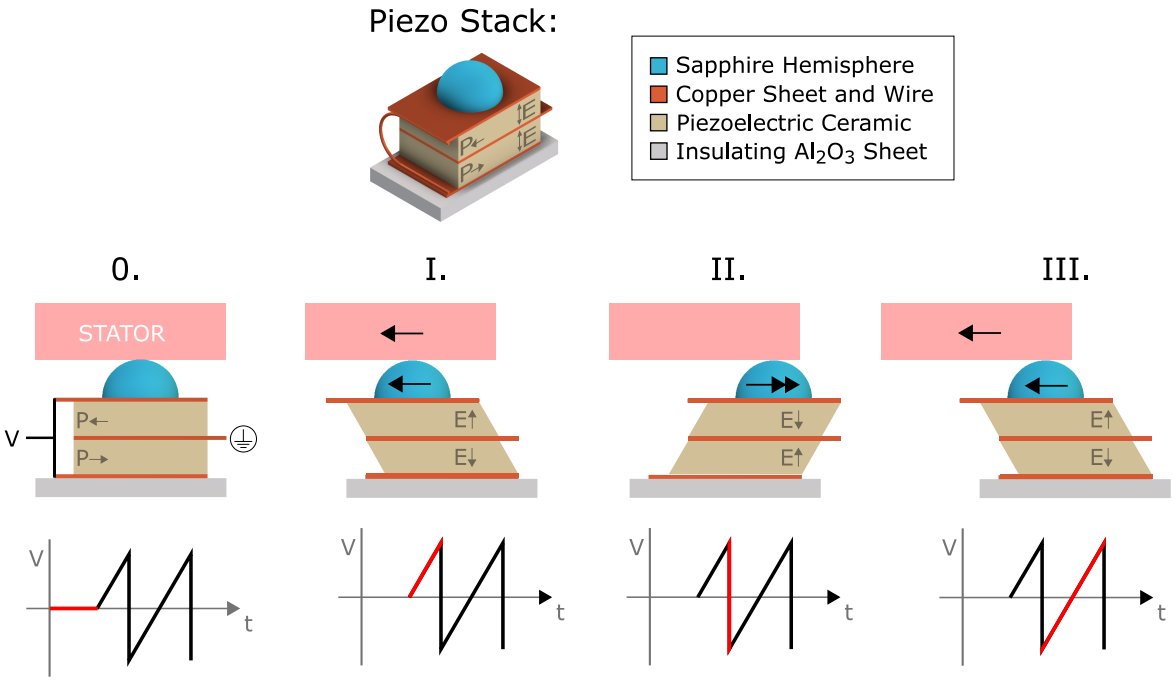

Figure 40: Principle of a stick slip piezo manipulator. 0.) Two or more thin plate piezoelectric ceramics are polarized (P) in a direction parallel to the bottom. These piezos can be glued on top of each other and the stack is topped by a sapphire half-sphere forming a point contact to the stator. I.) By slowly increasing a rising voltage (V), an electric field (E) perpendicular to the polarization causes a shear of the material. During this slow period, the stator can follow the shear actuator's movement due to friction. II.) An abrupt jump of the electric field in the opposite direction, the piezoelectric material bends in the opposite direction. During this fast period, the stator can not follow the actuator's movement due to its inertia. III.) By repeating the steps II. and III. at high frequency, a forward movement of the stator relative to the actuator can be achieved.

operation frequency rates are necessary to achieve long-range motions in an observable short amount of time.

To achieve an accurate linear motion of the stator relative to the actuator, the device must be stable, repeatable and durable. Central to moving a stator in one direction with the highest precision, the concept of kinematic constraint of ideal rigid bodies must be introduced [98]. This concept is concerned with the number of degrees of freedom that a mechanism features. If the mechanism does not exactly match the degrees of constraint with its freedom, the mechanism is either over- or under-defined and it is very unlikely that an ultra-precise

mechanism can be achieved. To explain this concept, one can think of a sphere in a Cartesian coordinate system. This unconstrained rigid body has 6 degrees of freedom (3 translational and 3 rotational). By introducing an idealized point contact of the sphere to a plane and assuming there is no friction in between, one can imply one single constraint and reduce one translational degree of freedom. To achieve a precise one-dimensional linear movement of a body, one must reduce all three rotational and two translational degrees of freedom and thus forming 5 constraints. This can be achieved by having two spheres in a v-groove and one sphere on a flat. To create friction and keep the carrier on the horizontal surface, magnetic clamping or mechanical spring force can be used. Figure 41 shows an example of adding constraints to a body on a horizontal plane and mentions the remaining degrees of freedom. For our purpose of linear translational motion, the concept shown in figure 41e) will be implemented.

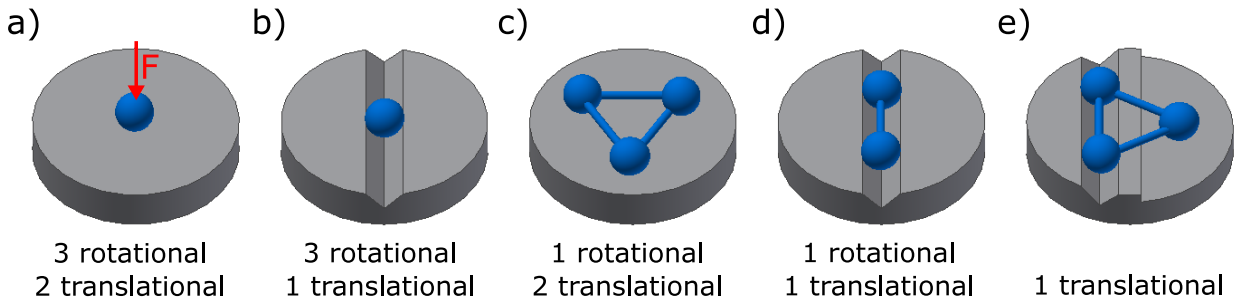

Figure 41: Degree of freedom constraints on a rigid body with their degrees of freedom left. a) A single degree of freedom constraint is provided by pressing a rigid sphere against a rigid flat with a frictionless surface. b) Two constraints can be envisaged by a sphere in a v-groove, c) three constraints by three linked spheres on a flat, d) four constraints by two linked spheres in a v-groove and e) five constraints with two spheres in a v-groove and one on a flat, all linked together. To keep the spheres at the same relative height, the flat in e) needs to be lowered depending on the angle of the v-groove and sphere radius.

4.4.2. Implementation

To build a piezo stack as shown in the top of figure 40, a thin piezo ceramic single sheet which is polarized in a direction parallel to the bottom and top plate was used to build the piezoelectric actuators. These piezo ceramic sheets are available with evaporated nickel on both sides which can be used as electrodes. Before cutting the plate into pieces, it is recommended to mark the direction of the polarization on every piece to be cut with a pencil and to mark the sizes. Since the ceramic is very brittle, both sides of the ceramic are covered with a thick layer of melted wax. By carefully cutting the ceramics using a ruler and a sharp razor blade, small pieces of 2.5 mm x 3.5 mm can be produced. To remove any residual wax efficiently from the ceramics, the pieces are rinsed in xylene, benzene, acetone, alcohol, twice with isopropanol and blow-dried between each step. Small pieces of copper foil (2.5 mm x 4.0 mm) are cut into size and a fine 600 grid sandpaper followed by an acetone and isopropanol ultrasonic bath are used to remove the native oxide layer. As we will run a high voltage through the piezos, it is important to insulate the stacking from the surrounding. As an insulating material, a thin sheet of Aluminum Oxide (Al_2O_3) can be cut into pieces (3.0 mm x 5.0 mm). Since Al_2O_3 is very hard to cut, a low speed rotating diamond saw was used to precisely cut the sheet into pieces. By using a conductive UHV compatible two component epoxy (Epo-Tek, H22), the pieces can be glued together according to figure 40. For our application, we glue two shear piezo ceramics on top of each other to increase the maximum shear of the actuator. The step size is highly dependent on the local contact roughness and the external loading. To create a rigid point-contact to the stator, sapphire hemispheres with a diameter of 2.0 mm (SwissJewel, H040) are glued on top of the stack. Six piezo stacks were built, where three are each used to form a linear translational motion. The piezos can now be glued to the translation stage and be wired with Kapton-insulated thin Cu-wires.

Next, the stage was designed. Since the stage requires a compact design, the two transla-

tional linear motions were placed directly on top of each other. Since clamping needs space that was not available, UHV compatible, ultra-high temperature resistive AlNiCo disc magnets (McMaster-Carr, 0.125 inch diameter, 0.25 inch thickness) were used instead to press the rigid spheres of the motors against the rigid flat. Since the magnets need a magnetic counterpart, thin hardened 440C stainless steel shafts (McMaster, Hardened Precision 440C Steel Shaft) were used. The additional carbon in the steel adds impurities that make the steel paramagnetic. However, the stainless steel is very hard and needed special precautions such as special hardened tools to properly machine the parts. Further, as the strength of the magnetic force can only be controlled by placing the magnet closer or further away, the magnets were placed in a hole and kept in place with flat set-screws that allowed to modify and control the exceeded magnetic force.

Next, special attention needed to be paid to the groves and flat surfaces where the sapphire hemispheres will touch. The sapphire hemispheres were chosen because they need to be hard enough that they don't deform and to form point contacts. Since the sapphires are hard and the piezos will run on high frequency, the sapphires will damage the surface and lead to an imprecise movement or even failure. To guarantee a long-term stability and usage, the grooves and the flat surfaces needed to be hardened. Titanium nitride (TiN) is known to be an extremely hard ceramic material and is often used as coating different metals to improve the substrate's surface properties. In figure 43, the schematics of the two parts are shown that needed to be partially coated. After branching out to companies for coating, a mask was produced and sent off for coating. However, the returned piece did not show the quality we aimed for as the coating was uneven and was dirty. As the risk of outgassing and failure was too high, another design was realized. Instead of post-processing the parts, the parts were directly made from hardened stainless steel (McMaster-Carr, Rockwell C50) and material from the CF275 flange was removed to properly fit the new design together. In figure 44 the

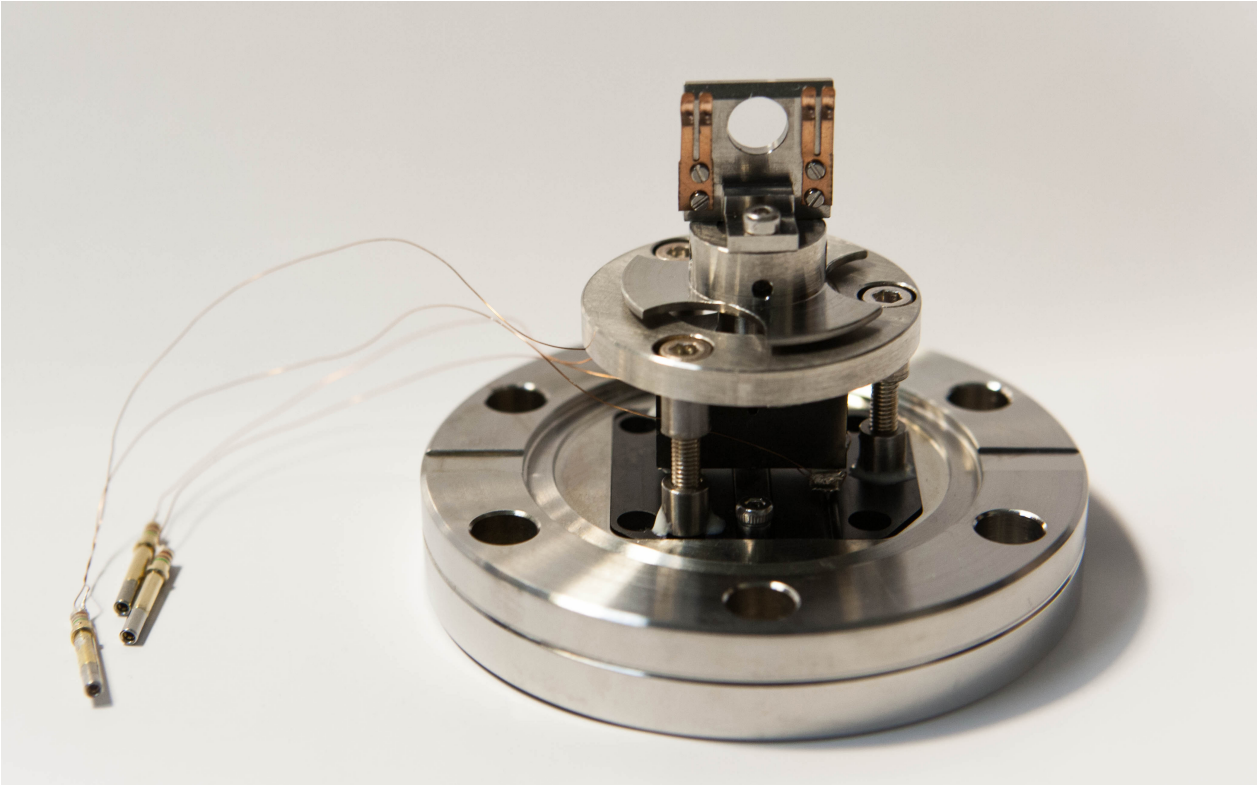

Figure 42: Piezo Assembly

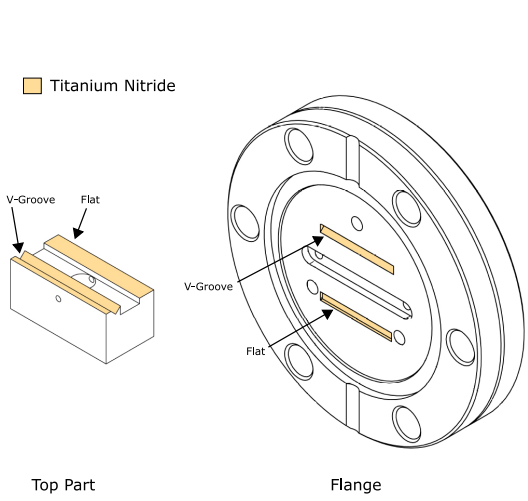

Figure 43: Masking.

new modification is shown. In addition, the surfaces were polished for further smoothing of the surface. Since this setup is only held together by magnets, transferring and removing a

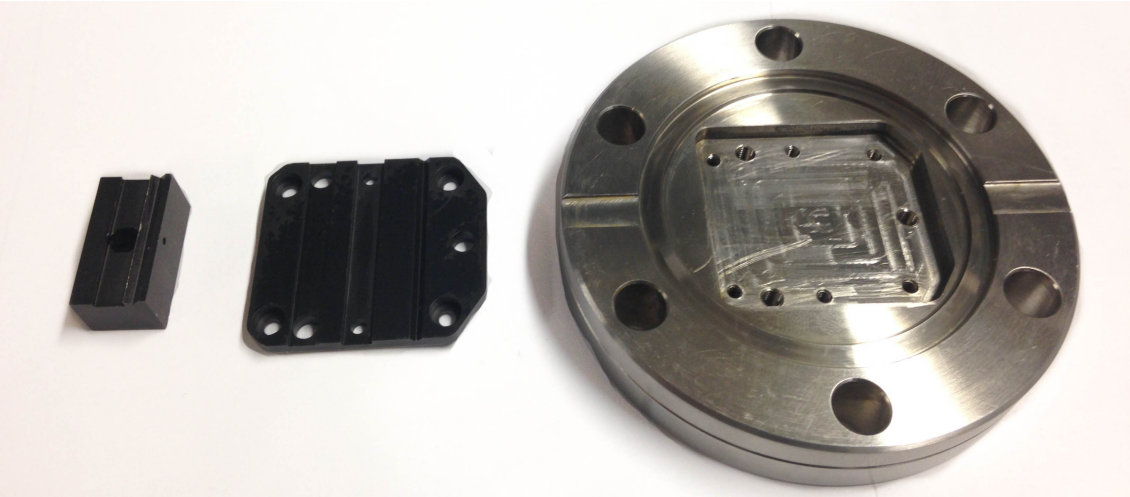

Figure 44: Special hardened stainless steel insets were produced in order to guarantee a long-term stability and usage of the piezo stage.

sample from and to this stage would not work. The modified JEOL sample-holder (drawings in appendix A.3) has a pin-hole, by which a modified micro-grabber can be used to catch, vertically transfer and release the sample (drawings of the micro-grabber in appendix A.5). Once mounted, the sample is held by copper clamps on the stage and if the clamps would be too strong, the whole stage would be lifted with the sample if one would try to remove it again. The issue was solved by placing a stationary retaining ring on top of the piezo structure that is sandwiched by two triangular propeller-shaped plates that move with the piezos. The spacing between these propeller-shaped plates and the retaining ring was kept small (on the order of 0.25 mm). This way, when the sample is removed and the magnets would not be strong enough to hold it, the piezos still could not fall out of the grooves when a sample is being transferred. Figure 45 shows a movie sequence of the piezo stage moving from left to right. The final implementation allows to move the sample by ± 5 mm in every direction from its center position.

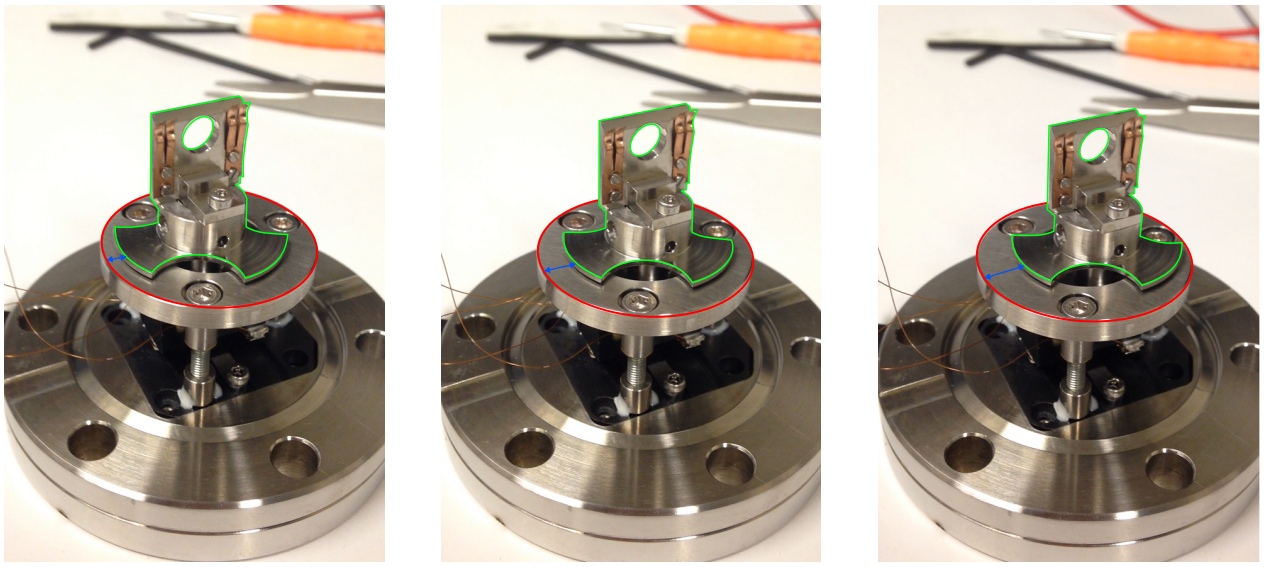

Figure 45: Video sequence of the movement of the piezo stage from left, to center, to right. For better indication, the red part is the stationary retaining ring, green is the moving sample holder and blue indicates the movement distance. From its center position, the stage can move ±5 mm in every direction (left, right, forward and backward).

4.4.3. Electronics

To drive the stick-slip motor, a high-voltage sawtooth wave must be applied to the piezo stacks in the system. As we want to operate the piezo motor independent of the presence of a computer, we use a micro-controller (Raspberry Pi) built into the electronics board to generate a sawtooth function that will be amplified. As the frequency desired frequency of the sawtooth function is around 1 kHz, a USB to Speaker sound adapter connected to the micro-controller can be used to generate the function. To remotely control the movement of the motor, a wireless remote controller can be used (Nintendo Wiimote Controller). A Bluetooth USB receiver is used on the micro-controller to establish communication with the Wiimote. Two factors that play a role in the execution of a coarse step are amplitude and frequency. The amplitude will define the size of the coarse step and the frequency affects the speed of movement. The simplest solution found was to keep the sawtooth amplitude and frequency from the micro-controller constant at 1 V and 1 kHz and to only change the

number of coarse steps that are executed each time the micro-controller receives a command to move. Figure 46 shows the different outputs generated by the micro-controller when a command has been received.

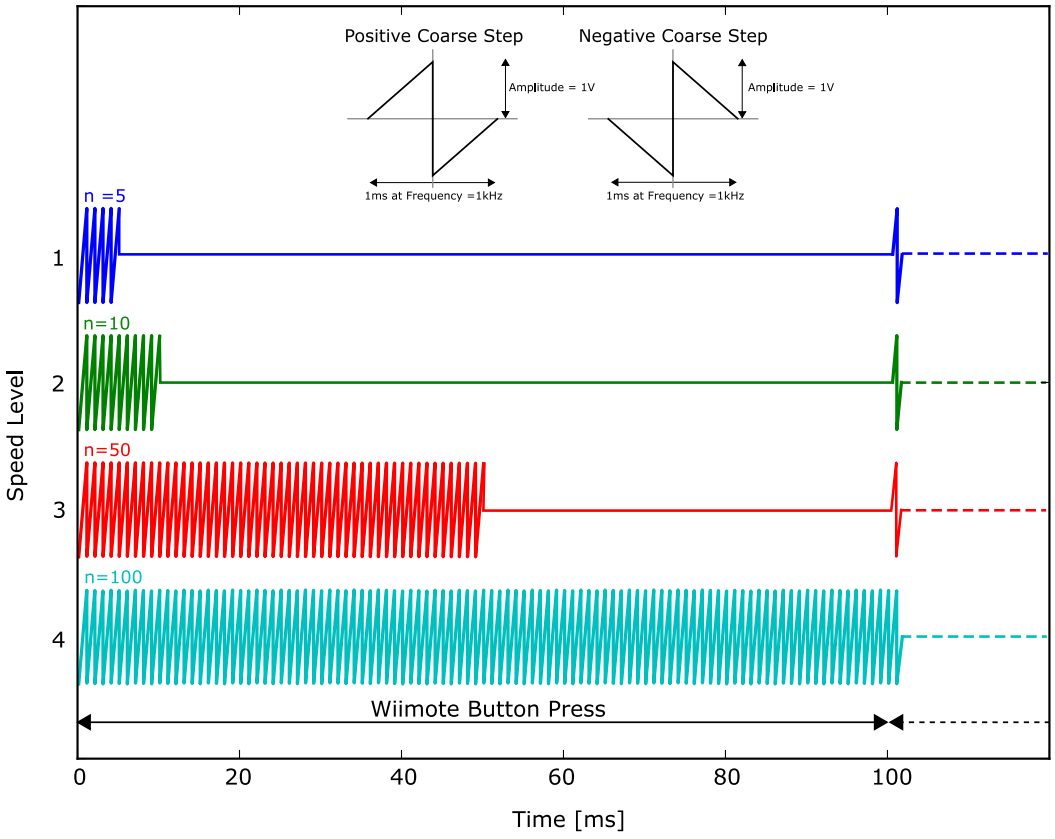

Figure 46: Illustration of the signal outputs from the micro-controller. Four different course speeds (1-4) are available where different amount of course steps n are executed each time the micro-controller receives a command to move. Both frequency and amplitude of the sawtooth function from the micro-controller are fixed. The direction of movement (positive and negative coarse steps) is being controlled by generating an inverted signal output.

The basic idea now is to generate a high-voltage sawtooth function by using a step-up transformer with a fixed gain of 25. To amplify the voltage of the audio signal, a high power op-amp (Texas Instrument, OPA227P) is used that operates on rails up to $\pm 12\,\mathrm{V}$ and runs

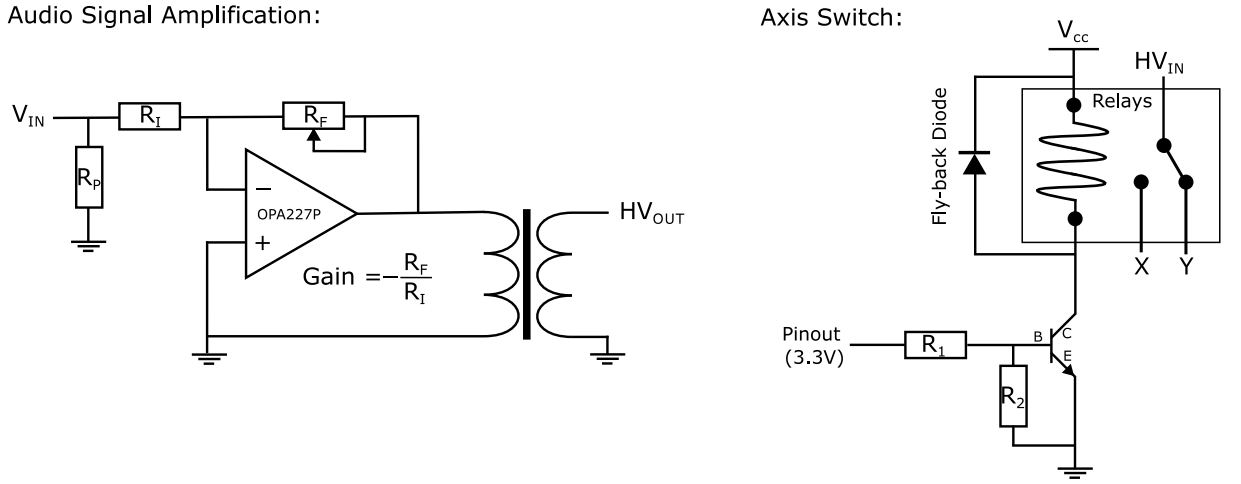

Figure 47: Schematic representation of the audio signal amplification and the axis switch. The amplitude of the sawtooth audio signal (V_{IN}) is being amplified by an inverting operational amplifier (op-amp) configuration. The amplified signal is fed into a high-power op-amp that then drives the step-up transformer with a fixed gain of 25. The used component values are $R_P = 10\,\mathrm{k\Omega}$, $R_I = 2\,\mathrm{k\Omega}$ and $R_F = 1\,\Omega$-$10\,\mathrm{k\Omega}$. A relay is used to switch the high-voltage signal between the x- and y-axis, allowing to use only one source and one high-voltage amplifier. A logic-high port of the microcontroller controls a transistor that drives the current through the relays, switching the axis. The used component values are $R_1 = 10\,\mathrm{k\Omega}$ and $R_2 = 10\,\mathrm{k\Omega}$.

as an inverting amplifier. In this inverting amplifier configuration, the gain is defined as

$$gain = -\frac{R_F}{R_I} \tag{25}$$

where R_F is a $10\,\mathrm{k\Omega}$ potentiometer and R_I is a fixed $2\,\mathrm{k\Omega}$ resistor. The potentiometer allows to adjust the amplitude of the amplified signal. An additional resistor R_P of $10\,\mathrm{k\Omega}$ is added to prevent noise being amplified in case the input is disconnected from the microcontroller. The amplified signal now goes into a high-power inverting amplifier (Texas Instruments, OPA541), which then drives the step-up transformer. The OPA541 has a fixed gain and is necessary to additionally amplify the current before it is transformed. As the power is conserved in a transformer, a voltage increase by a factor of 25 means the current drops by a factor of 25.

Allowing to use only one source and one high-voltage amplifier, a relay is used to switch the high-voltage signal from the x- to the y-axis. As the logic-high port of the micro-controller (3.3 V) does not provide enough voltage to directly gate the relay coil (RT314024F Power Relay), a transistor is used (2N3904) to draw the current. In this configuration, a flyback diode (1N4001) needs to be put in parallel with the relay coil to prevent damage to the components when the relay is turned off, as it allows the current in the coil to flow through the fly-back diode when turned off. The relay coil requires a current I_{Coil} of 33 mA and the transistor current gain (h_{FE}) is specified to be around 100. To draw the current from the coil from the collector to the emitter, the current through the base (I_{Base}) then is

$$I_{Base} = \frac{I_{Coil}}{h_{FE}} \approx 0.33mA. \tag{26}$$

The base-emitter voltage V_{BE} in our transistor is specified to be 0.7 V. If we fix R_2 to 10 kΩ, the current through R_2 then must be

$$I_{R_2} = \frac{0.7V}{10k\Omega} \approx 0.07mA. \tag{27}$$

As the currents of I_{Base} and I_{R_2} must sum up, R_1 then should be

$$R_1 = \frac{3.3V - 0.6V}{0.33mA + 0.07mA} \approx 6.5k\Omega. \tag{28}$$

With this configuration, a high-voltage sawtooth wave with a wanted repetition rate can be generated and can be successfully applied to the wanted axis. This setup allows to use one source and one HV amplifier for all signals. In our setup, both directions work at the same amplitude, however, in other setups the amplitude might need to be adjusted for each direction of operation.

4.4.4. Outgassing

Every component that is mounted to the suitcase needs to be UHV compatible and outgassing should be as small as possible, otherwise the implementation of the device would defeat the purpose of the suitcase. The pressure evolution and residual gases were monitored when the piezo stage is operated inside the UHV suitcase, shown in figure 48.

Since the piezo movement principle relies on friction, the motion can release bound surface

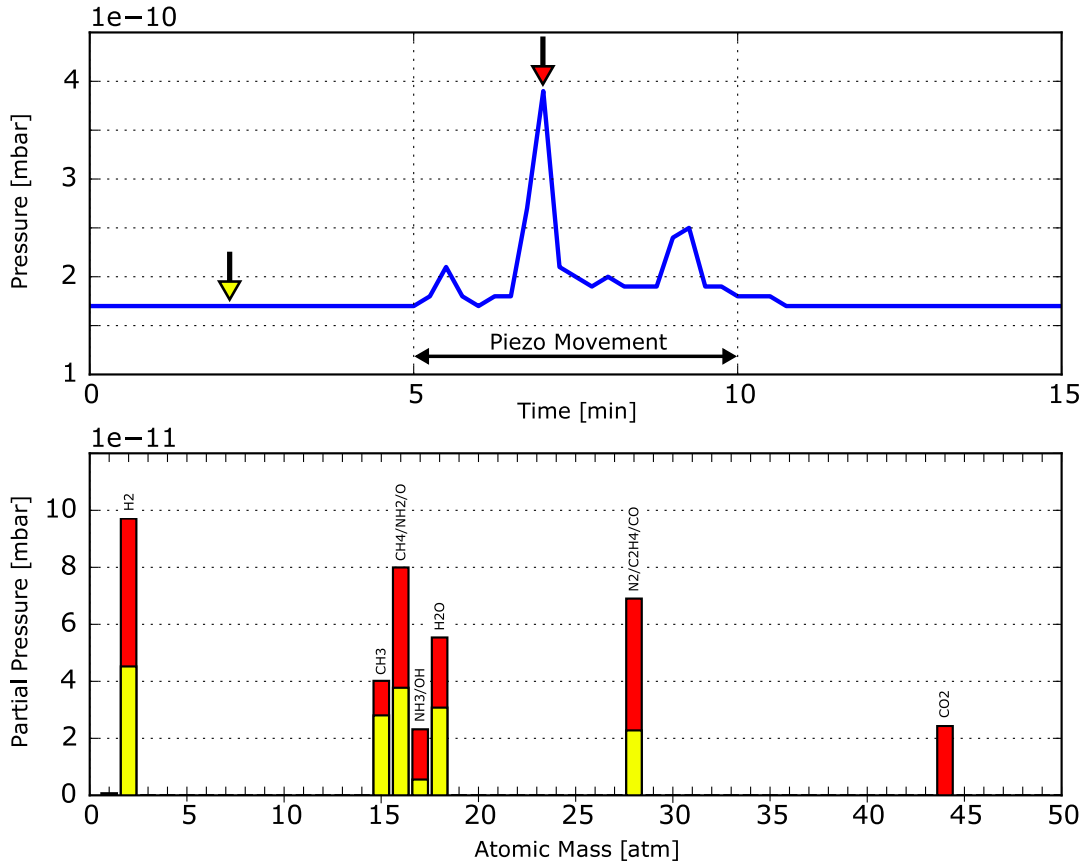

Figure 48: Outgassing of the two axis piezo stage. Top: When the stage is moved around inside the suitcase (t = 5–10 min), the pressure increased from 1.5×10^{-10} mbar to a peak pressure of 3.9×10^{-10} mbar. Bottom: Besides the already present gases in the UHV suitcase (yellow), CO_2 is the only additional monitored component that is being released from the surface upon piezo movement (red).

gases into the UHV. As shown in figure 48, the movement of the piezo increases the pressure in the suitcase, where the composition of gases released to the UHV are almost equal to the already present residual gases. Only additional CO_2 was detected, which can be efficiently pumped by the getter pump.

5. Results and Discussion

5.1. Probing Thin Film Organic Molecular Systems

In our study, we chose three different thin film molecular systems: Rubrene, pentacene and a pentacene derivative functionalized with tri-isopropylsilylethynyl side groups (TIPS-pentacene). The films had to be thick enough so that the films are not optically transparent and as much of the pump laser will be absorbed by the molecules. 1–2 µm thick films on diamond substrate were prepared by thermal evaporation of their powder form from Sigma-Aldrich and Alfa-Aesar (sublimed grade, >99.9 % purity grade). The molecules were outgassed at 100 °C at 1×10^{-9}–5×10^{-9} mbar. The molecules were evaporated at deposition rates of 0.5–1.0 Å/s. The films were prepared under the following conditions:

- Rubrene: T_{source}: 150 °C, P_{evap}: 8×10^{-8} mbar, ρ: 1.176 g/cm^3.
- Pentacene: T_{source}: 155 °C, P_{evap}: 5×10^{-8} mbar, ρ: 1.30 g/cm^3.
- TIPS-Pentacene: T_{source}: 160 °C, P_{evap}: 1×10^{-8} mbar, ρ: 1.104 g/cm^3.
- C_{60}: T_{source}: 440–500 °C, P_{evap}: 5×10^{-7} mbar, ρ: 1.65 g/cm^3.

The target diamond substrate was baked at 200 °C for >30 min and the substrate temperature was set to 100 °C for rubrene, and 85 °C for pentacene and TIPS-pentacene during evaporation as an increased substrate temperature yields larger crystal domains and exhibits improved photoconductive properties compared to substrate temperatures at room-temperature [61, 99]. At an early stage, the goal was to measure the optical properties and ultrafast carrier dynamics in these organic molecular films and the optical absorption spectra and transient photo-conductivity of the films should be correlated with the dc-conductivity measurements from the four-point probe. If the films can be photoexcited and charges are present in the film, a differential change in the THz transmission should be detected. From there, gas could

be leaked into the system and the influence of the increasing level of oxygen and water vapor could directly be measured.

A comprehensive study of the optical and transient photo-conductive properties of organic semiconducting thin films grown by UHV thermal deposition technique has found to be very difficult and not very successful due to various aspects. A major issue is the photo-degradation of the organic films. With a pump at an averaged energy of $E_{Avg} = 4\,\mu\text{J}$ and a beam spot diameter of $d = 1\,\text{mm}$, the fluence F of the laser is:

$$F = \frac{E_{Avg}}{A_{Laser}} = \frac{E_{Avg}}{1/4d^2\pi} \approx 500\,\mu\text{J/cm}^2 \tag{29}$$

Since the laser is pulsed with a repetition rate r_{Rep} of 1 kHz, the energy per pulse E_{Pulse} can be calculated:

$$E_{Pulse} = \frac{E_{Avg}}{r_{Rep}} \approx 4 \times 10^{-9}\,\text{J}. \tag{30}$$

At a wavelength λ of 400 nm, the energy per pulse E_{Pulse} is:

$$E_{Photon} = \frac{hc}{\lambda} \approx 5 \times 10^{-19}\,\text{J} \tag{31}$$

where c is the speed of light and h is the Planck constant. The number of photons per pulse n_{Pulse} can be estimated:

$$n_{Pulse} = \frac{E_{Pulse}}{E_{Photon}} \approx 8 \times 10^{9}\,\text{photons}. \tag{32}$$

The number of molecules on the surface is typically on the order of $10^{19}/\text{m}^2$. Assuming that typical organic dyes can undergo 10^5–10^6 absorption cycles until they are photo-bleached [100], one can estimate the number of laser pulses (n_{Pulses}) with beam spot of $d = 1\,\text{mm}$

needed until each molecule is photo-bleached.

$$\frac{A_{Laser} 10^{19}/\mathrm{m}^2}{n_{Pulses}} \approx 1000\,\mathrm{pulses} \tag{33}$$

In this scenario, only 1000 pulses are needed to fully photo-bleach a monolayer of molecules. At a repetition rate of 1 kHz, a monolayer bleaches within 1 s. Although this is a very rough estimation, and the assumption that treating the films as a collection of isolated molecules does not really apply for conjugated polymer films, it shows that the degradation time of the films might still be much faster than we set up the scans for, which was on the order of hours. Even under UHV conditions, there is always photo-induced degradation happening as these films are extremely prone to damage and the optical pulse energies are always high in any THz experiment. Ostroverkhova et al. [61] reported similar issues for measurements of the optical and transient photoconductive properties of 150–1000 nm thick TIPS-pentace films. They have grown TIPS-pentacene films from a solution (tetrahydrofuran, THF) and by thermal evaporation and have found that the solution processed films were more crystalline compared to the other ones. The thermal evaporated films were rather amorphous and these films degraded under pulsed illumination rather quickly. The transient photoconductive signals on the evaporated sample reduced by 20 % within 15–30 min with a pump at 580 nm and pump fluences of 0.9–1.5 $\mathrm{mJ/cm^2}$. To avoid the issue of degradation, they suggested in the paper to limit the pulsed illumination of the same spot on the TIPS-pentacene film to 2–10 min and then translate to a new region on the sample. The solution processed films however did not show photodegradation under pulsed illumination for hours from which they concluded that the morphology of the films is important for film stability. In our case where the samples are tested inside the UHV suitcase, translating to a new region is possible due to the piezostage that was implemented to the suitcase, however, due to the small sample size of 3 mm × 3 mm, we were only able to test the sample at two to three different spots. Since

calibration of the laser needs already to be done on the sample before a measurement can be done, there are only one to two measurements per sample possible before the sample is degraded. In figure 49, optical images of the samples were taken and overlapped to produce an overview over the full sample after a THz measurement. The two locations where the sample was probed at can be visibly seen. It is a reasonable assumption that the films are degraded. We tried to perform absorption spectroscopy on the sample in order to compare the spectrum before and after the measurement, however, both the spectrometer and light source were not ideal to perform absorptions spectra. The first spectrometer we used cuts everything below 450 nm and thus did not reveal how much the material absorbs in the blue before and after the measurement. Another spectrometer we used revealed that the light source is not bright enough and is not really white. The light source used has almost nothing in the blue and thus, again, the source could not be used to reveal how much the material absorbs in the blue.

Another issue is that the films were not thick enough and thus too transparent to completely absorb the pump. The sample response thus is low. Further, since the pump can penetrate through the sample, it can interact with the sample substrate, in our case the diamond. The diamond can be excited by the 400 nm pump as well, where a two photon absorption process can be induced. Normally, one would switch to another wavelength to pump, however, a second-harmonic generation at 400 nm (first harmonic at 800 nm) is much easier than to achieve stable wavelengths with the optical parametric amplifier (OPA). This absorption process in the diamond overwhelms the response of the film and thus makes it difficult to separate the sample response from the substrate response. Due to dimensional restrictions, the suitcase does not allow to simultaneously mount a clean substrate and a film sample at the same time that would allow to measure only the diamond and then switch to the films. To solve this issue, it was tried to make the films thicker (up to 2 µm) so that the 400 nm

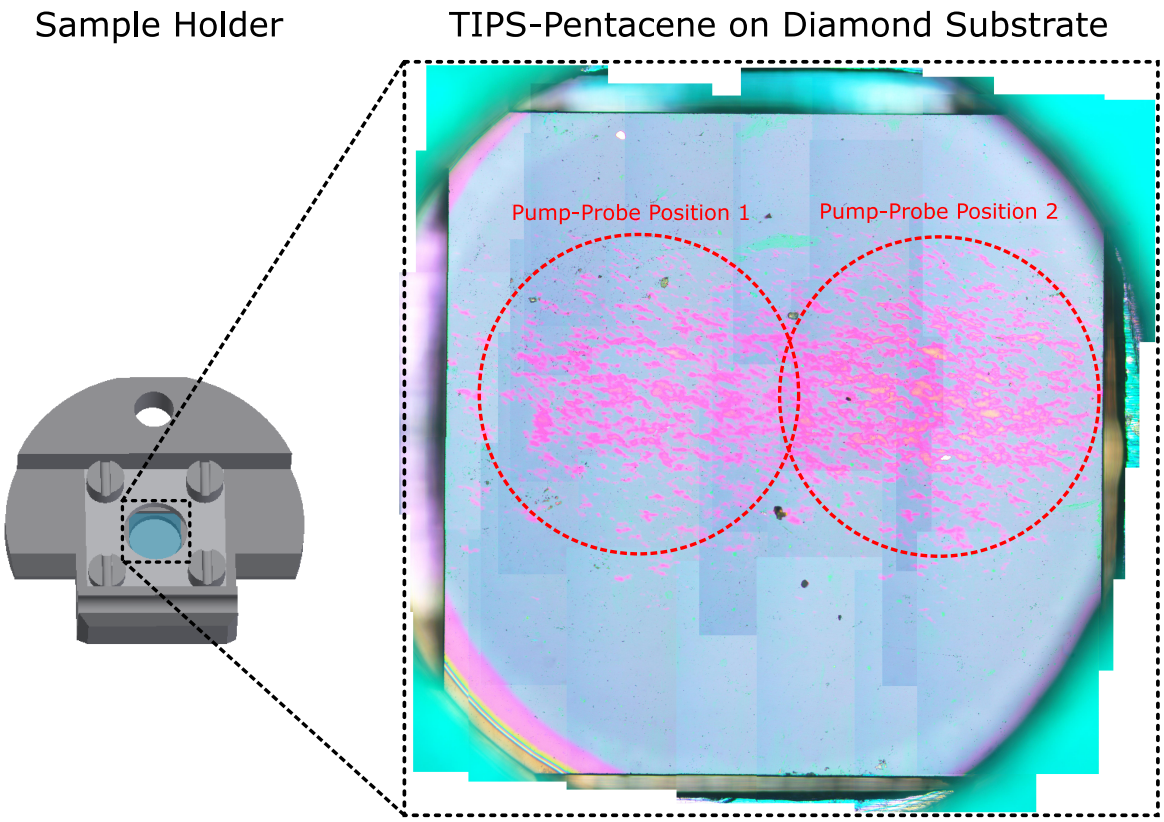

Figure 49: Bleached TIPS-Pentacene film after optical pump THz probe measurement. The two locations where the sample was probed at can be visibly seen after the measurements. The optical image consists of overlapped optical microscopy images in order to give a full overview over the sample.

pump gets completely absorbed by the organic film and thus would not excite the diamond. The issue however remained because the films were still too transparent. One could visibly see that a large fraction of the pump was transmitted through the suitcase and thus the issue of exciting the diamond substrate remained. What could be tested in future is to use Silicon Nitride Membranes that have shown good performances as a substrate material for THz measurements in order to prevent the substrate to be excited as well [101]. Norcada, for example, has membranes down to 10 nm thickness, sizes up to 500 µm × 500 µm and could be a promising candidate as a substrate material (see website reference [102]).

5.2. Probing Single-Layer Deposition Graphene

Graphene is a two-dimensional lattice of covalently bonded carbon atoms arranged in a honeycomb crystal structure. Graphene is a zero band gap semiconductor where its valence and conduction bands are touching each other at the corners of the Brillouin zone in the so called Dirac points [103, 104]. Many potential applications of graphene require precise and controllable doping with charge carriers. Being a two-dimensional material, graphene is extremely sensitive to surface adsorbates, where the electronic properties can be effectively modified by the deposition of different atoms and molecules. Due to the presence of charge carriers resulting from the presence surface adsorbates a surface transfer doping of the graphene can be implied. Depending on the type of adsorbate, electrons will flow either from graphene to the adsorbate making graphene p-type doped or the opposite n-type doped. This leads to an opening of the band gap (non-zero) where the Fermi level of graphene then depends on the type of adsorbate. This strong sensitivity on the environment thus can be used in application such as nanostructured gas sensing systems [105]. In our case, this extreme sensitivity is ideal in order to show the capability of our setup. Since we can bake samples up to 800 °C, transport the sample under UHV conditions, can controllably leak gases into the suitcase

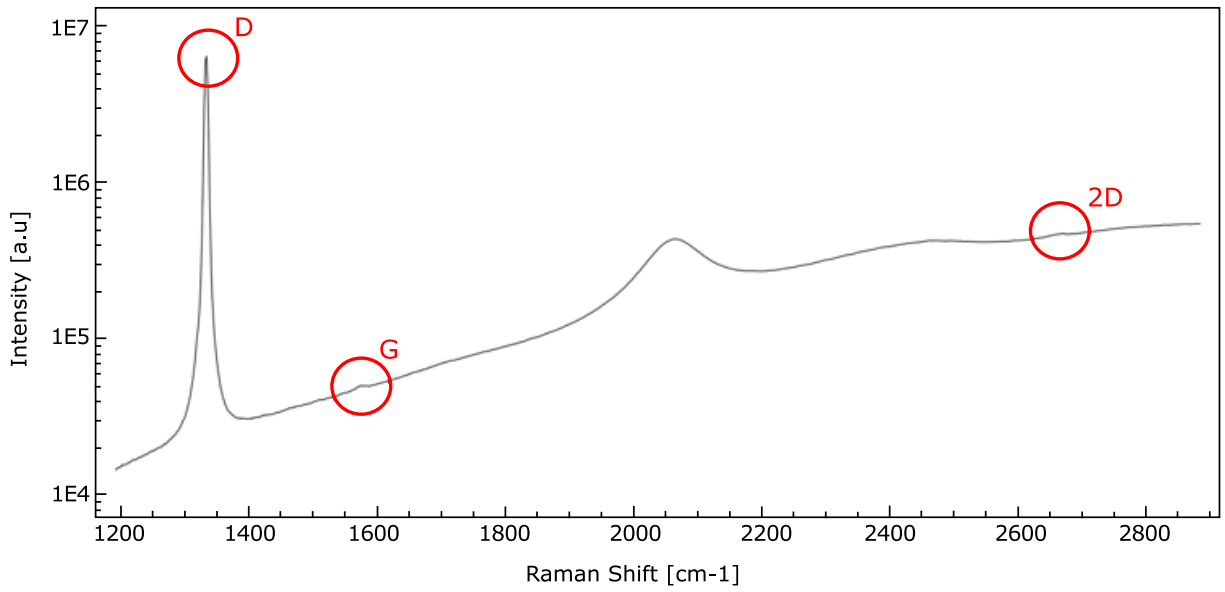

Figure 50: Raman-Spectrum of Graphene on a diamond substrate. Only small G ($1580\,\mathrm{cm}^{-1}$) and 2D ($2700\,\mathrm{cm}^{-1}$) peaks are visible. The large D peak ($1350\,\mathrm{cm}^{-1}$) indicates a large number of defects.

and can use the THz system to measure the conductivity on the intermolecular length scale, it would be possible to detect the major difference in the optically detected charge formation and transport if we controllably introduce impurities.

The CVD samples used first in this study were grown on copper foil and transferred to a diamond substrate by using PMMA (poly(methyl methacrylate)) as supporting layer [106]. Once the CVD graphene was transferred to the diamond substrate, it was further cleaned in an ultrasonic bath using acetone at 50 °C for 30 min, followed by rinsing in isopropyl alcohol and dried with N_2 gun to remove the PMMA and solvent residues. Important to note is that it is not recommended to use water in the cleaning process as it tends to destroy the graphene. Once transferred to the UHV chamber, the sample was baked at 200 °C for 15 min.

Normally, Raman microscopy can be used to reveal the quality of graphene and exhibits information about defect rate and if the graphene is of monolayer quality. Carbon allotropes show their fingerprints under Raman spectroscopy mostly by D, G, and 2D peaks around

1350 cm^{-1}, 1580 cm^{-1} and 2700 cm^{-1} respectively due to the change in electron bands. Identification of these features allows characterization of graphene layers in terms of number of layers present, and their effect of strain, doping concentration, and effect of temperature and presence of defects. The G band arises due to the in plane vibration of the sp^2 carbon atoms, whereas the 2D band is at almost double the frequency of the D band and originates from second order Raman scattering process. The D band appears due to the presence of disorder in atomic arrangement or edge effect of graphene, ripples and charge puddles. In figure 50, the Raman spectrum of the graphene peaks with a 100 s collection time is shown. Raman spectrum of our sample reveals a large D peak indicating defects, and only small G and 2D peaks. The large peak at $\sim$2100 cm^{-1} could be explained by the presence of sp^1 hybridized carbon [107, 108]. In figure 51, G band mapping of transferred graphene on a diamond substrate with the graphene peaks shown in figure 50. It turns out that Raman mapping of graphene on diamond is ineffective due to a low signal to noise ratio. In order to perform mapping, a $<$1 s collection time per data point is required. Figure 51 shows the spatial variation of the G-peak of sp^2 bonded carbon and thus defect free regions of graphene. The map suffers from noise, the features, however, are believed to be real. Looking at the Raman map, the two best flakes to probe in the THz setup are the ones centered near the top at (x,y) = (1250, 2100) and (x,y) = (750, 1250).

The sample was loaded to the UHV system and the sample was baked at high temperatures (460 °C at $<1 \times 10^{-8}$ mbar) in order to remove possible residues of PMMA. The sample was transferred to the suitcase and the THz setup in the Cooke laboratory was used to probe the sample.

So far, we have only tested films in the UHV suitcase that completely have covered the support substrate, it was the first time we measured flakes. Since only the substrate is transmissible for the THz signal inside the UHV suitcase, we always know that the coarse

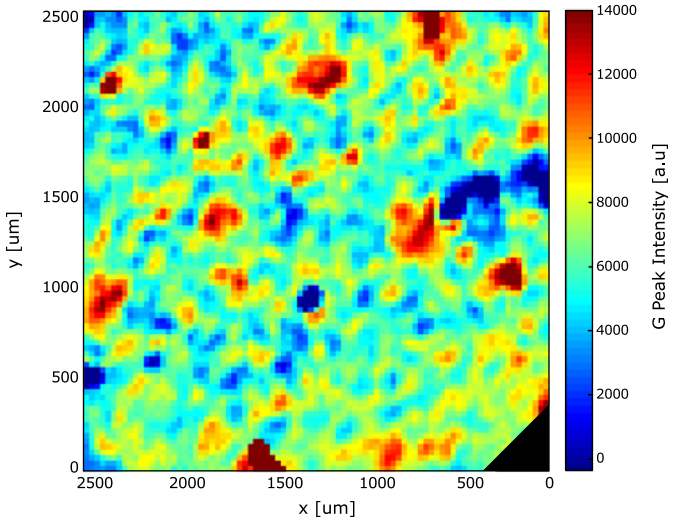

Figure 51: Raman G peak mapping of graphene on diamond.

alignment is given when a THz signal can be transmitted. In case of flakes on the substrate, the issue of positioning the flakes to the focal point was encountered. First, the two axis piezo stage only allows to position the sample in the horizontal plane (x and y), but there is no straight forward mechanism to position it vertically (z direction). Since the sample has to be mounted vibration-free, we chose a non-adjustable full-metal support structure (see appendix A.1) to place the suitcase and thus the sample in position. We used thin metal shims (0.5 mm thickness) to place between the suitcase and the support structure for adjusting the height. Since the clearance between the 90° off-axis parabolic mirrors and the suitcase is only a few millimeters, there was no easy way to get optical access inside the chamber that would allow to visibly adjust the sample position. Further, the two axis piezo stage has no position readout, which makes it difficult to verify if the flake is properly aligned without visible access.

As Raman microscopy has already revealed earlier that placing graphene on a diamond is ineffective to reveal if the graphene features are real or not, the same issues were encountered in the THz setup. Due to time constraints, it was not possible to identify if the features

measured were a convolution from the substrate and the graphene or if we were even properly aligned, thus we aborted the measurements and decided to measure epitaxial graphene samples grown on the carbon face of semi-insulating 6H−SiC wafers instead. One could possibly repeat the measurements on single-layer deposited graphene, but at this stage it is recommended to probe graphene with substantial area to avoid the issue of possibly not hitting a good region of graphene. Since CVD samples grown on copper foil and transferred by using PMMA are normally limited to sizes up to 300–500 µm in diameter [106], one could also try to measure a scotch-tape cleaved sample with more substantial area.

5.3. Probing Epitaxial Grown Graphene

The epitaxial graphene samples used in this work were grown on the carbon face of semi-insulating 6H−SiC wafers provided to us by the Ozaki group at INRS. The sample has a nearly 100 % graphene coverage and thus is ideal to be tested. The epitaxial graphene samples were placed at the focus of the 90° off-axis parabolic mirrors and excited with an optical pump (800 nm wavelength) at a pump fluence of 100–500 µJ/cm^2 with a spot size of ∼400 µm. Since the 6 H−SiC has a band gap of 3 eV, a filter was placed in in front of the 800 nm optical pump to avoid excitation of the substrate with the second harmonic of the laser (400 nm). The time-dependent transmission of the THz probe pulse through the optically excited sample was measured by delaying the optical pump pulse with respect to the THz probe. In figure 52, the original THz time domain waveforms transmitted through the suitcase are shown. In each scan, one can see that there are three consecutive peaks visible. The first peaks at $\tau_0 = 1.5$ ps is the reference signal that directly transmits through the suitcase. The second peaks at around $\tau_1 = 7$ ps is due to the reflection from the SiC substrate. The time delay between the two peaks correlates to a path delay of twice the thickness of the SiC substrate, which is 1 mm. The third peaks at $\tau_2 = 9$ ps is due to

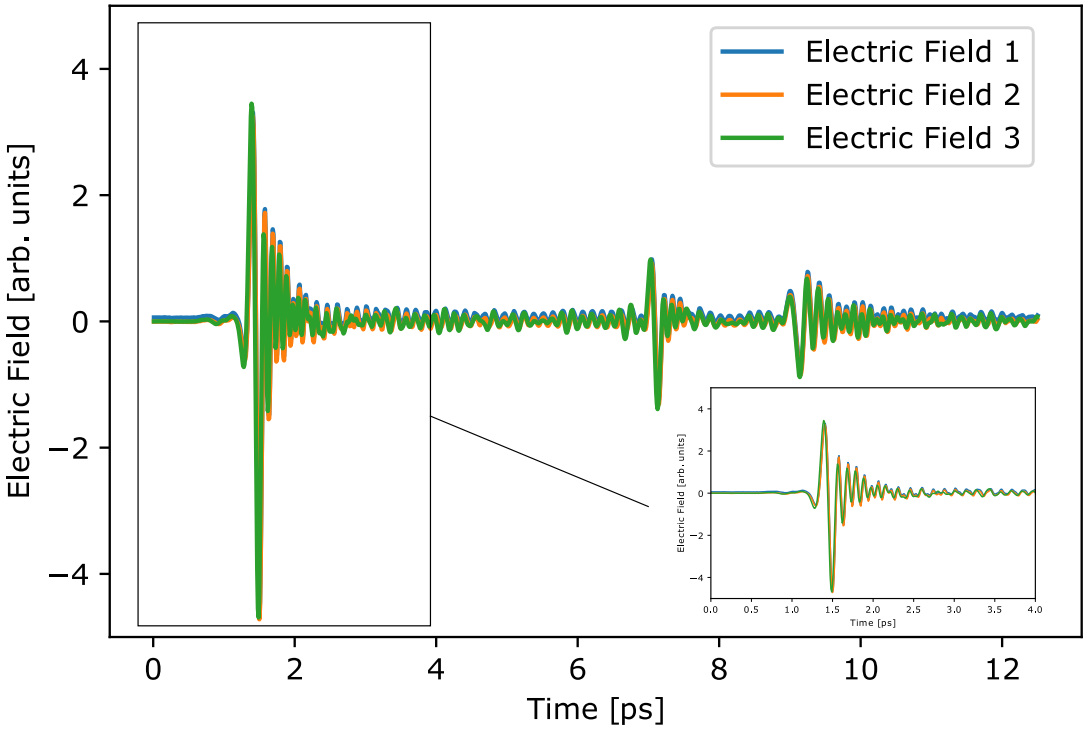

Figure 52: Original time-domain THz waveforms. The THz electric fields are transmitted through an unexcited epitacial graphene on 6 H−SiC substrate inside the ultra-high vacuum suitcase. The original waveform is visible at 1.5 ps and the inset shows the spectrum of the original transmitted THz pulse. Reflections from the substrate at $\tau_1 = 7$ ps and possibly from the diamond window at $\tau_2 = 9$ ps are also visible.

reflection from the diamond windows, where the time delay between τ_1 and τ_2 corresponds to 600 µm, which is twice the thickness of the diamond windows.

In order to test the sensitivity of the sample to oxygen, two different measurements were done: one under UHV conditions and one where oxygen was controllably leaked into the suitcase. In figure 53, the histograms of the present gases under UHV and with leaking oxygen are shown. Note that the histograms do not show partial pressures but counts. The reason is that in order to leak oxygen in the suitcase, the ion pump needs to be turned off, and the getter pump needs to be saturated. Since pressure readout in our suitcase is related to the current applied to the ion pump, we do not know the total pressure when the ion pump is turned off.

1D THz scans were performed by delaying the time of the probe to the pump and the charge carrier decay times were measured. In figure 54, the scans of the sample at a fluence of 248 µJ/cm^2 under UHV conditions and with leaking oxygen are shown. From the exponential fits, the decay times can be extracted under UHV conditions and when oxygen is leaked to the system. The decay times for both conditions are in the order of 0.4 ps and no significant change in the dynamics can be seen when oxygen is leaked to the system. Intraband relaxation times in the 0.4–1.7 ps range were measured by other researchers previously using optical-pump and optical-probe spectroscopy of epitaxial graphene and thus our measurements are in agreement [109, 110]. The reason why we can not see a difference between the two conditions might be the history and preparation of the sample. We knew that the samples was aged (it is at least three years old and was kept in air) and that the sample preparation is important and non-trivial in order to guarantee that we will see a change. Although the sample was annealed by us under UHV conditions and by baking it at 480 °C for 30 min, the temperature was maybe not sufficient enough to clean the sample properly. Another issue might be the waiting time between preparation and measurements, as it is not uncommon that it takes

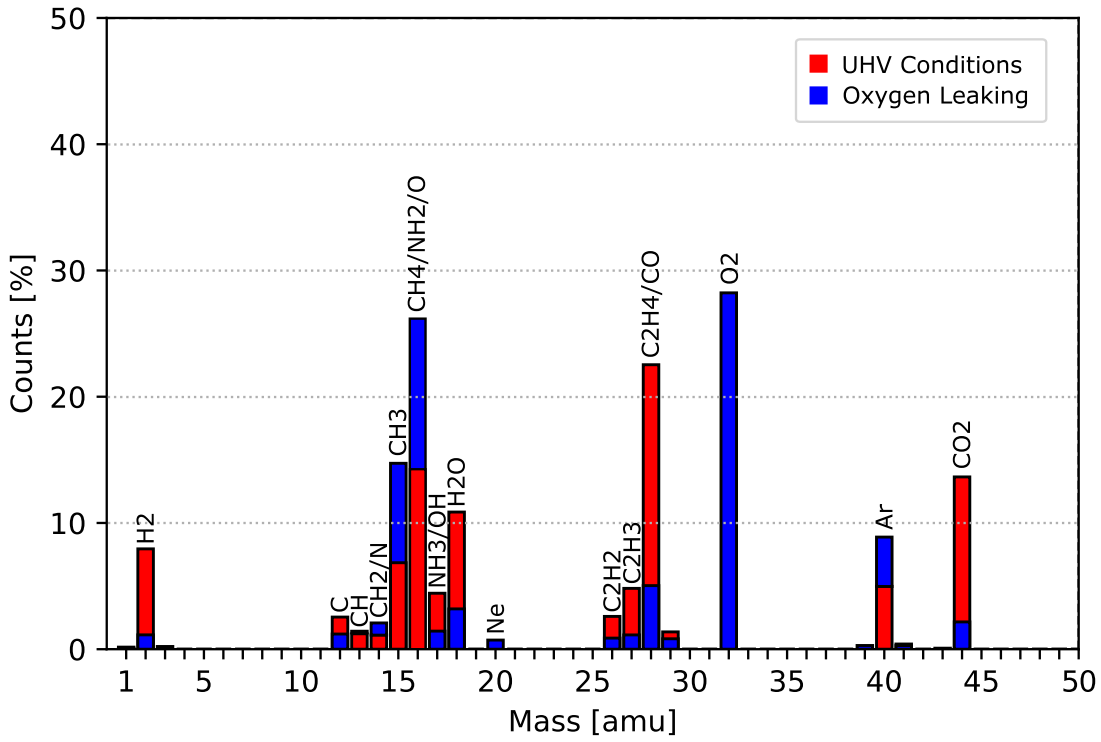

Figure 53: Residual gas histogram of the UHV suitcase under UHV conditions (left) and when oxygen is leaked into the setup (right).

days to adjust the setup until a measurement can be done. During this time, the sample might already have absorbed residual gases present in the UHV suitcase.

Further, to guarantee that the sample response is linear with the fluence and not saturated,

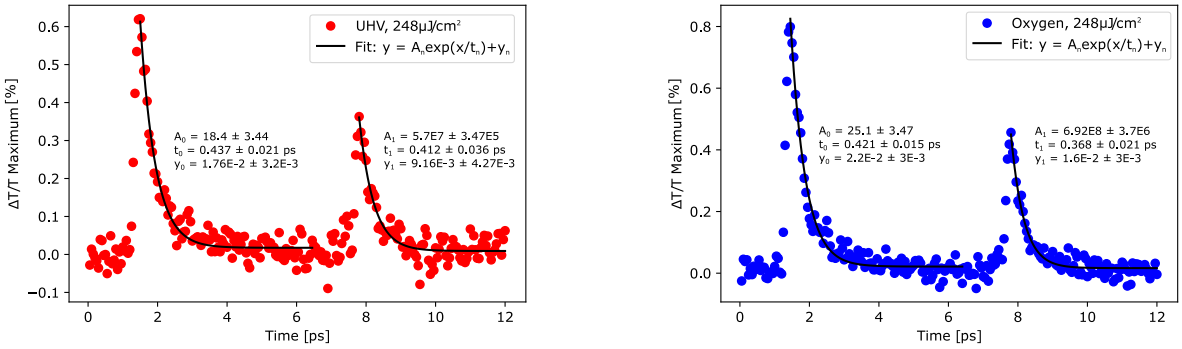

Figure 54: 1D THz Scan with a pump fluence of 248 µJ/cm^2 under UHV conditions (left) and with leaking oxygen (right). Decay times can be extracted, however, no significant change can be seen when oxygen is leaked to the system.

the peak heights of the sample response were tested at different fluences. In figure 55, the peak heights of the the first peak (τ_0) and the second peak (τ_1) are shown. The peak heights linearly increase with fluence and the ratio between the two peaks (τ_1/τ_0) stays constant. The conclusion of this experiment is that it is worth repeating it with a newly prepared sample annealed at higher temperatures.

After the THz measurements, the sample was transferred to the Jeol AFM setup to extract structural information about the sample. In order to be able to transfer samples under UHV from the evaporation chamber to the Jeol AFM setup, a second suitcase was built that allows to transfer samples to the load-lock of the Jeol system. Figure 56 shows the suitcase. Since the two systems are located in the same room and transport can be kept short, only a simple suitcase with a transfer arm, a viewport, a gate valve and without a pump was built. This suitcase can maintain a pressure below 10^{-6} mbar for >10 min, which is sufficient.

Recent updates on the AFM setup allow to spatially map the topography on a nanometer

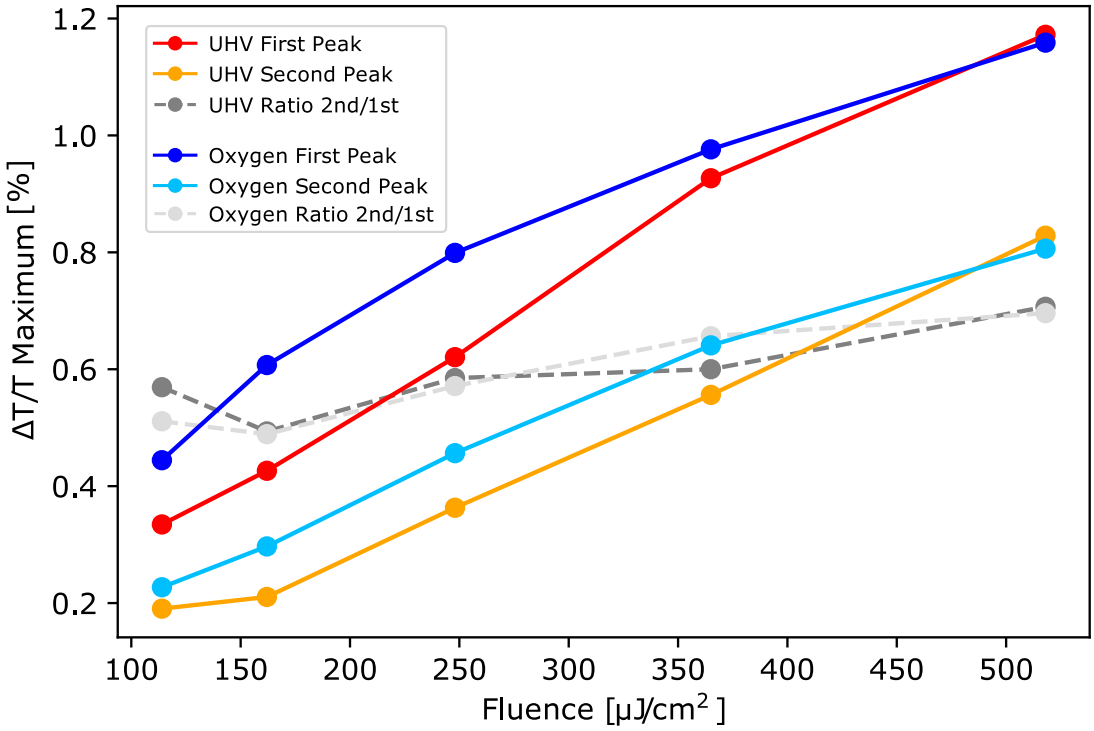

Figure 55: The first and second THz peaks are compared as a function of fluence, both under UHV conditions and when oxygen is leaked into the system.

Figure 56: Left: Jeol AFM Setup, right: Connected portable HV chamber (red) that allows to transfer samples from the UHV system to the load-lock of the JEOL system.

scale, as well as performing temporal resolved optical pump - optical probe measurements. The experimental implementation of this detection scheme by combining a UHV AFM system with a femtosecond pump-probe laser system is unique and recent measurements showed that the photocarrier lifetime in materials can be extracted (see publication [24] and [25], spatially and temporally resolved decay times on low-temperature grown GaAs). Since the 6 H−SiC substrate is covered nearly by 100 % with graphene, it was tried to find an interesting spot on the sample where a contrast can be measured. A spot where the substrate can be seen and the graphene was not found, however, we were able to conclude that although this is a monolayer graphene sample, there exist regions of bilayer or tri-layer graphenes on the sample. From literature [111] we know that hexagonal graphene patterns often appear around a grain. In figure 57, an AFM image of the sample is shown, where the grains are visible. The nucleation of bilayer and tri-layer graphene was reported to be facilitated by the presence of these grains, where the graphene layers grow from these grains outwards [112]. Figure 57 on the right highlights such patterns that can be seen. An issue encountered was that the step sizes however do not match with graphene. Single graphene sheets should reveal step sizes of 0.3 nm, whereas the features have step sizes above 5 nm. Although they do not match, it was believed that these features are real and are coming from the bi- and tri-layered graphene. In figure 58, a region was chosen to measure the difference in the surface photovoltage between the two regions under pulsed illumination. However, as soon as the laser was turned on, the sample charged up quickly, and approaching the surface to a manner where local variances could still be revealed. Normally, the distance between the sample and the tip of the AFM is in the order of a couple nanometers, in our case, due to the charge accumulation and the strong surface fields of the SiC, the tip-sample distance was more around 100 nm than in the order of 1 nm. With large sample-tip distances, local variances can not be seen anymore because the signals are now an average over the underlying structures. From there, different

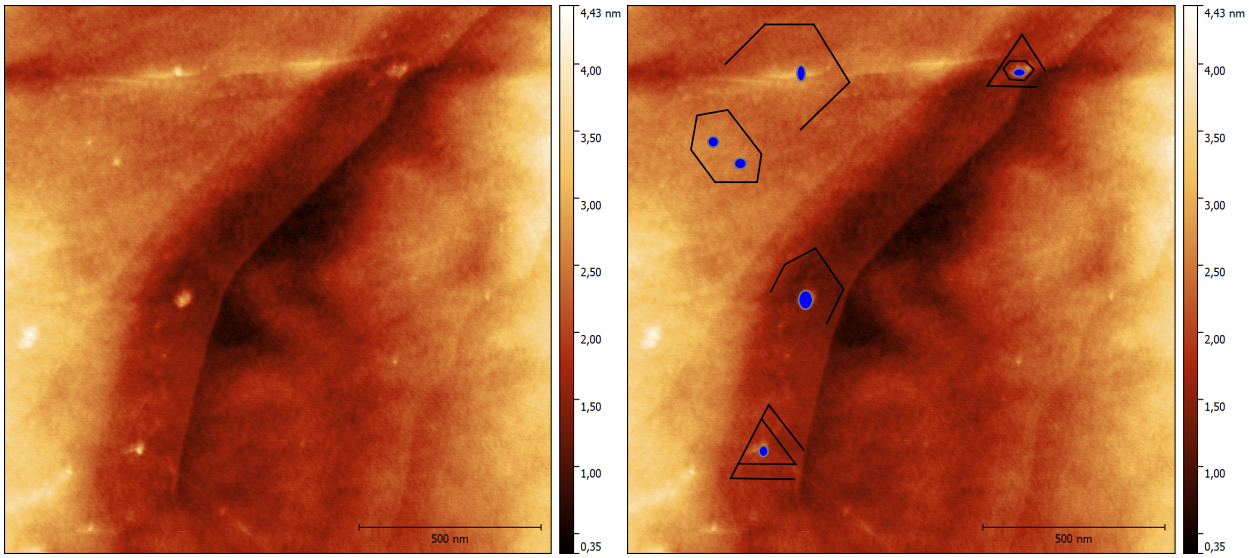

Figure 57: AFM image of epitaxially graphene grown on SiC substrate. The sample is covered nearly by 100 % by graphene. In order to see a contrast, interesting spots on the sample are grains, where bi- and tri-layers of graphene can be found.

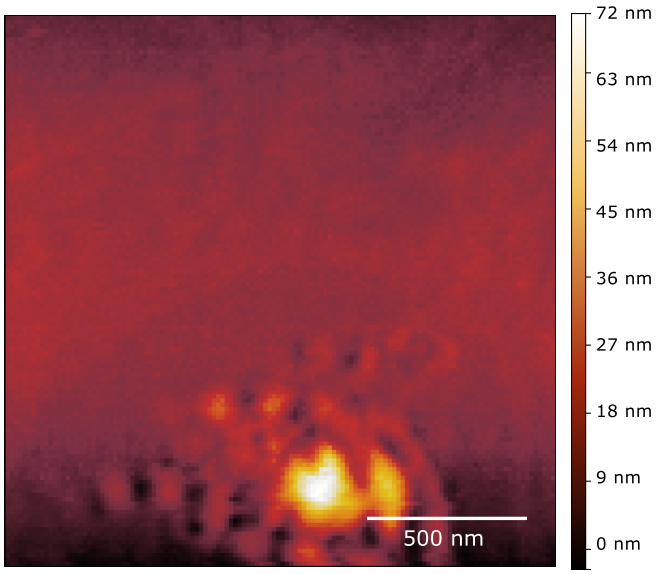

Figure 58: AFM image of a region around a grain.

approaches were made to bettering the signal. It was tried to actively drive the tip closer to the surface, however, the smaller the tip-sample distance became, the worse the frequency sweep became to the point where the q-factor went down to a point where it is no longer useful. What was not tested was to bake the sample again. Baking samples at high temperatures can dislodge trapped charge carriers and reduce accumulated surface charges. However, we did not try because in the time given, it was expected that the sample will charge up quickly again as soon as the laser is turned on again.

6. Conclusion and Outlook

The main purpose was to build a setup and to perform proof of concept measurements that show the capability of the setup. The main effort that was put into this work was to develop and build an ultra-high vacuum system that allows to grow molecular films using thermal molecule evaporators. Well-defined molecular films can be achieved by controlling and varying the substrate temperature during deposition and varying annealing protocols. Chemical defects can be introduced to the layers by controllably leak different gases to the samples. Unfortunately, a deeper investigation of different film morphologies and how they affect the charge formation could not be made, especially due to the slow progress on the four-point probe setup, which intentionally was designed to directly test and map the dc conductivity of the films during and after film growth. There were only a handful of successful measurements on very well known low resistive ohmic samples (gold and ruthenium). An experimental transition to molecular films (Rubrene, Pentacene, TIPS-Pentacene, C_{60}) , semiconducting wafers (n- and p-type doped Si), as well as a potentially interesting inorganic electride material ($Ca_{24}Al_{28}O_{64}$) could not be made. The idea of mapping the in-plane conductivity by using the revolute-revolute-prismatic actuation of the Kleindiek manipulator was completely abandoned because of its non-trivial actuation structure and because it would be too time-intensive to build a necessary closed-loop control feedback that is needed for the desired control accuracy. The idea of using cantilever-based micro four-point probes had to be put aside for the moment because major technical implementations had to be tested and improved, where macroscopic probes came in more handy. Not many probes are commercially available that can be used without further modifications, thus it might be necessary to microfabricate custom-made chips in future. An interesting side project would be to fabricate and test different probe designs with different spacings, spring constants, coatings and with and without sharp tips. In my opinion, I would try to make the probes at least

100 µm long which allows much better visual tracking during an approach; the used 30 µm long micro probes were barely visible with the long distance microscope only when good light conditions were given. Further, I would try to minimize the electrode spacing as much as possible (250 µm are definitely too wide for high resistive samples such as organic molecules); a deeper look into literature might reveal what spacings are feasible with common microfabrication methods where leakage currents are still not an issue. Further, the dimensions of the cantilevers should be chosen that the spring constants are in the range of 5–50 N/m; the same as the commercially available probes. For coating, my first attempt would be to use Ni due to its high mechanical stability, relative high work function with low oxidation rate and small contact resistance [49]. I would preferably test probes with sharp tips. Although the risk is higher to scratch fragile films with sharp tips, the setup would benefit from higher contact pressures and thus more reliable contact (especially when surfaces are oxidized). Preventing fragile films from being scratched can be achieved by bettering the alignment of the probes relatively to the sample. It is hoped that with putting more effort into improving the four-point probe system, samples can be tested and kept under UHV conditions. With the home-built surface detection mode and multiplexer board for the four-point probe system, major improvements could be made. Technically, samples with resistances up to 0.1–1 GΩ could be detected. In combination with the multiplexer board, each probe can now be finally tested if an electrical contact to the sample can be made which is fundamental for performing a successful measurement. At this stage however, without a working four-point probe system, the chamber can only be used to produce samples; there is no other measurement tool directly mounted to the system that allows to test the quality of the samples. This is troublesome, because we can not directly test the samples under different growth conditions. Transferring samples to the JEOL system, the THz setup or other potential setups that allow sample characterization is time-intensive, tedious and needs to be planned weeks ahead.

Thus, in order to increase the scientific output, it is inevitable to directly test the quality of the samples in the built evaporation chamber.

The built vacuum suitcase allows to keep the sample under UHV conditions even with the integrated ion pump turned off for more than 10 days. In combination with the residual gas analyzer and leak valve, both the quality of the vacuum can be monitored and controllably manipulated. To design the vacuum suitcase was a non-trivial and challenging part, since we had to make sure that the vacuum suitcase fulfills the size limitations and material requirements given by different experimental setups. The high-quality diamond windows, as a key component of the suitcase, transmit in the entire spectral range from the visible at 225 nm over the infrared-, the terahertz range and even up to radar frequencies. Thus the suitcase is not only limited to perform optical pump THz pulse measurements but any pump-probe measurement in this entire range can be done. Further, the designed and built two axis piezo stage fits perfectly inside the suitcase where only little space was originally available. With a total actuation of 10 mm in both x- and y- position, even larger samples can be positioned and scanned inside the suitcase. The only issue encountered with the two-axis piezo stage, was the absence of a position readout, which would be beneficial in case more measurements on small flakes should be performed in the future. The step sizes of slip-stick motion is often unpredictable and thus sample alignment is tough if there is no evident change in transmission observable when moved from the substrate to the flake.

In terms of organic molecules, the excitonic and molecular nature of the material lead to a lot of challenges in both experimentally revealing intrinsic properties of the material as well as finding ideal growth- and measurement conditions. The growth is difficult to optimize and growing samples with thicknesses above 1 µm is not ideal in a UHV environment, because the thick deposited films on the wall of the chamber are harder to bake and remove from the system. It might be a better approach to measure solution processed films in a non-UHV

environment first, and then see if differences are measurable if the films are brought and annealed under UHV conditions.

In terms of the graphene samples, we unfortunately could not show a difference in the electric field of the THz pulse transmitted through the samples as a function of delay time with respect to the optical pump pulse under UHV conditions and by leaking oxygen. However, we were able to show that these types of measurements can be performed with the suitcase. The conclusion from the measurement is that more effort needs to be put into finding the right sample conditions. The measurements on epitaxial grown graphene on 6 H−SiC however still look promising and should be repeated with a newly prepared sample or the one that is already available should be baked at higher temperatures.

In general, there are a lot of interesting materials that suffer from degradation in air and we can load and anneal a broad range of samples. There are especially many 2D materials being synthesized and available today, some which are more well-known than others. Besides graphene, there are also hexagonal boron nitride, and e.g. 2D bismuthene available. Bismuthene as a potential candidate is arrange in a hexagonal array of atoms and has been grown on many different substrate, such as SiC [113]. The electronic properties of 2D bismuthene is influenced by the substrate where different electronic properties can be achieved. For example, the material is a topological insulator at room-temperature and a novel material because most topological insulators normally operate at low temperatures. When bismuthene is stacked on a substrate, the electronic properties can range between metallic to semi-metallic and narrow band gap semiconducting states [114]. Since 2D materials are all surface and sensitive to the environment, a rich playground for new phenomena can be provided by the ability to controllably change the surface properties of such systems.

7. References

1. Jarvis, A. J., Leedal, D. T. & Hewitt, C. N. Climate-society Feedbacks and the Avoidance of Dangerous Climate Change. *Nature Climate Change* **2,** 668–671 (2012).

2. Keeling, C. D. The Concentration and Isotopic Abundances of Carbon Dioxide in the Atmosphere. *Tellus* **12,** 200–203 (1960).

3. Nemani, R. R. Climate-Driven Increases in Global Terrestrial Net Primary Production from 1982 to 1999. *Science* **300,** 1560–1563 (2003).

4. Lewis, N. S. *et al. Basic Research Needs for Solar Energy Utilization. Report of the Basic Energy Sciences Workshop on Solar Energy Utilization, April 18-21, 2005* tech. rep. (2005), 276.

5. Peumans, P., Bulovic, V. & Forrest, S. R. Efficient Photon Harvesting at High Optical Intensities in Ultrathin Organic Double-Heterostructure Photovoltaic Diodes. *Applied Physics Letters* **76,** 2650–2652 (2000).

6. Tang, C. W. & Vanslyke, S. A. Organic Electroluminescent Diodes. *Applied Physics Letters* **51,** 913–915 (1987).

7. Salleo, A., Chabinyc, M. L., Yang, M. S. & Street, R. A. Polymer Thin-Film Transistors with Chemically Modified Dielectric Interfaces. *Applied Physics Letters* **81,** 4383–4385 (2002).

8. He, Z. *et al.* Enhanced Power-Conversion Efficiency in Polymer Solar Cells using an Inverted Device Structure. *Nature Photonics* **6,** 591–595 (2012).

9. Li, G. *et al.* High-efficiency Solution Processable Polymer Photovoltaic Cells by Self-organization of Polymer Blends. *Nature Materials* **4,** 864–868 (2005).

10. Li, G., Zhu, R. & Yang, Y. Polymer Solar Cells. *Nature Photonics* **6,** 153–161 (2012).

11. Scharber, M. C. *et al.* Design Rules for Donors in Bulk-Heterojunction Solar Cells - Towards 10 Percent Energy-Conversion Efficiency. *Advanced Materials* **18,** 789–794 (2006).

12. Zhu, X.-Y., Yang, Q & Muntwiler, M. Charge-Transfer Excitons at Organic Semiconductor Surfaces and Interfaces. *Accounts of Chemical Research* **42,** 1779–1787 (2009).

13. Jailaubekov, A. E. *et al.* Hot Charge-transfer Excitons set the Time Limit for Charge Separation at Donor/Acceptor Interfaces in Organic Photovoltaics. *Nature Materials* **11,** 1–8 (2012).

14. Tsiper, E. V. & Soos, Z. G. Electronic Polarization in Pentacene Crystals and Thin Films. *Phys. Rev. B* **68,** 85301 (2003).

15. Muntwiler, M., Yang, Q., Tisdale, W. & Zhu, X.-Y. Coulomb Barrier for Charge Separation at an Organic Semiconductor Interface. *Physical Review Letters* **101,** 196403 (2008).

16. Grancini, G. *et al.* Hot Exciton Dissociation in Polymer Solar Cells. *Nature Materials* **12,** 29–33 (2013).

17. Provencher, F. *et al.* Direct Observation of Ultrafast Long-range Charge Separation at Polymer-Fullerene Heterojunctions. *Nature Communications* **5** (2014).

18. Coropceanu, V. *et al.* Charge Transport in Organic Semiconductors. *Chemical Reviews* **107,** 926–952 (2007).

19. Kaefer, D, El Helou, M, Gemel, C. & Witte, G. Packing of Planar Organic Molcules: Interplay of Van der Waals and Electronic Interaction. *Chrystal Growth Design* **8,** 3053 (2008).

20. Yang, Q., Muntwiler, M. & Zhu, X.-Y. Charge Transfer Excitons and Image Potential States on Organic Semiconductor Surfaces. *Physical Review B* **80,** 115214 (2009).

21. Kakudate, T, Yoshimoto, N, Kawamura, K & Saito, Y. Observation of Epitaxial Growth of Pentacene Thin Films on KCl Substrate by X-ray Diffractometry. *Journal of Crystal Growth* **306,** 27–32 (2007).

22. Burke, S. A., Topple, J. M. & Grutter, P. Molecular Dewetting on Insulators. *Journal of Physics: Condensed Matter* **21,** 423101 (2009).

23. Burke, S. A., Ledue, J. M., Topple, J. M., Fostner, S. & Grutter, P. Relating the Functional Properties of an Organic Semiconductor to Molecular Structure by NC-AFM. *Advanced Materials* **21,** 2029–2033 (2009).

24. Schumacher, Z., Miyahara, Y., Spielhofer, A. & Grutter, P. Measurement of Surface Photovoltage by Atomic Force Microscopy under Pulsed Illumination. *Physical Review Applied* **5,** 1–6 (2016).

25. Schumacher, Z., Spielhofer, A., Miyahara, Y. & Grutter, P. The Limit of Time Resolution in Frequency Modulation Atomic Force Microscopy by a Pump-Probe Approach. *Applied Physics Letters* **110,** 053111 (2017).

26. Wenner, F. A Method for Measuring Earth Resistivity. *Journal of the Franklin Institute* **180,** 373–375 (1915).

27. Valdes, L. Resistivity Measurements on Germanium for Transistors. *Proceedings of the IRE* **42,** 420–427 (1954).

28. Smits, F. M. Measurement of Sheet Resistivities with the Four-Point Probe. *Bell System Technical Journal* **37,** 711–718 (1958).

29. Green, M. & Gunn, M. Four-Point Probe Hall Effect and Resistivity Measurements upon Semiconductors. *Solid-State Electronics* **15,** 577–585 (1972).

30. Miccoli, I., Edler, F., Pfnuer, H. & Tegenkamp, C. The 100th Anniversary of the Four-Point Probe Technique: The Role of Probe Geometries in Isotropic and Anisotropic Systems. *Journal of Physics: Condensed Matter* **27,** 223201 (2015).

31. Vaughan, D. E. Four-Probe Resistivity Measurements on Small Circular Specimens. *British Journal of Applied Physics* **12,** 414–416 (1961).

32. Schroder, D. K. *Semiconductor Material and Device Characterization* **4,** 790 (John Wiley and Sons, Inc., Hoboken, NJ, USA, 2005).

33. Guise, O. *et al.* Development and Performance of the Nanoworkbench: A Four Tip STM for Conductivity Measurements down to Submicrometer Scales. *Review of Scientific Instruments* **76,** 045107 (2005).

34. Petersen, C. L., Grey, F., Shiraki, I. & Hasegawa, S. Microfour-Point Probe for Studying Electronic Transport through Surface States. *Applied Physics Letters* **77,** 3782–3784 (2000).

35. Boggild, P., Grey, F., Hassenkam, T., Greve, D. R. & Bjornholm, T. Direct Measurement of the Microscale Conductivity of Conjugated Polymer Monolayers. *Advanced Materials* **12,** 947–949 (2000).

36. Hasegawa, S. & Grey, F. Electronic Transport at Semiconductor Surfaces - from Point-Contact Transistor to Micro-Four-Point Probes. *Surface Science* **500,** 84–104 (2002).

37. Ansbaek, T. *et al.* Fundamental Size Limitations of Micro Four-Point Probes. *Microelectronic Engineering* **86,** 987–990 (2009).

38. Gammelgaard, L. *et al.* A Complementary Metal-Oxide-Semiconductor Compatible Monocantilever 12-Point Probe for Conductivity Measurements on the Nanoscale. *Applied Physics Letters* **93,** 91–94 (2008).

39. Hemami, A. & Labonville, R. Kinematic Equations and Solutions of a Human-Arm-Like Robot Manipulator. *Robotics and Autonomous Systems* **4,** 65–72 (1988).

40. Iliukhin, V. N., Mitkovskii, K. B., Bizyanova, D. A. & Akopyan, A. A. The Modeling of Inverse Kinematics for 5 DOF Manipulator. *Procedia Engineering* **176,** 498–505 (2017).

41. Denavit, J & Hartenberg, R. S. A Kinematic Notation for Lower-Pair Mechanisms based on Matrices. *Trans. of the ASME. Journal of Applied Mechanics* **22,** 215–221 (1955).

42. Saeidpourazar, R. & Jalili, N. Nano-robotic Manipulation using a RRP Nanomanipulator: Part A - Mathematical Modeling and Development of a Robust Adaptive Driving Mechanism. *Applied Mathematics and Computation* **206,** 618–627 (2008).

43. Saeidpourazar, R. & Jalili, N. Nano-robotic Manipulation using a RRP Nanomanipulator: Part B - Robust Control of Manipulator's Tip using Fused Visual Servoing and Force Sensor Feedbacks. *Applied Mathematics and Computation* **206,** 628–642 (2008).

44. Ju, B.-F., Ju, Y. & Saka, M. Fabrication of a Microscopic Four-Point Probe and its Application to Local Conductivity Measurement. *Journal of Micromechanics and Microengineering* **15,** 2277 (2005).

45. Tortonese, M, Barrett, R. C. & Quate, C. F. Atomic Resolution with an Atomic Force Microscope using Piezoresistive Detection. *Applied Physics Letters* **62,** 834–836 (1993).

46. Itoh, T. & Suga, T. Force Sensing Microcantilever using Sputtered Zinc Oxide Thin Film. *Applied Physics Letters* **64,** 37–39 (1994).

47. Itoh, T. & Suga, T. Self-excited Force-sensing Microcantilevers with Piezoelectric Thin Films for Dynamic Scanning Force Microscopy. *Sensors and Actuators A: Physical* **54,** 477–481 (1996).

48. Matula, R. A. Electrical Resistivity of Copper, Gold, Palladium, and Silver. *Journal of Physical and Chemical Reference Data* **8,** 1147–1298 (1979).

49. Cusati, T. *et al.* Electrical Properties of Graphene-metal Contacts. *Scientific Reports* **7,** 5109 (2017).

50. Haag, A.-L., Nagai, Y., Lennox, R & Grutter, P. Characterization of a Gold Coated Cantilever Surface for Biosensing Applications. *EPJ Techniques and Instrumentation* **2,** 1 (2015).

51. Haag, A. L., Schumacher, Z. & Grutter, P. Sensitivity Measurement of a Cantilever-based Surface Stress Sensor. *Journal of Chemical Physics* **145,** 1–7 (2016).

52. Lee, Y. H. Silicon Doping Effects in Reactive Plasma Etching. *Journal of Vacuum Science and Technology B: Microelectronics and Nanometer Structures* **4,** 468 (1986).

53. Kang, J. K. & Musgrave, C. B. The Mechanism of HF/H2O Chemical Etching of SiO2. *Journal of Chemical Physics* **116,** 275–280 (2002).

54. Petersen, D. H., Hansen, O., Hansen, T. M., Petersen, P. R. & Boggild, P. Static Contact Micro Four-point Probes with <11 nm Positioning Repeatability. *Microelectronic Engineering* **85,** 1092–1095 (2008).

55. Libioulle, L., Houbion, Y. & Gilles, J. M. Very Sharp Platinum Tips for Scanning Tunneling Microscopy. *Review of Scientific Instruments* **66,** 97–100 (1995).

56. Musselman, I. H. & Russell, P. E. Platinum/Iridium Tips with Controlled Geometry for Scanning Tunneling Microscopy. *Journal of Vacuum Science and Technology A: Vacuum, Surfaces, and Films* **8,** 3558–3562 (1990).

57. Hagedorn, T. *et al.* Refined Tip Preparation by Electrochemical Etching and Ultrahigh Vacuum Treatment to obtain Atomically Sharp Tips for Scanning Tunneling Microscope and Atomic Force Microscope. *Review of Scientific Instruments* **82** (2011).

58. Fotino, M. Nanotips by Reverse Electrochemical Etching. *Applied Physics Letters* **60,** 2935–2937 (1992).

59. Toda, Y., Kubota, Y., Hirano, M., Hirayama, H. & Hosono, H. Surface of Room-temperature-stable Electride [Ca24Al 28O64]4+(e-)4: Preparation and its Characterization by Atomic-resolution Scanning Tunneling Microscopy. *ACS Nano* **5,** 1907–1914 (2011).

60. Toda, Y. *et al.* Activation and Splitting of Carbon Dioxide on the Surface of an Inorganic Electride Material. *Nature Communications* **4,** 1–8 (2013).

61. Ostroverkhova, O. *et al.* Optical and Transient Photoconductive Properties of Pentacene and Functionalized Pentacene Thin Films: Dependence on Film Morphology. *Journal of Applied Physics* **98,** 033701 (2005).

62. Sinha, S., Wang, C.-H., Mukherjee, M., Mukherjee, T. & Yang, Y.-W. Oxidation of Rubrene Thin Films: An Electronic Structure Study. *Langmuir* **30,** 15433–15441 (2014).

63. Wang, Y., Motta, S. D., Negri, F. & Friedlein, R. Effect of Oxygen on the Electronic Structure of Highly Crystalline Picene Films. *Journal of the American Chemical Society* **133,** 10054–10057 (2011).

64. Hermenau, M. *et al.* Water and Oxygen Induced Degradation of Small Molecule Organic Solar Cells. *Solar Energy Materials and Solar Cells* **95,** 1268–1277 (2011).

65. Song, X. *et al.* Role of Oxygen Incorporation in Electronic Properties of Rubrene Films. *Applied Physics Letters* **97,** 032106 (2010).

66. Ly, J. T. *et al.* Oxidation of Rubrene, and Implications for Device Stability. *Journal of Materials Chemistry C* **6,** 3757–3761 (2018).

67. Crider, C. A., Cisneros, G., Mark, P. & Levine, J. D. Satellite Vacuum System for a Standard LEED AES System with Sample Transfer Capability. *Journal of Vacuum Science and Technology* **13,** 1202–1205 (1976).

68. Fleisch, T *et al.* System for Transferring Samples between Chambers in UHV. *Journal of Vacuum Science and Technology* **15,** 1756–1760 (1978).

69. Clausing, R. E., Heatherly, L & Emerson, L. C. Versatile UHV Sample Transfer System. *Journal of Vacuum Science and Technology* **16,** 708–710 (1979).

70. Jiricek, P., Cukr, M., Kolarik, V. & Koc, S. Transfer of Samples between Separated Ultrahigh Vacuum Intruments for Semiconductor Surface Studies. *Review of Scientific Instruments* **69,** 2804–2805 (1998).

71. Firpo, G, Buatier de Mongeot, F., Boragno, C & Valbusa, U. High Performance Portable Vacuum Suitcase. *Review of Scientific Instruments* **76,** 026108 (2005).

72. Firpo, G & Pozzo, A. New Getter Pump for Ultrahigh Vacuum Systems and Transportable Enclosure. *Review of Scientific Instruments* **75,** 4828–4832 (2004).

73. Watanabe, Y. *et al.* Portable Ultrahigh-Vacuum Sample Storage System for Polarization-dependent Total-reflection Fluorescence X-Ray Absorption Fine Structure Spectroscopy. *Journal of Vacuum Science and Technology A: Vacuum, Surfaces, and Films* **34,** 023201 (2016).

74. Benvenuti, C., Chiggiato, P., Cicoira, F. & L'Aminot, Y. Nonevaporable Getter Films for Ultrahigh Vacuum Applications. *Journal of Vacuum Science and Technology Technology A: Vacuum, Surfaces, and Films* **16,** 148–154 (1998).

75. Williams, F, Boudart, M & Frennet, A. Backstreaming of Hydrogen When Pumping Hydrocarbons with an Ion Pump. *Journal of Vacuum Science and Technology* **9,** 362–365 (1972).

76. Newport. Technical Note: Optical Materials. www.newport.com/n/optical-materials. *Website accessed on May 10th 2018* (2018).

77. Rayotek. Transparent Materials Comparison. www.rayotek.com/tech-specs/material-comparisons.htm. *Website accessed on May 10th 2018* (2018).

78. DiamondMaterials. Diamond Vacuum Windows. www.diamond-materials.com/. *Website accessed on May 10th 2018* (2018).

79. DelMarPhotonics. Ultra High Vacuum Viewports. www.dmphotonics.com/. *Website accessed on May 10th 2018* (2018).

80. Wei, L., Kuo, P. K., Thomas, R. L., Anthony, T. R. & Banholzer, W. F. Thermal Conductivity of Isotopically Modified Single Crystal Diamond. *Physical Review Letters* **70,** 3764–3767 (1993).

81. Kasugai, A. *et al.* Chemical Vapor Deposition Diamond Window for High-power and Long Pulse Millimeter Wave Transmission. *Review of Scientific Instruments* **69,** 2160–2165 (1998).

82. Mueckstein, R. *et al. Mapping the Distribution of Photo-currents responsible for Generation of Terahertz Pulses at Semiconductor Surfaces* in *2014 39th International Conference on Infrared, Millimeter, and Terahertz waves (IRMMW-THz)* (IEEE, 2014), 1–2.

83. He, J. *et al.* Generation and Evolution of the Terahertz Vortex Beam. *Optics Express* **21,** 20230 (2013).

84. Noble, A. & Kasevich, M. UHV Optical Window Seal to Conflat Knife Edge. *Review of Scientific Instruments* **65,** 3042–3043 (1994).

85. Cox, S. G., Griffin, P. F., Adams, C. S., DeMille, D. & Riis, E. Reusable Ultrahigh Vacuum Viewport Bakeable to 240 degC. *Review of Scientific Instruments* **74,** 3185–3187 (2003).

86. Weatherill, K. J. *et al.* A Versatile and Reliably Reusable Ultrahigh Vacuum Viewport. *Review of Scientific Instruments* **80,** 1–8 (2009).

87. Arora, P. & Gupta, A. S. Note: Reliable and Reusable Ultrahigh Vacuum Optical Viewports. *Review of Scientific Instruments* **83,** 4–7 (2012).

88. Gebhardt, P., Helbig, R. & Hummer, K. An Optical Window for Metal Cryostats. *Cryogenics* **16,** 735–736 (1976).

89. Crane, S. & Ekstrom, C. R. Nonmagnetic UHV Optical Viewports. *Proceedings of the IEEE International Frequency Control Symposium and Exposition* **2005,** 297–300 (2005).

90. Hartman, P. L. Notes on UHV Beryllium Windows. *Review of Scientific Instruments* **57,** 2564–2567 (1986).

91. Takahashi, K. *et al.* Development of Reliable Diamond Window for EC Launcher on Fusion Reactors. *Fusion Engineering and Design* **74,** 305–310 (2005).

92. Takahashi, K. *et al.* High Power Millimeter Wave Experiment of Torus Diamond Window Prototype for ITER EC H and CD System. *Fusion Engineering and Design* **88,** 85–93 (2013).

93. Pohl, D. W. Dynamic Piezoelectric Translation Devices. *Review of Scientific Instruments* **58,** 54–57 (1987).

94. Lyding, J. W., Skala, S, Hubacek, J. S., Brockenbrough, R & Gammie, G. Variable Temperature Scanning Tunneling Microscope. *Review of Scientific Instruments* **59,** 1897–1902 (1988).

95. Renner, C., Niedermann, P., Kent, A. D. & Fischer, O. A Vertical Piezoelectric Inertial Slider. *Review of Scientific Instruments* **61,** 965–967 (1990).

96. Howald, L., Rudin, H. & Guntherodt, H. J. Piezoelectric Inertial Stepping Motor with Spherical Rotor. *Review of Scientific Instruments* **63,** 3909–3912 (1992).

97. Gupta, A. K. & Ng, K. W. Compact Coarse Approach Mechanism for Scanning Tunneling Microscope. *Review of Scientific Instruments* **72,** 3552–3555 (2001).

98. Smith, S. T. *Foundations of Ultra-Precision Mechanism Design* 364 (CRC Press, Taylor and Francis Group, 1992).

99. Lin, K. Y. *et al.* Rubrene Polycrystalline Films Growth from Vacuum Deposition at Various Substrate Temperatures. *Journal of Crystal Growth* **439,** 54–59 (2016).

100. Song, L., Hennink, E., Young, I. & Tanke, H. Photobleaching Kinetics of Fluorescein in Quantitative Fluorescence Microscopy. *Biophysical Journal* **68,** 2588–2600 (1995).

101. Bala, R. & Marwaha, A. Investigation of Graphene Based Miniaturized Terahertz Antenna for Novel Substrate Materials. *Engineering Science and Technology, an International Journal* **19,** 531–537 (2016).

102. Norcada. MEMS Technology Company. www.norcada.com/products/xray-microscopy/. *Website accessed on July 13th 2018* (2018).

103. Wallace, P. R. The Band Theory of Graphite. *Physical Review* **71,** 622–634 (1947).

104. Singh, V. *et al.* Graphene Based Materials: Past, Present and Future. *Progress in Materials Science* **56,** 1178–1271 (2011).

105. Varghese, S. S., Lonkar, S., Singh, K. K., Swaminathan, S. & Abdala, A. Recent Advances in Graphene Based Gas Sensors. *Sensors and Actuators, B: Chemical* **218,** 160–183 (2015).

106. Caldwell, J. D. *et al.* Technique for the Dry Transfer of Epitaxial Graphene onto Arbitrary Substrates. *ACS Nano* **4,** 1108–1114 (2010).

107. Ferrari, A. C. & Robertson, J. Raman Spectroscopy of Amorphous, Nanostructured, Diamond-like Carbon, and Nanodiamond. *Philosophical Transactions of the Royal Society A: Mathematical, Physical and Engineering Sciences* **362,** 2477–2512 (2004).

108. Casari, C. S. *et al.* Low-frequency Modes in the Raman Spectrum of sp-sp2 Nanostructured Carbon. *Physical Review B - Condensed Matter and Materials Physics* **77** (2008).

109. Dawlaty, J. M., Shivaraman, S., Chandrashekhar, M., Rana, F. & Spencer, M. G. Measurement of Ultrafast Carrier Dynamics in Epitaxial Graphene. *Applied Physics Letters* **92,** 042116 (2008).

110. George, P. A. *et al.* Ultrafast Optical-Pump Terahertz-Probe Spectroscopy of the Carrier Relaxation and Recombination Dynamics in Epitaxial Graphene. *Nano Letters* **8,** 4248–4251 (2008).

111. Tai, L. *et al.* Direct Growth of Graphene on Silicon by Metal-Free Chemical Vapor Deposition. *Nano-Micro Letters* **10,** 1–9 (2018).

112. Whiteway, E., Yang, W., Yu, V. & Hilke, M. Time Evolution of the Growth of Single Graphene Crystals and High Resolution Isotope Labeling. *Carbon* **111,** 173–181 (2017).

113. Reis, F. *et al.* Bismuthene on a SiC Substrate: A Candidate for a High-temperature Quantum Spin Hall Material. *Science* **357,** 287–290 (2017).

114. Kadioglu, Y. *et al.* Modification of Electronic Structure, Magnetic Structure, and Topological Phase of Vismuthene by Point Defects. *Physical Review B* **96,** 245424 (2017).

A. Technical Drawings

A.1. Vacuum Suitcase

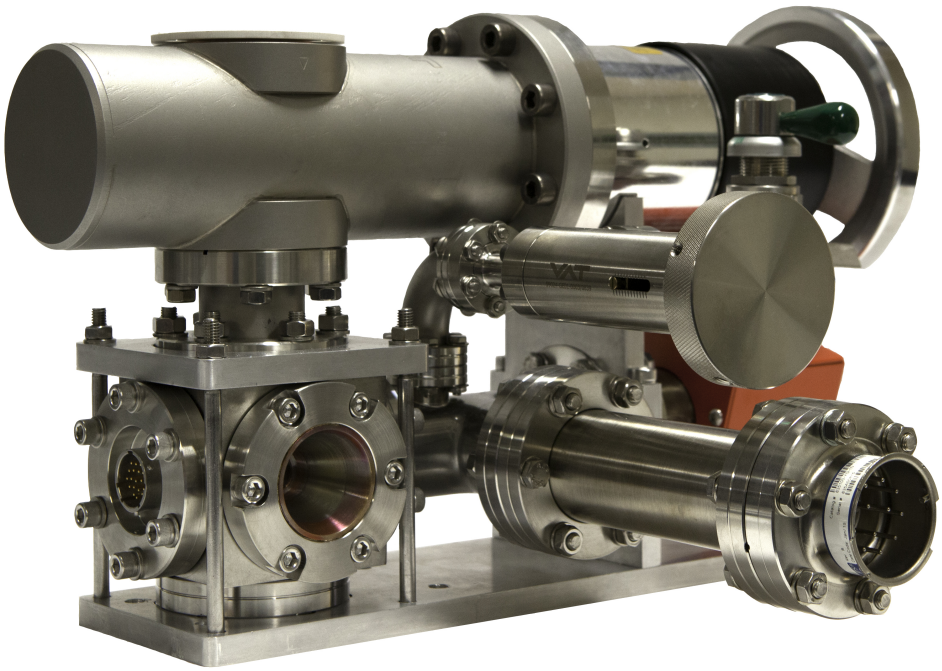

Figure 59: Home-built Vacuum Suitcase. The suitcase allows to transport samples at while maintaining pressures below 10^{-10} mbar. A non-evaporable getter pump and ion pump sufficiently pump chemically active gases and thus keep samples clean at any given time. The suitcase is equipped with an all-metal gate-valve for sample transferring, consists of a home-built piezostage that allows to fine position samples very accurately with nanometer precision and is equipped with custom-made diamond windows that allow ultra-broadband transmission. Further, a Residual Gas Analyzer allows to monitor the quality of the vacuum and a leak valve allows to controllably leak gases inside the chamber to monitor its effect on the physical properties of the sample.

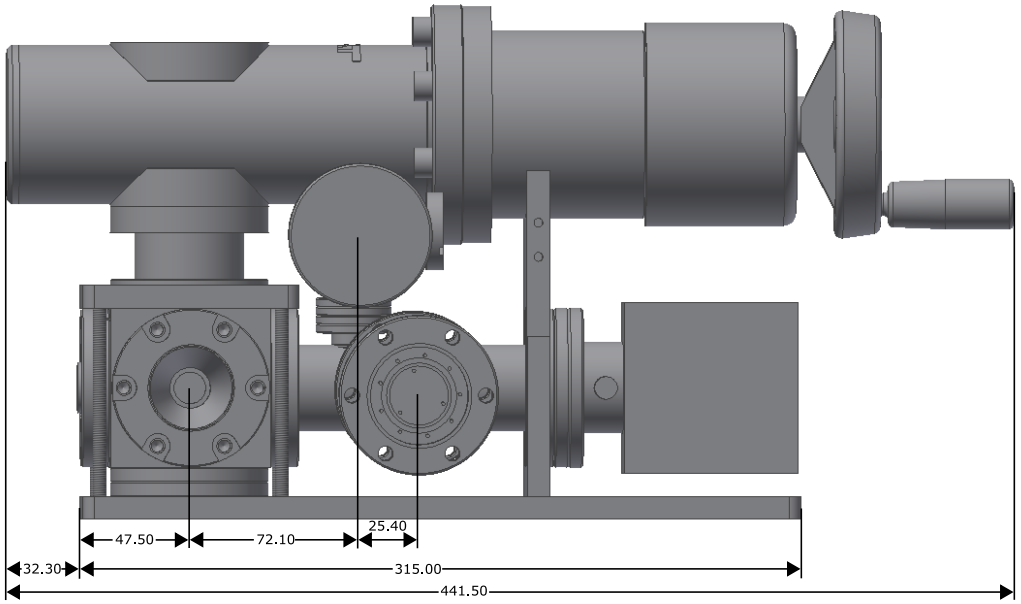

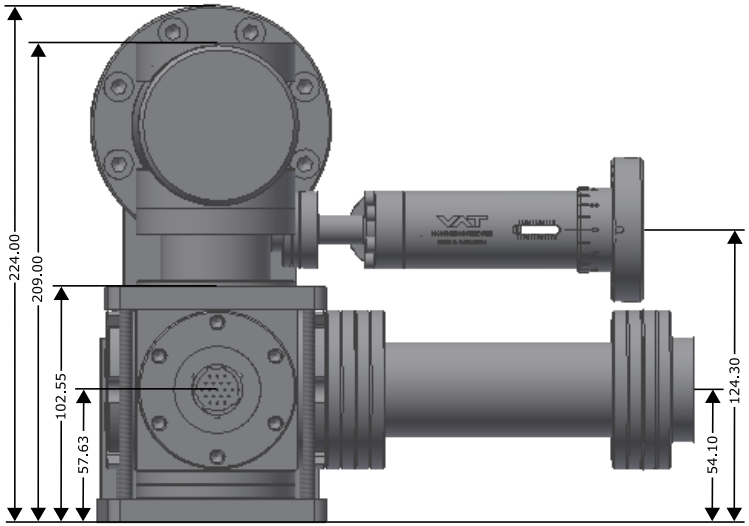

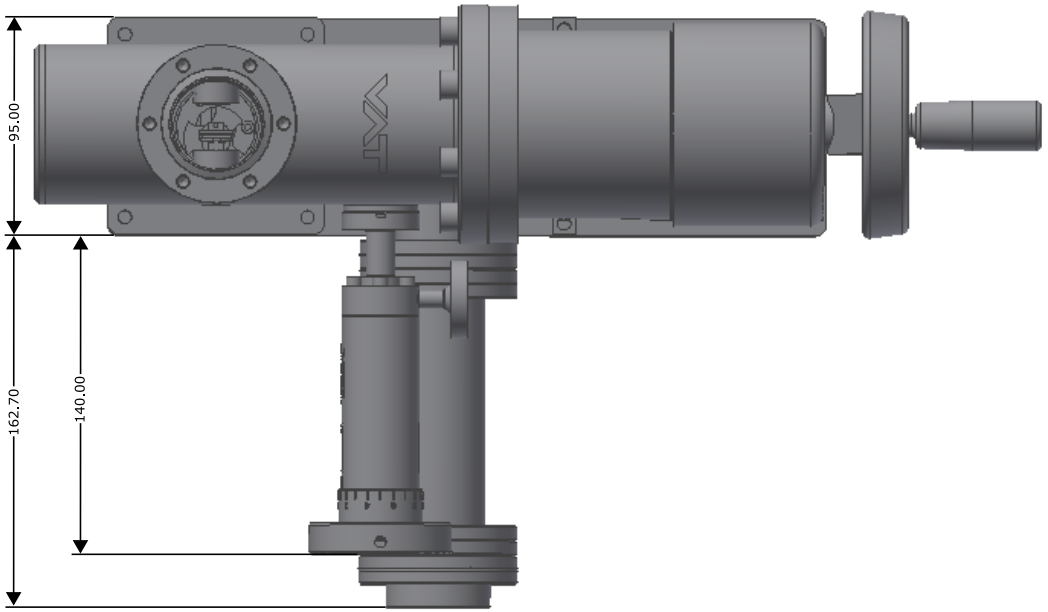

DRAWN Andreas Spielhofer	5/17/2018	SPM Grutter Group
CHECKED		TITLE: Vacuum Suitcase Dimensions
QA		
MFG		
APPROVED		
		SIZE C / DWG NO / REV
		SCALE / SHEET 1 OF 1

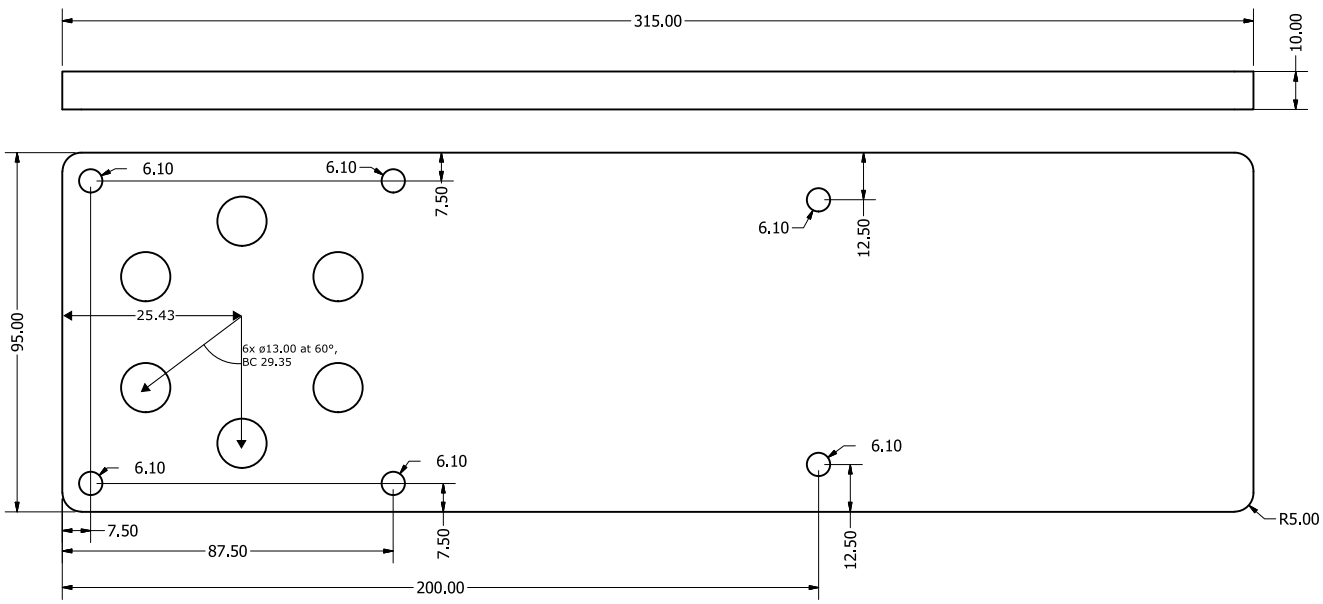

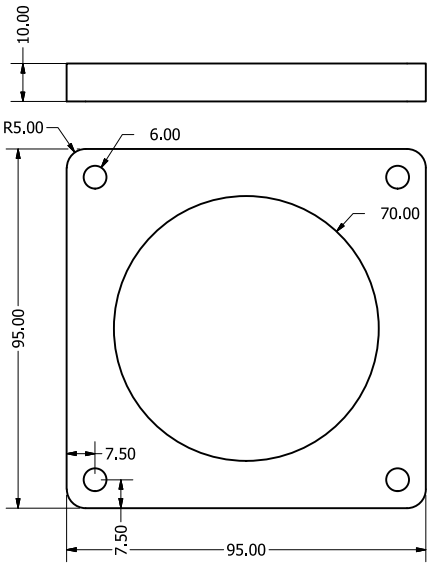

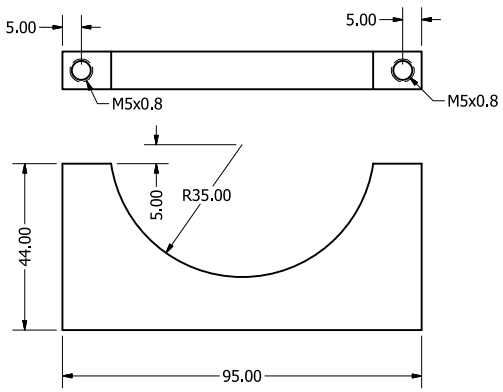

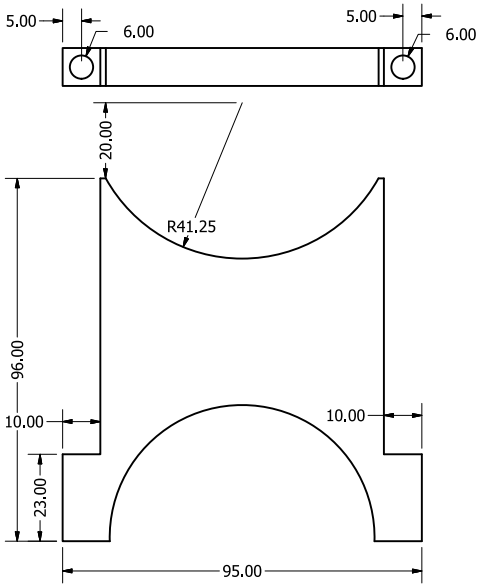

DRAWN Andreas Spielhofer	07/12/2015	Grutter SPM Group
CHECKED		TITLE: Vacuum Suitcase Support Plates
QA		
MFG		
APPROVED		
		SIZE C / DWG NO Baseplate2 / REV
		SCALE 1 / SHEET 1 OF 1

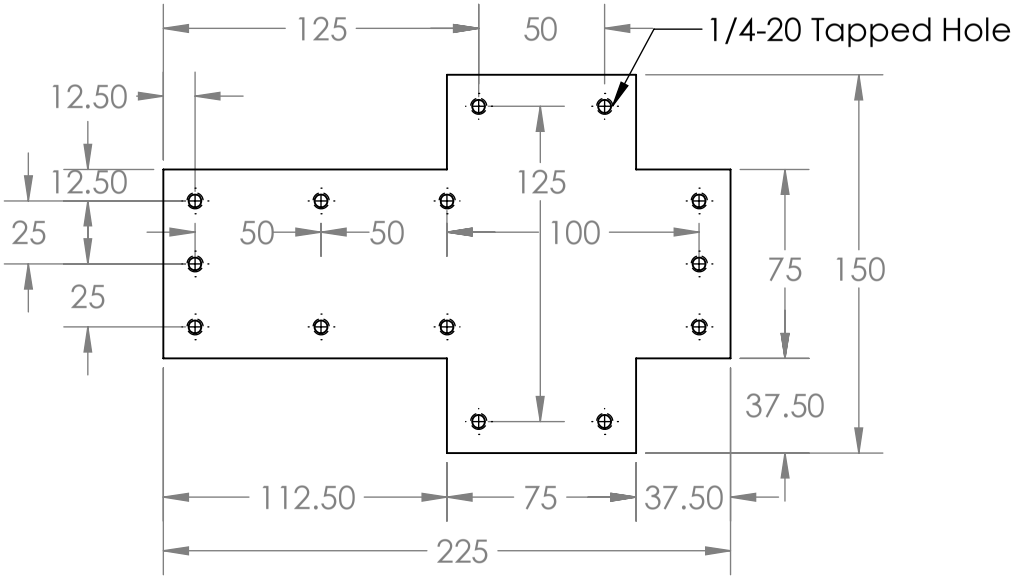

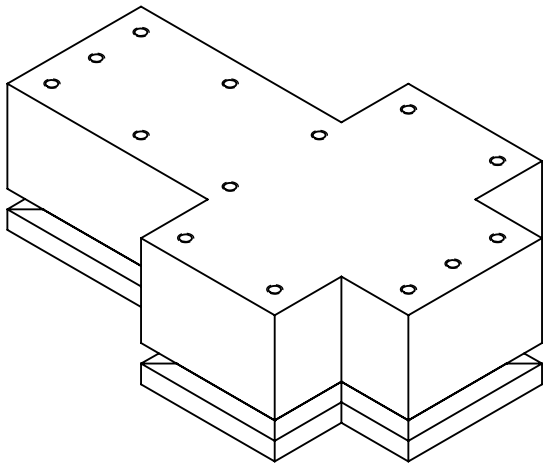

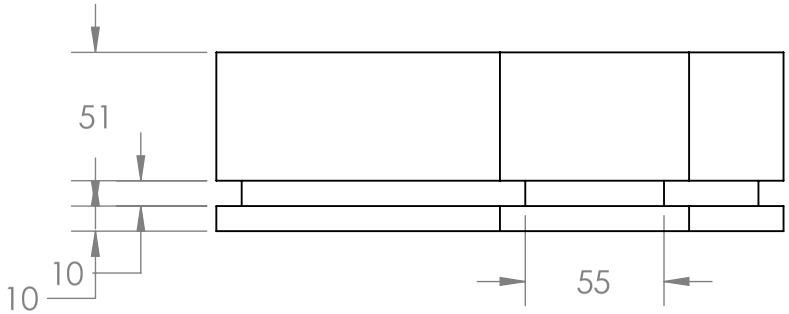

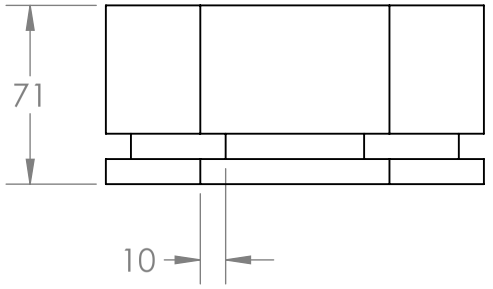

		UNLESS OTHERWISE SPECIFIED:		NAME	DATE
		DIMENSIONS ARE IN INCHES TOLERANCES: FRACTIONAL ± ANGULAR: MACH ± BEND ± TWO PLACE DECIMAL ± THREE PLACE DECIMAL ±	DRAWN		
			CHECKED		
			ENG APPR.		
			MFG APPR.		
		INTERPRET GEOMETRIC TOLERANCING PER:	Q.A.		
		MATERIAL	COMMENTS:		
NEXT ASSY	USED ON	FINISH			
APPLICATION		DO NOT SCALE DRAWING			

PROPRIETARY AND CONFIDENTIAL

THE INFORMATION CONTAINED IN THIS DRAWING IS THE SOLE PROPERTY OF <INSERT COMPANY NAME HERE>. ANY REPRODUCTION IN PART OR AS A WHOLE WITHOUT THE WRITTEN PERMISSION OF <INSERT COMPANY NAME HERE> IS PROHIBITED.

TITLE:

Vacuum Chamber Baseplate - D

SIZE	DWG. NO.	REV
A		
SCALE: 1:3	WEIGHT:	SHEET 1 OF 1

A.1.1. Two-Axis Piezostage

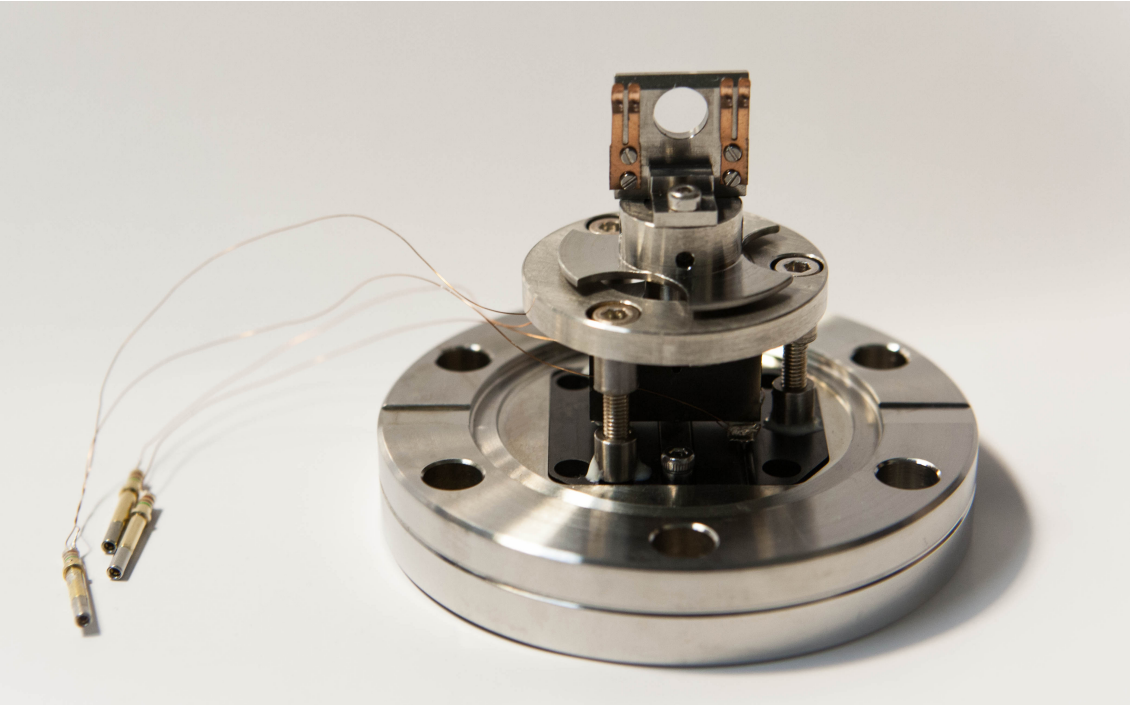

Figure 60: Home-built two axis piezostage. The stage allows to fine-position samples in optical pump-probe setups. The sample can move by ±5 mm in every direction. Special hardened parts prevent the surfaces from scratches when the sapphire hemispheres move over the surfaces allowing long-term precision and stability.

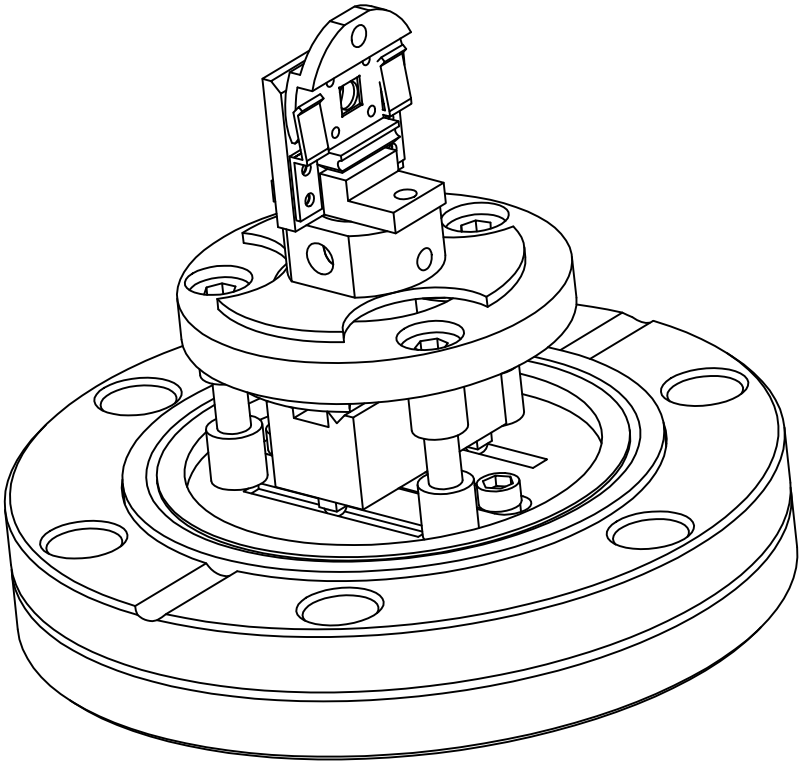

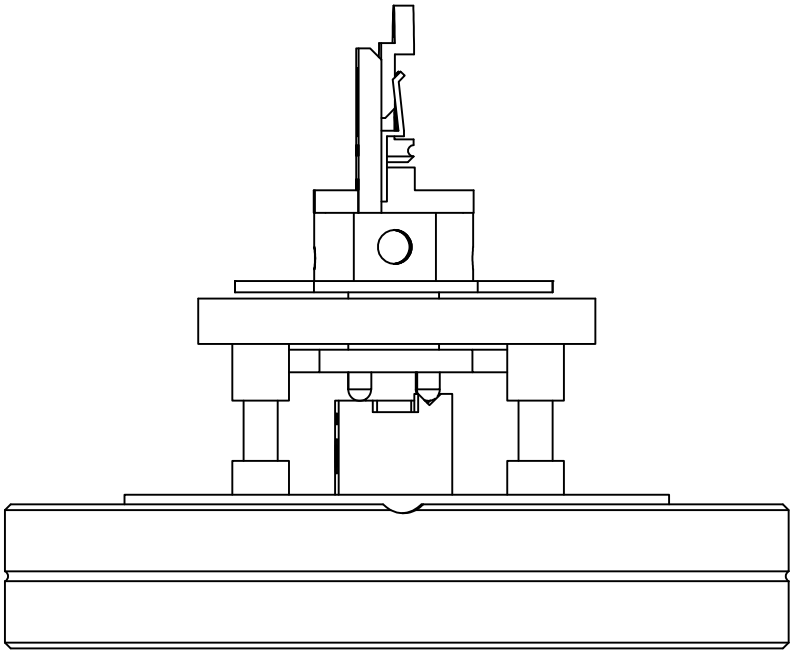

DRAWN Andreas Spielhofer	29/07/2014	Grutter SPM group	
CHECKED		TITLE	
QA		Piezostage for the vacuum suitcase	
MFG			
APPROVED			
		SIZE C	DWG NO 0/10 REV
		SCALE	SHEET 1 OF 1

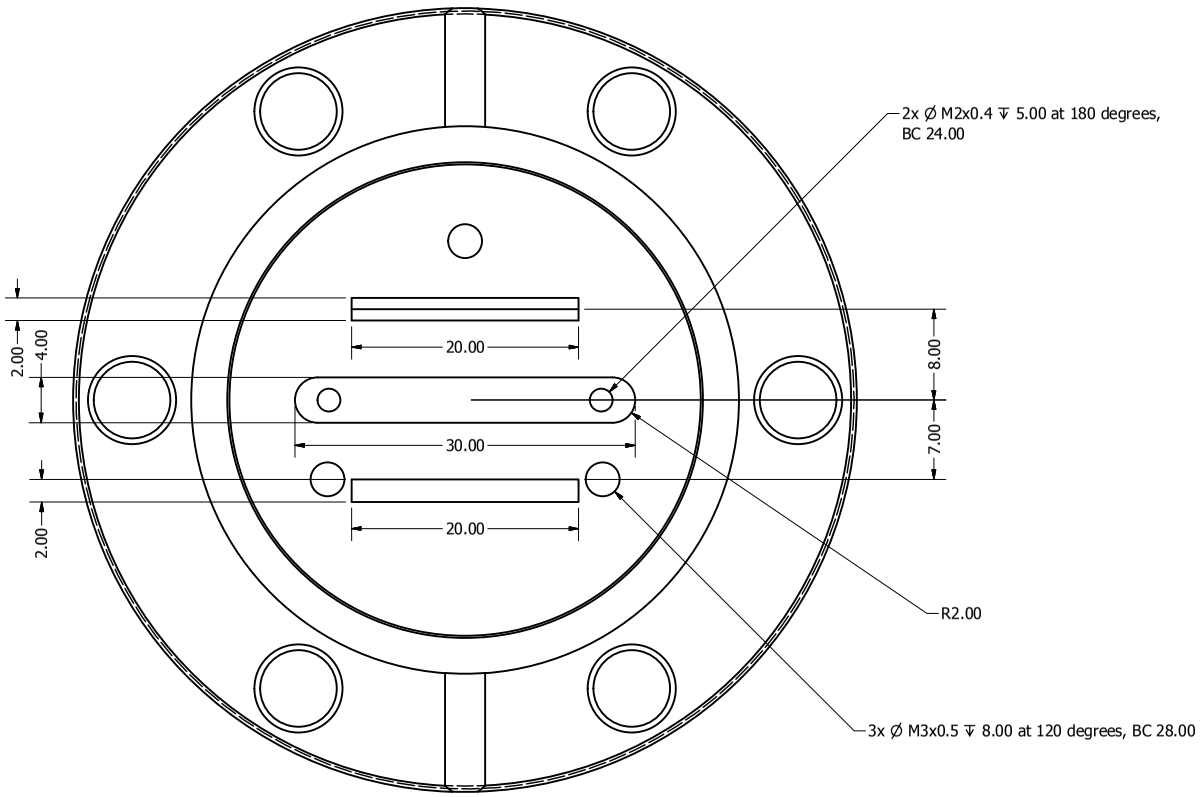

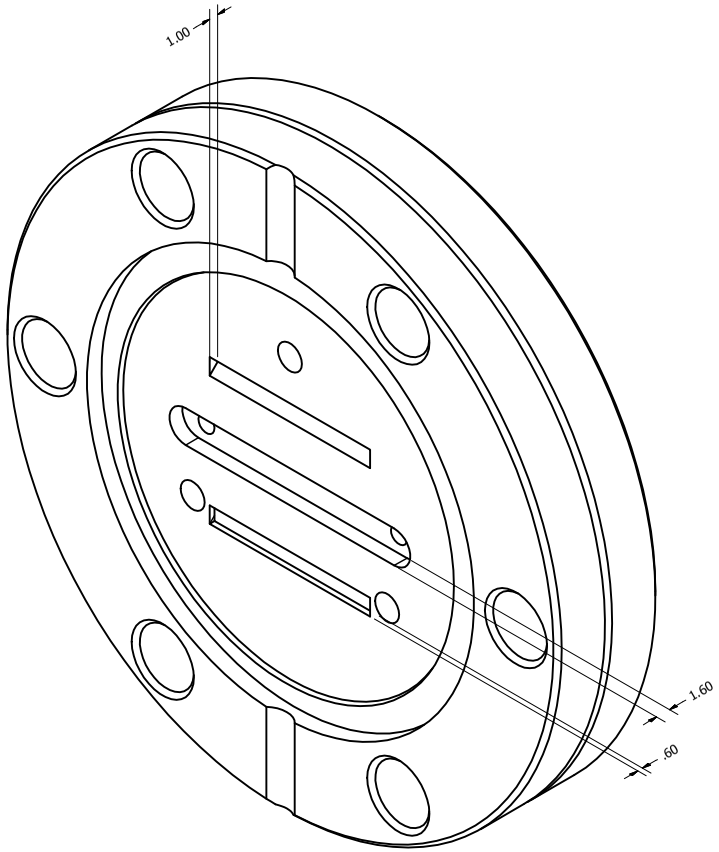

Please call me or send me an email when this part is done together with dwg no. 3/10. I will have to send it to a company to coat parts of it with TiN.

2 3/4" blank flange, stainless steel, 1 piece

DRAWN Andreas Spielhofer	29/07/2014	Grutter SPM group
CHECKED		TITLE: Flange with V-shaped grooves, threads and channel for Piezostage
QA		
MFG		
APPROVED		
		SIZE C / DWG NO 1/10 / REV
		SCALE / SHEET 1 OF 1

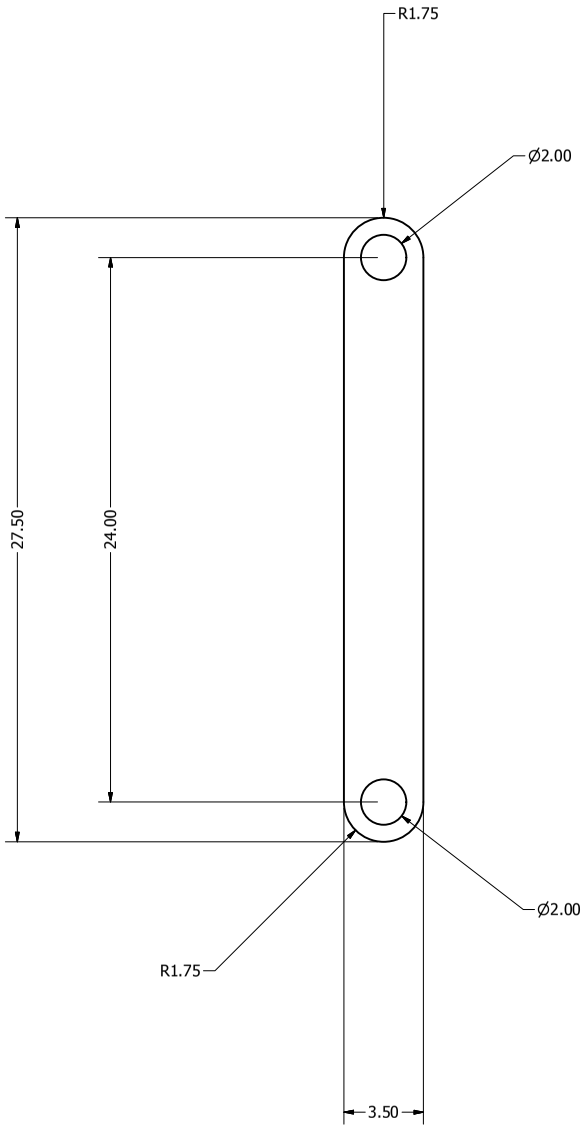

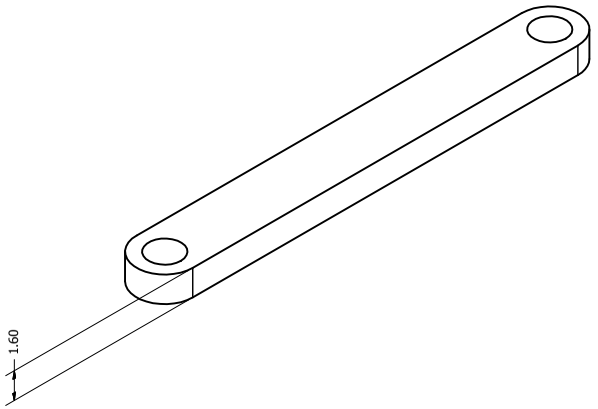

Material: 440C stainless steel,
can be bought at McMaster Carr, thickness ~ 1.6mm, 1 piece

DRAWN Andreas Spielhofer	29/07/2014	Grutter SPM group
CHECKED		TITLE: Magnetic counterpart, made out of 440C stainless steel, for Piezostage
QA		
MFG		
APPROVED		
		SIZE C / DWG NO 2/10 / REV
		SCALE / SHEET 1 OF 1

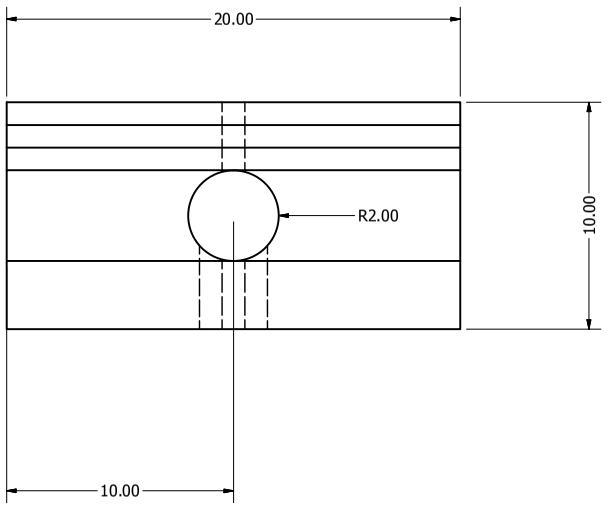

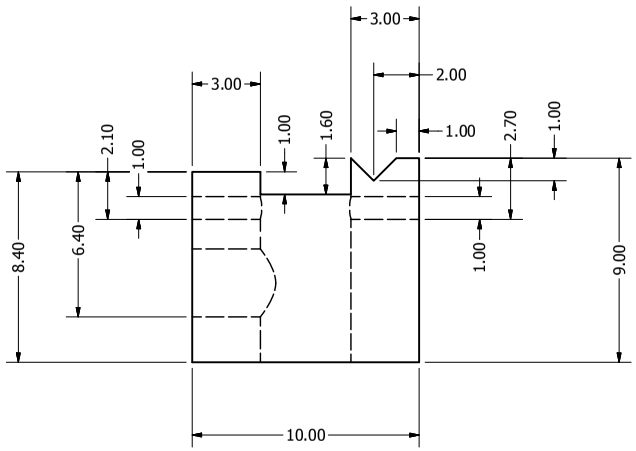

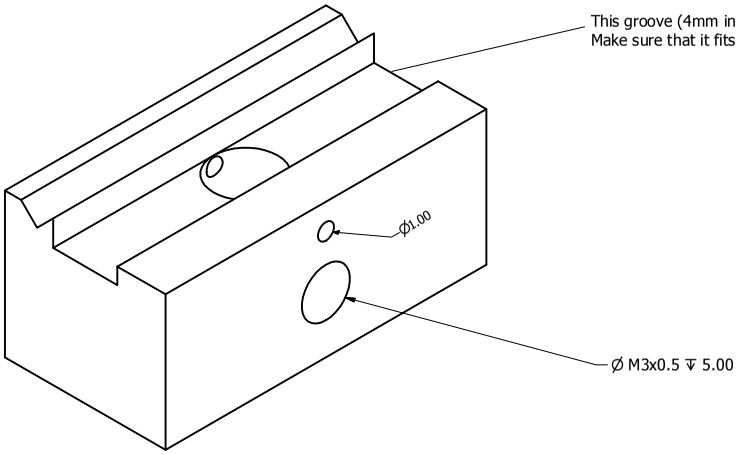

Please call me or send me an email when this part is done together with dwg no. 1/10. I will have to send it to a company to coat parts of it with TiN.

Material: stainless steel, 1 piece

DRAWN Andreas Spielhofer	29/07/2014	Grutter SPM group	
CHECKED		TITLE	
QA		Middle part with magnet hole and V-shaped grooves on top, for Piezostage	
MFG			
APPROVED			
		SIZE C	DWG NO 3/10 REV
		SCALE	SHEET 1 OF 1

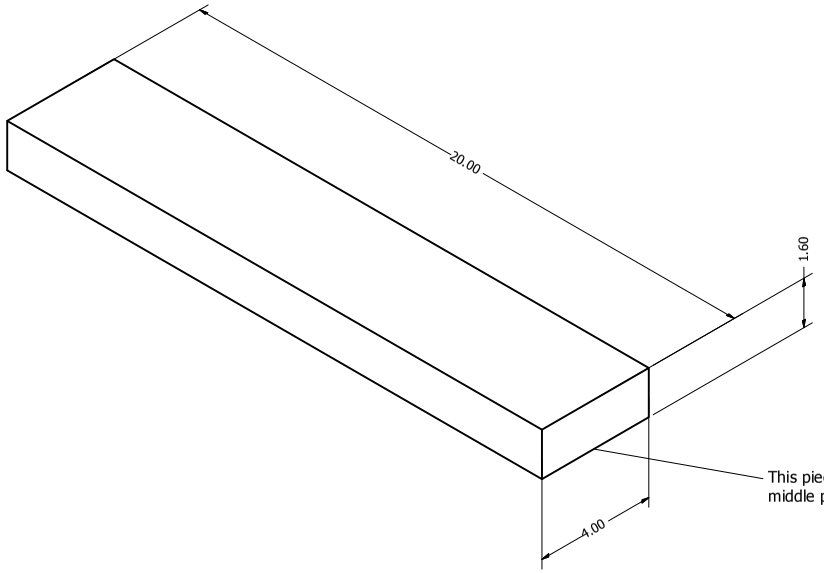

This piece (4mm in width) has to fit into the groove of the middle part (dwg no. 4/10). This dimension can be slightly smaller.

Material: 440C stainless steel,
can be bought at McMaster Carr, thickness ~ 1.6mm, 1 piece

DRAWN Andreas Spielhofer	29/07/2014	Grutter SPM group
CHECKED		TITLE: Magnetic counterpart for Piezostage, made out of 440C stainess steel
QA		
MFG		
APPROVED		
		SIZE C / DWG NO 4/10 / REV
		SCALE / SHEET 1 OF 1

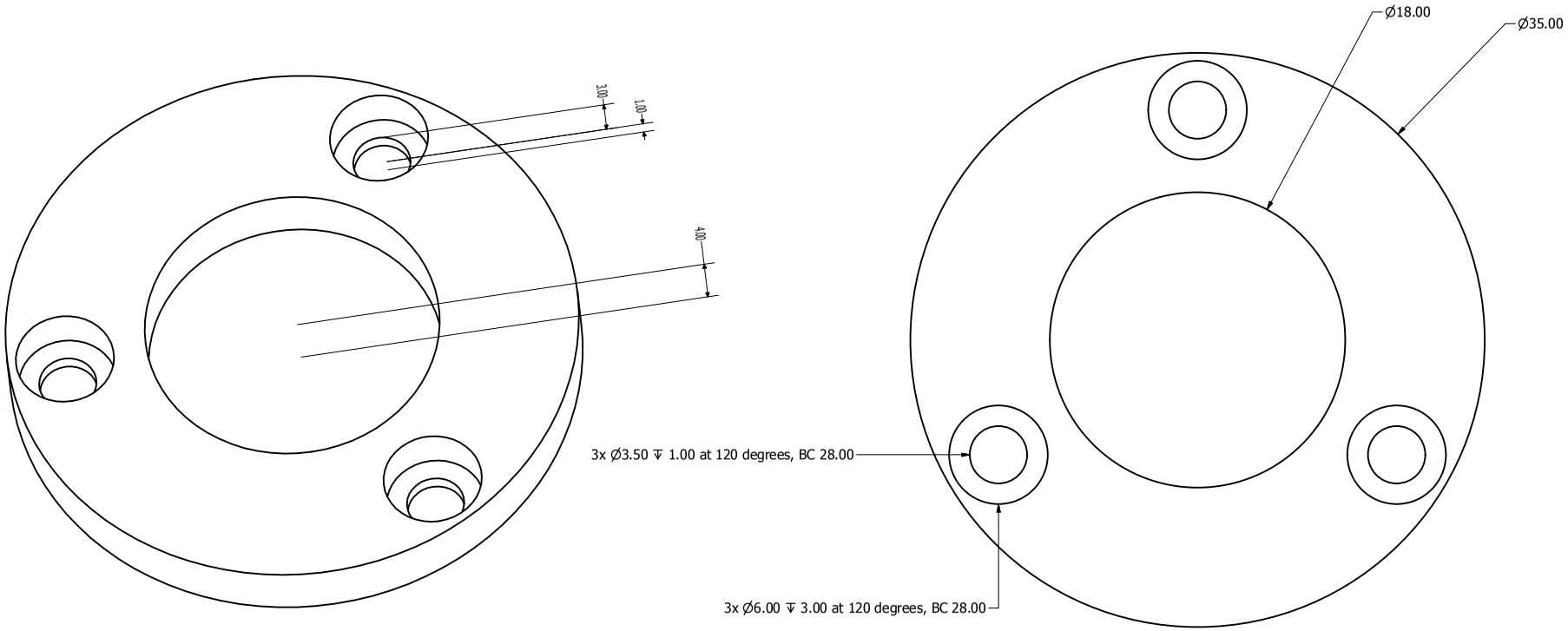

Material: stainless steel, 1 piece

DRAWN Andreas Spielhofer	29/07/2014	Grutter SPM group	
CHECKED		TITLE	
QA		Ring with 3 holes for screws, for Piezostage	
MFG			
APPROVED			
		SIZE C	DWG NO 5/10 REV
		SCALE	SHEET 1 OF 1

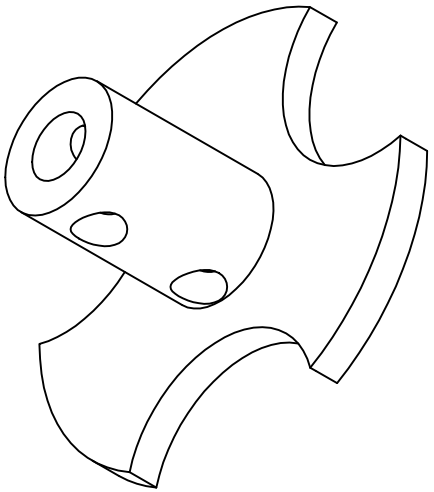

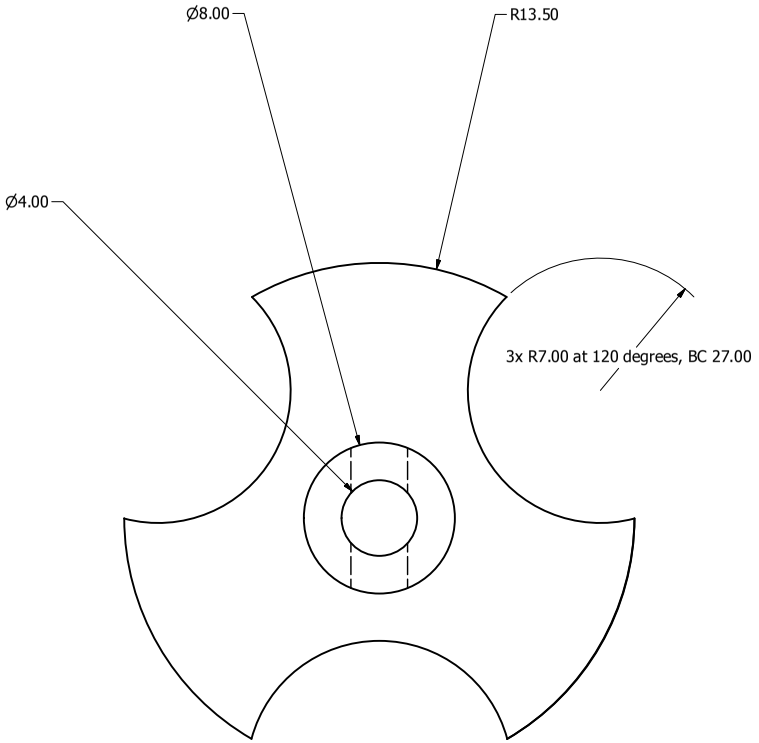

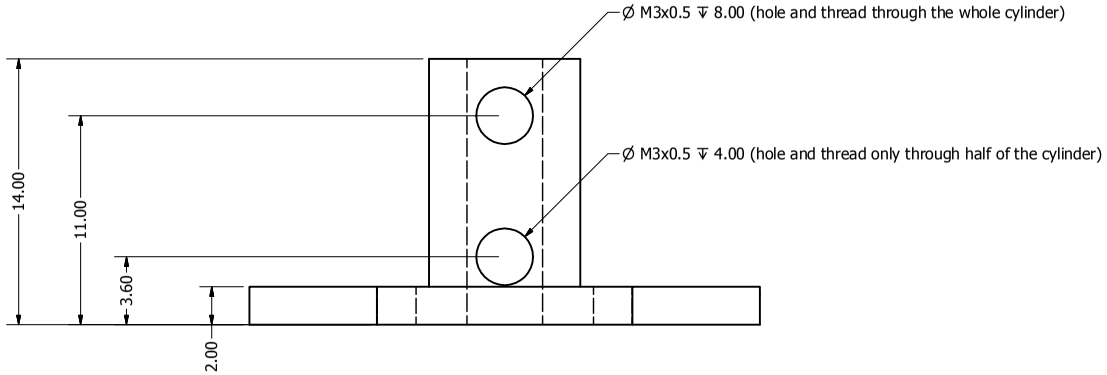

Material: stainless steel, 1 piece

DRAWN Andreas Spielhofer	29/07/2014	Grutter SPM group
CHECKED		TITLE
QA		Upper counterpart for Piezostage.
MFG		
APPROVED		
		SIZE C / DWG NO 6/10 / REV
		SCALE / SHEET 1 OF 1

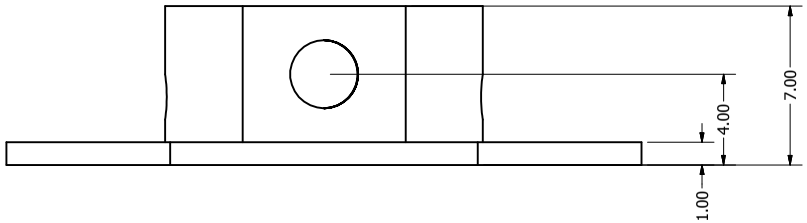

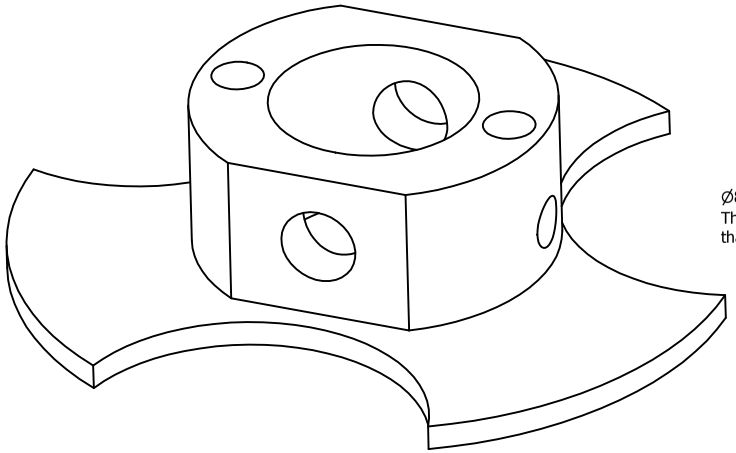

Ø8.00 or slightly bigger.
This hole hast to be big enough
that cylinder from dwg no. 6/10 fits through

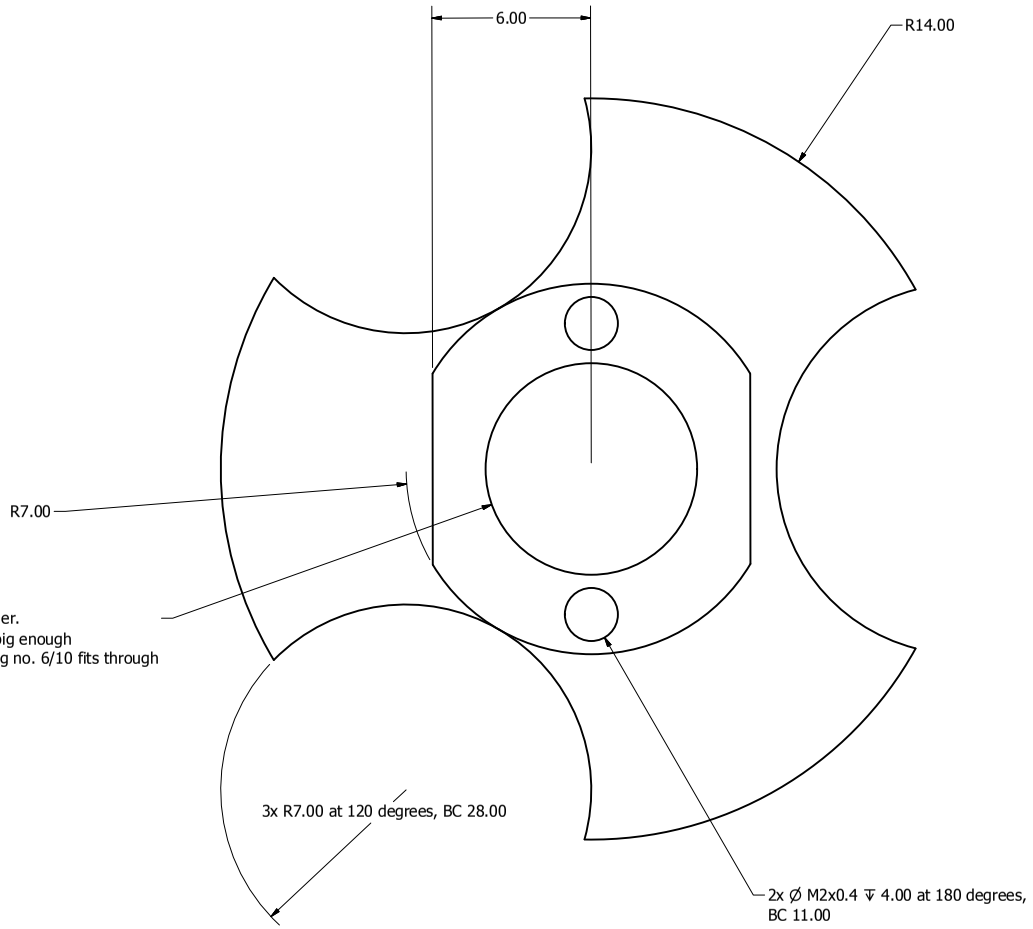

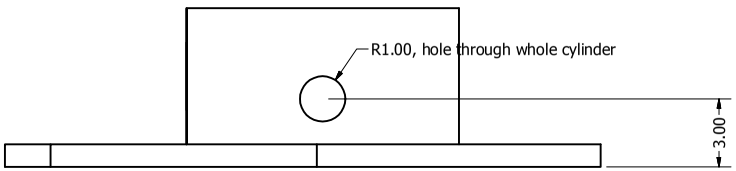

Material: stainless steel, 1 piece

DRAWN Andreas Spielhofer	29/07/2014	Grutter SPM group	
CHECKED		TITLE	
QA		Upper holder of the piezo stage, holds the sample holder, for Piezostage.	
MFG			
APPROVED		SIZE C	DWG NO 7/10 REV
		SCALE	SHEET 1 OF 1

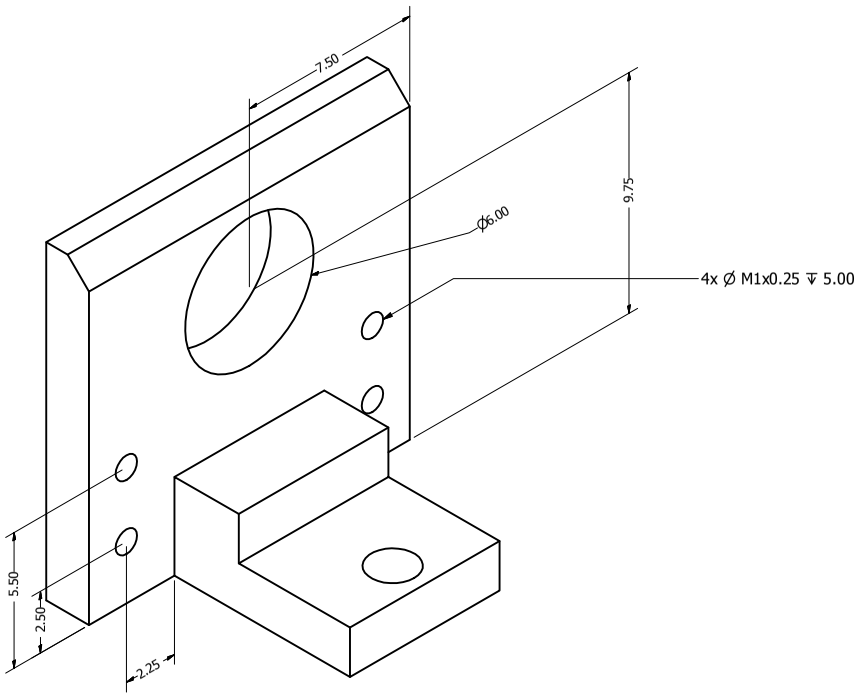

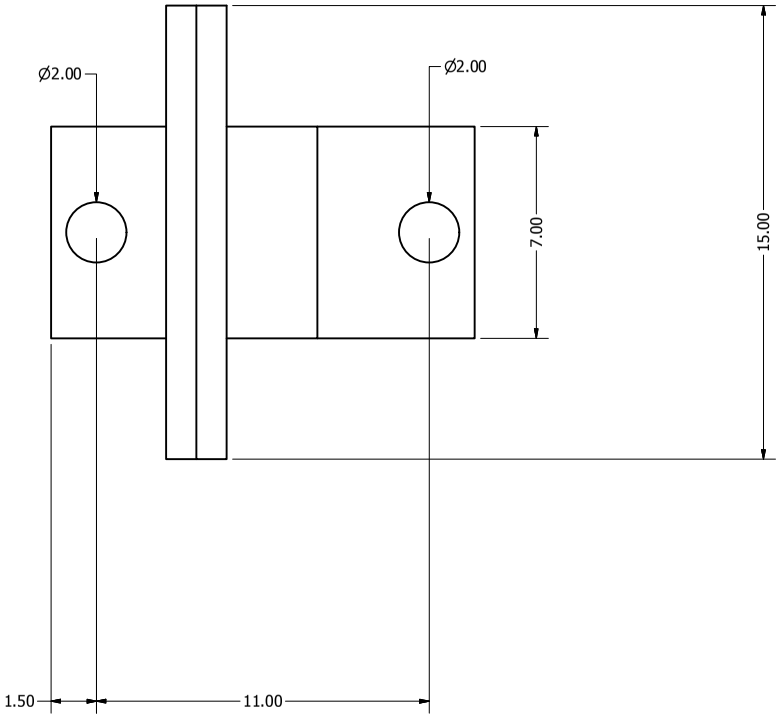

This dimension is important. This holder will be screwed on dwg no. 7/10.
The holes should fit on each other.

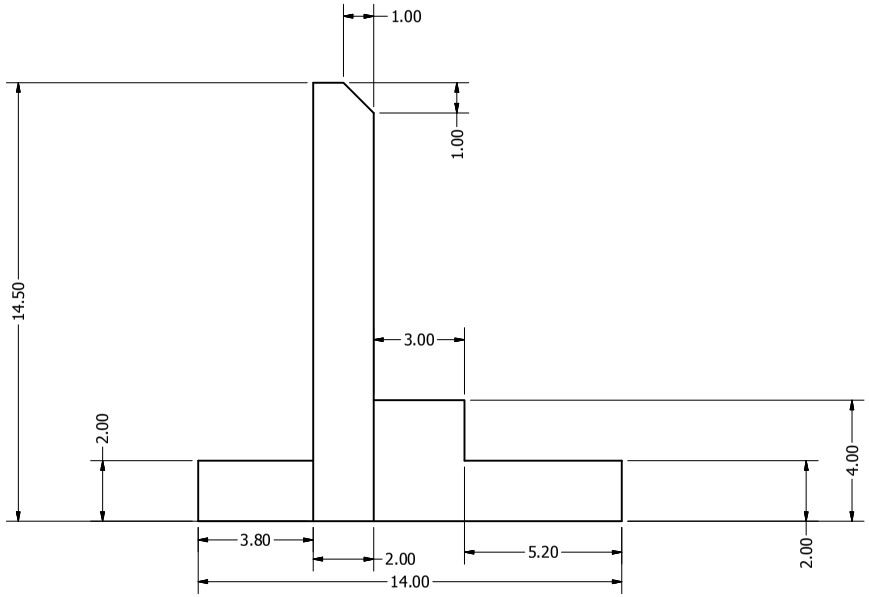

Material: stainless steel, 1 piece

DRAWN Andreas Spielhofer	29/07/2014	Grutter SPM group	
CHECKED		TITLE	
QA		Jeol sample holder holder for the Piezostage	
MFG			
APPROVED			
		SIZE C / DWG NO 8/10	REV
		SCALE	SHEET 1 OF 1

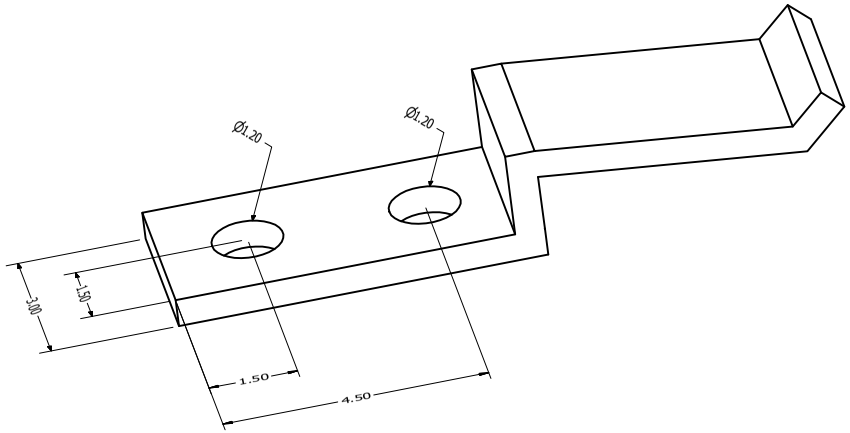

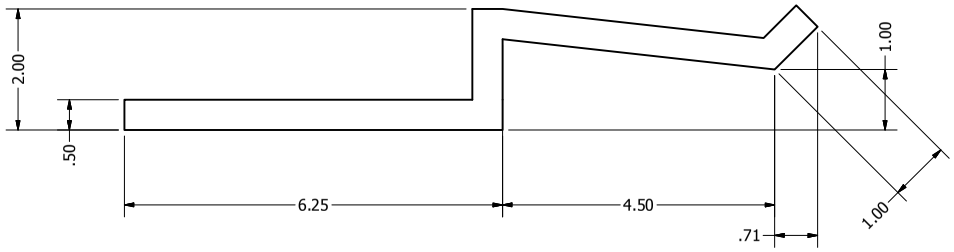

Material: copper beryllium , 2 pieces

DRAWN Andreas Spielhofer	29/07/2014	Grutter SPM group
CHECKED		TITLE
QA		Springs for the Jeol sample holder holder
MFG		
APPROVED		
		SIZE C / DWG NO 9/10 / REV
		SCALE / SHEET 1 OF 1

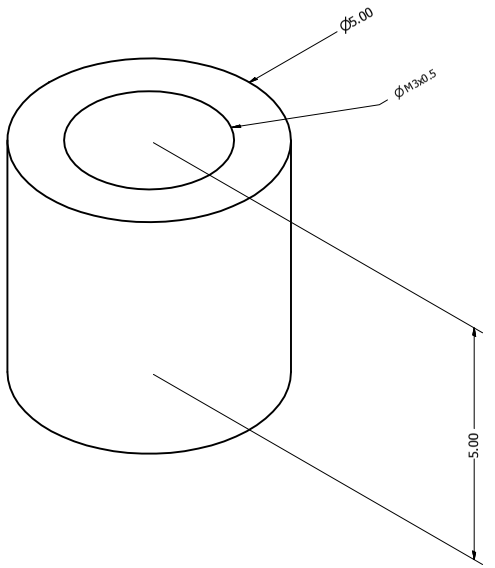

Material: stainless steel, 6 pieces

DRAWN Andreas Spielhofer	29/07/2014	Grutter SPM group
CHECKED		TITLE
QA		Female threaded bushing for Piezostage.
MFG		
APPROVED		
		SIZE C / DWG NO 10/10 / REV
		SCALE / SHEET 1 OF 1

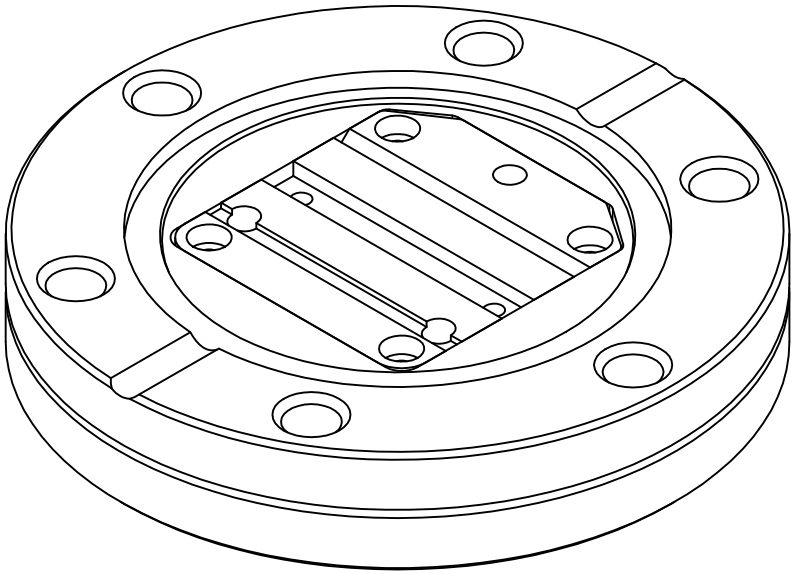

DRAWN Andreas Spielhofer	05/12/2014	Grutter SPM group
CHECKED		TITLE: Improved version of v-shaped grooves in a flange. It is removable and parts will be made of hardened steel
QA		
MFG		
APPROVED		
		SIZE C | DWG NO 1/3 | REV
		SCALE 3 : 1 | SHEET 2 OF 2

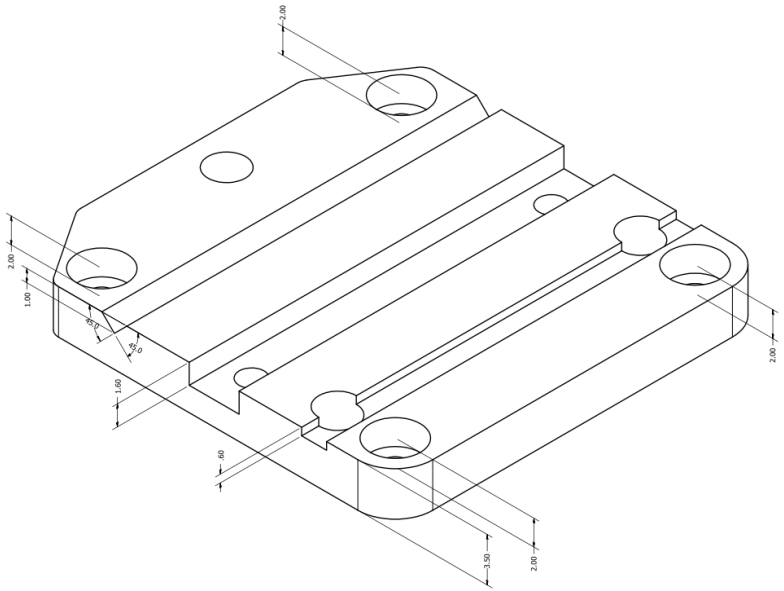

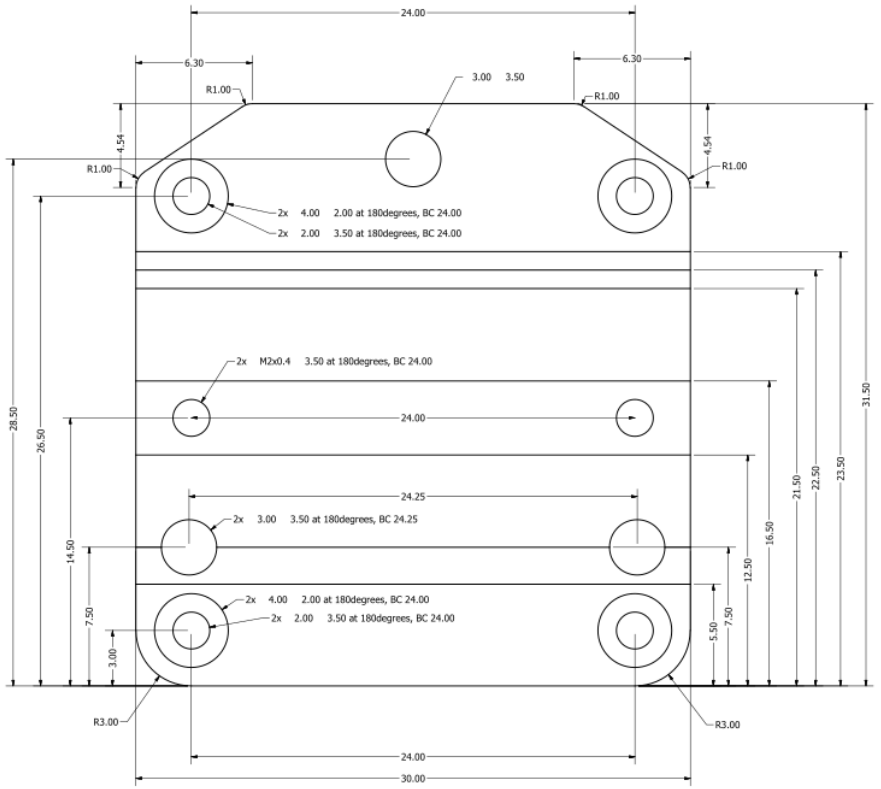

Material: Hardened Steel (Rockwell C30 to C60). The harder the better.
Material can be bought from McMaster Carr (1/4" thickness)

DRAWN Andreas Spielhofer	05/12/2014	SPM Grutter group
CHECKED		TITLE: Inlet with the grooves for the 2-3/4 Flange. Material: Hardened Stainless Steel (Rockwell C30 - Rockwell C60)
QA		
MFG		
APPROVED		
		SIZE C / DWG NO 2/3 / REV
		SCALE / SHEET 2 OF 2

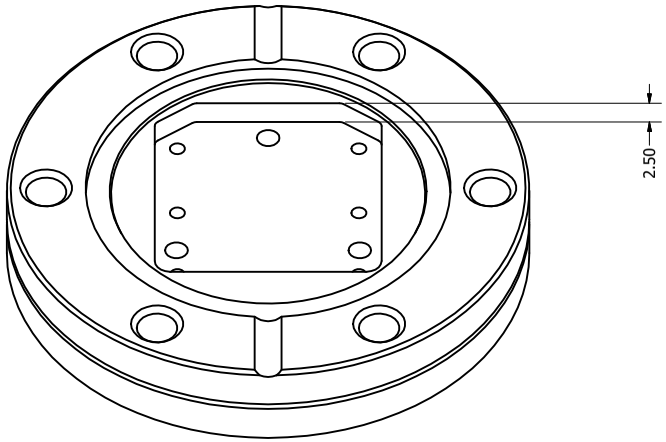

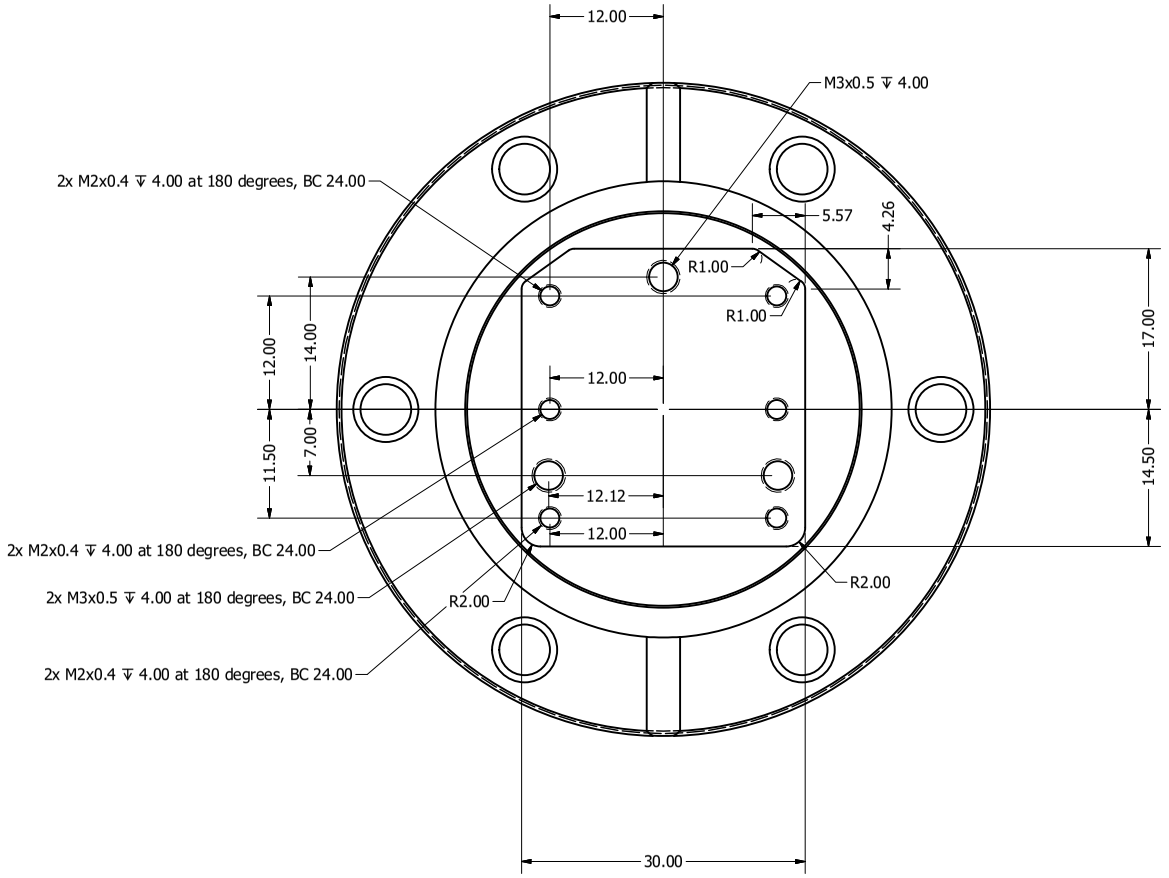

Please keep in mind that the 2-3/4 flange has a six-fold symmetry. The inset has to fit according to the orientation of the flange on the suitcase.

DRAWN Andreas Spielhofer	05/12/2014	SPM Grutter group	
CHECKED		TITLE	
QA		2-3/4 Flange modification for Inset	
MFG			
APPROVED		SIZE C	DWG NO 3/3 REV
		SCALE 2.5 : 1	SHEET 2 OF 2

A.1.2. Vacuum Suitcase - Diamond Windows

Figure 61: Custom-made diamond windows for broadband optical-pump THz-probe experiments. The windows have a 14 mm free aperture and the conical opening allows a distortion free propagation of the THz beam through the suitcase.

Frontview

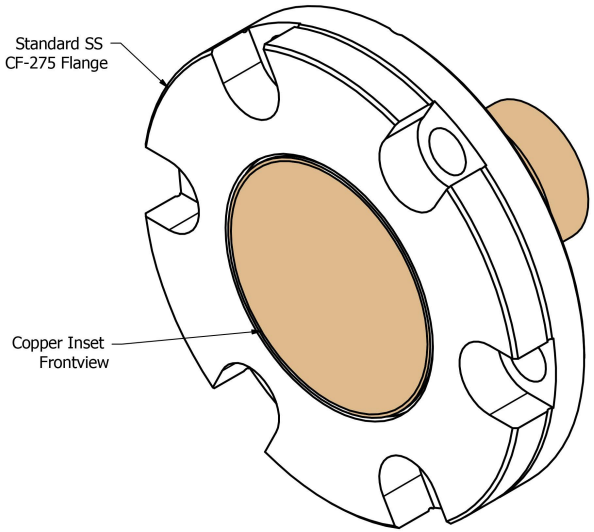

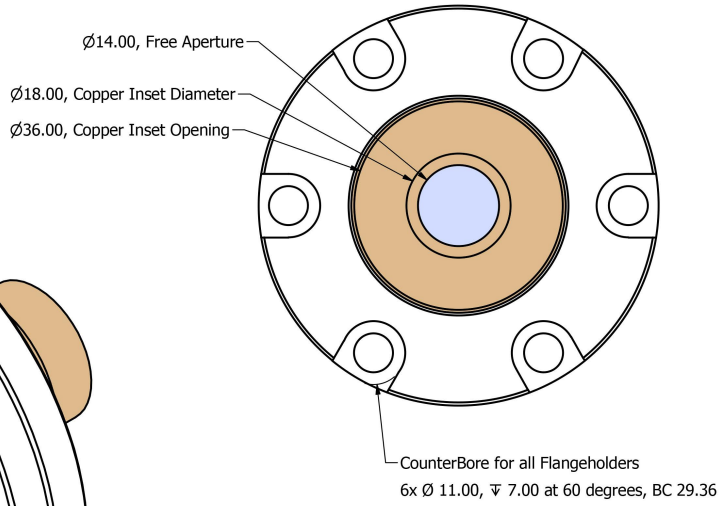

Backview

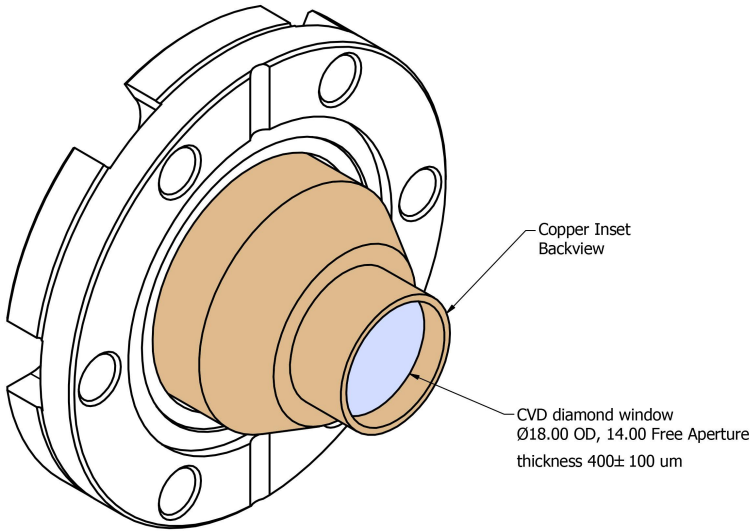

Specifications:

Diamond Windows:
- CVD diamond window, optical quality
- flat faces polished, surface roughness <20 nm RMS
- thickness 400± 100 um
- wedge <0.1°
- side faces laser cut
- diameter 18 mm, clear aperture 14 mm

Flange and Mounting:
- window braze-sealed into Conflat UHV flange
- flange size: standard 2.75 inch Conflat (DIN: DN40CF)

UHV Specifications:
- window bakeable at 200°C
- window tested to 1 bar diff. pressure
- leak rate < 1x10^-10 bar.cm^3/sec He

Quantity: 2

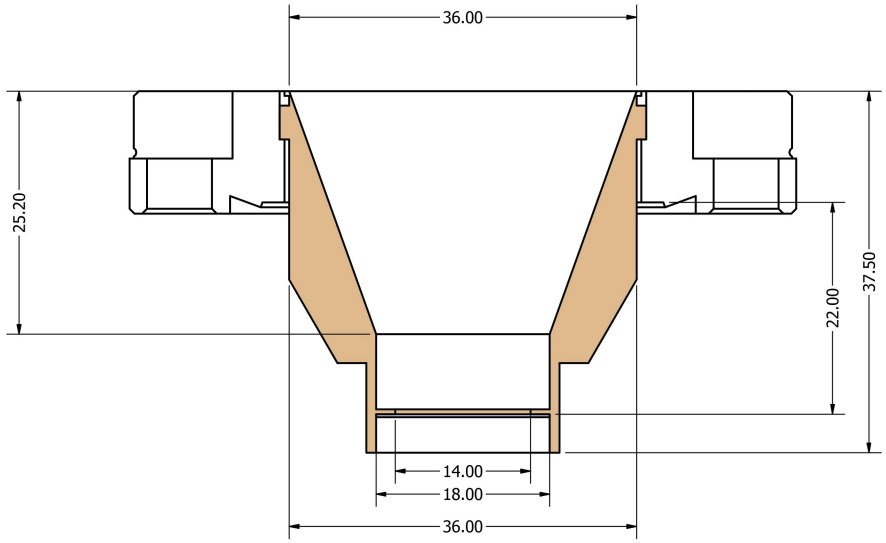

DRAWN Andreas Spielhofer	11/02/2016	SPM Grutter group
CHECKED Diamond Materials		TITLE: UHV Diamond Window for Ultra-broadband pump-probe experiments. Standard CF-275 Flange, with Copper Inset and Diamond Window (14mm free aperture, optical quality). Brazed and Leak Tested
QA		
MFG		
APPROVED		
		SIZE C; DWG NO Diamond Materials - Diamond Window; REV
		SCALE 1.5 : 1; SHEET 1 OF 1

A.2. UHV Four Point-Probe

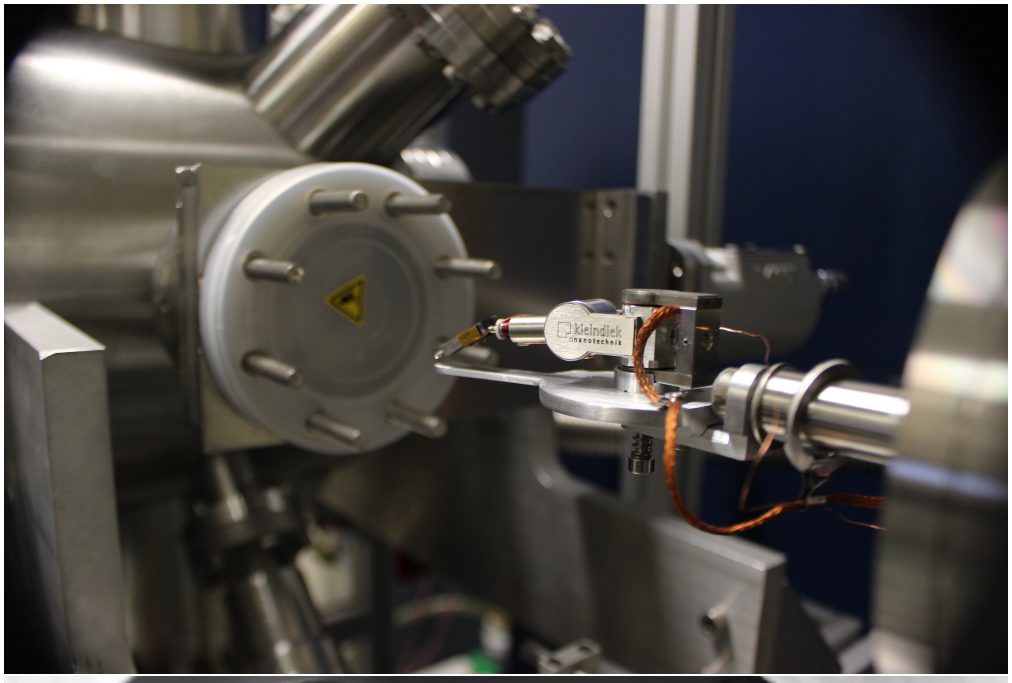

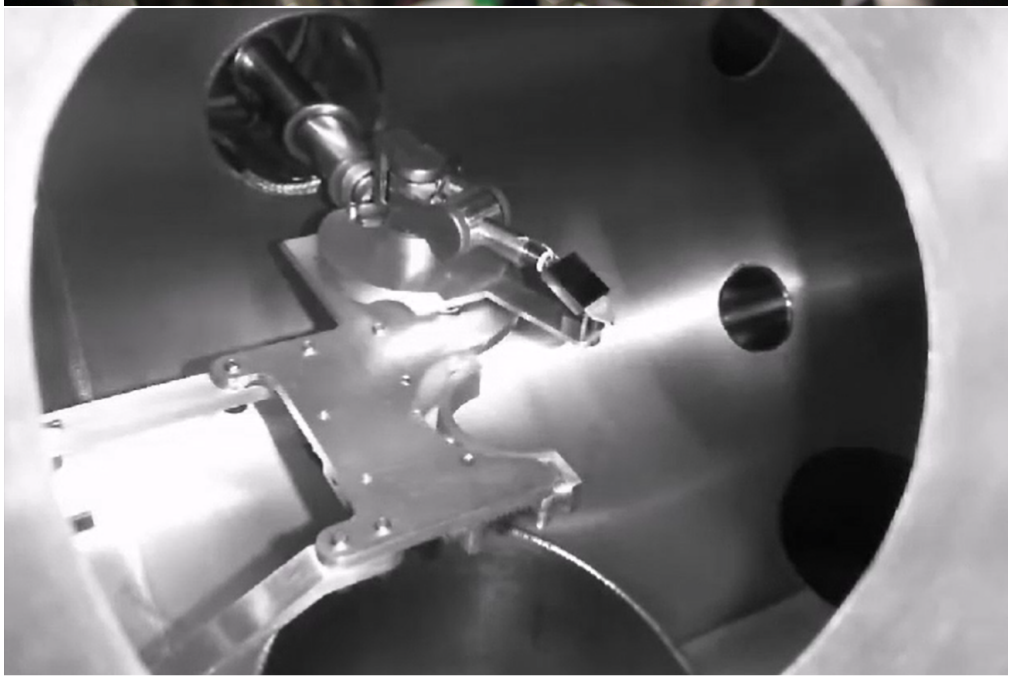

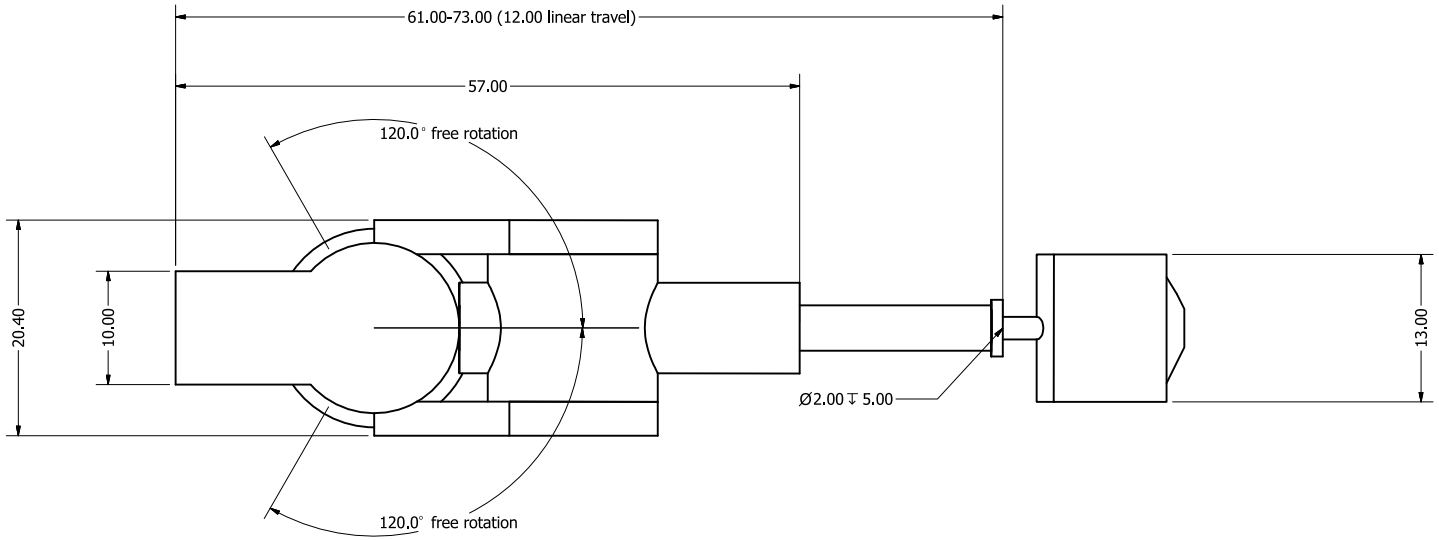

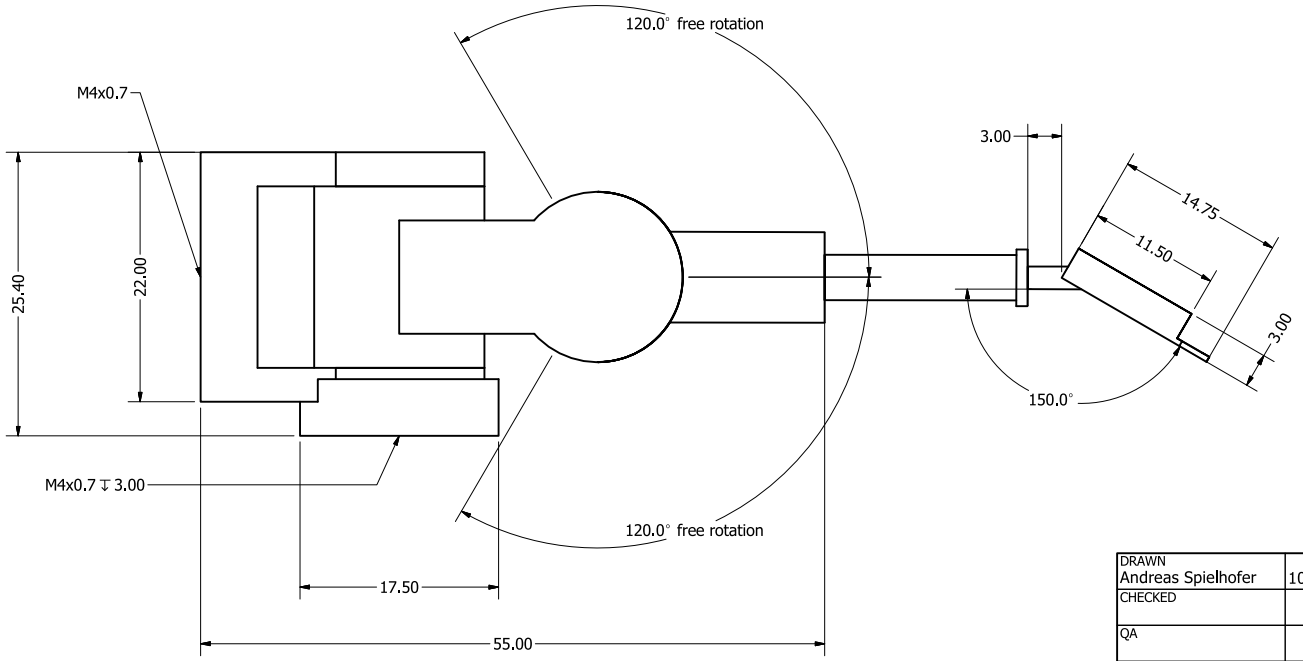

DRAWN Andreas Spielhofer	10/01/2014	SPM Grutter group
CHECKED		TITLE: Kleindiek MM3A Micromanipulator with Capres Chipholder Extension
QA		
MFG		
APPROVED		
		SIZE C | DWG NO Assembly-Micromanipulator-MM3A | REV
		SCALE 3 : 1 | SHEET 1 OF 1

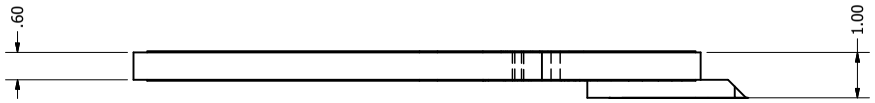

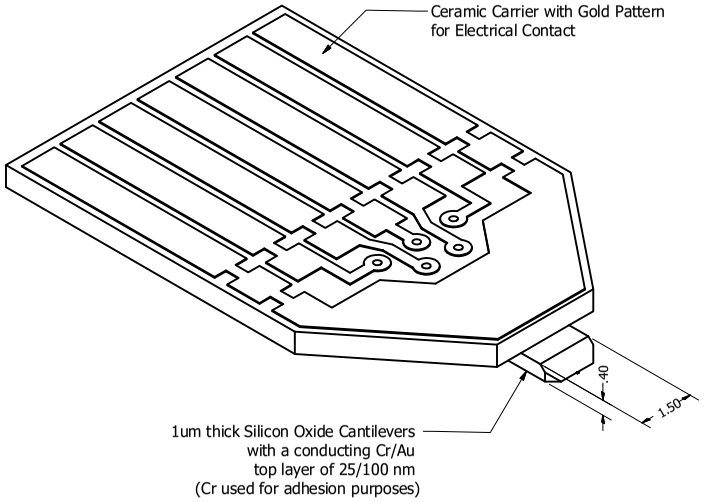

Electrode Spacing: - 5, 10, 15, 20, 25 and 30 um
Cantilever Spring Constants: 1-10 N/m

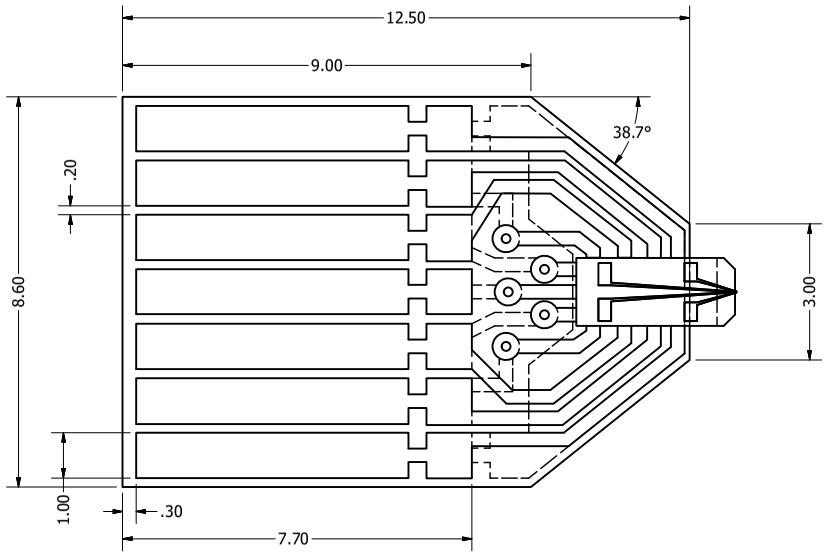

In case you are going to design your own chips, use the dimensions given here to make sure the chip fits into the chipholder!

DRAWN Andreas Spielhofer	10/17/2016	SPM Grutter group
CHECKED		TITLE
QA		Capres Micro Four Point-Probe Chip Holder
MFG		
APPROVED		
		SIZE C / DWG NO CapresChip / REV
		SCALE 12 : 1 / SHEET 1 OF 1

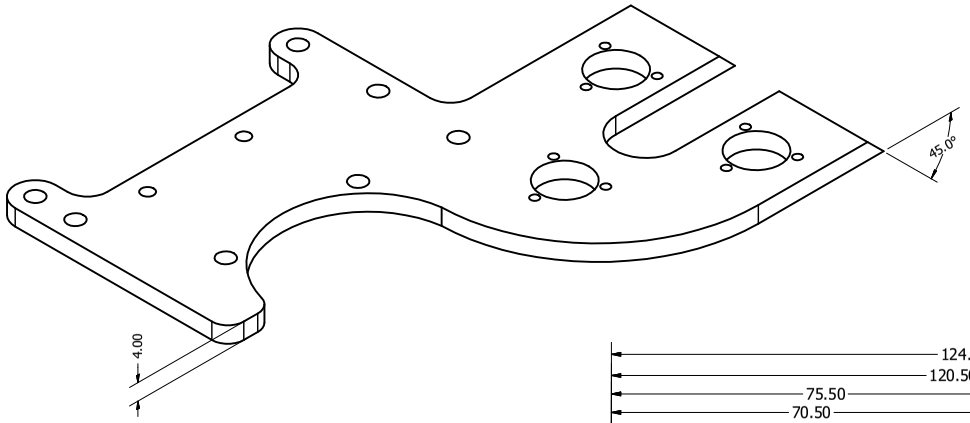

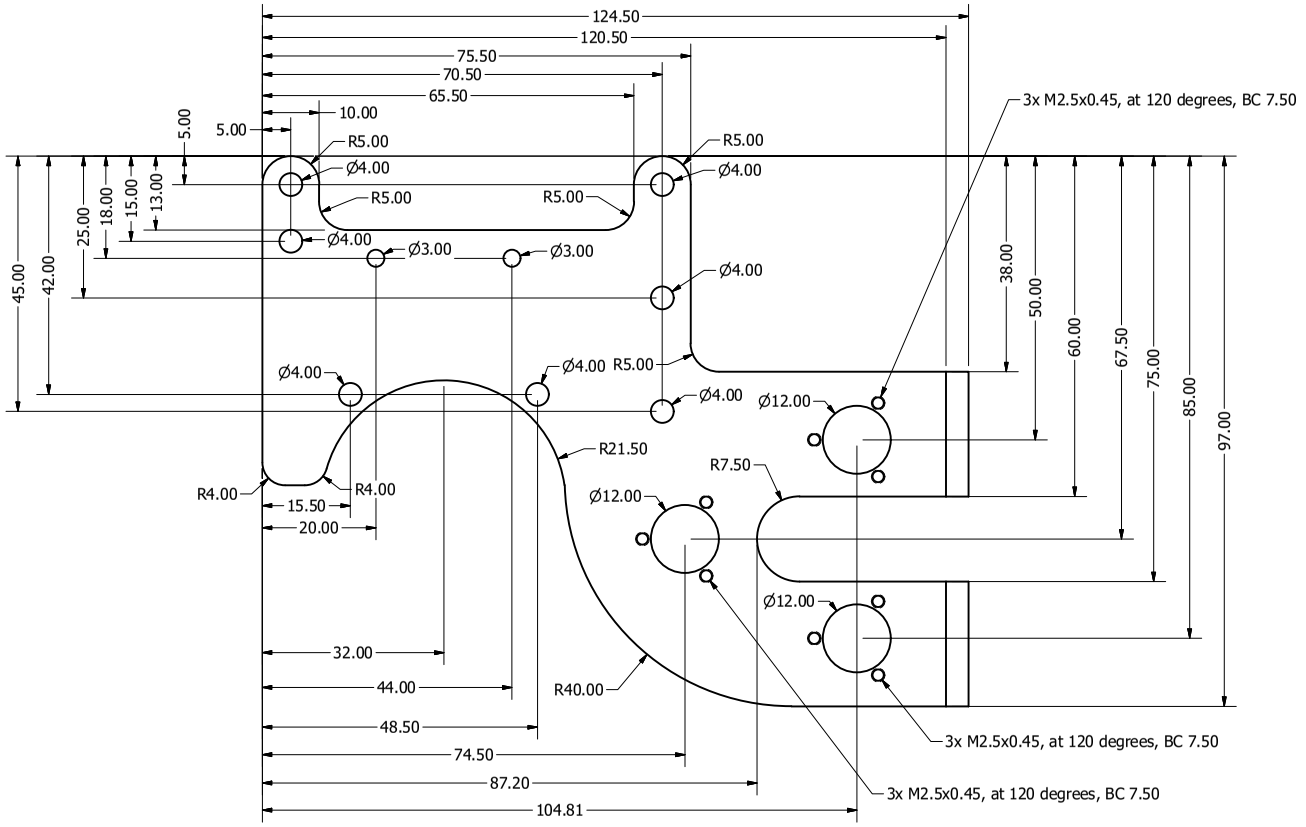

DRAWN Andreas Spielhofer	01/23/2016	Grutter SPM group
CHECKED		TITLE: Base Plate for Four Point-Probe inside the UHV preparation chamber
QA		
MFG		
APPROVED		
		SIZE C | DWG NO Block | REV
		SCALE 1.5 : 1 | SHEET 1 OF 1

Rod #1:

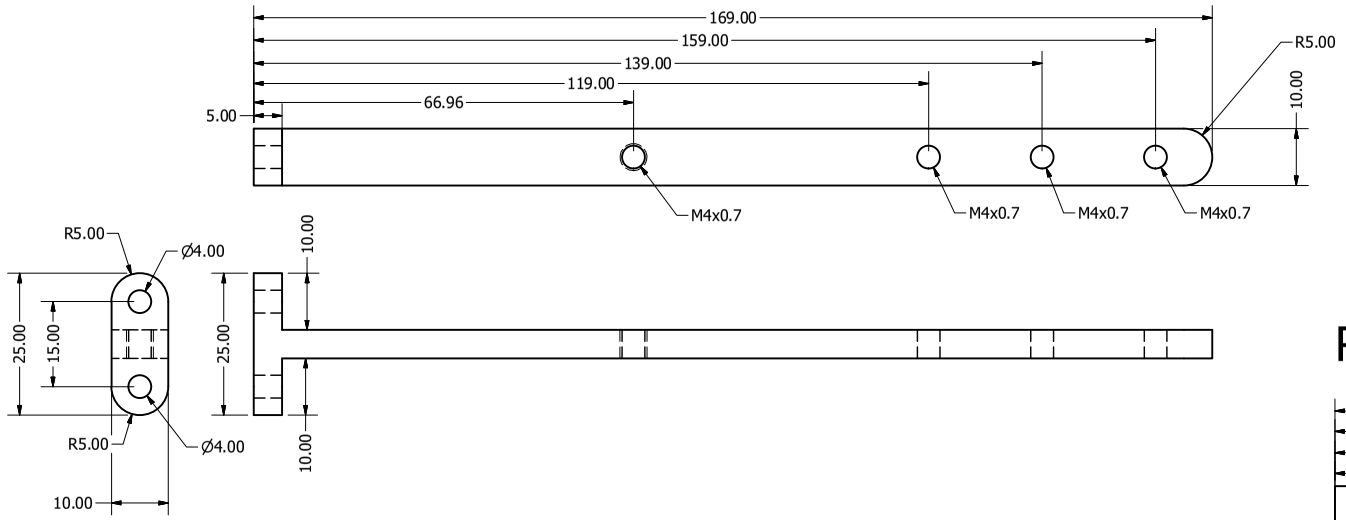

Rod #3:

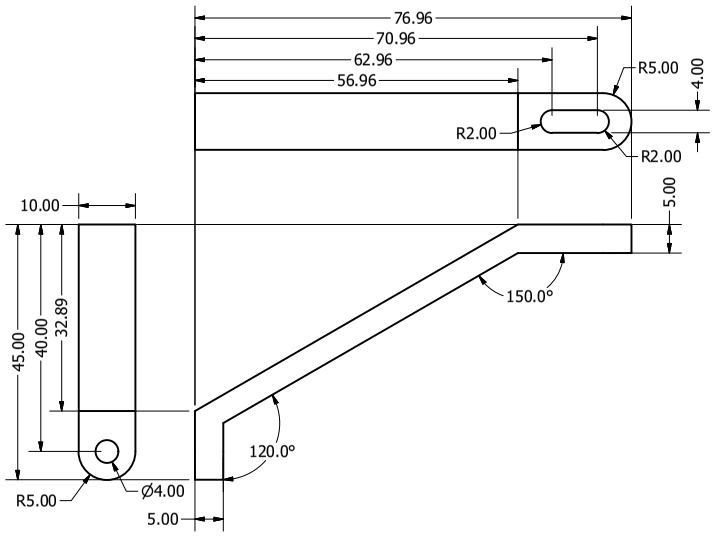

Rod #2:

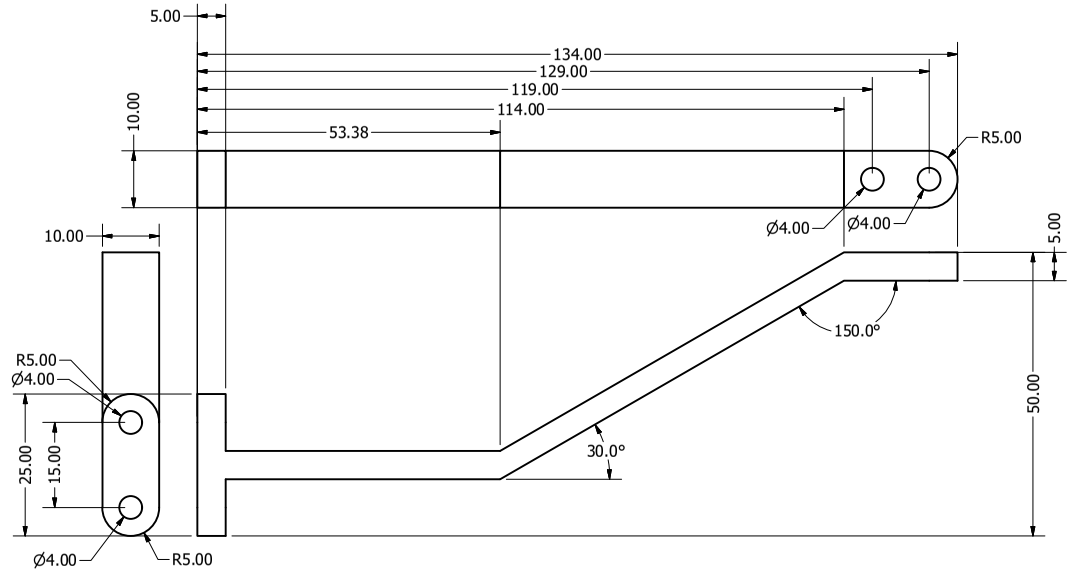

DRAWN Andreas Spielhofer	01/23/2016	Grutter SPM group
CHECKED		TITLE
QA		Rod Extensions to attach the Base Plate of the Four Point-Probe to the CF4-1/2 Flange
MFG		
APPROVED		
		SIZE C / DWG NO FlangetoBase / REV
		SCALE 1.5 : 1 / SHEET 1 OF 1

Spring Loader Assembly

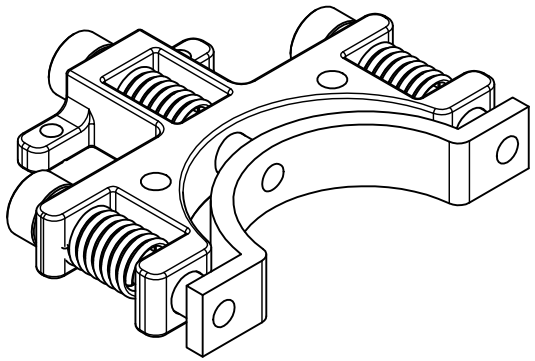

Spring Loader Part #1:

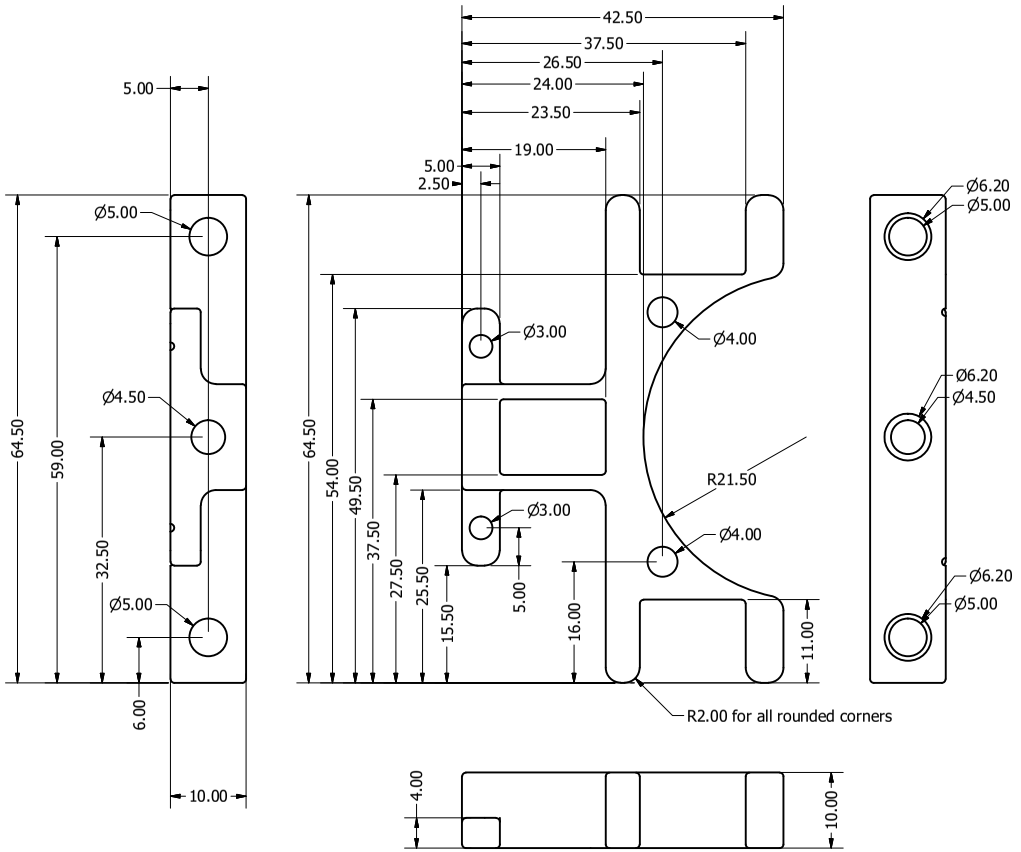

Spring Loader Part #2:

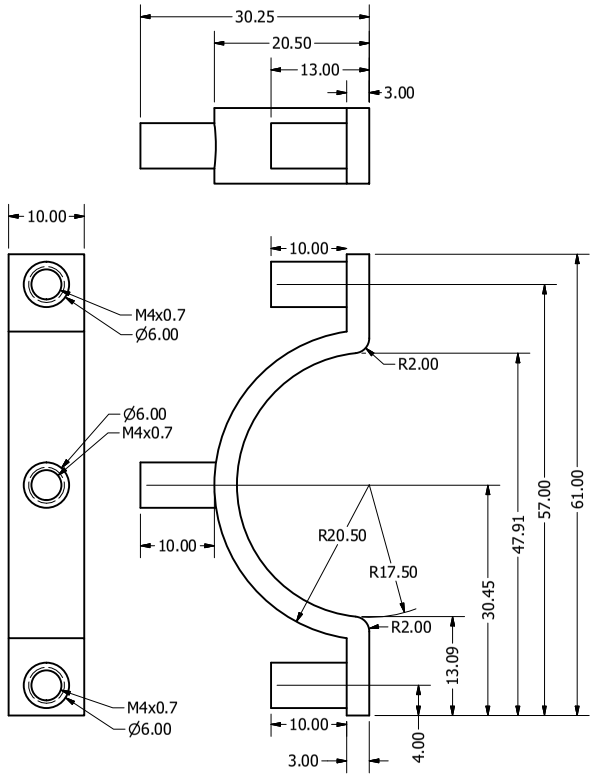

DRAWN Andreas Spielhofer	01/23/2016	Grutter SPM group
CHECKED		
QA		TITLE: Spring Loader Assembly. Pushes the UHV Design Multicentre Manipulator towards the Base Plate; for stabilization
MFG		
APPROVED		
		SIZE C / DWG NO SpringLoaderassembly / REV
		SCALE 2 : 1 / SHEET 1 OF 1

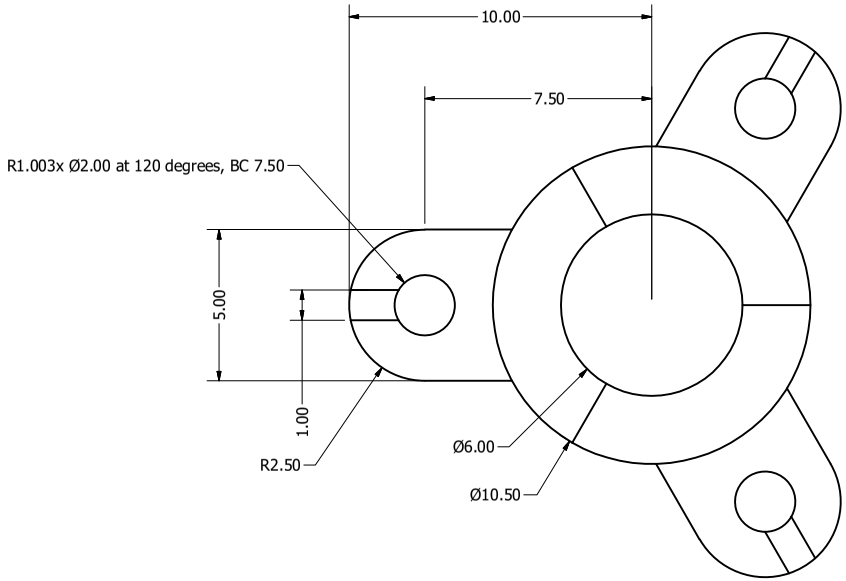

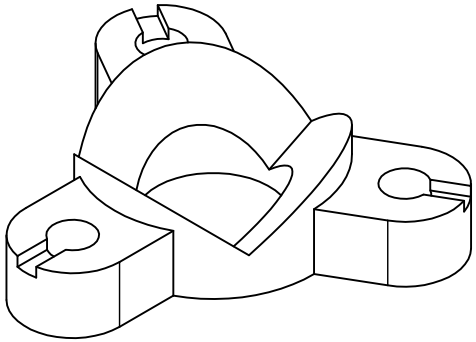

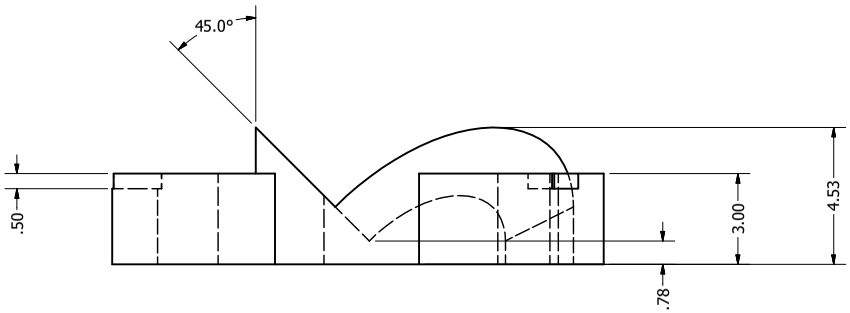

DRAWN Andreas Spielhofer	01/23/2016	Grutter SPM group
CHECKED		TITLE: Conical Kinematic Ball Holder at an Angle of 45 degrees.
QA		
MFG		
APPROVED		
		SIZE C | DWG NO Ball_Holder | REV
		SCALE 8 : 1 | SHEET 1 OF 1

Assembly Drawing

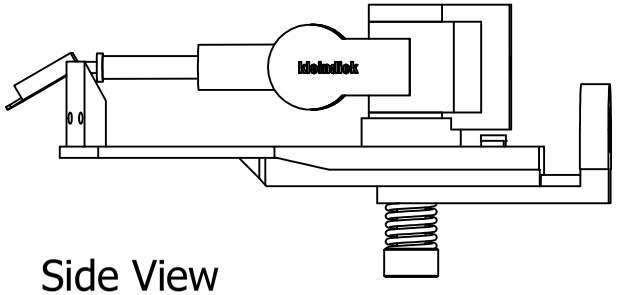

Side View

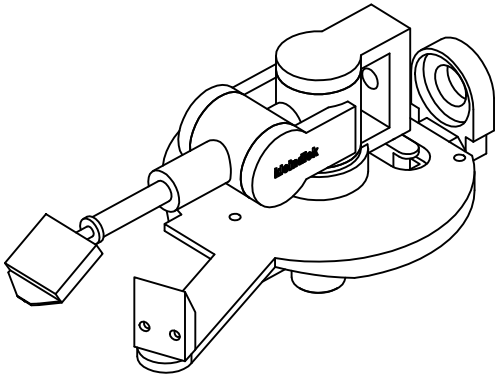

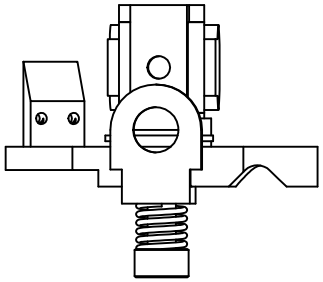

Back View

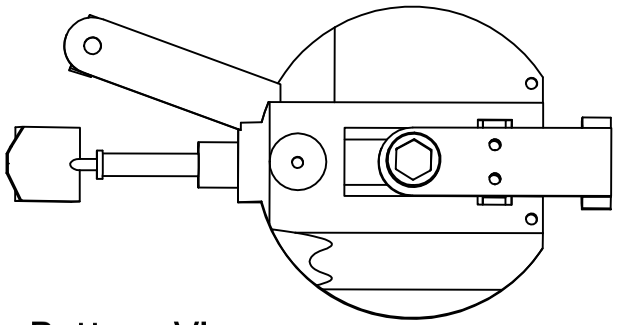

Bottom View

DRAWN Andreas Spielhofer	01/23/2016	Grutter SPM group	
CHECKED		TITLE Spring Loaded Kinematic Connector Assembly for Kleindiek MM3A Micromanipulator	
QA			
MFG			
APPROVED			
		SIZE C	DWG NO SpringLoaded_Manipulator_Assembly
		SCALE 1.5: 1	SHEET 1 OF 1

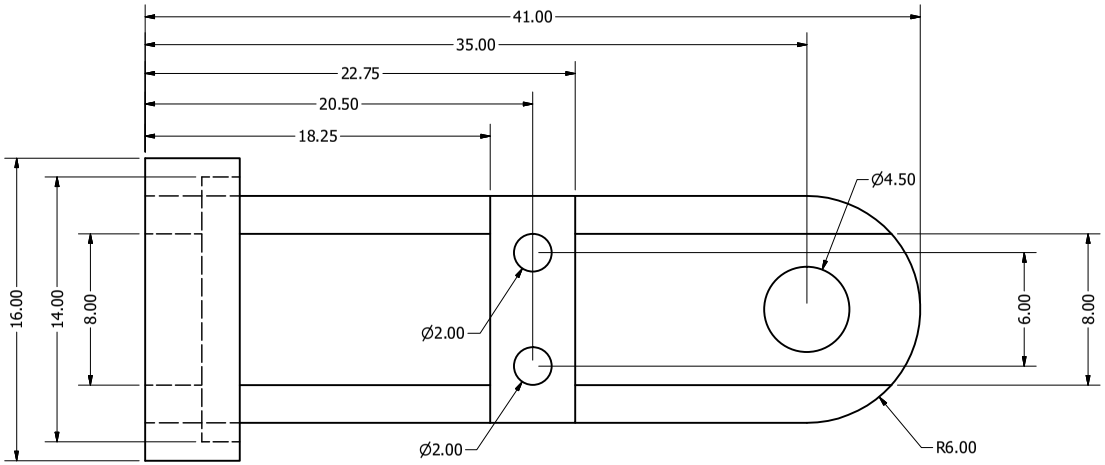

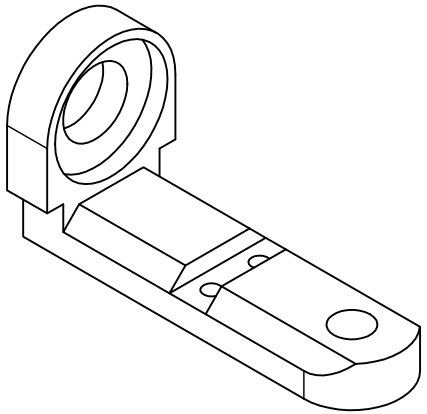

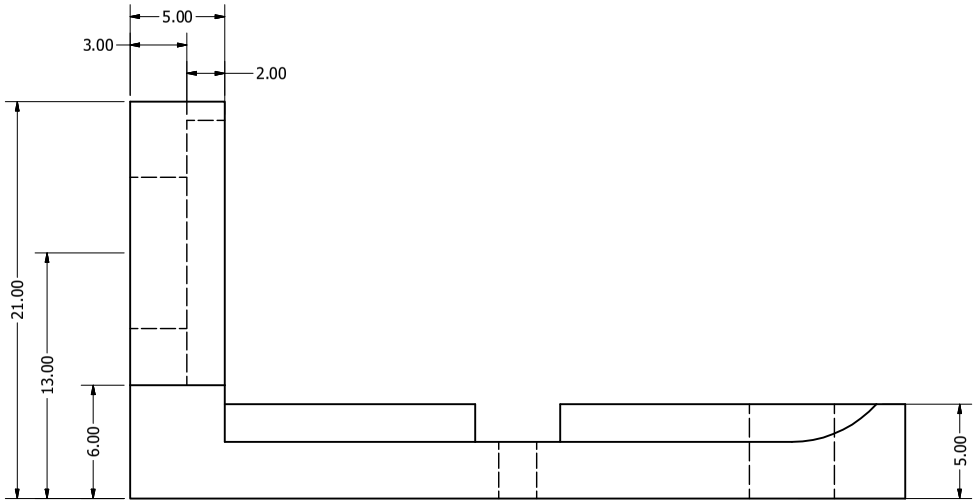

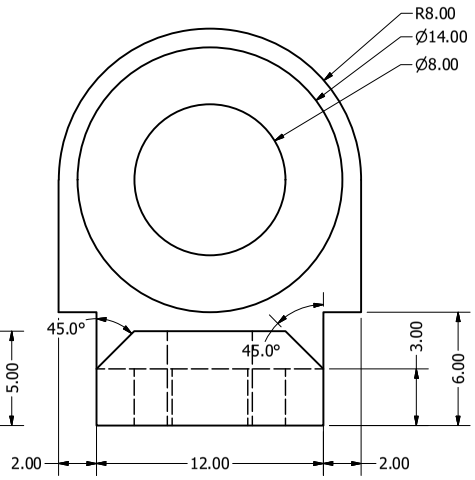

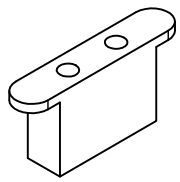

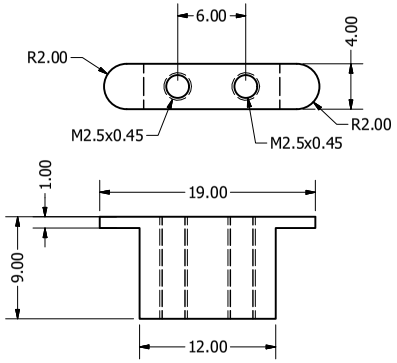

DRAWN Andreas Spielhofer	01/23/2016	Grutter SPM group
CHECKED		TITLE: Holder allowing to transfer the Micromanipulator inside the UHV Chamber. Will be mounted directly on a Linear Rotatable Transfer Arm
QA		
MFG		
APPROVED		
		SIZE C | DWG NO Pull_Assembly | REV
		SCALE 3 : 1 | SHEET 1 OF 1

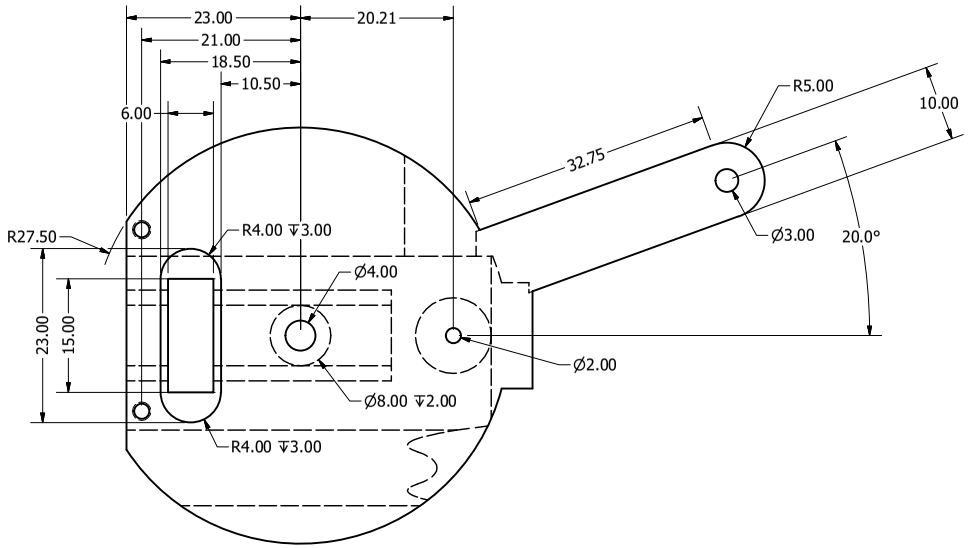

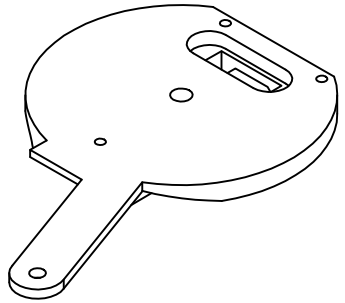

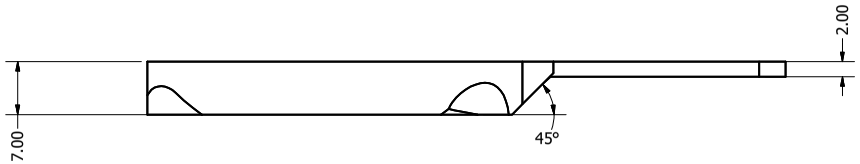

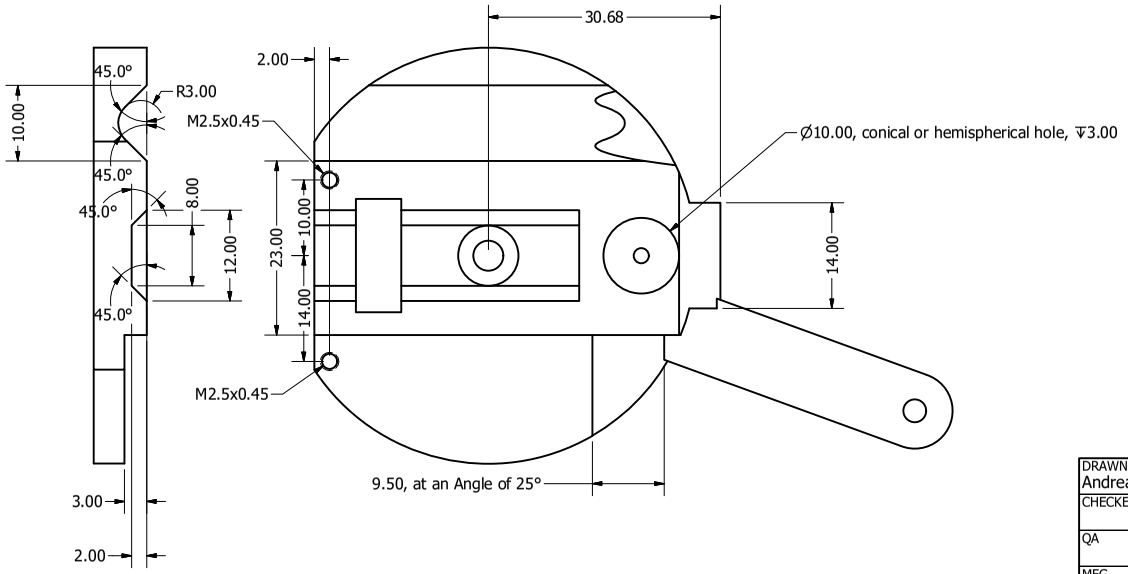

DRAWN Andreas Spielhofer	01/23/2016	Grutter SPM group
CHECKED		TITLE: Kinematic Connection Base Plate for Micromanipulator. The Base Plate will sit on 3 Spheres creating a well-defined Position relative to the Sample.
QA		
MFG		
APPROVED		
		SIZE C | DWG NO Upper_Kinematic_connector | REV
		SCALE 2 : 1 | SHEET 1 OF 1

A.3. JEOL Sample Holder - Modifications

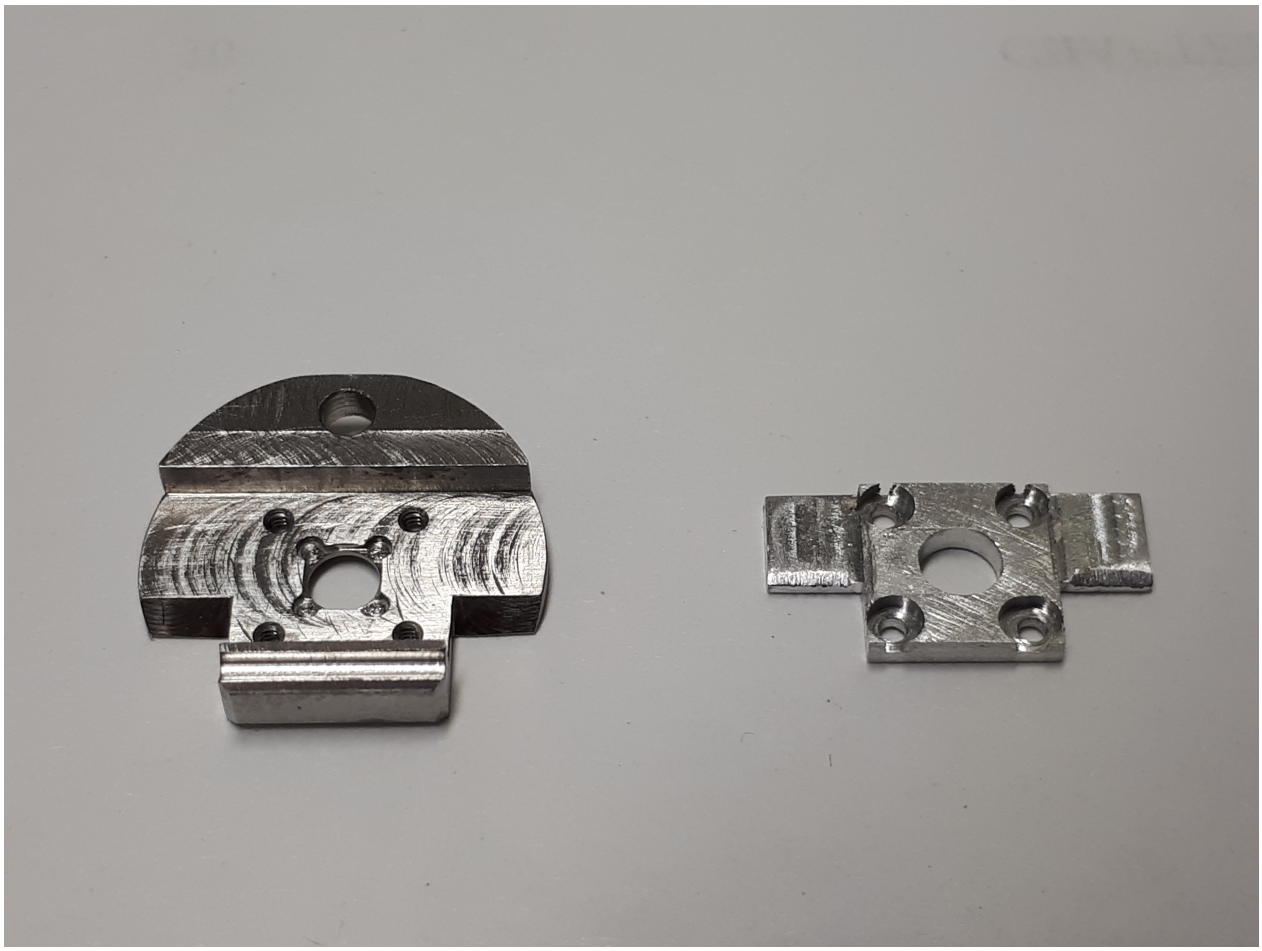

Figure 62: Modified JEOL sample holder. The modifications allow to mount 3 cm × 3 cm CVD diamond substrates and allowing optical and THz Laser to propagate through the sample.

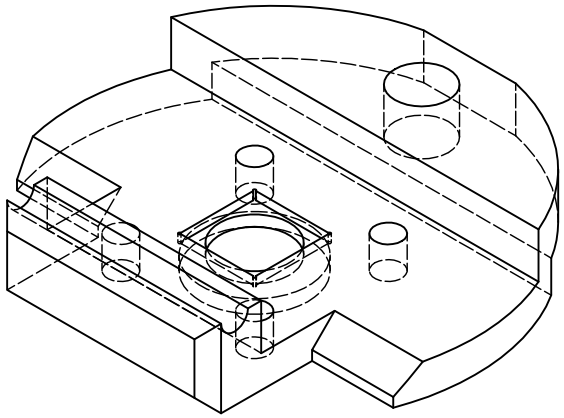

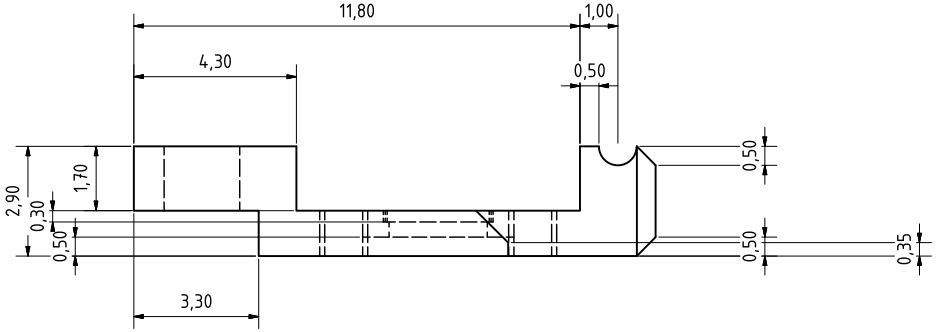

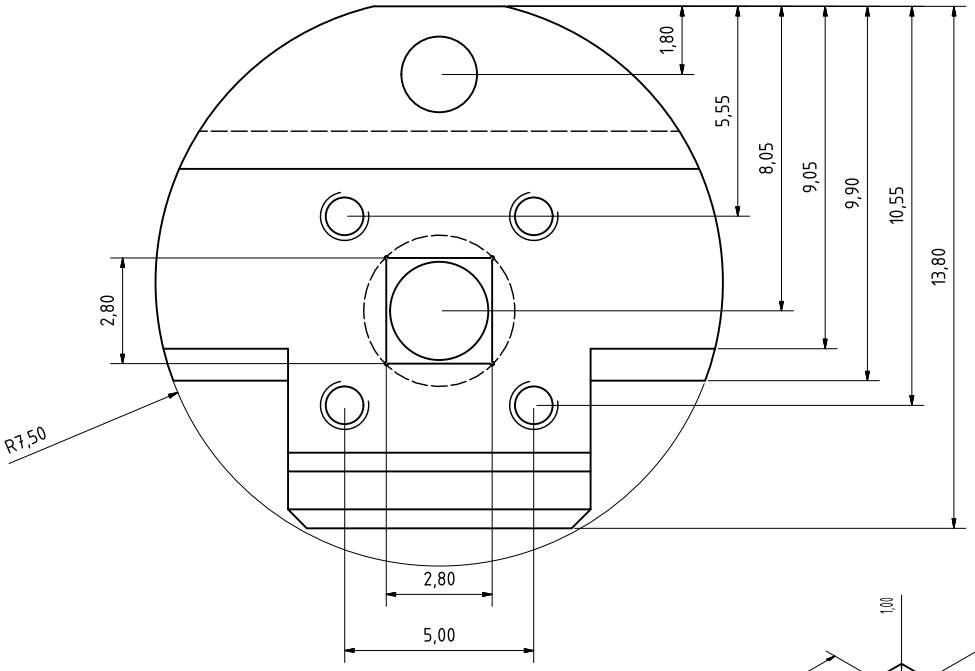

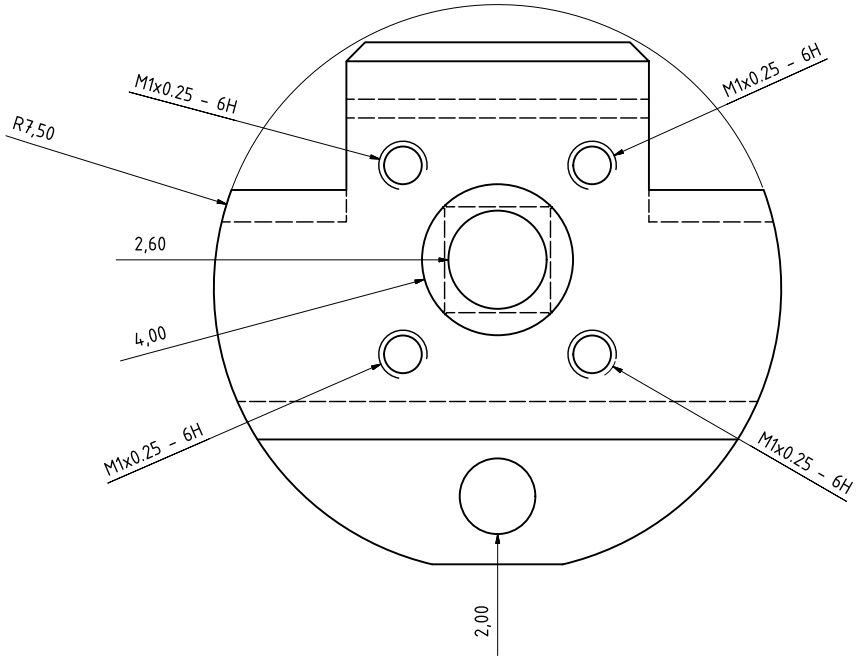

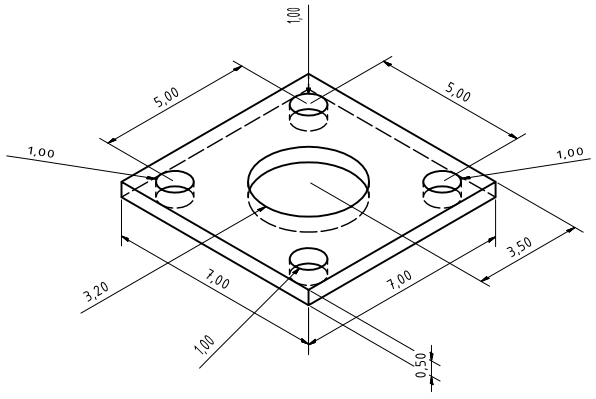

DRAWN Andreas Spielhofer	05/06/2014	Grutter SPM group
CHECKED		TITLE: Jeol Sample Holder, to hold a 3mmx3mm 0.3mm thick diamond substrate; fits into Jeol System, Suitcase and on Sample Puck
QA		
MFG		
APPROVED		
		SIZE C / DWG NO Sample Holder Jeol System / REV fina 2
		SCALE / SHEET 1 OF 1

Important Note:
This extension is needed if you want to transfer the sample to the JEOL UHV AFM!

Without this extension, you will have two issues:
1.) You can't approach the AFM on the substrate due to the very short coarse approach range of the Jeol System (a few 100um).
The sample surface always needs to be flushed with the top of the sample holder.
2.) Without this extension, the sample can't be properly clamped inside the boat with the springs, and a sample tranfer is almost impossible.

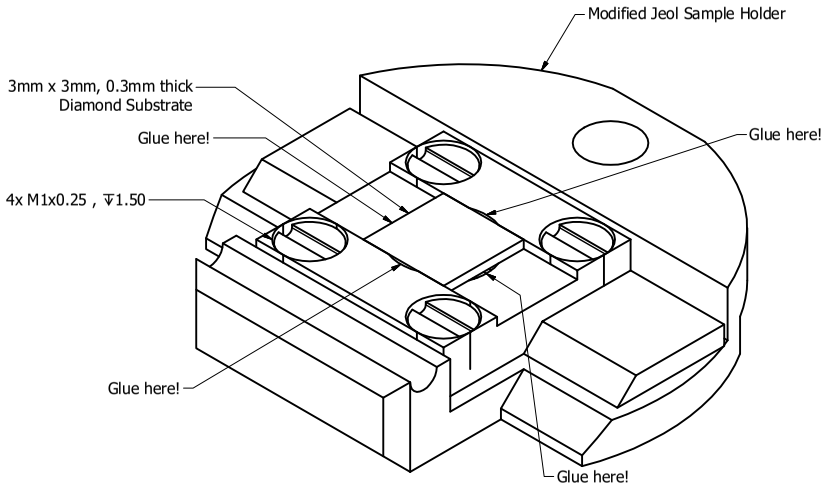

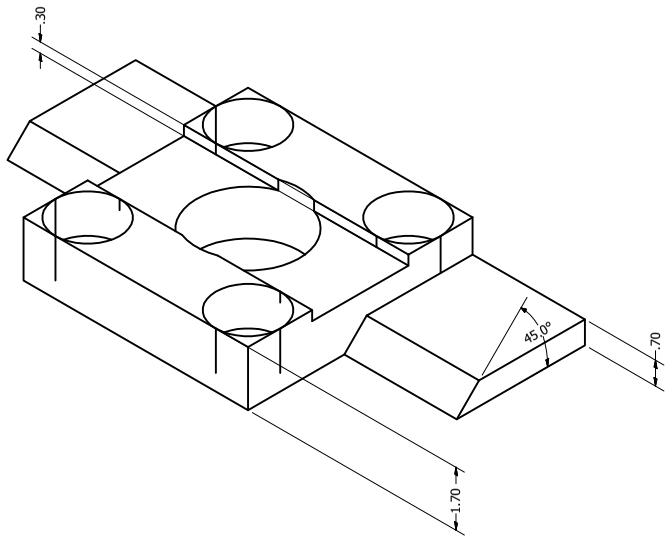

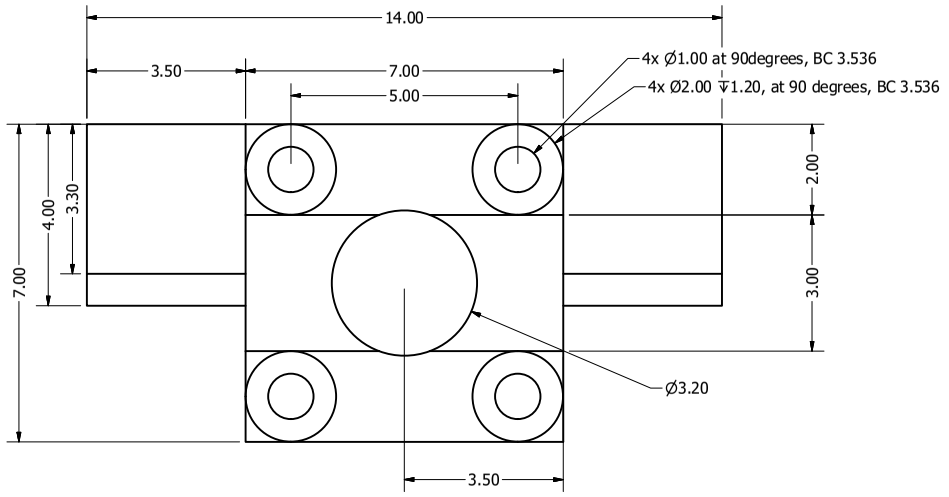

DRAWN Andreas Spielhofer	08/08/2016	Grutter SPM group
CHECKED		TITLE: Extension for Jeol Sample Holder; needed to be able to approach with the Jeol UHV AFM
QA		
MFG		
APPROVED		
		SIZE C | DWG NO Jeol_Sample_Holder_Extension | REV
		SCALE 10 : 1 | SHEET 1 OF 1

A.4. Ultra-high Vacuum Preparation Chamber Design

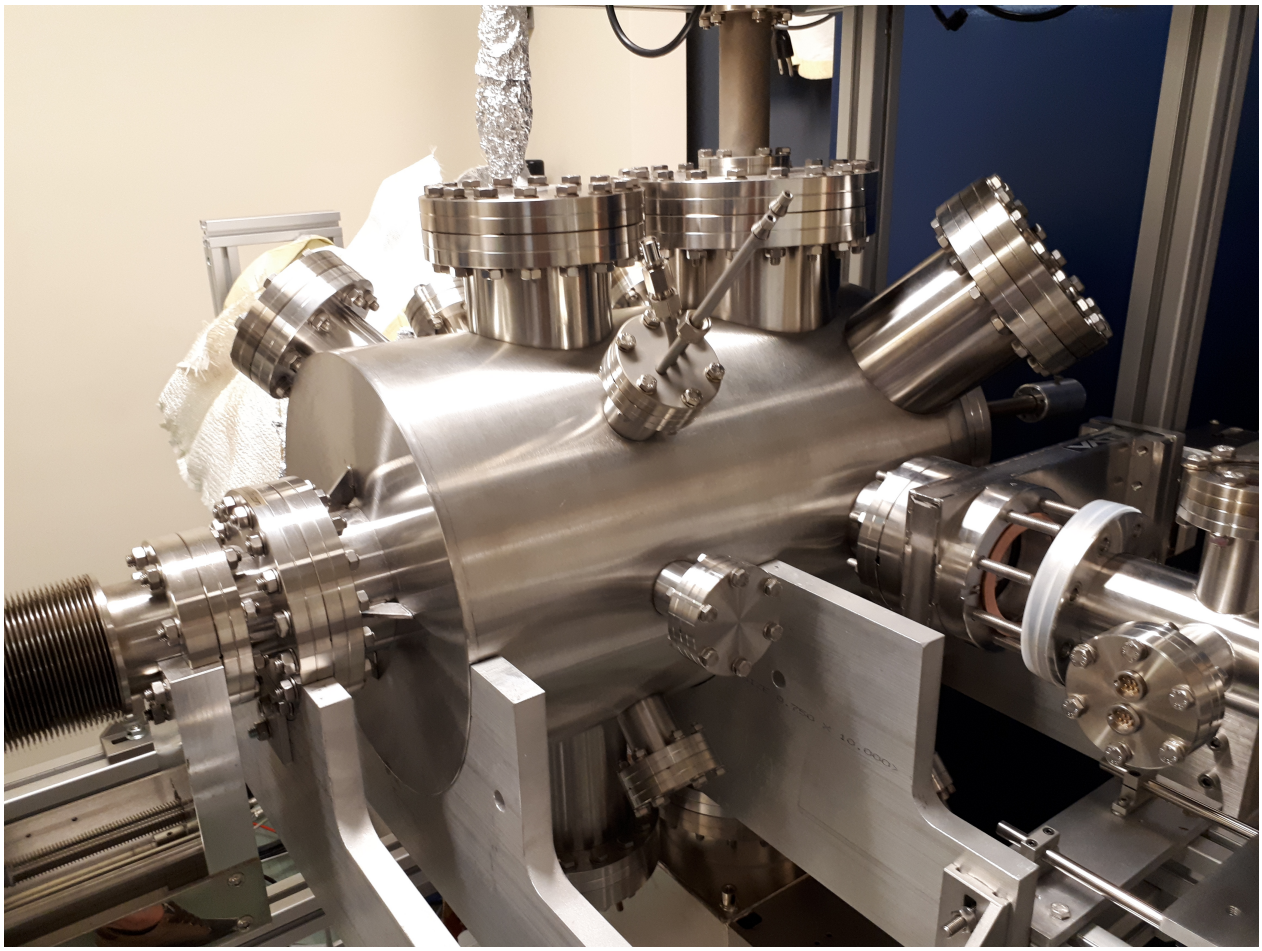

Figure 63: Custom-made chamber with enough ports to mount instruments to manipulate, prepare and measure samples and to record the quality of the UHV system.

- Mounting Brackets?
- Gussets on Ports?
- 6.3" Tube?
- Orientation of Ion Pump Flange?
- Are Flange Orientations OK?

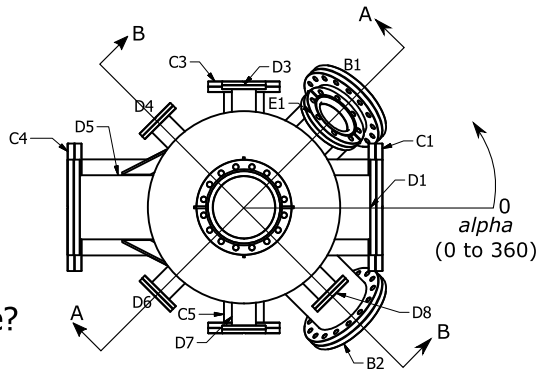

Flange Identification and Specification Table

PORT	FLANGE/BOM	TUBE	TUBE CUT LENGTH	PORT LENGTH	PORT LG TOL +/-	FOCAL LENGTH	FOCAL LG TOL +/-	FOCAL PT DATUM	FOCAL PT TOL DIA	ALPHA α	BETA β
A1	F0800X600N	SST-0600PI	1.88	-	-	-	-	-	-	-	180
A2	F0600X400N	SST-0400I	1.88	-	-	-	-	-	-	-	0
B1	F0600X400N	SST-0400I	4.22	-	-	10.44	0.13	C	1/4	45	117
B2	F0600X400N	SST-0400I	4.22	-	-	10.44	0.13	C	1/4	315	117
C1	F0800X600N	SST-0600PI	3.11	2.66	0.13	-	-	-	-	0	90
C2	F0275X150N	SST-0150I	1.84	1.87	0.13	-	-	-	-	45	90
C3	F0450X250N	SST-0250I	1.76	1.87	0.13	-	-	-	-	90	90
C4	F0800X600N	SST-0600PI	5.44	5.02	0.13	-	-	-	-	180	90
C5	F0275X150N	SST-0150I	1.84	1.87	0.13	-	-	-	-	270	90
C6	F0450X250N	SST-0250I	1.76	1.87	0.13	-	-	-	-	315	90
D1	F0600X400N	SST-0400I	2.68	2.66	0.13	-	-	-	-	0	90
D2	F0275X150N	SST-0150I	1.84	1.87	0.13	-	-	-	-	45	90
D3	F0275X150N	SST-0150I	1.84	1.87	0.13	-	-	-	-	90	90
D4	F0275X150N	SST-0150I	1.84	1.87	0.13	-	-	-	-	135	90
D5	F0600X400N	SST-0400I	5.06	5.02	0.13	-	-	-	-	180	90
D6	F0275X150N	SST-0150I	1.84	1.87	0.13	-	-	-	-	225	90
D7	F0275X150N	SST-0150I	1.84	1.87	0.13	-	-	-	-	270	90
D8	F0275X150N	SST-0150I	1.84	1.87	0.13	-	-	-	-	315	90
E1	F0450X250N	SST-0250I	2.94	-	-	9.38	0.13	D	1/4	45	60

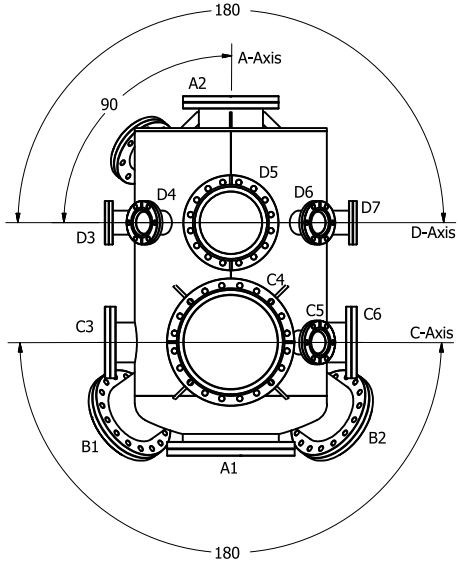

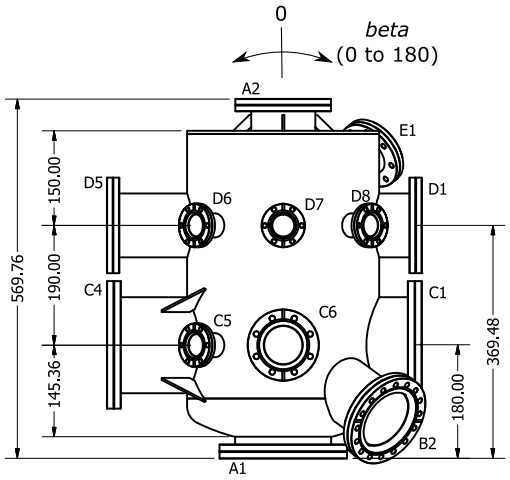

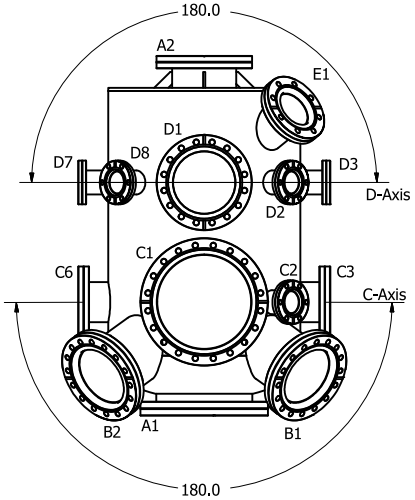

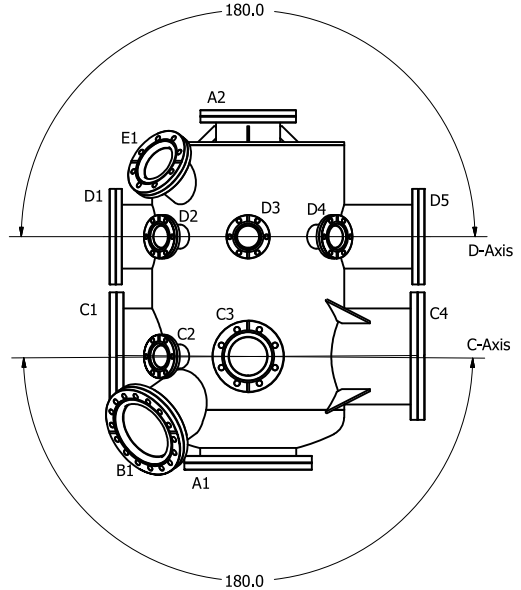

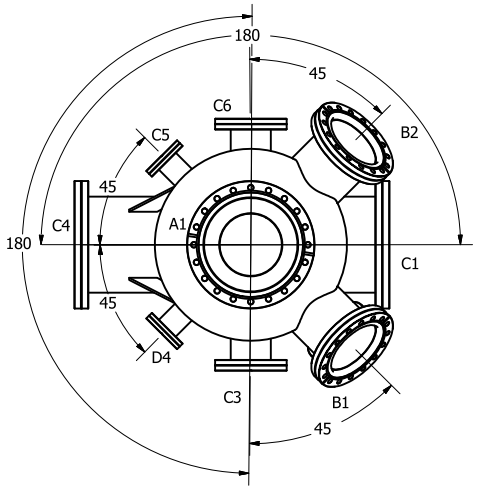

Notes:
1. All Dimensions are in millimeters [mm]
2. Orient Flanges as shown
3. Surface Finish: Brush
4. All Welds to be internal, Full Fusion
   (Vacuum Welds unless otherwise noted)
5. Vacuum Welds to be Leak Checked

DRAWN Andreas Spielhofer	2/14/2014	SPM Grutter group
CHECKED Kurt J. Lesker		TITLE
QA		UHV Preparation Chamber, Cylindrical, 12"OD x 21.6" OAL, Dome one End, 304L SS
MFG		
APPROVED		
		SIZE C / DWG NO 1/1 / REV
		SCALE 1 / 6 / SHEET 1 OF 1

A.5. Vertical Sampletransfer - Modifications

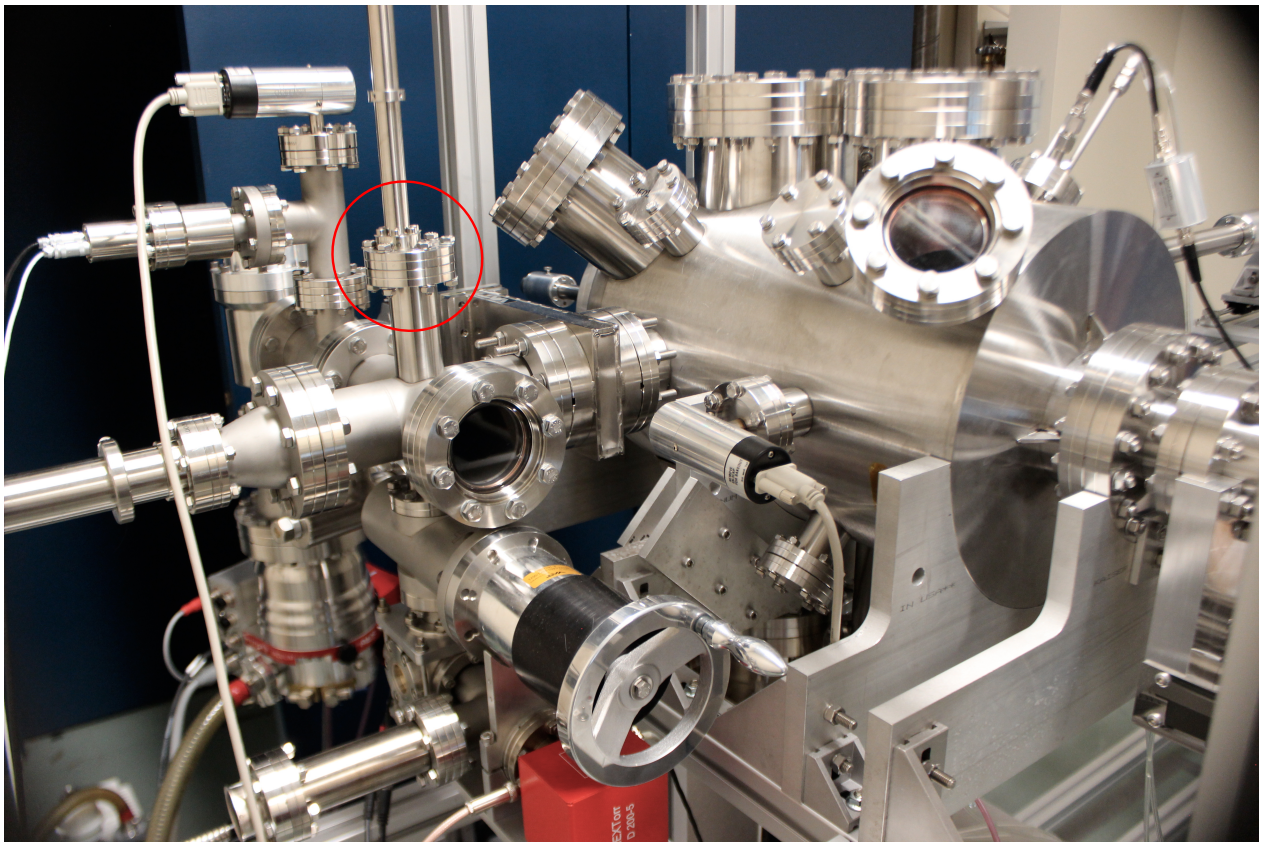

Figure 64: Modified Micrograbber (red circle) allowing to transfer the JEOL Sample Holder vertically between load-lock and UHV suitcase.

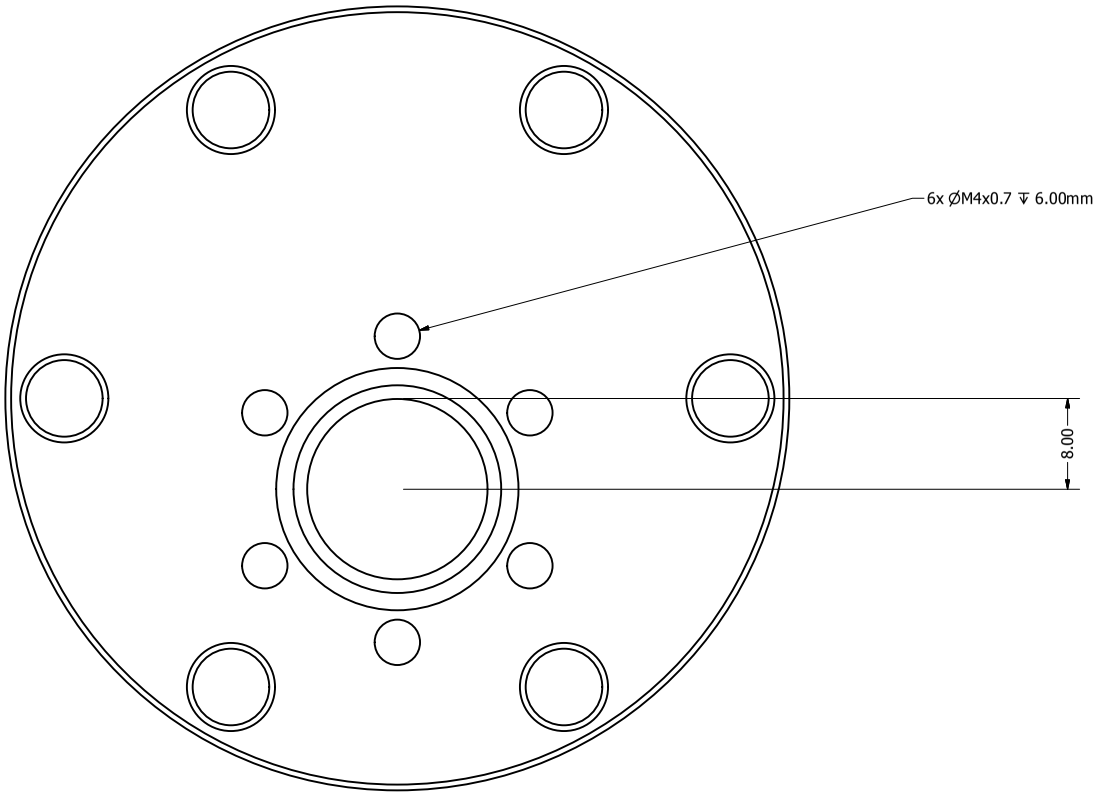

The new center position of the 1 1/3" CF flange
is 8mm off center on the 2 3/4 CF flange

Drawing of the 1 1/3" CF Flange

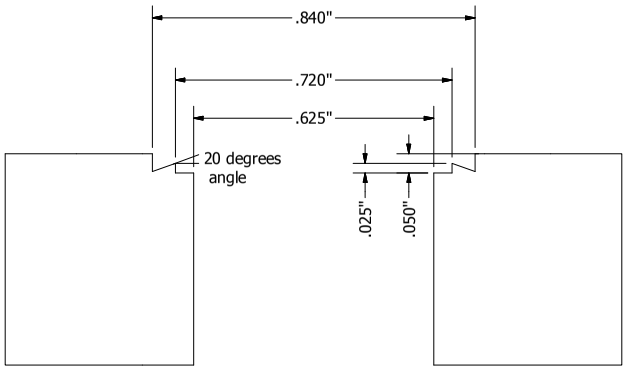

DRAWN Andreas Spielhofer	30-09-2014	Grutter SPM Group
CHECKED		TITLE
QA		1 1/3" CF Kinfe Edge, 8mm off center for transfer arm
MFG		
APPROVED		SIZE / DWG NO / REV
		SCALE

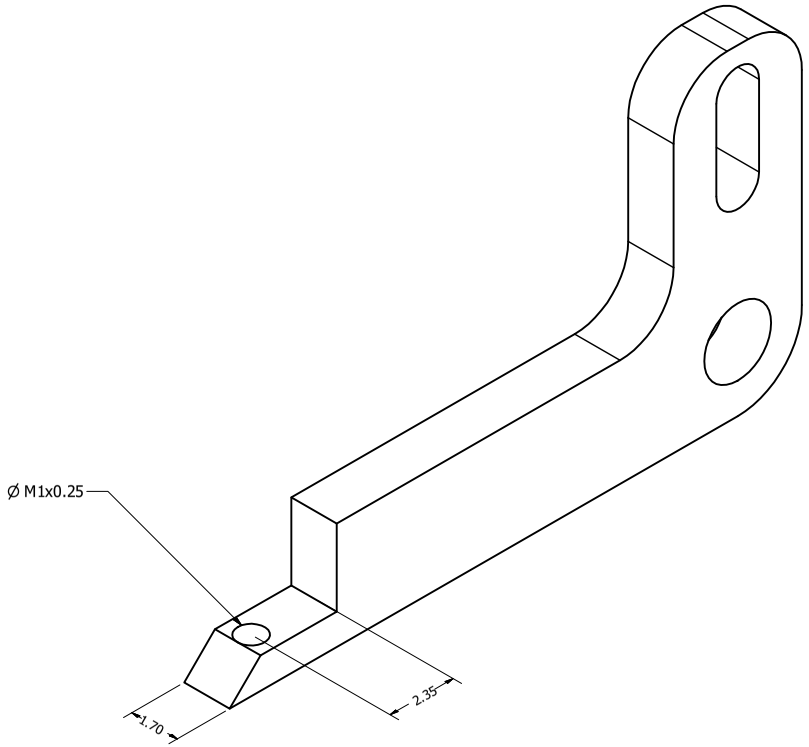

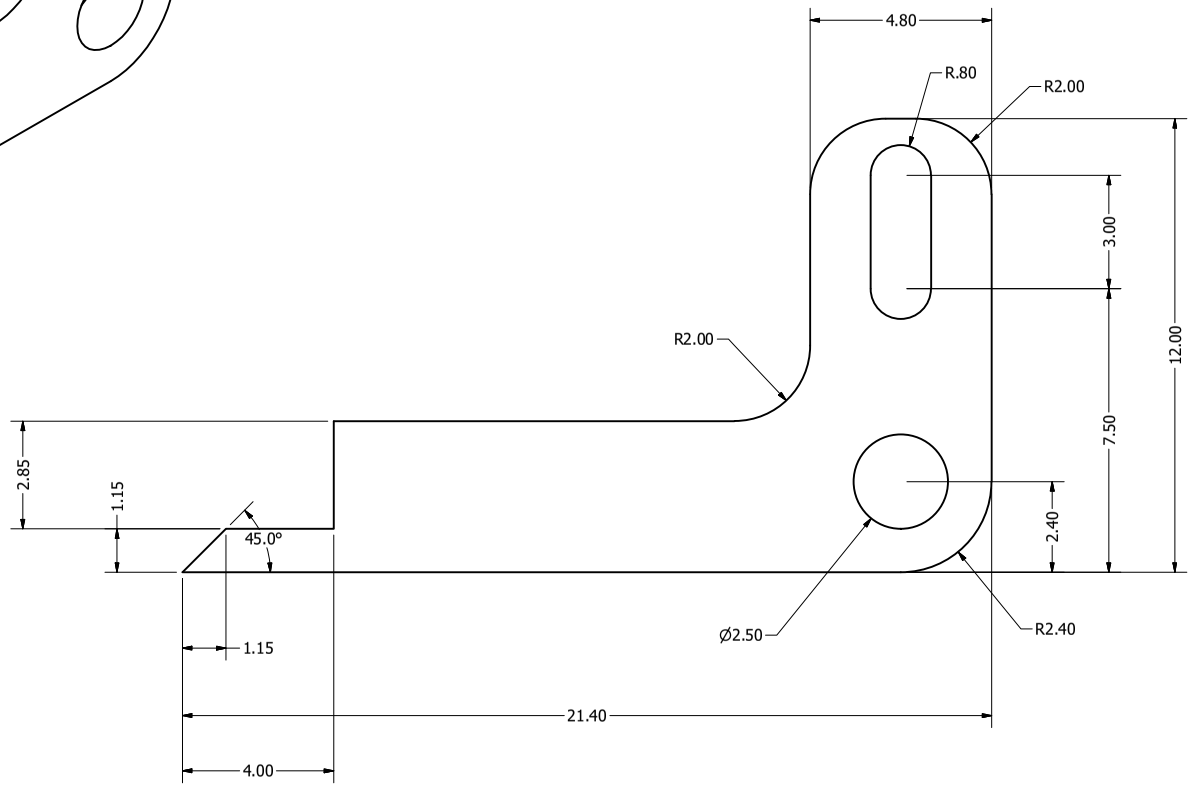

DRAWN Andreas Spielhofer	29/07/2014	SPM Grutter group
CHECKED		TITLE: Gripper Finger (Omicron, WS-PO-004-R4), modified to grip samples horizontally with a pin
QA		
MFG		
APPROVED		
		SIZE: C; DWG NO: WS-PO-004-R2 thread-2; REV
		SCALE; SHEET 1 OF 1

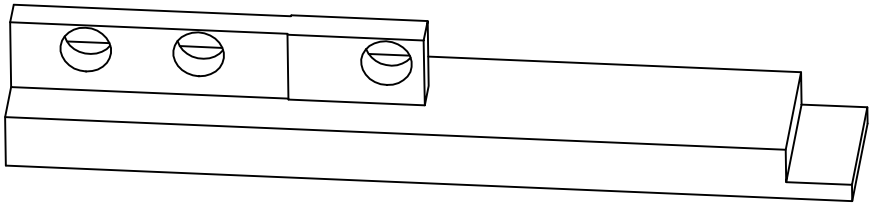

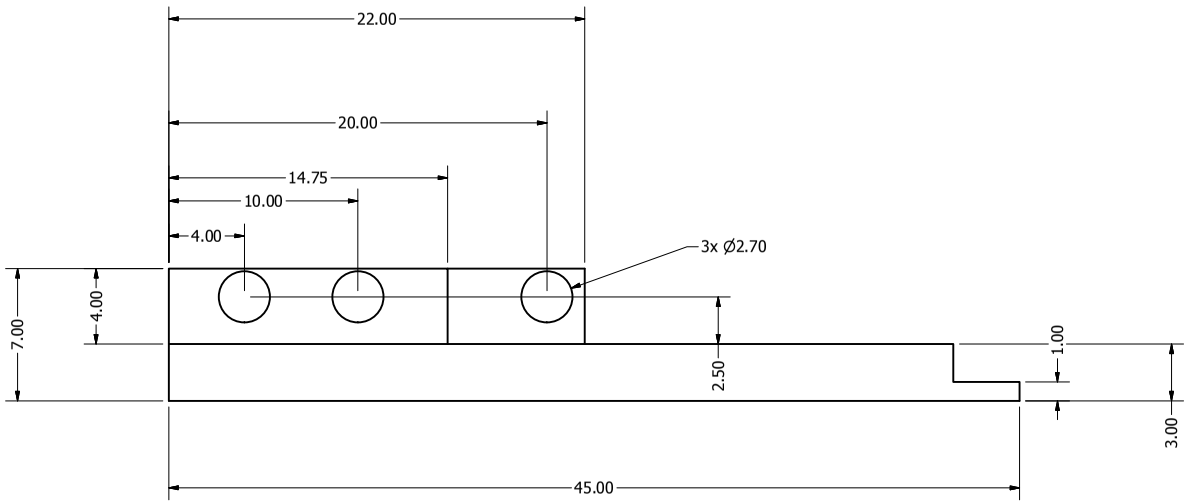

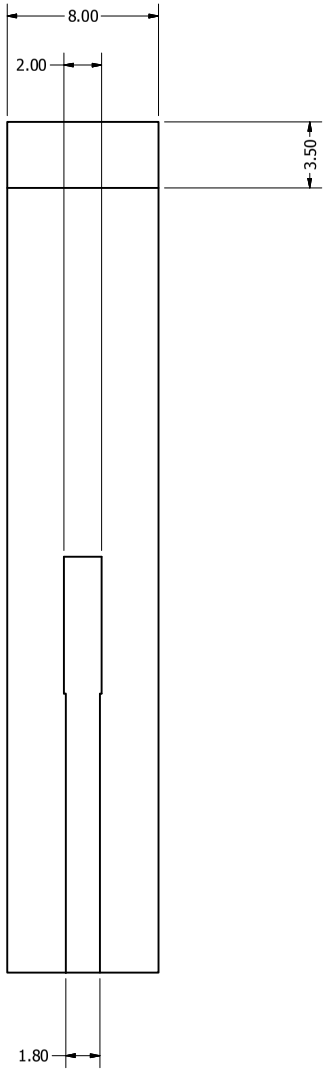

DRAWN Andreas Spielhofer	29/07/2014	Grutter SPM group
CHECKED		TITLE
QA		WS-PO-004-R4 modified Pincer Stick Base
MFG		
APPROVED		SIZE C / DWG NO WS-PO-004-R4-modificated / REV
		SCALE / SHEET 1 OF 1

B. Electronics

B.1. Four-Point Probe Multiplexer Board

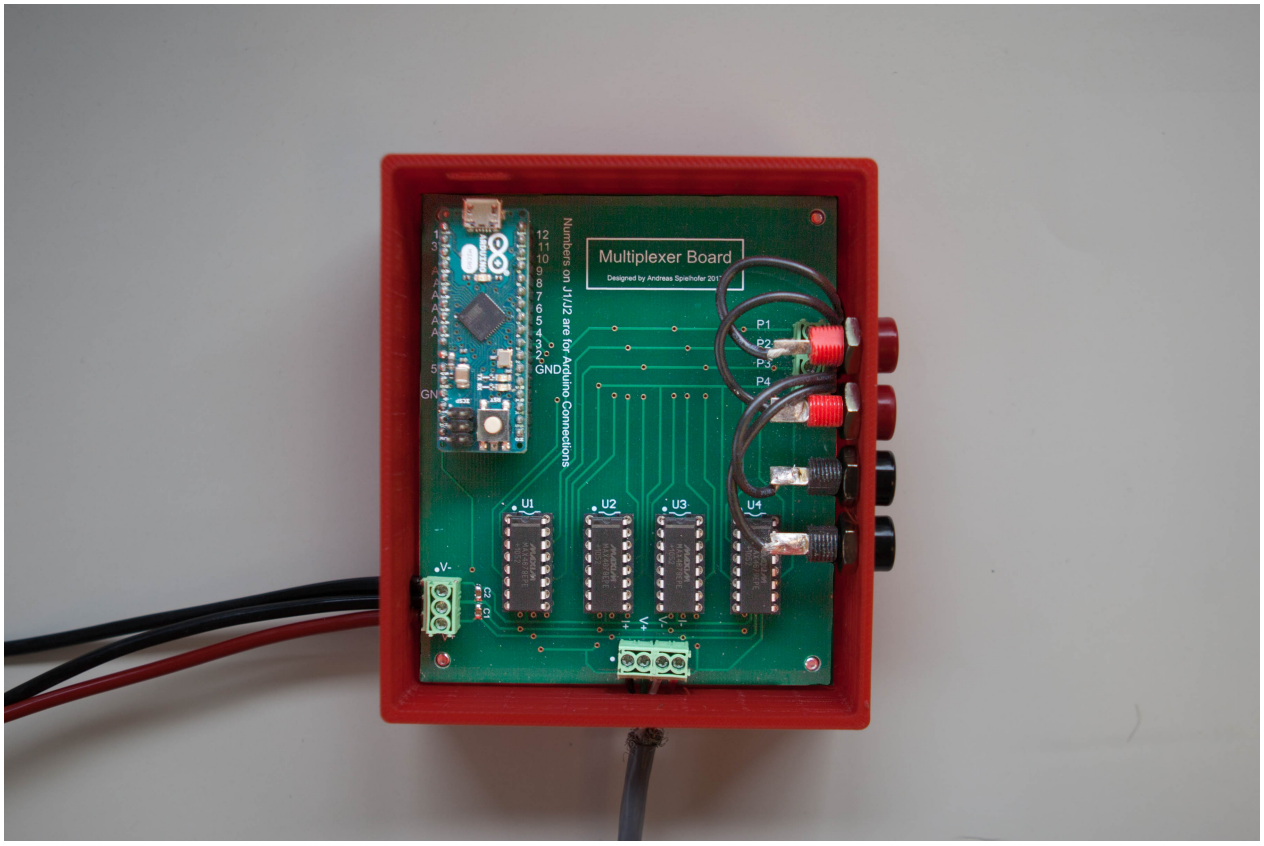

Figure 65: Home-built multiplexer board with 3D printed enclosure.

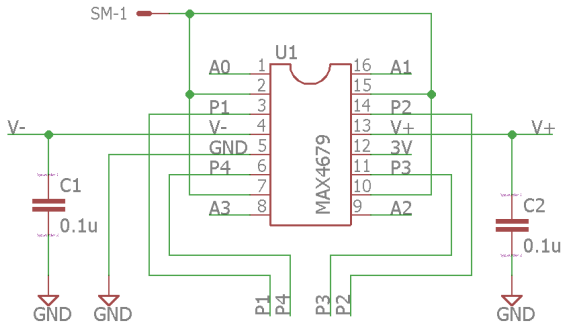

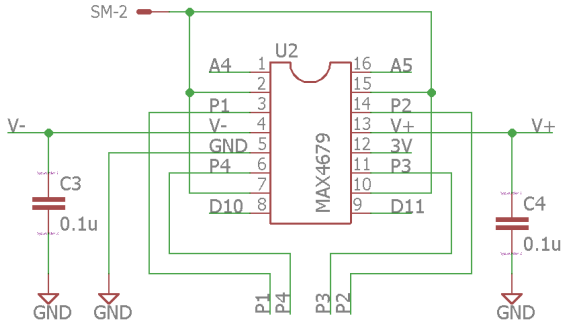

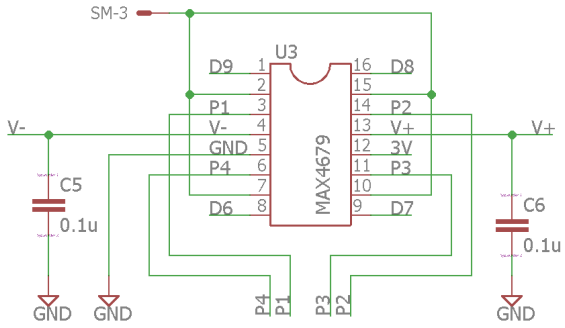

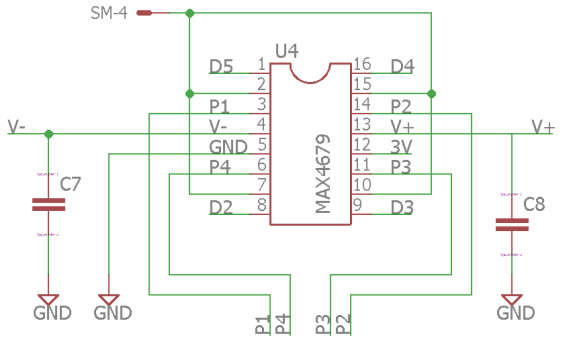

For this Project needed:
- 1x Arduino Micro 5V
- DC Power Supply
- 4x MAX4679 CMOS
- 4x Capacitor 0.1uF

Recommended Connectors:
- 4x DIP Socket 16 Pin
- 2x 2.54mm Female Header 17 Pos
- 2x Molex

Power Supply (TENMA 72-7245) Input:

SourceMeter Keithley 2400LV Input

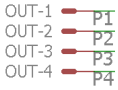

Arduino Micro 5V:

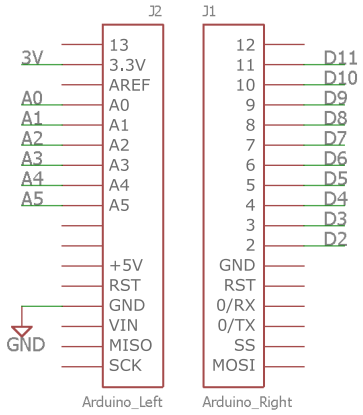

TITLE: 4PP-Switchboard	
Document Number: 4PP-Switchboard.brd	REV:
Date: 12/17/2017	Sheet: 1/1

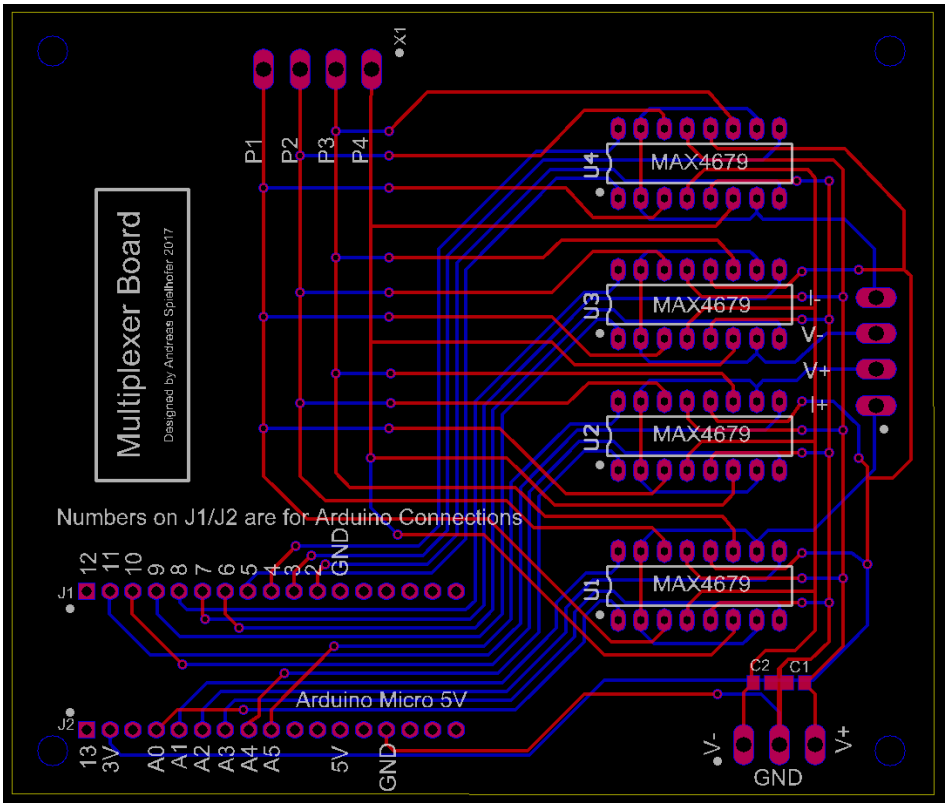

Figure 66: Eagle board design file. *Filename:* Switchboard_v6.brd. Gerber files for routing and milling can be shared upon request.

B.2. Data Logger

There are many ways how to monitor background data such as the pressure of a UHV system, the temperature of the system (e.g. for bake-out) and other relevant parameters (e.g. room temperature and humidity). Often, the data loggers are directly connected to the main computer and the data can only be accessed from this one computer and it can be tricky to access the data for example from home to quickly check the conditions of the system. Some people program little notifiers that either send email (e.g. smtplib library with Python), SMS (e.g. Twilio) or are put on e.g. Twitter (python-twitter library with Python) on a timed interval or as a timed alert. However, this data is still not well accessible if one wants to quickly plot the data and make use out of it. To record data and do make it accessible also often requires further knowledge of different programming languages that might be difficult to understand and to implement in a short amount of time.

To get around this issue, a microcontroller (in our case a Raspberry Pi) can be used as a server to both record data and to make it accessible in a very simple way to the outside. Bokeh is an interactive visualization library that targets modern web browsers for presentation. Bokeh can stream datasets in a quick and easy way from Python (or other languages) and is simple to set up. This package is used to stream data and to create a server app to visualize data with an output given in figure 67. The Raspberry Pi allows to run Python programs and many packages are nowadays available to execute a browser application that does not need further understanding of assembly, C or Java. The microcontroller further has USB ports that allows to connect to controllers that are often equipped with RS232 ports. Further, the general purpose input/output (GPIO) pins allow to set up sensor breakout boards to record e.g. temperature and humidity. Four MAX31855 K-Type Thermocouple Chips have been used to read the temperature of four thermocouples independently. K-type thermocouples are ideal to read temperatures up to 1300 °C. The chips run on 3.3 V and thus are ideal to

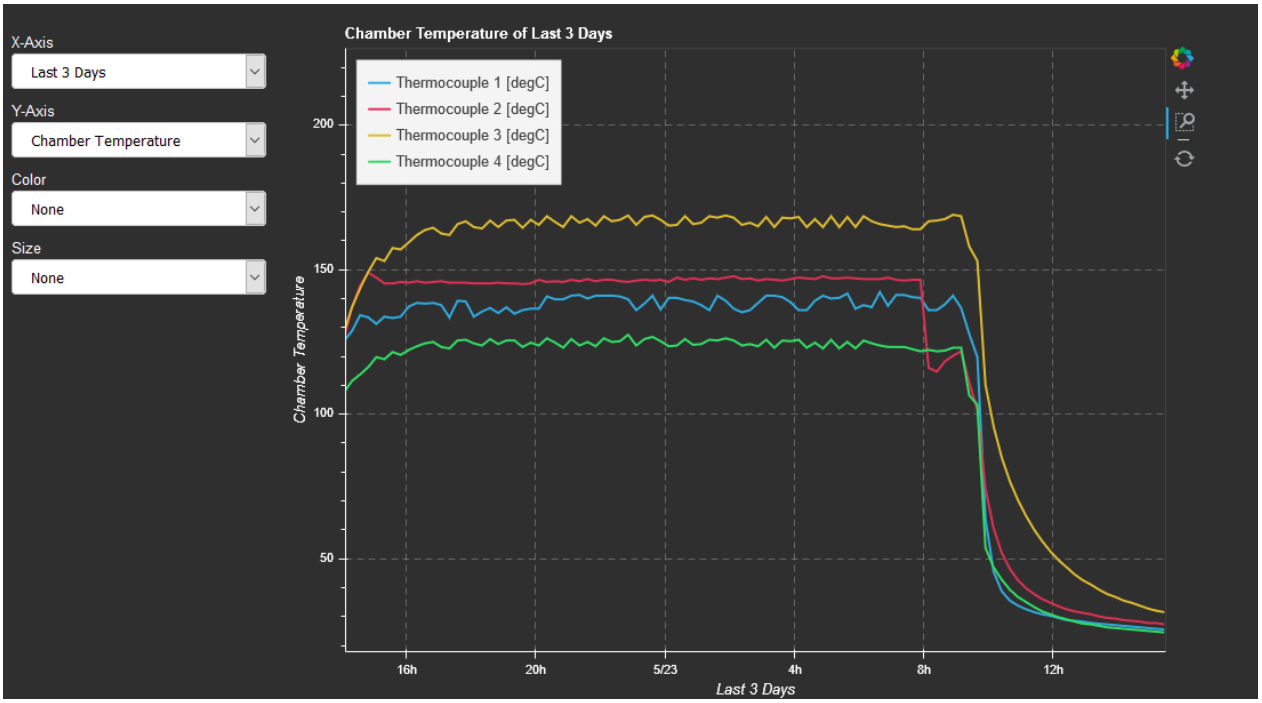

Figure 67: Browser-based graphical user interface that allows to monitor pressure, chamber temperature, room temperature and -humidity.

interface with a Raspberry Pi. The chips are set up by the SPI serial communication protocol and require a clock (CLK), chip select (CS), Master In Slave Out (MISO) port. The CS line selects a chip and the chip sends data to the MOSI port of the Raspberry Pi. This way, a single MOSI signal can be shared between all parties on the bus. A PCB was designed and the chips were soldered according to the schematics. Codes,installation instructions and gerber files for routing and milling can be shared upon request.

For this Project Needed:
- 5x MAX31855 Chips
- 5x Capacitor 0.1uF
- 5x Capacitor 10uF
- 1x DHT22 or DHT11 Sensor
- 1x 10kOhm Resistor

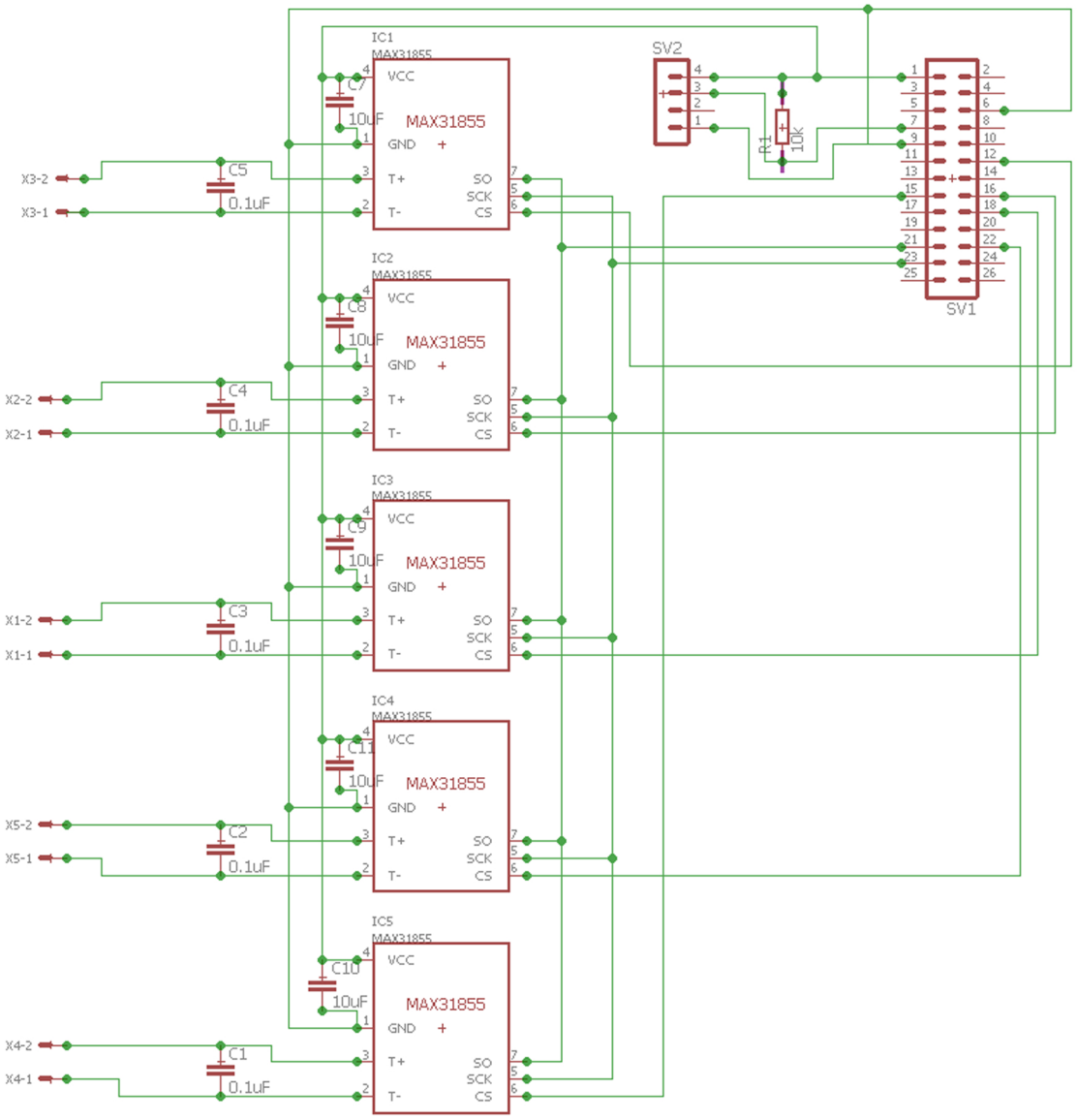

TITLE: Raspberry Pi Temperature Logger Board	
Document Number: RaspberryPiTemperatureLogger.brd	REV:
Date: 10/13/2017	Sheet: 1/1

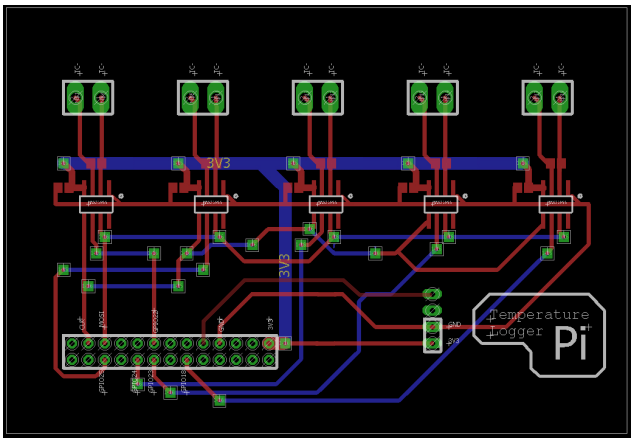

Figure 68: Eagle board design file. *Filename:* Temperature_Logger.brd. Gerber files for routing and milling can be shared upon request.

C. Serial Communication

C.1. Description

The following python codes allow to communicate the the Kleindiek MM3A Micromanipulator, the Keithley SourceMeter 2400LV, the Multiplexer Board and the MKS937 Pressure Controller. The file **__defines.py** has the relevant serial-ports and baudrates of each controller and in case there is a communication problem with the controllers, only this file needs to be adjusted by changing the ports to the right one. This is technically easy to solve by scanning automatically through the ports and try to connect and compare the identity of the controller with what is expected. This serial scanner however has brought more harm than good and thus the ports were hard-coded. However, if interested, the serial scanning script can be shared upon request. Since the communication protocols presented here are the backbone of the bigger GUI (explained in appendix E.3), I decided to add them to here. It should be simple to adapt the codes to other purposes. The codes were successfully tested and used on a Windows 7 64-bit machine.

```
# -*- coding: utf-8 -*-
"""
Created on Fri Jul 14 18:18:26 2017

@author:    Andreas Spielhofer
            Ph.D. Candidate
            Physics Departement
            McGill University
            Montreal, Canada
@contact:   andreas.spielhofer@mail.mcgill.ca
@filename:  _defines.py
"""

#DEFAULT_SERIAL for Linux = '/dev/ttyUSB0'
#DEFAULT_SERIAL for Windows = 'COM0'

# Serial and Baudrate for the Kleindiek MM3A Micromanipulator:
MM3A_SERIAL = 'COM20'
MM3A_BAUDRATE = 115200

# IP address and Port number for the Capres Four Point-Probe System:
CAPRES_HOST = '192.168.1.80'
CAPRES_PORT = 23

#Serial and Baudrate for Keithley 2400LV SourceMeter
KEITHLEY_SERIAL = 'COM7'
KEITHLEY_BAUDRATE = 9600

# Serial and Baudrate for the Arduino Multiplexer Board:
ARDUINO_SERIAL = 'COM16'
ARDUINO_BAUDRATE = 9600

# Serial and Baudrate for MKS 937B Pressure Controller:
MKS_SERIAL = 'COM8'
MKS_BAUDRATE = 9600

# Serial and Baudrate for NEXTorr D 200-5 Pump
NEXTORR_SERIAL = 'COM5'
NEXTORR_BAUDRATE = 115200

# IP address for Raspberry Pi Temperature/Pressure/Humidity Logger:
RASPBERRY_HOST = '132.206.186.19'
RASPBERRY_PORT = 80
```

C.2. Kleindiek MM3A Micromanipulator

```
"""
Created on Sat Dec 03 12:04:12 2016

@author:    Andreas Spielhofer
            Ph.D. Candidate
            Physics Departement
            McGill University
            Montreal, Canada
@contact:   andreas.spielhofer@mail.mcgill.ca
@filename:  _base.py
"""

import serial
import time
import _defines as _d

class NanoControl():
    # _initialx = 0
    # _initialy = 0

    def __init__(self, port=None):
        print "Now initializing"
        try:
            print "Trying hard"

            if port is None:
                self._serial = serial.Serial(
                                        _d.MM3A_SERIAL,
                                        _d.MM3A_BAUDRATE,
                                        parity = 'N',
                                        stopbits = 1,
                                        timeout=0.1
                                        )
                print self._serial.name
            else:
                print "tried"
                self._serial = serial.Serial(
                                        port = 'COM20',
                                        baudrate = 115200,
                                        parity = 'N',
                                        stopbits = 1,
                                        timeout = 0.1
                                        )
```

```
        except:
            self._serial.close()
            raise RuntimeError('Could not open serial connection')

        if self._serial is None:
            raise RuntimeError('Could not open serial connection')
            print "did not work"

        print('NanoControl initialized on port %s' %self._serial.name)
        self._serial.write('version\r')
        print('Firmware Version: ' + self._read_return_status())
        #self._initialx, self._initialy = self._counterread()
        self._serial.write('speed ?\r')
        self._serial.readline()


    def _read_return_status(self):
        buf = self._serial.read(512)
        buf = buf.split("\t")

        if buf[0] == 'e':
           raise RuntimeError('Return Status reported an error')
           return buf

        if len(buf) > 1:
            return buf[1]
        else:
            return buf[0]


    def _get_speed(self):
        self._serial.write('speed ?\r')
        speed = self._read_return_status()
        speed = speed.split(' ')
        self.speed0 = speed[0]
        self.speed1 = speed[1]
        self.speed2 = speed[2]
        self.speed3 = speed[3]
        return self._read_return_status()


    def _speed(self, speed):
        self._serial.write('speed '+ str(speed) + '\r')
        self._serial.write('speed ?\r')
```

```
88          speed = self._read_return_status()
89          speed = speed.split(' ')
90          self.speed0 = speed[0]
91          self.speed1 = speed[1]
92          self.speed2 = speed[2]
93          self.speed3 = speed[3]
94          print(speed)
95
96          for index in range(0,5):
97              print('Speed%d: ' + speed[index]) %(index)
98          return self._read_return_status()
99
100
101     def _coarse(self, channel, steps):
102         if channel in ('A','B','C'):
103             if (steps >= -65520) & (steps <= 65520):
104                 self._serial.write('coarse '+channel+' '\
105                 +str(steps)+'\r')
106
107                 return self._read_return_status()
108         raise RuntimeError('illegal parameters in'/
109                 +'_coarse(channel, steps)')
110
111
112     def _get_coarse_counter(self):
113         print('Test A')
114         self._serial.write('coarse ?\r')
115         print('Test B')
116         position=self._read_return_status()
117         position=position.split(' ')
118         self.position0 = position[0]
119         self.position1 = position[1]
120         self.position2 = position[2]
121         self.position3 = position[3]
122
123         for index in range(0,4):
124             print('Position%d: ' + position[index]) %(index)
125         return
126
127
128     def _coarse_reset(self):
129         self._serial.write('coarsereset\r')
130         return
131
```

```
132
133     def _fine(self, channel, steps):
134         if channel in ('A','B'):
135             if (steps >= -2048) & (steps <= 2047):
136                 self._serial.write('fine '+channel+' '\
137                 +str(int(steps))+'\r')
138                 return self._read_return_status()
139         raise RuntimeError('illegal parameters in _fine()')
140
141
142     def _get_fine_counter(self):
143         """
144         :return:
145         """
146         print('Test A')
147         self._serial.write('fine ?\r')
148         print("Test B")
149         return self._read_return_status()
150         position=self._read_return_status()
151         position=position.split(' ')
152         self.position0 = position[0]
153         self.position1 = position[1]
154         self.position2 = position[2]
155         self.position3 = position[3]
156
157         for index in range(0,4):
158             print('Position%d: ' + position[index]) %(index)
159         print("Test C")
160
161         return
162
163
164     def _relax(self):
165         """
166         relax all channels (no voltage on the piezos)
167
168         :return: return status
169         """
170         self._serial.write('relax\r')
171
172         return self._read_return_status()
173
174
175     def _moveabs(self, x=None, y=None, channel=None, pos=None):
```

```
176         """
177         move stage to absolute coordinates (only when stage has
178         encoders !)
179 
180         :param x: move x-axis to the x position in nanometers
181         :param y: move y-axis to the y position in nanometers
182         :param channel: if you only want to move one
183         channel/axis, define channel here (A=x,B=y)
184         :param pos: position in nm the channel is moved to
185         :return: return status
186         """
187         if (x is not None) & (y is not None):
188             self._serial.write('moveabs '+str(x)+' '+str(y)+'\r')
189         elif (channel in ('A','B')) & (pos is not None):
190             self._serial.write('moveabs '+channel+' '+str(pos)+'\r')
191         return self._read_return_status
192 
193 
194     def _moverel(self, dx=None, dy=None):
195         """
196         move the stage by dx and dy [nm]
197 
198         :param dx: move x-axis by dx nanometers
199         :param dy: move y-axis by dy nanometers
200         :return: return status, values of the counters
201         """
202         x, y = self._counterread()
203         self._moveabs(x=x+dx,y=y+dy)
204         return self._read_return_status()
205 
206 
207     def _counterread(self):
208         """
209         return position in nm
210         """
211         self._serial.write('counterread\r')
212         buf = self._read_return_status()
213         buf = buf.split(' ')
214         return int(buf[0]), int(buf[1])
215 
216 
217     def _counterreset(self):
218         """
219         resets all position counters
```

```
220
221         :return: return status, values of the counters
222         """
223         self._serial.write('counterreset\r')
224         return self._read_return_status()
225
226
227     def home(self):
228         """
229         homes both axes of the stage
230
231         :return: returns counter values after homing
232         """
233         self._moveabs(x=-200000,y=-200000)
234         self._counterreset()
235         self._moveabs(x=1000,y=1000)
236         time.sleep(0.2)
237         self._relax()
238         time.sleep(0.2)
239         return self._counterreset()
240
241 #n = NanoControl()
```

C.3. Keithley SourceMeter 2400LV

```
# -*- coding: utf-8 -*-
"""
Created on Sat Apr 09 16:03:27 2016

@author:    Andreas Spielhofer
            Ph.D. Candidate
            Physics Departement
            McGill University
            Montreal, Canada
@contact:   andreas.spielhofer@mail.mcgill.ca
@filename:  Keithley.py
"""

import serial
import time
import numpy as _np
import _defines as _d

class Keithley():
    def __init__(self, port=None):
        print "Now initializing"
        try:
            if port is None:
                ser = serial.Serial(
                                    _d.KEITHLEY_SERIAL,
                                    _d.KEITHLEY_BAUDRATE,
                                    parity=serial.PARITY_NONE,
                                    stopbits=serial.STOPBITS_ONE,
                                    bytesize=serial.EIGHTBITS,
                                    xonxoff=0,
                                    rtscts=1,
                                    timeout=0.15
                                    )
                self.ser = ser
                self.port = port
                print self.ser.name
            else:
                print "tried"
        except:
            self.ser.close()
            raise RuntimeError('Could not open Serial Connection')

        if self.ser is None:
```

```
44              raise RuntimeError('Could not open Serial Connection')
45          print('Keithley initialized on port %s' %self.ser.name)
46          self.ser.write('*IDN?' + '\r')
47          self.firmware = self.ser.readline()
48          print('Firmware Version:'+ self.firmware)
49
50
51      def close_connection(self):
52          self.ser.close()
53          print('Connection closed')
54
55
56      def open_connection(self):
57          self.ser.open()
58
59
60      def current_mode(self):
61          '''
62          Set the Keithley SourceMeter to current measurement mode
63          '''
64          self.ser.write("SOUR:FUNC VOLT"+ '\r')
65          self.ser.write("SOUR:VOLT 0"+ '\r')
66          self.ser.write("CONF:CURR"+ '\r')
67          self.ser.write("FORM:ELEM CURR"+ '\r')
68
69
70      def enable_live_readings(self):
71          '''
72          Set the Keithley SourceMeter to provide live readings
73          '''
74          self.ser.write("ARM:COUN INF")  # infinite arm count
75          self.ser.write("TRIG:DEL 0")    # zero trigger delay
76          self.ser.write("INIT")          # start measurements
77
78
79      def enable_voltage_source(self):
80          '''
81          This function is a placeholder to maintain
82          compatibility with the Keithley 617 module.
83          '''
84          pass
85
86
87      def disable_voltage_source(self):
```

```
88          '''
89          This function is primarily a placeholder to maintain
90          compatibility with the keithley617 module, it sets the
91          output of the Keithleys internal voltage source to
92          zero Volts.
93          '''
94          self.ser.write("SOUR:VOLT 0")
95
96
97      def do_nothing(self, *dummy):
98          '''
99          This function is the default value of the function
100         parameter for the read function below
101         '''
102         pass
103
104
105     def resistance_mode(self):
106         '''
107         Set the Keithley SourceMeter to measure resistance
108         '''
109         self.ser.write("CONF:RES" + '\r')
110         self.ser.write("FORM:ELEM RES"+ '\r')
111
112
113     def set_voltage_source(self, voltage):
114         '''
115         Set the value of the Keithley SourceMeters internal
116         voltage source.
117         '''
118         if abs((voltage / 5e-6) - round(voltage / 5e-6)) > 1e-10:
119             print 'Warning: Voltage source has a ' \
120             'maximum resolution of 5 uV.'
121         self.ser.write("SOUR:VOLT " + str(voltage)+ '\r')
122
123
124     def voltage_mode(self):
125         '''
126         This function sets the Keithley to measure voltage.
127         '''
128         self.ser.write("SOUR:FUNC CURR"+ '\r')
129         self.ser.write("SOUR:CURR 0"+ '\r')
130         self.ser.write("CONF:VOLT"+ '\r')
131         self.ser.write("FORM:ELEM VOLT"+ '\r')
```

```
132
133
134     def output(self, status):
135         if status == "ON":
136             self.output = "ON"
137             self.ser.write("OUTP ON" +'\r')
138         elif status == "OFF":
139             self.output = "OFF"
140             self.ser.write("OUTP OFF" +'\r')
141         else:
142             print('Input not vaild. Write as argument OFF or ON')
143
144
145     def measure(self):
146         self.ser.write("TRIG:COUN 1" + '\r')
147         self.ser.write("INIT" + "\r")
148         self.ser.write("read?" + '\r')
149         return self.ser.readline()
150
151
152     def voltread(self, voltage):
153         """
154         This function reads the Voltage.
155         """
156         if -11.0 <= voltage <=  11.0:
157             if voltage == 0.0:
158                 voltage = 0.1
159             self.ser.write(':SOUR1:VOLT:LEV:IMM:AMPL '\
160                            +str(voltage) +'\r')
161             self.ser.write(":READ?" + "\r")
162             data = self.ser.readline()
163             data = _np.array([float(item) for item in data.split(',')])
164
165             return data
166         else:
167             print "The voltage is out of range"
168             return
169
170
171     def currentread(self,current):
172         """
173         This function reads the Current.
174         """
175         if -0.1 <= current <= 0.1:
```

```
176
177             if current == 0.0:
178                 current=1e-8
179             self.ser.readline()
180             self.ser.write(':SOUR1:CURR:LEV:IMM:AMPL '+str(current)+'\r')
181             self.ser.write(':READ?'+'\r')
182             time.sleep(0.2)
183             data=self.ser.readline()
184             #print data
185             data=_np.array([float(item) for item in data.split(',')])
186             #print data
187             return data
188
189
190     def format_element(self):
191         self.ser.write('format:elements?' +'\r')
192         print self.ser.readline()
193
194
195     def beep(self):
196         '''
197         Makes a beep sound.
198         '''
199         self.ser.write(":SYST:BEEP 200,1 \r")
200
201 #k = Keithley()
```

C.4. Arduino Multiplexer Board

```
# -*- coding: utf-8 -*-
"""
Created on Fri Jul 14 18:18:26 2017

@author:    Andreas Spielhofer
            Ph.D. Candidate
            Physics Departement
            McGill University
            Montreal, Canada
@contact:   andreas.spielhofer@mail.mcgill.ca
@filename:  arduino.py
"""

import serial
import time
import _defines as _d

class Arduino():
    def __init__(self, port=None):
        try:
            if port is None:
                s= serial.Serial(
                                    _d.ARDUINO_SERIAL,
                                    _d.ARDUINO_BAUDRATE,
                                    timeout=1
                                    )
                self.s = s
                self.port = port
                print self.s.name
            else:
                print "Problems with Connecting"
        except:
            self.s.close()
            raise RuntimeError('Could not open Serial Connection')
        if self.s is None:
            raise RuntimeError('Could not open Serial Connection')
            print "Did not work"
        print('Arduino initialized on Port %s' %self.s.name)
        self.s.write("Connected to Arduino Micro\n")
        time.sleep(0.1)
        self.firmware = self.s.readline()
        print(self.firmware)

```

```
44
45      def switch(self,pin,status):
46          """
47          status = 0 : turn all LEDs off
48          status = 1 : turn all LEDs on
49          Digital pins available: 2-13
50          Analog pins available: 14(A0)-19(A5)
51          """
52          if pin ==14:    #Analog Output A0
53              pin = "A0"
54          if pin == 15:    #Analog Output A1
55              pin = "A1"
56          if pin == 16:    #Analog Output A2
57              pin = "A2"
58          if pin == 17:    #Analog Output A3
59              pin = "A3"
60          if pin == 18:    #Analog Output A4
61              pin = "A4"
62          if pin == 19:    #Analog Output A5
63              pin = "A5"
64
65          if status == 1: #Turn on
66              self.message = str(pin)+str("on\n")
67          if status == 0: #Turn off
68              self.message = str(pin)+str("off\n")
69          self.send()
70
71
72      def send(self):
73          self.s.write(self.message)
74
75
76      def close(self):
77          self.s.close()
78
79
80      def switch_all(self,status):
81          '''
82          status = 0 : turn all LEDs off
83          status = 1 : turn all LEDs on
84          '''
85          for i in range (2,20):
86              print i
87              self.switch(i,status)
```

```
88
89
90      def LED_on(self,pin):
91          if pin ==14:
92              pin = "A0"
93          if pin == 15:
94              pin = "A1"
95          if pin == 16:
96              pin = "A2"
97          if pin == 17:
98              pin = "A3"
99          if pin == 18:
100             pin = "A4"
101         if pin == 19:
102             pin = "A5"
103
104         self.message = str(pin)+str("on\n")
105         self.send()
106
107
108     def LED_off(self,pin):
109         if pin ==14:
110             pin = "A0"
111         if pin == 15:
112             pin = "A1"
113         if pin == 16:
114             pin = "A2"
115         if pin == 17:
116             pin = "A3"
117         if pin == 18:
118             pin = "A4"
119         if pin == 19:
120             pin = "A5"
121         self.message = str(pin)+str("off\n")
122         self.send()
```

C.5. MKS 937B Pressure Controller

```
# -*- coding: utf-8 -*-
"""
Created on Tue May 19 14:29:57 2015

@author:    Andreas Spielhofer
            Ph.D. Candidate
            Physics Departement
            McGill University
            Montreal, Canada
@contact:   andreas.spielhofer@mail.mcgill.ca
@filename:  MKS937.py
"""

import serial as _s
import time
import sys
import _defines as _d

#param={'P1':'mbar','P3':'mbar','P5':'mbar','P6':'mbar'}

class MKS():

    def __init__(self, port=None):
        print "Now initializing"
        try:
            if port is None:
                self._serial = _s.Serial(
                                        _d.MKS_SERIAL,
                                        _d.MKS_BAUDRATE,
                                        bytesize=_s.EIGHTBITS,
                                        parity = _s.PARITY_NONE,
                                        xonxoff = False,
                                        stopbits = _s.STOPBITS_ONE,
                                        timeout = 2
                                        )
                print 'Initialized'
                print self._serial.name
            else:
                print "Could not connect"
        except:
            self._serial.close()
            raise RuntimeError('Could not open serial connection')

```

```
44
45      def measureallgauges(self):
46          '''
47          The Gauge normally returns a string in form of
48          @253ACK2.1OE-09 NOGAUGE 4.5OE-07 NOGAUGE LO<E-03 LO<E-03;FF
49
50          self.pressure[0], [2] are the pressures of the ion gauges
51          self.pressure[4] and [5] are the ones from the Pirani
52          '''
53          stri="@253"+"PRZ?"+";FF\r\n"
54          print stri
55          self.pressure = self._serial.write(stri)
56          pressure = self._serial.readline()
57          print pressure
58
59          # remove from the string:
60          pressure = pressure.replace("@253ACK","")
61          # remove from the string:
62          pressure = pressure.replace(";FF","")
63          self.pressure = pressure.split(" ")
64          print self.pressure
65
66          if self.pressure[4] == "LO<E-03":
67              print "Main = %s" %  self.pressure[0]
68          else:
69              print "Main = %s" % self.pressure[4]
70
71          if self.pressure[5] == "LO<E-03":
72              print "Prep = %s" % float(self.pressure[2])
73          else:
74              print "Prep = %s" %  self.pressure[5]
75
76  # m = MKS()
```

D. Specification Sheets

The following appendix includes the specification sheets for both the source-meter (Keithley 2400LV) and the MAX4679 CMOS switches. For the MAX4679 CMOS switches, the dual-supply electrical characteristics have to be considered.

Model 2400, 2400-LV, 2400-C, and 2401 SourceMeter® Specifications

SOURCE SPECIFICATIONS[1]

VOLTAGE PROGRAMMING ACCURACY (LOCAL OR REMOTE SENSE)

MODEL	RANGE	PROGRAMMING RESOLUTION	ACCURACY (1 Year) 23°C ±5°C ±(% rdg. + volts)	NOISE (peak-peak) 0.1Hz – 10Hz
	200.00 mV	5 µV	0.02% + 600 µV	5 µV
	2.00000 V	50 µV	0.02% + 600 µV	50 µV
	20.0000 V	500 µV	0.02% + 2.4 mV	500 µV
2400-C and 2400 Only:	200.00 V	5 mV	0.02% + 24 mV	5 mV

TEMPERATURE COEFFICIENT (0°-18°C & 28°-50°C): ±(0.15 × accuracy specification)/ °C.

MAX. OUTPUT POWER: 22W, four quadrant source or sink operation.

SOURCE/SINK LIMITS:

MODEL 2400, 2400-C: ±21V @ ±1.05A, ±210V @ ±105 mA.

MODEL 2400-LV, 2401: ±21V @ ±1.05A.

VOLTAGE REGULATION: Line: 0.01% of range. **Load:** 0.01% of range + 100µV.

NOISE 10Hz – 1MHz (p-p): 20mV typical into a resistive load.

OVERVOLTAGE PROTECTION: User selectable values, 5% tolerance. Factory default = none.

CURRENT LIMIT: Bipolar current limit (compliance) set with single value. Min. 0.1% of range.

OVERSHOOT: <0.1% typical (full scale step, resistive load, 10mA range).

CURRENT PROGRAMMING ACCURACY (LOCAL OR REMOTE SENSE)

RANGE	PROGRAMMING RESOLUTION	ACCURACY (1 Year)[3] 23°C ±5°C ±(% rdg. + amps)	NOISE (peak-peak) 0.1Hz – 10Hz
1.00000 µA	50 pA	0.035% + 600 pA	5 pA
10.0000 µA	500 pA	0.033% + 2 nA	50 pA
100.000 µA	5 nA	0.031% + 20 nA	500 pA
1.00000 mA	50 nA	0.034% + 200 nA	5 nA
10.0000 mA	500 nA	0.045% + 2 µA	50 nA
100.000 mA	5 µA	0.066% + 20 µA	500 nA
1.00000 A[2]	50 µA	0.27% + 900 µA	25 µA

TEMPERATURE COEFFICIENT (0°-18°C & 28°-50°C): ±(0.15 × accuracy specification)/ °C.

MAX. OUTPUT POWER: 22W, four quadrant source or sink operation.

SOURCE/SINK LIMITS:

MODEL 2400, 2400-C: ±21V @ ±1.05A, ±210V @ ±105 mA.

MODEL 2400-LV, 2401: ±21V @ ±1.05A.

CURRENT REGULATION: Line: 0.01% of range. **Load:** 0.01% of range + 100pA.

VOLTAGE LIMIT: Bipolar voltage limit (compliance) set with single value. Min. 0.1% of range.

OVERSHOOT: <0.1% typical (1mA step, RL = 10kΩ, 20V range).

ADDITIONAL SOURCE SPECIFICATIONS

TRANSIENT RESPONSE TIME: 30µs minimum for the output to recover to its spec. following a step change in load.

COMMAND PROCESSING TIME: Maximum time required for the output to begin to change following the receipt of :SOURce:VOLTage|CURRent <nrf> command. **Autorange On:** 10ms. **Autorange Off:** 7ms.

OUTPUT SETTLING TIME: Time required to reach 0.1% of final value after command is processed and output slew. 100µs typical. Resistive load. 10µA to 100mA range.

OUTPUT SLEW RATE (±30%): 0.5V/µs, 200V range, 100mA compliance. (2400 and 2400-C only) 0.08V/µs, 20V range, 100mA compliance.

DC FLOATING VOLTAGE: Output can be floated up to ±250VDC from chassis ground.

REMOTE SENSE: Up to 1V drop per load lead.

COMPLIANCE ACCURACY: Add 0.3% of range and ±0.02% of reading to base specification.

OVER TEMPERATURE PROTECTION: Internally sensed temperature overload puts unit in standby mode.

RANGE CHANGE OVERSHOOT: Overshoot into a fully resistive 100kΩ load, 10Hz to 1MHz BW, adjacent range changes between 200mV, 2V and 20V ranges, 100mV typical.

MINIMUM COMPLIANCE VALUE: 0.1% of range.

1. Specifications valid for continuous output currents below 105mA. For operation above 105mA continuous for > 1 minute, derate accuracy 10%/35mA above 105mA.
2. Full operation (1A) regardless of load to 30°C. Above 30°C ambient, derate 35mA/°C and prorate 35mA/Ω load. 4-wire mode. For current sink operation on 1A range, maximum continuous power is limited to approximately 1/2 rated power or less, depending on current, up to 30°C ambient. See power equations in the User's Manual to calculate allowable duty cycle for specific conditions.
3. For sink mode, 1µA to 100mA range, accuracy is: ±(0.15% + offset*4)
   For 1A range, accuracy is: ±(1.5% + offset*8)

Model 2400, 2400-LV, 2400-C, and 2401 SourceMeter® Specifications

MEASURE SPECIFICATIONS[1,2]

VOLTAGE MEASUREMENT ACCURACY (LOCAL OR REMOTE SENSE)

MODEL	RANGE	DEFAULT RESOLUTION	INPUT RESISTANCE	ACCURACY (1 Year) 23°C ±5°C ±(% rdg. + volts)
	200.00 mV	1 µV	>10 GΩ	0.012% + 300 µV
	2.00000 V	10 µV	>10 GΩ	0.012% + 300 µV
	20.0000 V	100 µV	>10 GΩ	0.015% + 1.5 mV
2400-C and 2400 Only:	200.000 V	1 mV	>10 GΩ	0.015% + 10 mV

TEMPERATURE COEFFICIENT (0°-18°C & 28°-50°C): ±(0.15 × accuracy specification)/ °C.

CURRENT MEASUREMENT ACCURACY (LOCAL OR REMOTE SENSE)

RANGE	DEFAULT RESOLUTION	VOLTAGE BURDEN[3]	ACCURACY (1 Year) 23°C ±5°C ±(% rdg. + amps)
1.00000 µA	10 pA	<1 mV	0.029% + 300 pA
10.0000 µA	100 pA	<1 mV	0.027% + 700 pA
100.000 µA	1 nA	<1 mV	0.025% + 6 nA
1.00000 mA	10 nA	<1 mV	0.027% + 60 nA
10.0000 mA	100 nA	<1 mV	0.035% + 600 nA
100.000 mA	1 µA	<1 mV	0.055% + 6 µA
1.00000 A	10 µA	<1 mV	0.22% + 570 µA

TEMPERATURE COEFFICIENT (0°-18°C & 28°-50°C): ±(0.10 × accuracy specification)/ °C.

RESISTANCE MEASUREMENT ACCURACY (LOCAL OR REMOTE SENSE)

RANGE	DEFAULT RESOLUTION	DEFAULT TEST CURRENT	NORMAL ACCURACY (23°C ±5°C) 1 YEAR, ±(% rdg. + ohms)	ENHANCED ACCURACY (23°C ±5°C)[5] 1 YEAR, ±(% rdg. + ohms)
<2.00000 Ω[4]	10 µΩ	-	Source I_{ACC} + Meas. V_{ACC}	Meas I_{ACC} + Meas. V_{ACC}
20.0000 Ω	100 µΩ	100 mA	0.10% + 0.003 Ω	0.07% + 0.001 Ω
200.000 Ω	1 mΩ	10 mA	0.08% + 0.03 Ω	0.05% + 0.01 Ω
2.00000 kΩ	10 mΩ	1 mA	0.07% + 0.3 Ω	0.05% + 0.1 Ω
20.0000 kΩ	100 mΩ	100 µA	0.06% + 3 Ω	0.04% + 1 Ω
200.000 kΩ	1 Ω	10 µA	0.07% + 30 Ω	0.05% + 10 Ω
2.00000 MΩ	10 Ω	1 µA	0.11% + 300 Ω	0.05% + 100 Ω
20.0000 MΩ	100 Ω	1 µA	0.11% + 1 kΩ	0.05% + 500 Ω
200.000 MΩ	1 kΩ	100 nA	0.66% + 10 kΩ	0.35% + 5 kΩ
>200.000 MΩ[4]	-	-	Source I_{ACC} + Meas. V_{ACC}	Meas I_{ACC} + Meas. V_{ACC}

TEMPERATURE COEFFICIENT (0°-18°C & 28°-50°C): ±(0.15 × accuracy specification)/ °C.

SOURCE I MODE, MANUAL OHMS: Total uncertainty = I source accuracy + V measure accuracy (4-wire remote sense).

SOURCE V MODE, MANUAL OHMS: Total uncertainty = V source accuracy + I measure accuracy (4-wire remote sense).

6-WIRE OHMS MODE: Available using active ohms guard and guard sense. Max. Guard Output Current: 50mA (except 1A range). Accuracy is load dependent. Refer to White Paper no. 2033 for calculation formula.

GUARD OUTPUT IMPEDANCE: <0.1Ω in ohms mode.

CONTACT CHECK SPECIFICATIONS

SPEED: 350µs for verification and notification.

CONTACT CHECK:	2Ω	15Ω	50Ω
No contact check failure	<1.00Ω	<13.5Ω	<47.5Ω
Always contact check failure	>3.00Ω	>16.5Ω	>52.5Ω

1. Speed = Normal (1 PLC). For 0.1 PLC, add 0.005% of range to offset specifications, except 200mV, 1A ranges, add 0.05%. For 0.01 PLC, add 0.05% of range to offset specifications, except 200mV and 1A ranges, add 0.5%.
2. Accuracies apply to 2- or 4-wire mode when properly zeroed.
3. 4-wire mode.
4. Manual ohms only.
5. Source readback ON, offset compensation ON, add system noise but don't include offsets.

Model 2400, 2400-LV, 2400-C, and 2401 SourceMeter® Specifications

SYSTEM SPEEDS

MEASUREMENT[1]

MAXIMUM RANGE CHANGE RATE: 75/second.

MAXIMUM MEASURE AUTORANGE TIME: 40ms (fixed source)[2].

SWEEP OPERATION[3] READING RATES (rdg./second) FOR 60Hz (50Hz):

SPEED	NPLC/TRIGGER ORIGIN	MEASURE		SOURCE-MEASURE[5]		SOURCE-MEASURE PASS/FAIL TEST[4,5]		SOURCE-MEMORY[4,5]	
		TO MEM.	TO GPIB	TO MEM	TO GPIB	TO MEM.	TO GPIB	TO MEM.	TO GPIB
Fast	0.01 / internal	2081 (2030)	1754	1551 (1515)	1369	902 (900)	981	165 (162)	165
IEEE-488.1 Mode	0.01 / external	1239 (1200)	1254	1018 (990)	1035	830 (830)	886	163 (160)	163
Fast	0.01 / internal	2081 (2030)	1198 (1210)	1551 (1515)	1000 (900)	902 (900)	809 (840)	165 (162)	164 (162)
IEEE-488.2 Mode	0.01 / external	1239 (1200)	1079 (1050)	1018 (990)	916 (835)	830 (830)	756 (780)	163 (160)	162 (160)
Medium	0.10 / internal	510 (433)	509 (433)	470 (405)	470 (410)	389 (343)	388 (343)	133 (126)	132 (126)
IEEE-488.2 Mode	0.10 / external	438 (380)	438 (380)	409 (360)	409 (365)	374 (333)	374 (333)	131 (125)	131 (125)
Normal	1.00 / internal	59 (49)	59 (49)	58 (48)	58 (48)	56 (47)	56 (47)	44 (38)	44 (38)
IEEE-488.2 Mode	1.00 / external	57 (48)	57 (48)	57 (48)	57 (47)	56 (47)	56 (47)	44 (38)	44 (38)

SINGLE READING OPERATION READINGRATES (rdg./second) FOR 60Hz (50Hz):

SPEED	NPLC/TRIGGER ORIGIN	MEASURE TO GPIB	SOURCE-MEASURE TO GPIB[5]	SOURCE-MEASURE PASS/FAIL TEST[4,5] TO GPIB
Fast (488.1)	0.01 / internal	537	140	135
Fast (488.2)	0.01 / internal	256 (256)	79 (83)	79 (83)
Medium (488.2)	0.10 / internal	167 (166)	72 (70)	69 (70)
Normal (488.2)	1.00 / internal	49 (42)	34 (31)	35 (30)

COMPONENT INTERFACE HANDLER TIME FOR 60Hz (50Hz):[4,6,8]

SPEED	NPLC/TRIGGER ORIGIN	MEASURE TO GPIB	SOURCE PASS/FAIL TEST	SOURCE-MEASURE PASS/FAIL TEST[5,7] TO GPIB
Fast	0.01/ external	1.04 ms (1.08 ms)	0.5 ms (0.5 ms)	4.82 ms (5.3 ms)
Medium	0.10 / external	2.55 ms (2.9 ms)	0.5 ms (0.5 ms)	6.27 ms (7.1 ms)
Normal	1.00 / external	17.53 ms (20.9 ms)	0.5 ms (0.5 ms)	21.31 ms (25.0 ms)

1. Reading rates applicable for voltage or current measurements. Auto zero off, autorange off, filter off, display off, trigger delay = 0, binary reading format, and source auto-clear off.
2. Purely resistive load. 1µA and 10µA ranges <65ms.
3. 1000 point sweep was characterized with the source on a fixed range.
4. Pass/Fail test performed using one high limit and one low math limit.
5. Includes time to re-program source to a new level before making measurement.
6. Time from falling edge of START OF TEST signal to falling edge of END OF TEST signal.
7. Command processing time of :SOURce:VOLTage|CURRent:TRIGgered <nrf> command not included.
8. Models 2400, 2400-LV, and 2400-C.

GENERAL

NOISE REJECTION:

	NPLC	NMRR	CMRR
Fast	0.01	-	80 dB
Medium	0.1	-	80 dB
Slow	1	60 dB	100 dB[1]

1. Except lowest 2 current ranges – 90dB.

LOAD IMPEDANCE: Stable into 20,000pF typical.

COMMON MODE VOLTAGE: 250V DC.

COMMON MODE ISOLATION: $>10^9\Omega$, <1000pF.

OVERRANGE: 105% of range, source and measure.

MAX. VOLTAGE DROP BETWEEN INPUT/OUTPUT AND SENSE TERMINALS: 5V.

MAX. SENSE LEAD RESISTANCE: 1MΩ for rated accuracy.

SENSE INPUT IMPEDANCE: $>10^{10}\Omega$.

GUARD OFFSET VOLTAGE: <300µV, typical.

SOURCE OUTPUT MODES:
Fixed DC level
Memory List (mixed function)
Stair (linear and log)

SOURCE MEMORY LIST: 100 points max.

MEMORY BUFFER: 5,000 readings @ 5.5 digits (two 2,500 point buffers). Includes selected measured value(s) and time stamp. Lithium battery backup (3 yr+ battery life).

PROGRAMMABILITY: IEEE-488 (SCPI-1996.0), RS-232, 5 user-definable power-up states plus factory default and *RST.

DIGITAL INTERFACE:
Output Enable: Active low input.
Handler Interface: Start of test, end of test, 3 category bits. +5V@ 300mA supply. Model 2400, 2400-LV, 2400-C only.
Digital I/O: 1 trigger input, 4 TTL/Relay Drive outputs (33V @ 500mA, diode clamped). Model 2400, 2400-LV, 2400-C only. Model 2401 uses the trigger input (SOT) line but not the four digital output lines.

POWER SUPPLY: 100V to 240V rms, 50–60Hz (automatically detected at power up). 190VA.

WARRANTY: 1 year.

EMC: Conforms to European Union EMC Directive.

SAFETY: UL listed to UL 61010B-1:2003. Conforms to European Union Low Voltage Directive.

WARM-UP: 1 hour to rated accuracies.

DIMENSIONS: 89mm high × 213mm wide × 370mm deep (3 1/2 in × 8 3/8 in × 14 9/16 in). Bench Configuration (with handle & feet):104mm high × 238mm wide × 370mm deep (4 1/8 in × 9 3/8 in × 14 9/16 in).

WEIGHT: 3.21kg (7.08 lbs).

ENVIRONMENT:
For Indoor Use Only: Maximum 2000m above Sea Level
Operating: 0°–50°C, 70%R.H. up to 35°C. Derate 3% R.H./°C, 35°–50°C.
Storage: –25°C to 65°C.

ACCESSORIES SUPPLIED: Test Leads, User's Manual, Quick Start Guide, Service Manual (downloadable), LabVIEW Drivers (downloadable for Models 2400 and 2400-C only).

Specifications subject to change without notice.

19-1713; Rev 0; 4/00

MAXIM

2Ω, Quad, SPST, CMOS Analog Switches

General Description

The MAX4677/MAX4678/MAX4679 quad analog switches feature 1.6Ω max on-resistance (R_{ON}) when operating from a dual ±5V supply. R_{ON} is matched between channels to 0.3Ω max and is flat (0.4Ω max) over the specified signal range. Each switch can handle Rail-to-Rail® analog signals. Off-leakage current is 0.1nA at +25°C. These switches are ideal in low-distortion applications and are the preferred solution over mechanical relays in automated test equipment. They have low power requirements, require less board space, and are more reliable than mechanical relays.

The MAX4677 has four normally closed (NC) switches, and the MAX4678 has four normally open (NO) switches. The MAX4679 has two NC and two NO switches and features guaranteed break-before-make switching.

The MAX4677/MAX4678/MAX4679 operate from either a single +2.7V to +11V or dual ±2.7V to ±5.5V supplies, making them ideal for use in digital card applications and single-ended 75Ω systems.

These devices feature a separate logic supply input that operates from +2.7V to V+, allowing independent logic and analog supplies.

Applications

Reed Relay Replacement	Avionics
Test Equipment	ADC Systems
Communications Systems	Data-Acquisition Systems
Audio Signal Routing	PBX/PABX Systems

Features

- **On-Resistance 1.6Ω max**
- **On-Resistance Flatness 0.4Ω max**
- **On-Resistance Matching 0.3Ω max**
- **Dual ±2.7V to ±5.5V or Single +2.7V to +11V Supply Range**
- **TTL/CMOS-Logic Compatible**
- **Crosstalk -84dB at 1MHz**
- **Off-Isolation -65dB at 1MHz**
- **-3dB Bandwidth: 66MHz**
- **Rail-to-Rail Signal Range**

Ordering Information

PART	TEMP. RANGE	PIN-PACKAGE
MAX4677EUE	-40°C to +85°C	16 TSSOP
MAX4677EPE	-40°C to +85°C	16 DIP
MAX4678EUE	-40°C to +85°C	16 TSSOP
MAX4678EPE	-40°C to +85°C	16 DIP
MAX4679EUE	-40°C to +85°C	16 TSSOP
MAX4679EPE	-40°C to +85°C	16 DIP

Rail-to-Rail is a registered trademark of Nippon Motorola, Ltd.

Pin Configurations/Functional Diagrams/Truth Tables

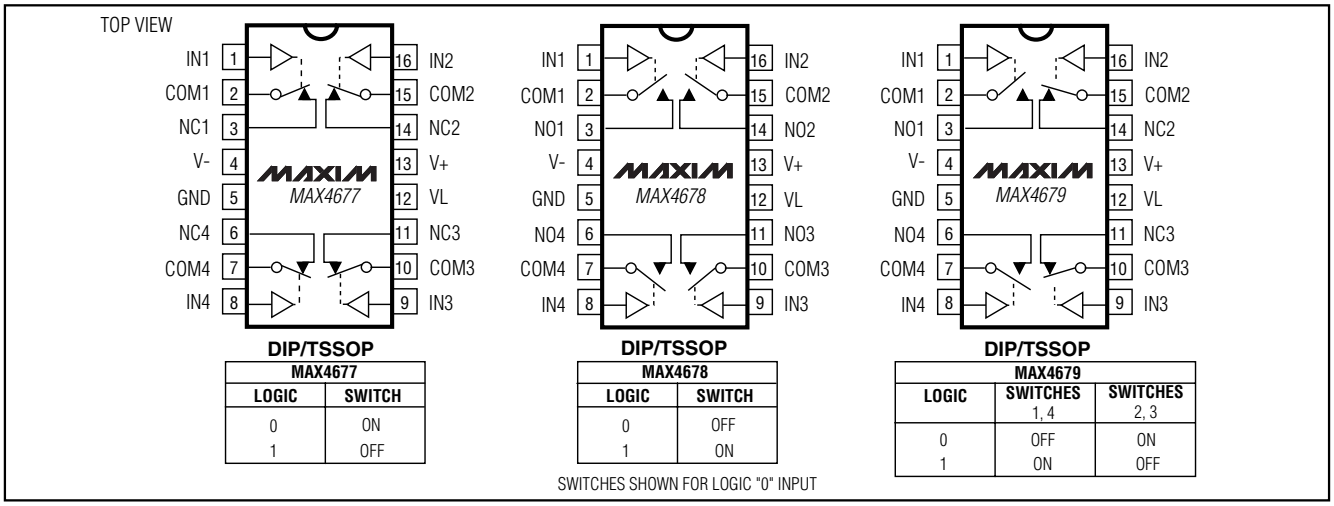

MAX4677

LOGIC	SWITCH
0	ON
1	OFF

MAX4678

LOGIC	SWITCH
0	OFF
1	ON

MAX4679

LOGIC	SWITCHES 1, 4	SWITCHES 2, 3
0	OFF	ON
1	ON	OFF

SWITCHES SHOWN FOR LOGIC "0" INPUT

For free samples and the latest literature, visit www.maxim-ic.com or phone 1-800-998-8800. For small orders, phone 1-800-835-8769.

2Ω, Quad, SPST, CMOS Analog Switches

ABSOLUTE MAXIMUM RATINGS

V+ to GND .....-0.3V to +12V
V- to GND .....+0.3V to -12V
V+ to V- .....+12V
V_L, IN_ to GND (Note 1) .....-0.3V to (V+ + 0.3V)
$V_{COM_}$, $V_{NC_}$, $V_{NO_}$ (Note 1).....V- to V+
Current (any terminal).....±50mA
Continuous Current (COM_, NC_, NO_).....±100mA
Peak Current (COM_, NC_, NO_
pulsed at 1ms 10% duty cycle) .....±200mA

Continuous Power Dissipation (T_A = +70°C)
16-Pin Plastic DIP (derate 10.5mW/°C above +70°C)..842mW
16-Pin TSSOP (derate 5.7mW/°C above +70°C).....457mW
Operating Temperature Range .....-40°C to +85°C
Storage Temperature Range .....-65°C to +150°C
Junction Temperature .....+150°C
Lead Temperature (soldering, 10s) .....+300°C

Note 1: Signals on NC_, NO_, COM_, or IN_ exceeding V+ or V- are clamped by internal diodes. Limit forward diode current to maximum current rating.

Stresses beyond those listed under "Absolute Maximum Ratings" may cause permanent damage to the device. These are stress ratings only, and functional operation of the device at these or any other conditions beyond those indicated in the operational sections of the specifications is not implied. Exposure to absolute maximum rating conditions for extended periods may affect device reliability.

ELECTRICAL CHARACTERISTICS–Dual Supplies

(V+ = +5V ±10%, V- = -5V ±10%, V_L = +2.7V to V+, GND = 0, V_{IH} = +2.4V, V_{IL} = +0.8V, T_A = T_{MIN} to T_{MAX}, unless otherwise noted. Typical values are at T_A = +25°C.) (Note 2)

PARAMETER	SYMBOL	CONDITIONS		MIN	TYP	MAX	UNITS
ANALOG SWITCH							
Input Voltage Range	$V_{COM_}$, $V_{NO_}$, $V_{NC_}$			V-		V+	V
On-Resistance	R_{ON}	V+ = 4.5V, V- = -4.5V, $I_{COM_}$ = 50mA, $V_{NO_}$ or $V_{NC_}$ = ±3.3V	T_A = +25°C		1.2	1.6	Ω
			T_A = T_{MIN} to T_{MAX}			2	
On-Resistance Match Between Channels (Note 3)	ΔR_{ON}	V+ = 4.5V, V- = -4.5V, $I_{COM_}$ = 50mA, $V_{NO_}$ or $V_{NC_}$ = ±3.3V	T_A = +25°C		0.2	0.3	Ω
			T_A = T_{MIN} to T_{MAX}			0.5	
On-Resistance Flatness (Note 4)	R_{FLAT}	V+ = 4.5V, V- = -4.5V, $I_{COM_}$ = 50mA, $V_{NO_}$ or $V_{NC_}$ = ±3.3V, 0	T_A = +25°C		0.2	0.4	Ω
			T_A = T_{MIN} to T_{MAX}			0.5	
NC_ or NO_ Off-Leakage Current (Note 5)	$I_{N_(OFF)}$	V+ = +5.5V, V- = -5.5V, $V_{NO_}$ or $V_{NC_}$ = ±4.5V, $V_{COM_}$ = ∓4.5V	T_A = +25°C	-1	0.1	1	nA
			T_A = T_{MIN} to T_{MAX}	-10		10	
COM_ Off-Leakage Current (Note 5)	$I_{COM_(OFF)}$	V+ = +5.5V, V- = -5.5V, $V_{NO_}$ or $V_{NC_}$ = ±4.5V, $V_{COM_}$ = ∓4.5V	T_A = +25°C	-1	0.1	1	nA
			T_A = T_{MIN} to T_{MAX}	-10		10	
COM_ On-Leakage Current (Note 5)	$I_{COM_(ON)}$	V+ = +5.5V, V- = -5.5V, $V_{COM_}$ = ±4.5V, $V_{NO_}$ or $V_{NC_}$ = ±4.5V or floating	T_A = +25°C	-2	0.2	2	nA
			T_A = T_{MIN} to T_{MAX}	-25		25	
LOGIC INPUT							
Input Logic High	V_{IH}	V_L = V+		2.4			V
Input Logic Low	V_{IL}	V_L = V+				0.8	V
Input Leakage Current	I_{IN}	V_L = V+		-1	0.005	1	µA

ELECTRICAL CHARACTERISTICS–Dual Supplies (continued)

(V+ = +5V ±10%, V- = -5V ±10%, V_L = +2.7V to V+, GND = 0, V_{IH} = +2.4V, V_{IL} = +0.8V, T_A = T_{MIN} to T_{MAX}, unless otherwise noted. Typical values are at T_A = +25°C.) (Note 2)

PARAMETER	SYMBOL	CONDITIONS		MIN	TYP	MAX	UNITS
POWER SUPPLY							
Positive Supply Voltage	V+			+2.7		+5.5	V
Negative Supply Voltage	V-			-2.7		-5.5	V
Logic Supply Voltage	V_L			2.7		V+	V
Positive Supply Current	I+	IN_ = GND or V_L			0.001	1	µA
Negative Supply Current	I-	IN_ = GND or V_L				-1	µA
Logic Supply Current	I_L	IN_ = GND or V_L				1	µA
Ground Current	I_{GND}	IN_ = 0 or V+, V+ = 5.5V, V- = -5.5V				1	µA
DYNAMIC							
Turn-On Time	t_{ON}	V+ = +4.5V, V- = -4.5V, $V_{NC_}$ or $V_{NO_}$ = ±3.3V, V_L = V+, Figure 2	T_A = +25°C		200	350	ns
			T_A = T_{MIN} to T_{MAX}			500	
Turn-Off Time	t_{OFF}	V+ = +4.5V, V- = -4.5V, $V_{NC_}$ or $V_{NO_}$ = ±3.3V, V_L = V+, Figure 2	T_A = +25°C		110	150	ns
			T_A = T_{MIN} to T_{MAX}			350	
Break-Before-Make Delay	t_{BBM}	Figure 3, MAX4679 only, R_L = 300Ω, C_L = 35pF		5			ns
Charge Injection	Q	R_{GEN} = 0, C_L = 1nF, V_{GEN} = 0, Figure 4			85		pC
Off-Isolation	V_{ISO}	R_L = 50Ω, C_L = 5pF, f = 1MHz, Figure 5a			-65		dB
Crosstalk		R_L = 50Ω, C_L = 5pF, f = 1MHz, Figure 6a			-84		dB
-3dB Bandwidth	BW	R_S = 50Ω, R_L = 50Ω, Figure 7a			66		MHz
NC or NO Off-Capacitance	$C_{(N_OFF)}$	f = 1MHz, Figure 8			85		pF
COM Off-Capacitance	$C_{(COMOFF)}$	f = 1MHz, Figure 8			85		pF
On-Capacitance	$C_{(ON)}$	f = 1MHz, Figure 8			350		pF

ELECTRICAL CHARACTERISTICS–Single Supply

(V+ = +5V ±10%, V- = 0, V_L = +2.7V to V+, GND = 0, V_{IH} = +2.4V, V_{IL} = +0.8V, T_A = T_{MIN} to T_{MAX}, unless otherwise noted. Typical values are at T_A = +25°C.) (Note 2)

PARAMETER	SYMBOL	CONDITIONS		MIN	TYP	MAX	UNITS
ANALOG SWITCH							
Input Voltage Range	$V_{COM_}$, $V_{NO_}$, $V_{NC_}$			0		V+	V
On-Resistance	R_{ON}	V+ = +4.5V, $I_{COM_}$ = 50mA, $V_{NO_}$ or $V_{NC_}$ = 3.3V	T_A = +25°C		1.8	2.7	Ω
			T_A = T_{MIN} to T_{MAX}			3.5	
On-Resistance Match Between Channels (Note 3)	ΔR_{ON}	V+ = +4.5V, $I_{COM_}$ = 50mA, $V_{NO_}$ or $V_{NC_}$ = 3.3V	T_A = +25°C		0.05	0.15	Ω
			T_A = T_{MIN} to T_{MAX}			0.3	
On-Resistance Flatness (Note 4)	R_{FLAT}	V+ = +4.5V, $I_{COM_}$ = 50mA, $V_{NO_}$ or $V_{NC_}$ = 3.3V, 1.5V	T_A = +25°C		0.15	0.25	Ω
			T_A = T_{MIN} to T_{MAX}			0.4	
NC_ or NO_ Off-Leakage Current (Note 5)	$I_{N_(OFF)}$	V+ = +5.5V; $V_{NO_}$ or $V_{NC_}$ = 4.5V, 1V; $V_{COM_}$ = 1V, 4.5V	T_A = +25°C	-1	0.1	1	nA
			T_A = T_{MIN} to T_{MAX}	-10		10	
COM_ Off-Leakage Current (Note 5)	$I_{COM_(OFF)}$	V+ = +5.5V; $V_{NO_}$ or $V_{NC_}$ = 4.5V, 1V; $V_{COM_}$ = 1V, 4.5V	T_A = +25°C	-1	0.1	1	nA
			T_A = T_{MIN} to T_{MAX}	-10		10	
COM_ On-Leakage Current (Note 5)	$I_{COM_(ON)}$	V+ = +5.5V; $V_{COM_}$ = 1V, 4.5V; $V_{NO_}$ or $V_{NC_}$ = 1V, 4.5V, or floating	T_A = +25°C	-2	0.2	2	nA
			T_A = T_{MIN} to T_{MAX}	-25		25	
LOGIC INPUT							
Input Low Voltage	V_{IL}	V_L = V+				0.8	V
Input High Voltage	V_{IH}	V_L = V+		2.4			V
Input Leakage Current	I_{IN}	V_L = V+		-1	0.005	1	µA
POWER SUPPLY							
Positive Supply Voltage	V+			2.7		6	V
Logic Supply Voltage	V_L			2.7		V+	V
Positive Supply Current	I+	$V_{IN_}$ = 0 or V_L, V_L = V+			1	1	µA
Logic Supply Current	I_L	$V_{IN_}$ = 0 or V_L, V+ = 5.5V				1	µA
Ground Current	I_{GND}	$V_{IN_}$ = 0 or V_L, V+ = 5.5V			1	10	µA
DYNAMIC							
Turn-On Time	t_{ON}	V_L = V+, V+ = +4.5V; $V_{NC_}$ or $V_{NO_}$ = 3.3V, R_L = 300Ω, C_L = 35pF, Figure 2	T_A = +25°C		600	1000	ns
			T_A = T_{MIN} to T_{MAX}			1400	
Turn-Off Time	t_{OFF}	V_L = V+, V+ = +4.5V; $V_{NC_}$ or $V_{NO_}$ = 3.3V, R_L = 300Ω, C_L = 35pF, Figure 2	T_A = +25°C		120	165	ns
			T_A = T_{MIN} to T_{MAX}			400	

ELECTRICAL CHARACTERISTICS–Single Supply (continued)

(V+ = +5V ±10%, V- = 0, V_L = +2.7V to V+, GND = 0, V_{IH} = +2.4V, V_{IL} = +0.8V, T_A = T_{MIN} to T_{MAX}, unless otherwise noted. Typical values are at T_A = +25°C.) (Note 2)

PARAMETER	SYMBOL	CONDITIONS	MIN	TYP	MAX	UNITS
Break-Before- Make Delay	t_{BBM}	MAX4679 only, R_L = 300Ω, C_L = 35pF, Figure 3	5			ns
Charge Injection	Q	R_{GEN} = 0, C_L = 1nF, V_{GEN} = 0, Figure 4		9		pC
Off-Isolation	V_{ISO}	R_L = 50Ω, C_L = 5pF, f = 1MHz, Figure 5b		-65		dB
Crosstalk		R_L = 50Ω, C_L= 5pF, f = 1MHz, Figure 6b		-84		dB
-3dB Bandwidth	BW	R_S = 50Ω, R_L = 50Ω, Figure 7b		63		MHz
NC or NO Off-Capacitance	$C_{(N_OFF)}$	f = 1MHz, Figure 8		85		pF
COM Off-Capacitance	$C_{(COMOFF)}$	f = 1MHz, Figure 8		85		pF
On-Capacitance	$C_{(ON)}$	f = 1MHz, Figure 8		350		pF

Note 2: The algebraic convention, where the most negative value is a minimum and the most positive value a maximum, is used in this data sheet.

Note 3: $\Delta R_{ON} = R_{ON(MAX)} - R_{ON(MIN)}$.

Note 4: Flatness is defined as the difference between the maximum and minimum value of on-resistance as measured over the specified analog signal ranges.

Note 5: Leakage parameters are 100% tested at maximum-rated hot operating temperature and the highest supply voltage, and guaranteed by correlation at +25°C.

Typical Operating Characteristics

(T_A = +25°C, unless otherwise noted.)

ON-RESISTANCE vs. V_{COM} (DUAL SUPPLY)

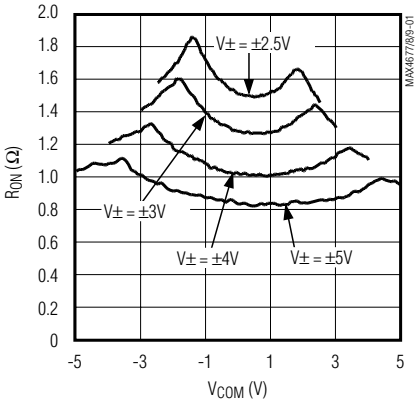

ON-RESISTANCE vs. V_{COM} (SINGLE SUPPLY)

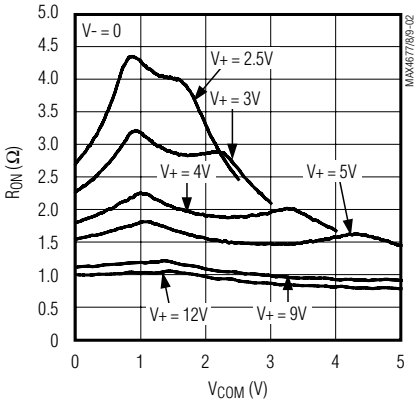

ON-RESISTANCE vs. V_{COM} AND TEMPERATURE (DUAL SUPPLIES)

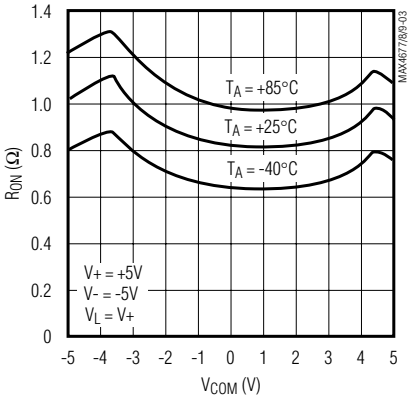

2Ω, Quad, SPST, CMOS Analog Switches

Typical Operating Characteristics (continued)

(T_A = +25°C, unless otherwise noted.)

ON-RESISTANCE vs. V_{COM} AND TEMPERATURE (SINGLE SUPPLY)

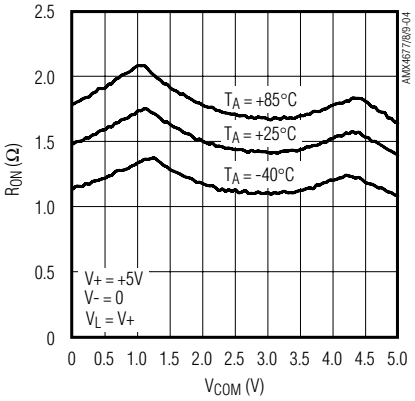

ON-/OFF-LEAKAGE CURRENT vs. TEMPERATURE

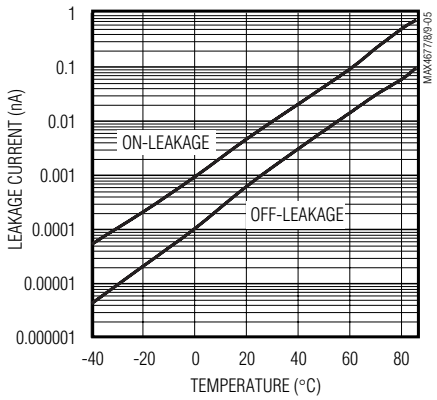

CHARGE INJECTION vs. V_{COM}

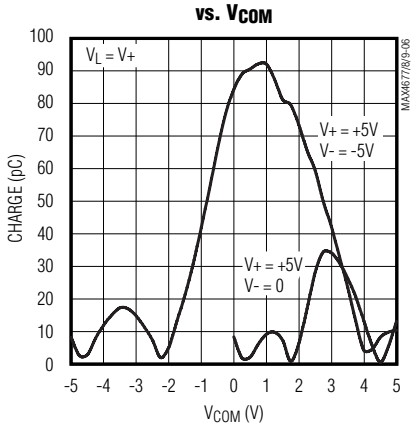

t_{ON}, t_{OFF} vs. SUPPLY VOLTAGE (DUAL SUPPLIES)

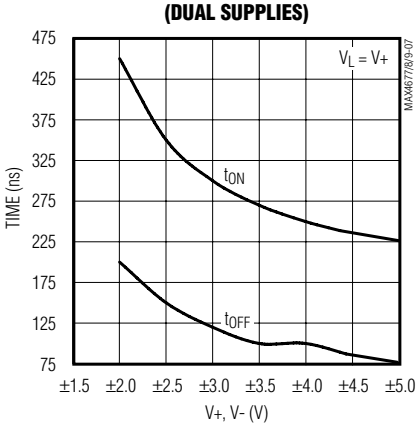

t_{ON}, t_{OFF} vs. TEMPERATURE

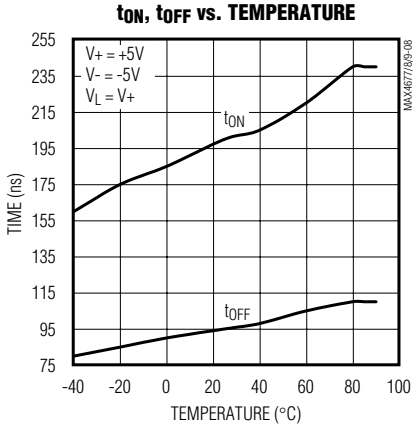

t_{ON}, t_{OFF} vs. LOGIC SUPPLY

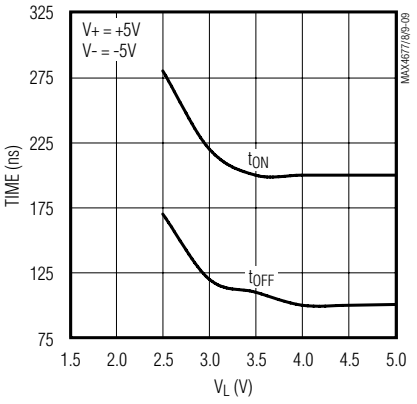

INPUT THRESHOLD vs. LOGIC SUPPLY

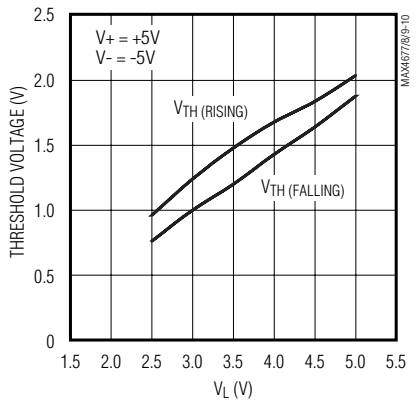

POWER-SUPPLY CURRENT vs. TEMPERATURE

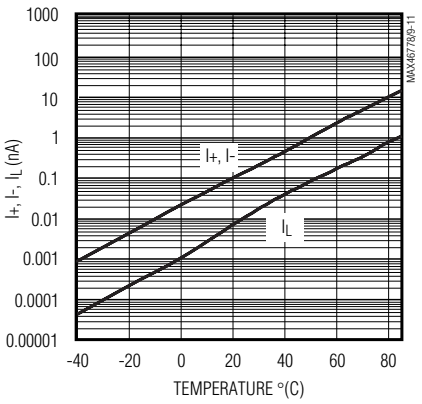

Typical Operating Characteristics (continued)

(T_A = +25°C, unless otherwise noted.)

INSERTION LOSS, OFF-ISOLATION, AND CROSSTALK vs. FREQUENCY (DUAL SUPPLIES)

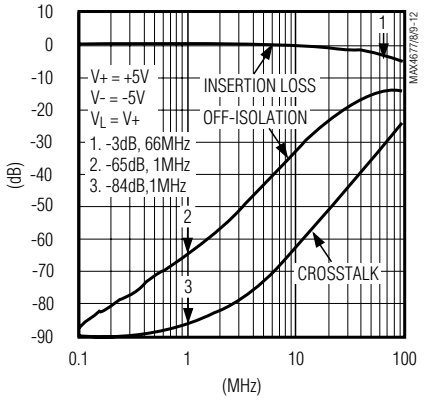

INSERTION LOSS, OFF-ISOLATION, AND CROSSTALK vs. FREQUENCY (SINGLE SUPPLY)

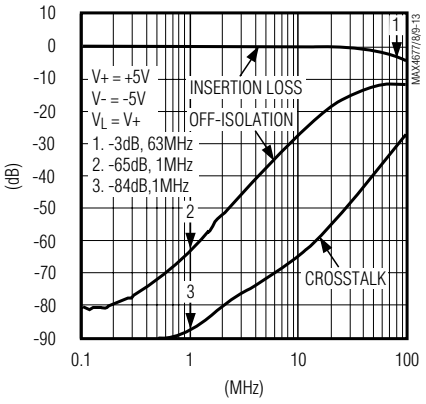

Pin Description

PIN				
MAX4677	MAX4678	MAX4679	NAME	FUNCTION
1, 8, 9, 16	1, 8, 9, 16	1, 8, 9, 16	IN1, IN2, IN3, IN4	Logic Inputs
2, 7, 10, 15	2, 7, 10, 15	2, 7, 10, 15	COM1, COM2, COM3, COM4	Analog Switch Common Terminals
3, 6, 11, 14	—	—	NC1, NC2, NC3, NC4	Analog Switch Normally Closed Terminals
—	3, 6, 11, 14	—	NO1, NO2, NO3, NO4	Analog Switch Normally Open Terminals
—	—	3, 6	NO1, NO4	Analog Switch Normally Open Terminals
—	—	11, 14	NC2, NC3	Analog Switch Normally Closed Terminals
4	4	4	V-	Negative Supply-Voltage Input. Connect to GND for single-supply operation.
5	5	5	GND	Ground
12	12	12	V_L	Logic Supply Input
13	13	13	V+	Positive Supply Input

Applications Information

Overvoltage Protection

Proper power-supply sequencing is recommended for all CMOS devices. Do not exceed the absolute maximum ratings because stresses beyond the listed ratings can cause permanent damage to the devices. Always sequence V+ on first, then V-, then V_L followed by the logic inputs, NO_, NC_, or COM. If proper power-supply sequencing is not possible, add two small signal diodes (D1, D2) in series with the supply pins, and a Schottky diode between V+ and V_L for overvoltage protection (Figure 1). Adding diodes reduces the analog signal range to one diode drop below V+ and one diode drop above V-, but does not affect the devices' low switch resistance and low leakage characteristics. Device operation is unchanged, and the difference between V+ and V- should not exceed 11V.

Power-supply bypassing improves noise margin and prevents switching noise from propagating from the V+ supply to other components. A 0.1µF capacitor connected from V+ to GND is adequate for most applications.

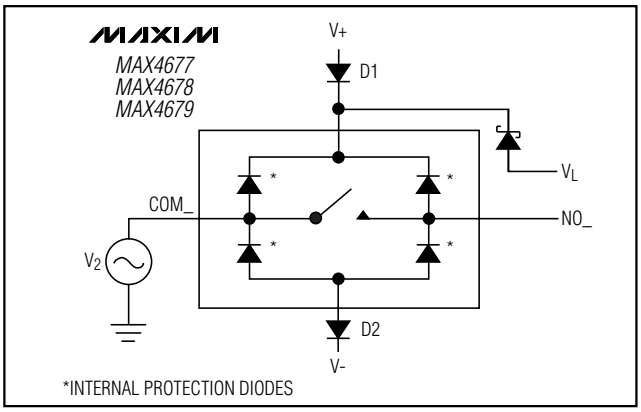

Figure 1. Overvoltage Protection Using External Blocking Diodes

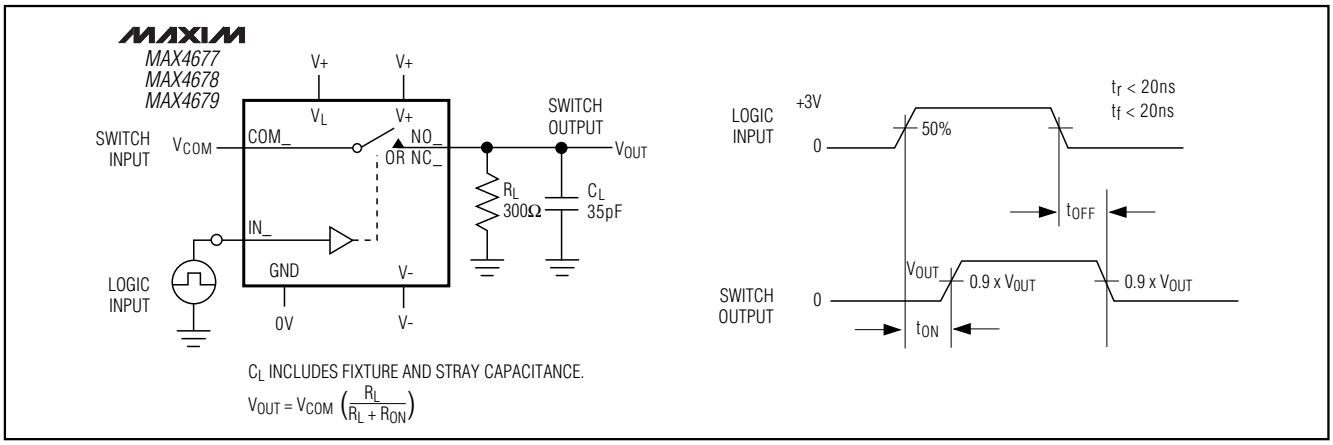

Figure 2. Switching Time

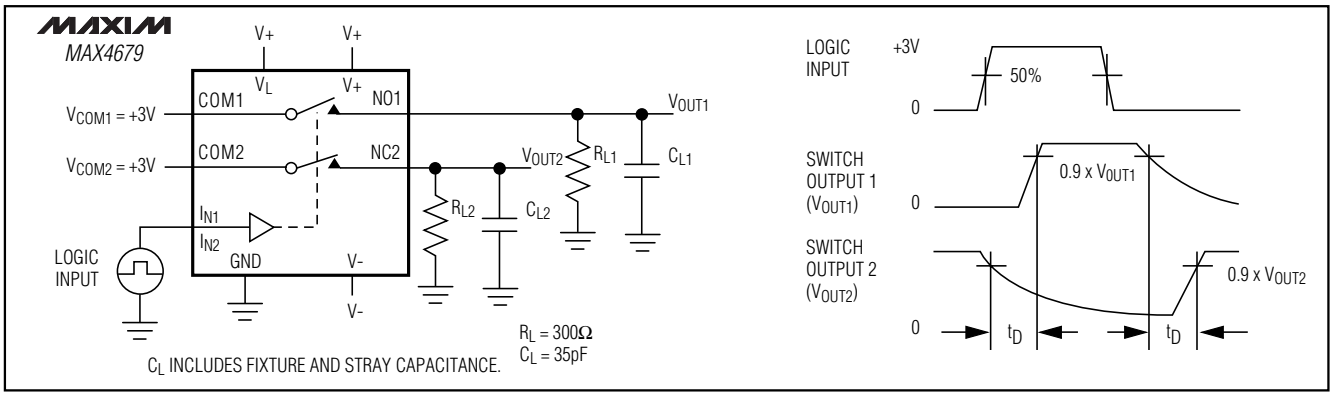

Figure 3. Break-Before-Make Interval (MAX4679 Only)

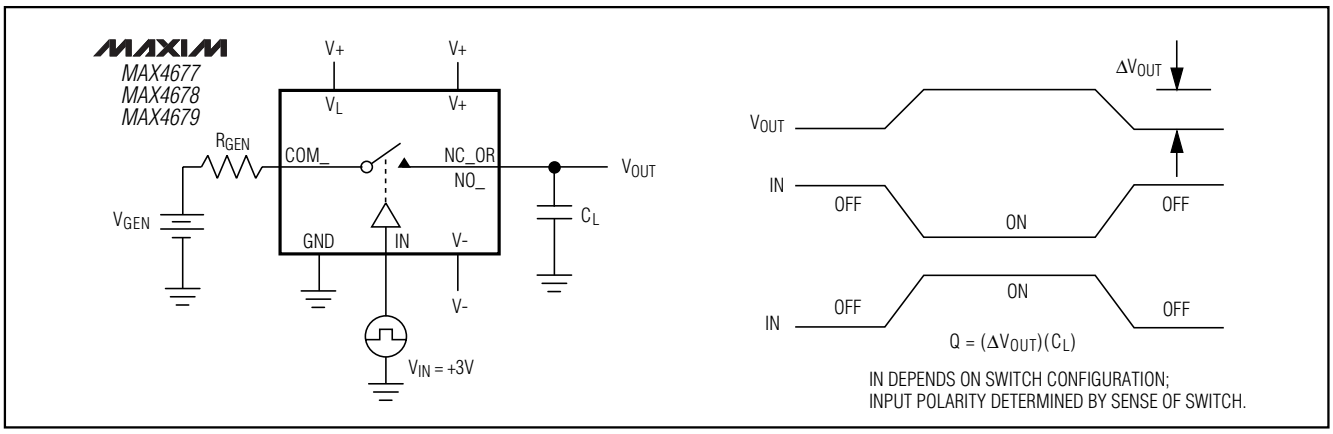

Figure 4. Charge Injection

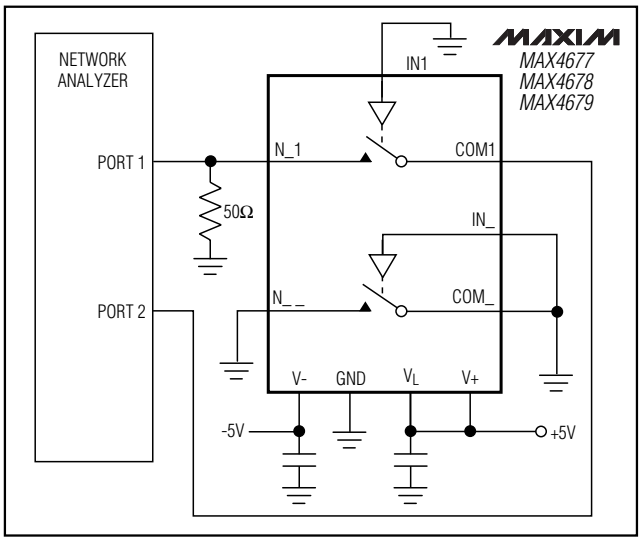

Figure 5a. Off-Isolation Test Circuit, Dual Supplies

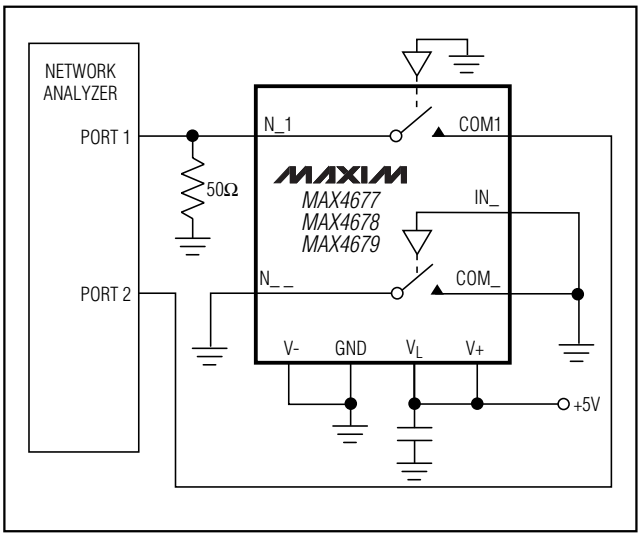

Figure 5b. Off-Isolation Test Circuit, Single Supply

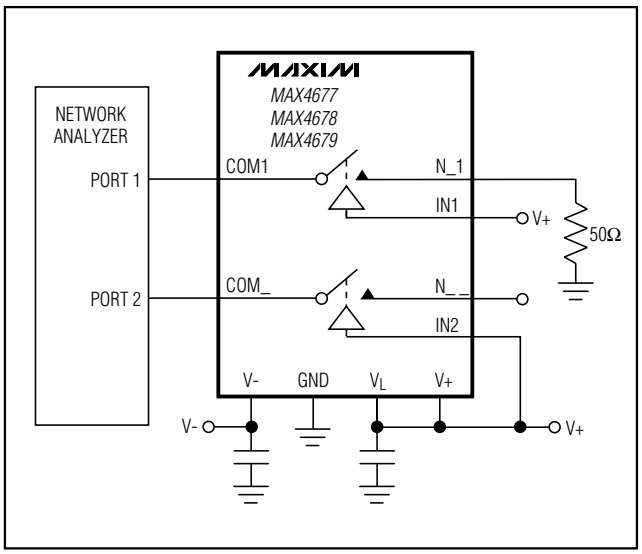

Figure 6a. Crosstalk Test Circuit, Dual Supplies

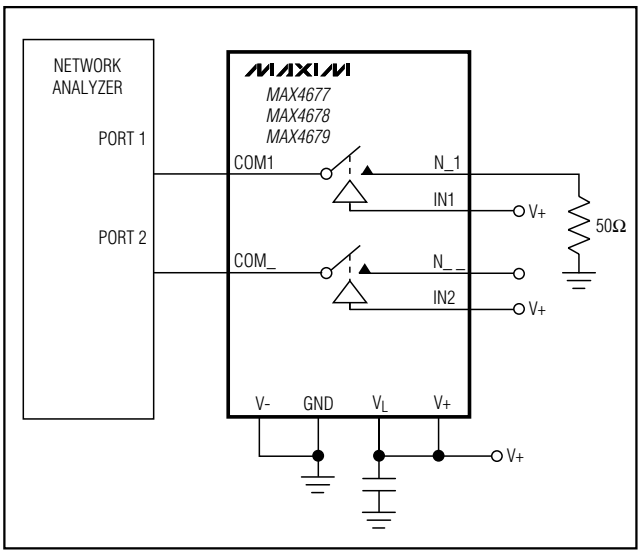

Figure 6b. Crosstalk Test Circuit, Single Supply

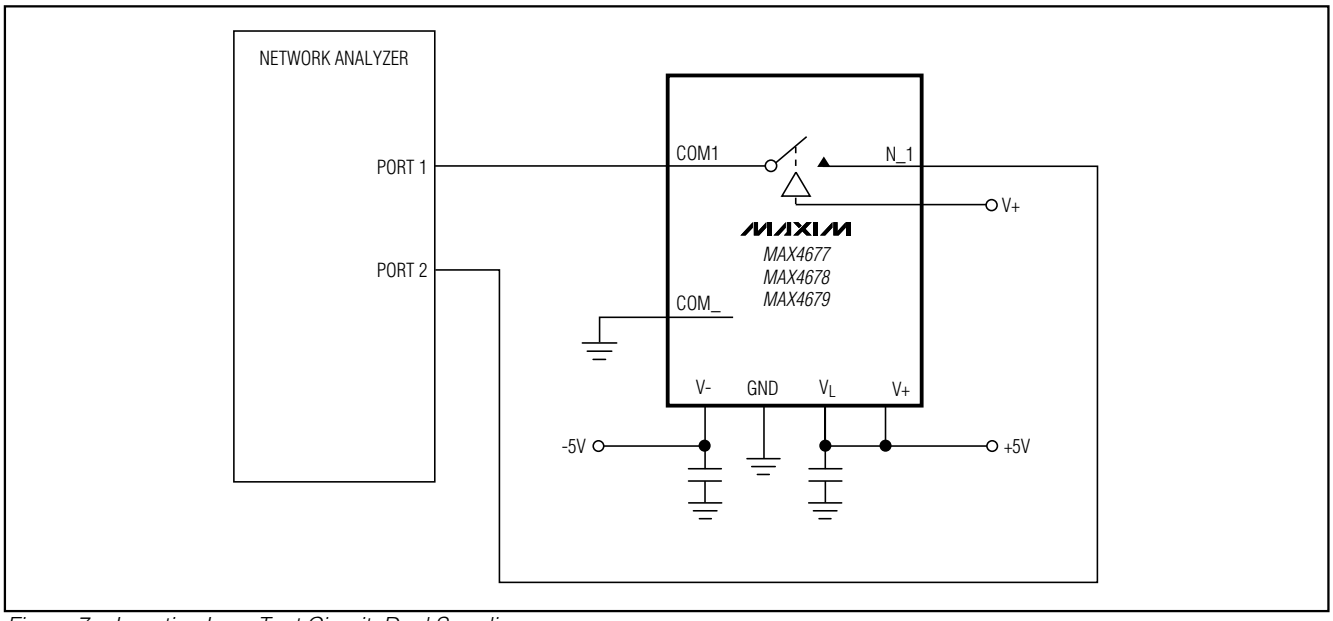

Figure 7a. Insertion Loss Test Circuit, Dual Supplies

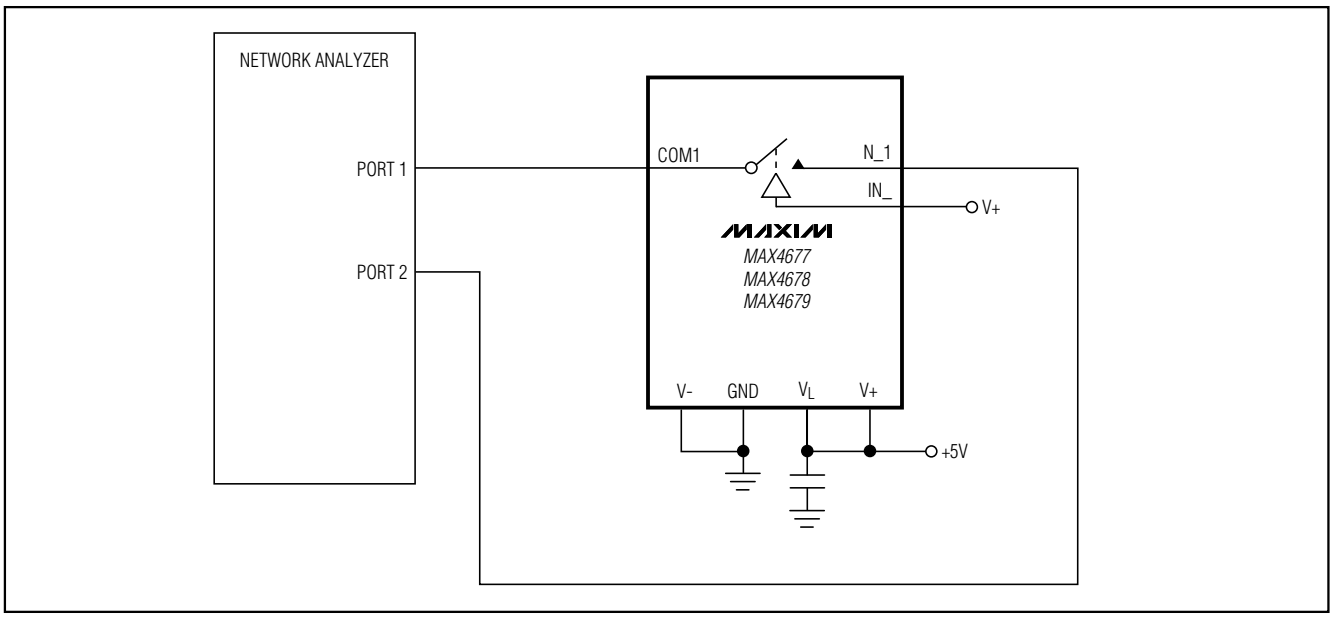

Figure 7b. Insertion Loss Test Circuit, Single Supply

Chip Information

TRANSISTOR COUNT: 240

PROCESS: CMOS

2Ω, Quad, SPST, CMOS Analog Switches

Package Information

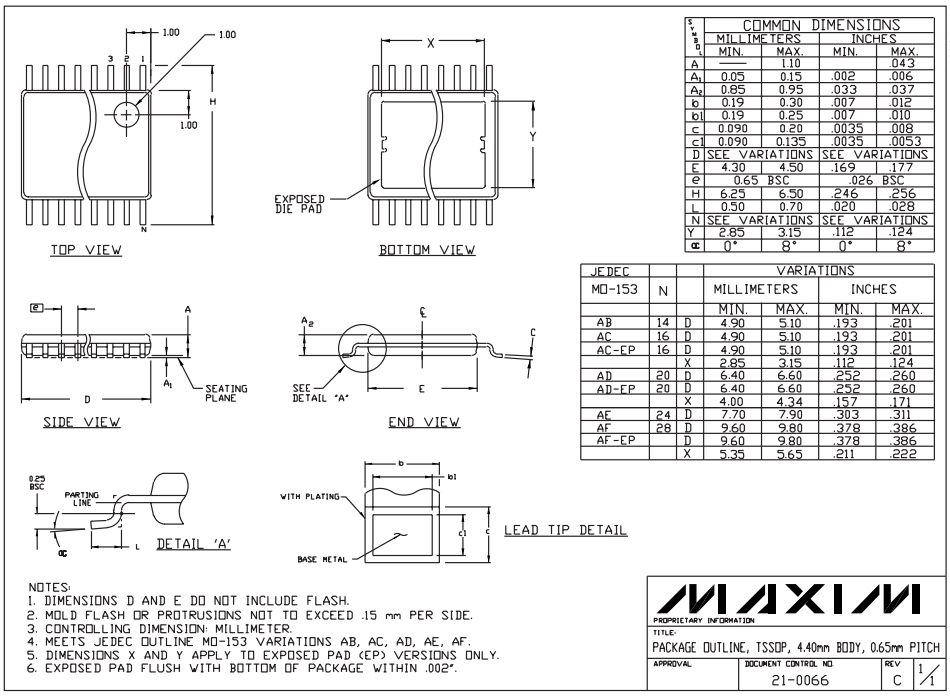

TSSOP.EPS

SYMBOL	COMMON DIMENSIONS			
	MILLIMETERS		INCHES	
	MIN.	MAX.	MIN.	MAX.
A	----	1.10		.043
A_1	0.05	0.15	.002	.006
A_2	0.85	0.95	.033	.037
b	0.19	0.30	.007	.012
b1	0.19	0.25	.007	.010
c	0.090	0.20	.0035	.008
c1	0.090	0.135	.0035	.0053
D	SEE VARIATIONS		SEE VARIATIONS	
E	4.30	4.50	.169	.177
e	0.65 BSC		.026 BSC	
H	6.25	6.50	.246	.256
L	0.50	0.70	.020	.028
N	SEE VARIATIONS		SEE VARIATIONS	
Y	2.85	3.15	.112	.124
α	0°	8°	0°	8°

JEDEC			VARIATIONS			
MO-153	N		MILLIMETERS		INCHES	
			MIN.	MAX.	MIN.	MAX.
AB	14	D	4.90	5.10	.193	.201
AC	16	D	4.90	5.10	.193	.201
AC-EP	16	D	4.90	5.10	.193	.201
		X	2.85	3.15	.112	.124
AD	20	D	6.40	6.60	.252	.260
AD-EP	20	D	6.40	6.60	.252	.260
		X	4.00	4.34	.157	.171
AE	24	D	7.70	7.90	.303	.311
AF	28	D	9.60	9.80	.378	.386
AF-EP		D	9.60	9.80	.378	.386
		X	5.35	5.65	.211	.222

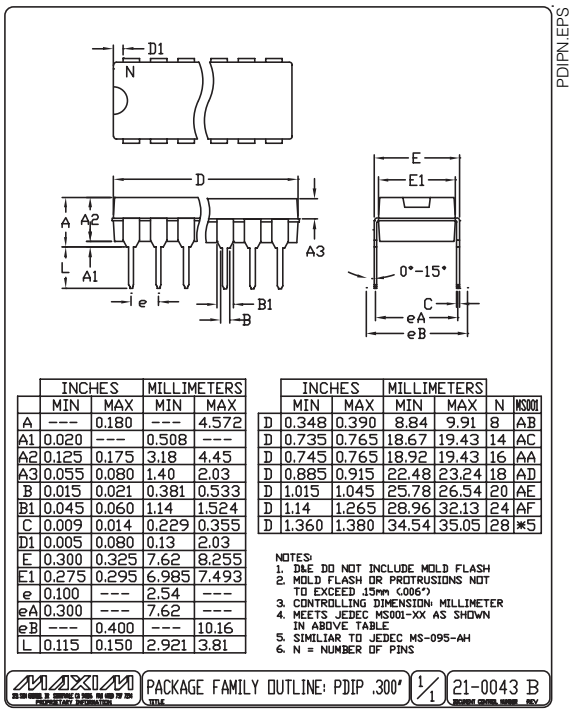

PDIPN.EPS

	INCHES		MILLIMETERS	
	MIN	MAX	MIN	MAX
A	---	0.180	---	4.572
A1	0.020	---	0.508	---
A2	0.125	0.175	3.18	4.45
A3	0.055	0.080	1.40	2.03
B	0.015	0.021	0.381	0.533
B1	0.045	0.060	1.14	1.524
C	0.009	0.014	0.229	0.355
D1	0.005	0.080	0.13	2.03
E	0.300	0.325	7.62	8.255
E1	0.275	0.295	6.985	7.493
e	0.100	---	2.54	---
eA	0.300	---	7.62	---
eB	---	0.400	---	10.16
L	0.115	0.150	2.921	3.81

	INCHES		MILLIMETERS			
	MIN	MAX	MIN	MAX	N	MS001
D	0.348	0.390	8.84	9.91	8	AB
D	0.735	0.765	18.67	19.43	14	AC
D	0.745	0.765	18.92	19.43	16	AA
D	0.885	0.915	22.48	23.24	18	AD
D	1.015	1.045	25.78	26.54	20	AE
D	1.14	1.265	28.96	32.13	24	AF
D	1.360	1.380	34.54	35.05	28	*5

Maxim cannot assume responsibility for use of any circuitry other than circuitry entirely embodied in a Maxim product. No circuit patent licenses are implied. Maxim reserves the right to change the circuitry and specifications without notice at any time.

© 2000 Maxim Integrated Products Printed USA MAXIM is a registered trademark of Maxim Integrated Products.

E. Manuals

E.1. Electrical Shutdown - How to turn the UHV System off and on again

In case of a scheduled electrical shutdown in the Wong building, the following procedure should be done. Important: This list has last been updated in April 2018, so in case there are more electrical parts that were added to the system, please make sure that they are turned off properly too. Ideally, the students working on the system keep this manual updated. Ideally, the manual should be printed and be visibly placed in the laboratory so that technicians can find it in case of an emergency.

E.1.1. Before Shutdown - How to turn the System off

1) Open all the manual valves so that the load-lock, four-point probe- and measurement chamber are connected to each other by open gates. This will allow all parts under UHV to be pumped by the Ti sublimation pump.

2) Make sure that all bellows are extended!

3) Please write the time and pressure from the MKS gauge controller in a notebook.

4) Close the angle valve towards the turbo pump (flip the Switch to *CLOSE*).

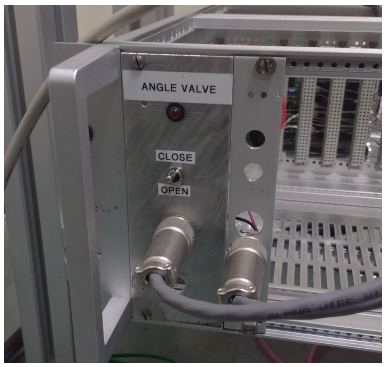

5) Turn off the turbo pump (diamond-shaped button on controller), then the roughing pump (switch on the pump) and vent through the turbo pump (open valve on the pump counterclockwise).

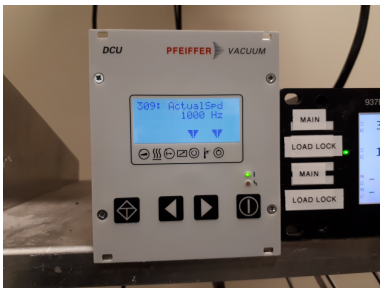

6) Please write the pressure from the MKS gauge controller in a notebook. The pressure should not have changed much.

7) Turn off the Ion Pump: Press *Stop HV* on the touchscreen (top right) for at least 3 s and the HV will shut down. Then switch the power button on the ion pump controller to *OFF-O*. Have a look at the MKS gauge controller again and write the pressure down.

8) Turn off the MKS gauge controller (switch on the backside).

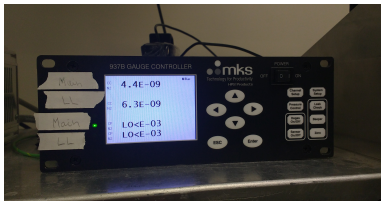

9) If necessary, turn every other controller and computer off if not done so yet and unplug everything from the wall plugs.

E.1.2. After Shutdown - How to turn the System on

1. Switch the power button of the MKS gauge controller to *ON*. With the arrow keys (up and down), go to the two bottom gauges and turn both on (Press button *Sensor ON/OFF*)

Now the tricky part starts. If the pressure is below 10^{-3} mbar on both gauges, continue with steps 2-3. If the pressure is higher than 10^{-3} mbar continue with step 4.

2. The pressure is below 10^{-3} mbar. Start the two other gauges by selecting them on the MKS controller (two top ones and press button *Sensor ON/OFF*)

3. A) If the pressure is below 10^{-5} mbar that the gauges read out, turn on the ion pump controller (switch power to *ON-I* and on the touch screen, press the button *HV ON* for at least 3 s). The ion pump will start to ramp up and you are all set. B) If the pressure in the chamber was higher than 10^{-5} mbar, continue with step 4.

4. Continue with the following steps (4-8) if the pressure was not low enough to directly turn on the ion pump. What you now have to do is to pump through the roughing pump and the turbo first before you can start the ion pump. For that, check that the vent valve on the turbo pump is fully closed and start the roughing pump (switch button to *ON*)

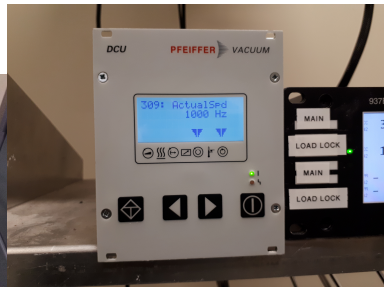

5. Wait 5 min and turn on the turbo pump (turn on on backside and then press diamond-shaped symbol). The turbo pump should ramp up to 1000 Hz within minutes.

6. Wait 30 min.

7. Open the angle valve by flipping the switch to *OPEN*.

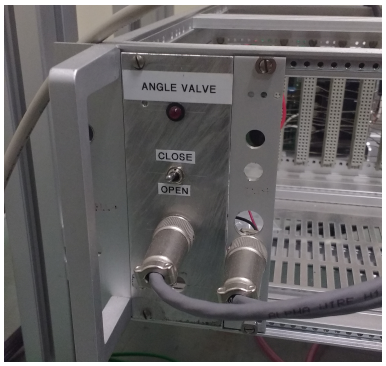

8. The pressure in the chamber should now go down. Wait until the pressure is below 10^{-5} mbar and then turn on the ion pump, see step 3.A)

E.2. Bake-out

Before starting a bake, it is best to make sure that everything that is installed on the system is working. It is also recommended to check the system for large leaks (if the pressure is not going below 1×10^{-7} mbar). An easy test to detect leaks is to squirt methanol onto suspected flanges that might leak. If there is a large leak, methanol will be sucked into the system and the chamber pressure will increase. Further, a helium leak detector can be used to detect much smaller leaks, where the RGA on the suitcase or the additional leak tester can be used. In order to detect leaks with helium, spray helium onto suspect flanges, wait at least one minute where the RGA/leak detector will detect the increase. Once it is made sure that no bigger leak is on the system, you can prepare for a bake-out.

E.2.1. Preparation

- Remove all non-bakeable items from the chamber (plastics, magnets, electronics, sample tubes, tapes, anything on the instrument table)
- Blow out the water lines
- Give the chamber a good clean with ethanol and dust-free tissues to remove dust, fingerprints and other residues on the outside of the chamber.
- Make sure that all bellows are extended and manipulator arms are moved back.
- Open all necessary valves towards the turbopump. During the bake-out, the chamber has to be pumped through the turbopump to prevent high gas loads into the ion pump. The turbopump must be on during a bake-out at all times, otherwise there is an increased risk of corrosion inside the chamber.
- Wrap any fragile components (windows, electrical feed-throughs, bellows) in 3 to 5

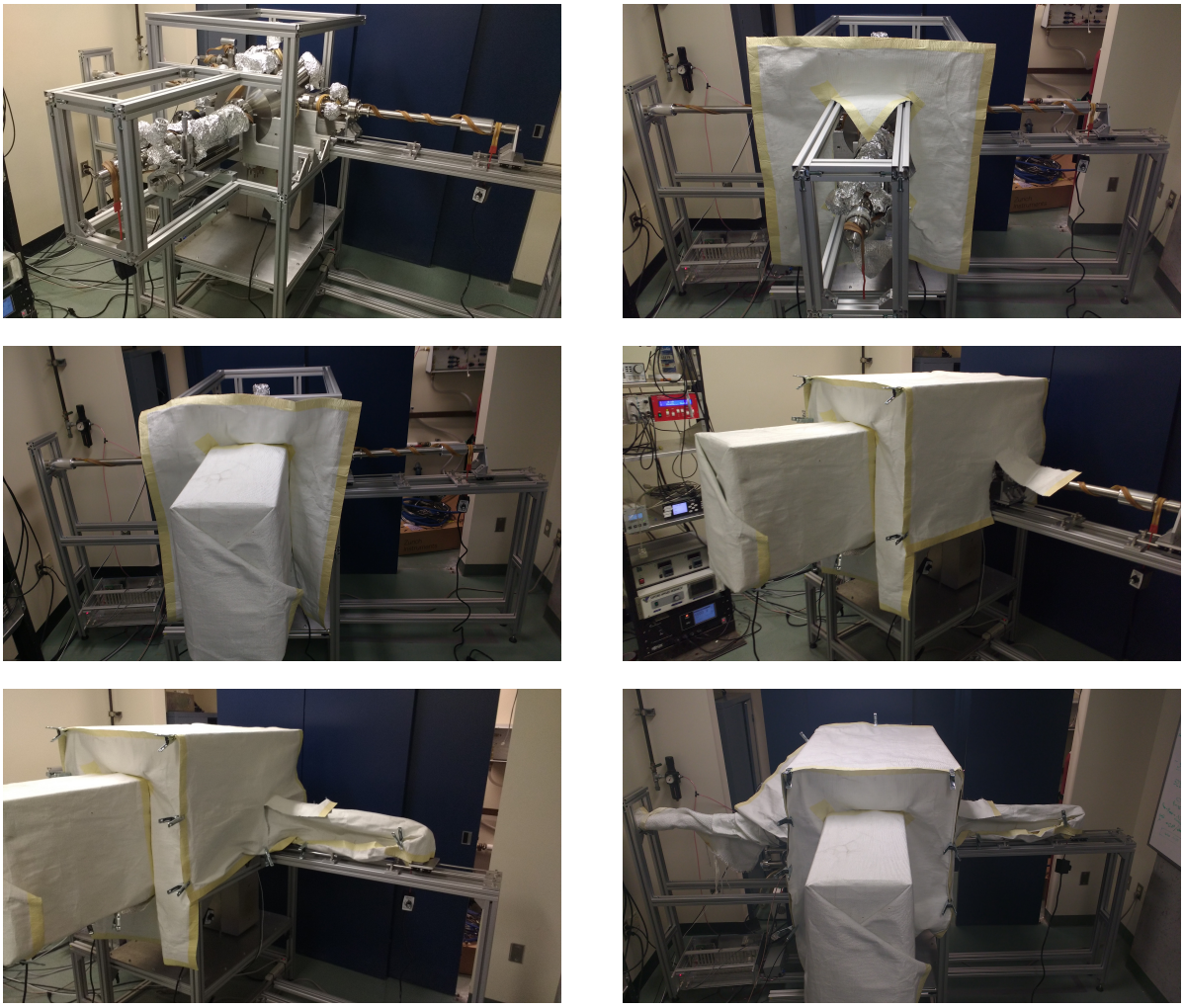

Figure 69: Bake-out Tent Preparation. From top to bottom: After distrubuting the heating tapes around the chamber and using aluminum foil to cover fragile sensitive parts, the custom-made fiberglass sheets can be used to cover the whole system for bake-out. All-metal spring clamps are used to tightly hold the sheets in place and to seal the tent.

layers of aluminum foil. This will allow these parts to heat more gradually and will not undergo as much strain from heating.

- Attach the heaters and thermocouples to the chamber. Do not overlay the heating tapes on top of each other.

- Cover the chamber using the appropriate bake-out tent.

- Make sure that the percentage controllers on the heating tapes are turned off and then plug them into the wall plugs. Important to note: Do not plug all heating tapes on the same wall-plug line. Since the tapes draw a couple of amperes each, it is recommended to spread them and connect to as many different wall-plugs as possible. Since the risk of a failure of the turbopump during a bake-out should be reduced, no heat tape should be connected to the same line where the turbopump is pluged in.

- Have someone else to check your work! Make sure that you know the maximum temperatures you can bake at for each component of your system!

E.2.2. During Bake-out

Once the chamber is covered and all preparations were made, turn off the ion pumps and turn on the heaters. The ion pump will be turned off during the bake-out and only turned on at the very last stage of the bake-out. It is recommended to gradually increase the temperature, while closely monitoring the temperature and pressure. As high temperature gradients due to uneven heating induce a lot of strain to the components and can lead to damage, increase the temperature only slowly. The data logger explained in appendix B.2 comes in very handy as it allows to monitor temperature and pressure online.

- Go to about 50 °C first, watch the pressure to increase and wait until the pressure is down to the same pressure level as started.

- Increase the temperature slowly in periodic steps to the finite temperature. The pressure should not jump up more than two orders of magnitude at the time, otherwise wait for long enough for the pressure to come down.

- Closely monitor temperature and pressure. Too high of a temperature can damage components (we typically do not go above 150 °C, and if only a service bake-out is

performed, we normally bake at 120 °C) and if they pressure is too high this may indicate a leak that was missed.

Pressure should initially increase as species are outgassed and then decrease as bake continues. Bake at least 36 h or until pressure decrease levels off. At the last stage of the bake-out (last 2 h), degas the ion getter pump if the suitcase is baked as well. In the last 1 h of the bake-out, turn on the ion pump. Turning the ion pump on again will lead to a large spike in pressure but will come down within an hour to the pressure level before turning it on.

E.2.3. Post Bake-out

- Turn the heaters off and start to remove the bake-out apparatus about 2 h after the heaters have been turned off. This will allow the system to cool down gradually.
- Once the bake-out tent has been removed, let the system cool down to room temperature
- Plug in all non-bakeable components again and test the components after the bake-out.
- Your pressure may still not be below 1×10^{-9} mbar , but that is okay. You still need to degas any filaments or relevant components (degas filaments of the titanium sublimation pump, degas RGA, degas sample holder). Filaments tend to absorb gases very strongly and need to be locally heated at higher temperatures than achieved in a bake-out.

Once post bake-out has been performed, the additional pumps after the bake (ion pump and TSP) will decrease the pressure to the 1×10^{-11}–1×10^{-10} mbar range.

E.3. UHV Four-Point Probe Software - Quick Guide

This manual describes how to start the homebuilt four-point probe software. This interface has been created using Python. Most of the graphical design has been implemented using *Spinmob* package from Jack Sankey (https://github.com/Spinmob/spinmob/wiki). To connect to the controllers, the *Serial* package has been used. Drivers for the different hardware have been attached to appendix C. The camera integration has been done using the *OpenCV* package, data handling and plotting has been implemented using *matplotlib*- and the *Filemanagement* package.

E.3.1. Start-up

- Open the Desktop App *Python(x,y)* and start *Spyder* (options: none (IDE))
- Open the Manipulator Graphical Interface (MGI) version 14 (**MGI14.py**).
- Press F6 for *Run Settings* or go under *Run->Configure...* and make sure *Execute in a new dedicated Python console* and *Interact with the Python console after execution* is selected (see figure 70).

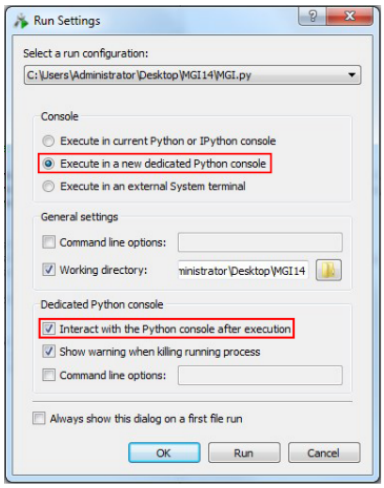

Figure 70: Run Settings in Spyder 2.7.

- Run the application. The User Interface should start.

E.3.2. Overview

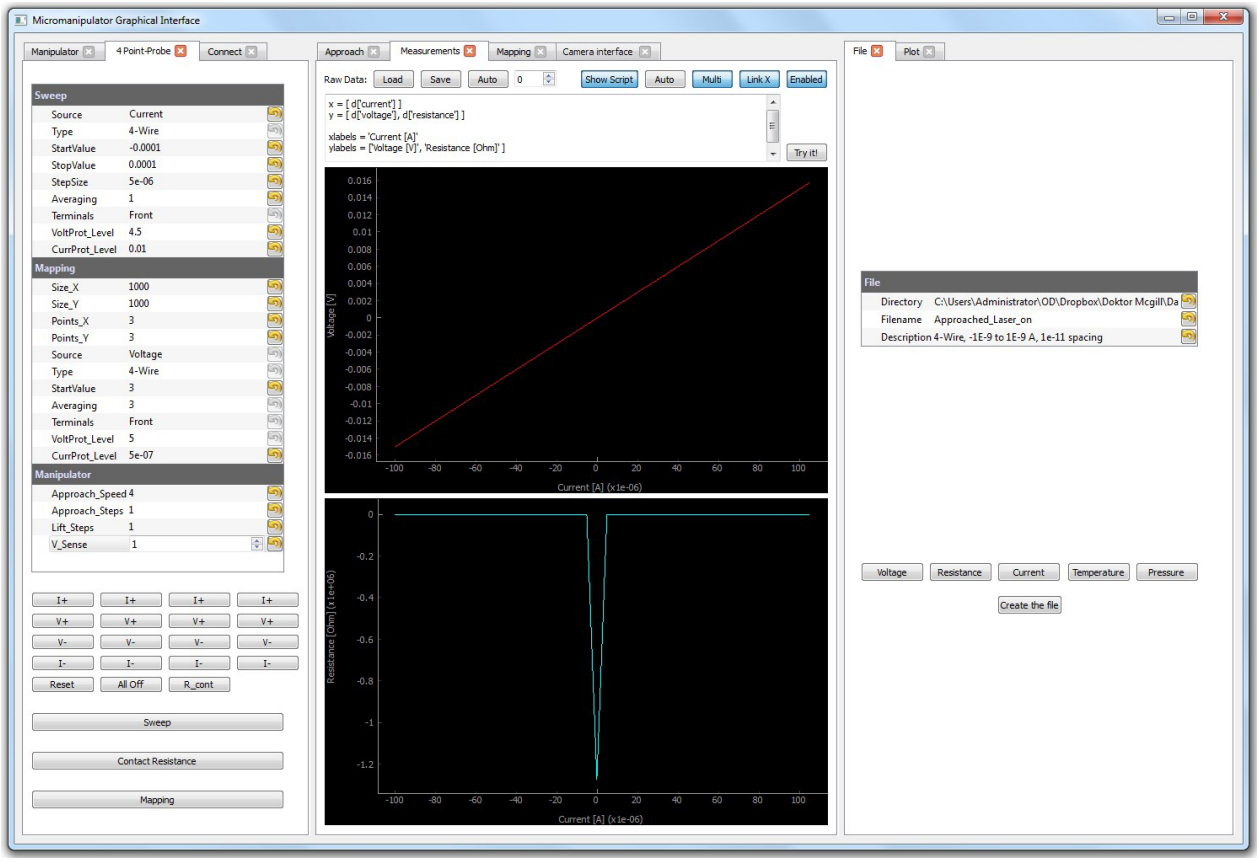

Figure 71: Overview of the User Interface

Once the application has been started, the main User Interface should look similar to figure 71. This is a work in progress so you might observe differences. However, the software is **separated in three different columns**. The first column is for **manipulation**. Here you can connect to the controllers, operate the four-point probe and manipulate the RRP microcontroller. The second column is for **measurements**. Here you can observe in real-time what the controller reads out while approaching, can check the four-point probe measurements and can have a look at the position of the four-point probe inside the chamber. The third column

is for **data handling**. You can define the name of the file and where you want to store it, and you can post-process the files and graph it. For further references, only the names of the tabs will be mentioned. For simplification, all tabs for manipulation, measurement and data-handling are shown in figures 72, 73 and 74.

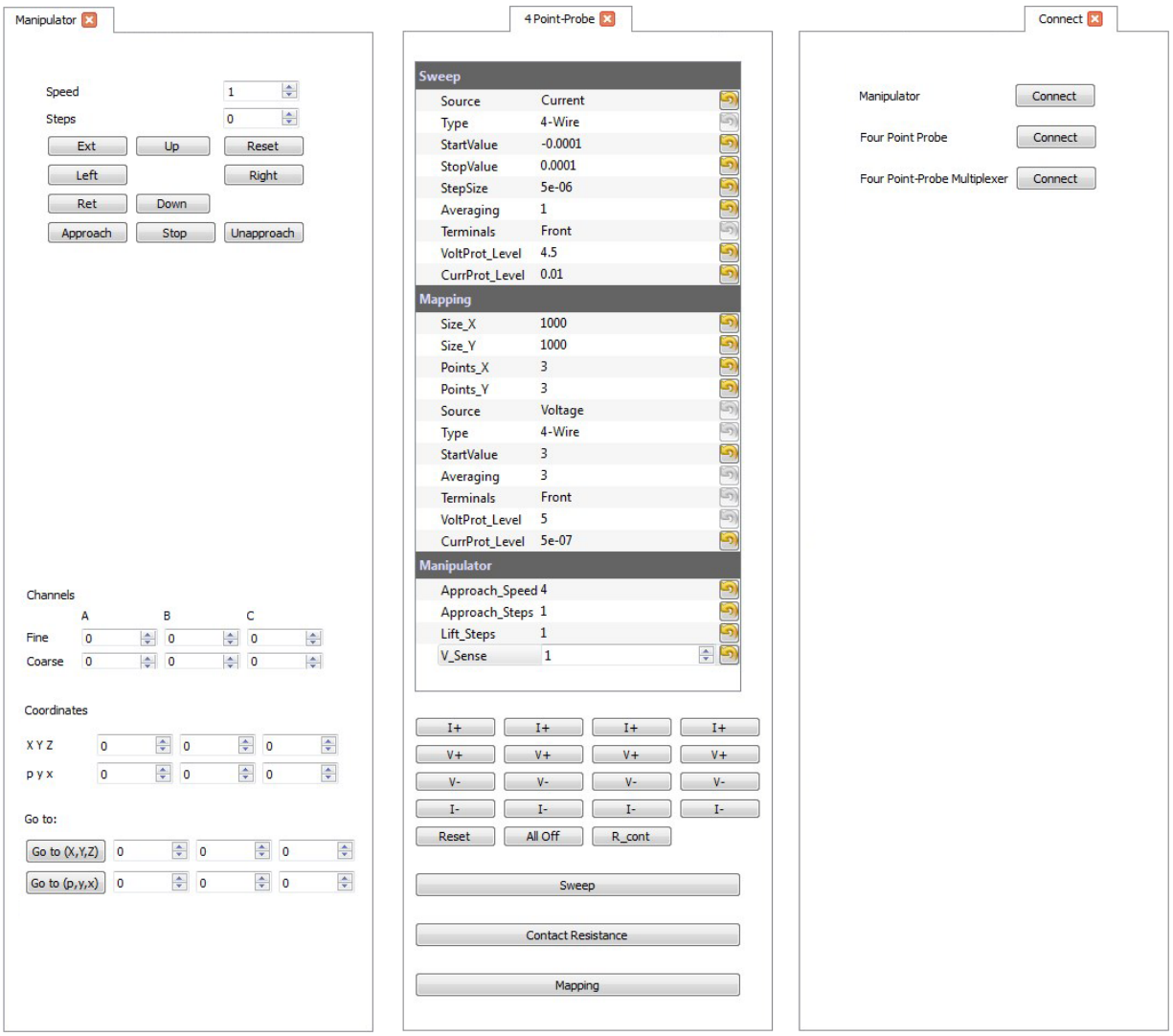

Figure 72: Overview of the Manipulation Tabs.

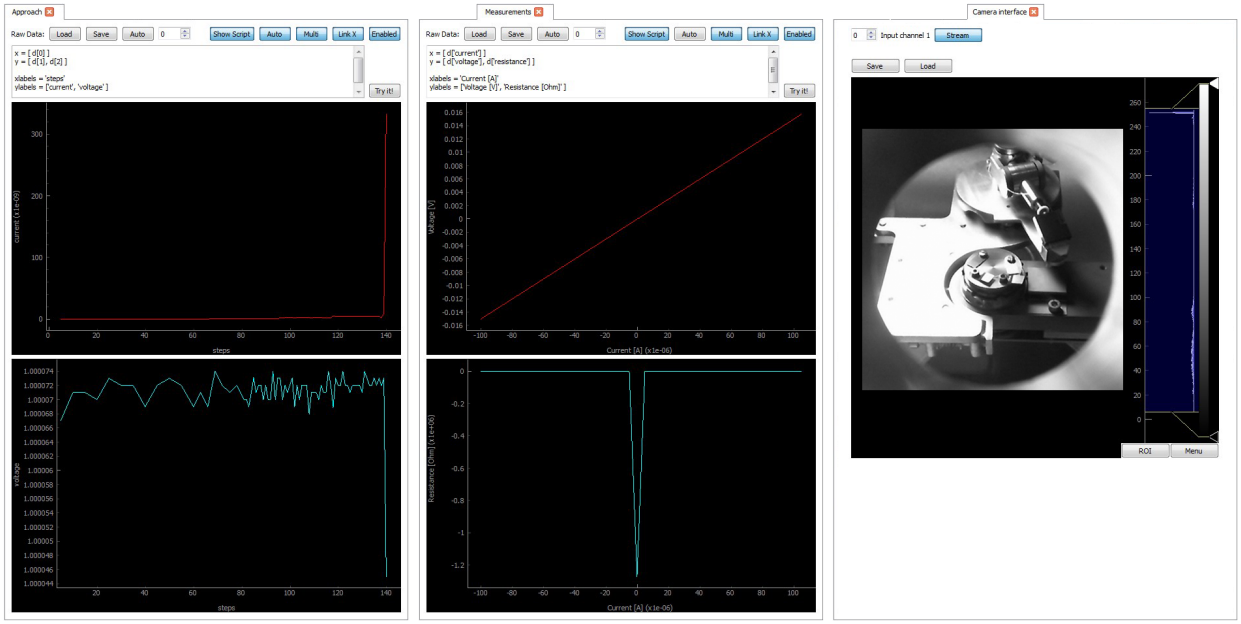

Figure 73: Overview of the Measurement Tabs.

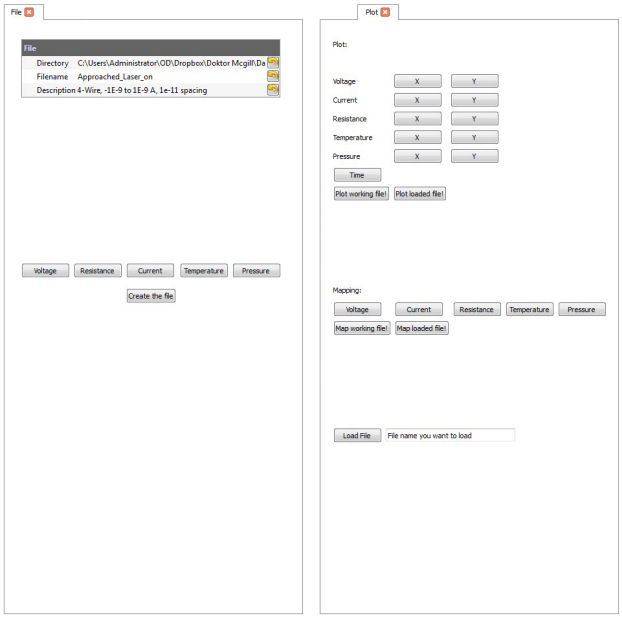

Figure 74: Overview of the Data Handling Tabs.

E.3.3. Connecting to Controllers

Under *Connect*, press the button *Connect* for the manipulator (Kleindiek MM3a), Four-Point Probe (Keithley 2400LV) and Four-Point Probe Multiplexer (Arduino). It is important to note here that the software uses the drivers attached in appendix C. They are the foundation of the software. While connecting, the Spyder software will print the status of the connection, so it is important to have a look at it while connecting. In case there is an issue with connecting, either the controllers are not properly pluged in OR the Serial Ports have changed. In case no connection can be made, the file **__defines.py** needs to be opened (also attached in appendix C). This file defines the **ports**, **baudrates**, and **host names** of all controllers. The ports are hard-coded, which means that it has to be defined at what COM-port the software has to look to make a connection. If the port changes, the controller cannot be found. Thus, modify the ports in case you have problems to connect. To find the device, run *Device Manager* under Windows and find the COM-port under Ports. **If the multiplexer board is used**, it is important to that after a connection has been established, that under the *4-Point Probe* tab the multiplexer is set to its reset state. Press *Reset* if the buttons are not activated according to figure 75.

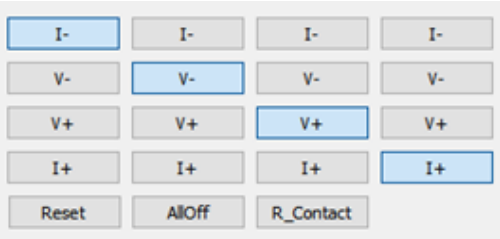

Figure 75: Multiplexer Board Reset Configuration.

E.3.4. Micromanipulator Control and Approach Mechanism

Once connected to the Kleindiek Manipulatior and the Keithley 2400LV, the manipulator can be moved and an approach can be attempted. Under *Manipulator*, the *Speed* and *Steps* can

be chosen to move the manipulator. Always start small and go higher. There are **6 speed levels**, where 1-3 are *fine* and 4-6 are the *coarse* steps of the manipulator. Underneath *Speed* and *Steps*, a matrix for the manipulation is given. Extend (*Ext*), retract (*Ret*), move *left*, *right* and go *Up* and *Down* by pressing the according buttons. The executed step size of the movement will be affected by the *Speed* and *Steps* you have chosen. *Reset* and everything under *Channels*, *Coordinates* and *Go to* can be neglected and is currently **not in use** as it was a handy tool to error solve the mapping of the sample.

To approach to the sample, the buttons *Approach*, *Stop* and *Unapproach* can be used. Before using it, go the *4-Point Probe* tab, reset the Multiplexer board and set up the Manipulator settings properly. This approach mechanism has been separated from the Manipulator tab because it is easy to forget that coarse movements have been done before with high step sizes. This is a protection so that the approach mechanism works independently from the manipulator tab. Set *Approach_Speed* to a value of 4, *Approach_Steps* to 1 (start low and go higher if not satisfied). The *Lift_Steps* are for the unapproach mechanism (I called it unapproach so that it doesn't confuse with retract from the manipulator) and defines how many up-steps should be executed when you want to automatically un-approach. *V_Sense* defines the voltage that is applied to the two outer probes. A value of 0.5–1 V has been found efficient.

Once the setup has been made, go back to *Manipulator* tab and press *Approach* or *Unapproach*. The button *Stop* interferes with the automated process and stops the approach and unapproach mechanism. It is handy to use the Camera now to observe what is going on. Under *Camera Interface* tab, choose the *Input Channel* and press *Stream*. Under the *Approach* tab, a live-stream will be generated that shows the voltage applied and current measured while approaching and un-approaching. If no live-stream appears, press *Show Script* and make sure that the input field shows the same entry as shown in figure 73.

During the approach mechanism, the source-meter will change to a 2-Wire configuration state and will only use the two outer probes to detect the current. If other than the two outer probes should be used to detect the current, the multiplexer board can be used to change the output. The approach mechanism will automatically stop when a current will be detected, however, if the contacts are not good the probe will crash. Thus, always compare Camera, Approach signal and press *Stop* if there is a problem. If the data from the approach wants to be stored, press *Save* in the *Approach* tab and save the data as a raw-file.

E.3.5. Four-Point Probe Measurement

To make a measurement and to check the contacts between the probes, the *4-Point Probe* tab can be used. Use the Sweep tab to set the right conditions of your measurement. The following options are available:

- *Source*: Defines if a current is being outputted or a voltage (set always to Current unless you really want to change it).
- *Type*: Defines if a 2-Wire or 4-Wire measurement should be performed (standard: 4-Wire).
- *Start-* and *Stop-Value*: Defines the range of the source for the current- and voltage-sweep. If the magnitude of the expected resistance is unknown, set a low current (e.g. 1 nA) and go higher from there.
- *StepSize*: Defines the step-size between the start and stop values when sweeped.
- *Averaging*: Defines how many measurements per value have to be made and averaged. Normally, set it to 1. It has been found that the measurements sometimes interrupt and abort if higher values are used. In case there is an interruption while sweeping the source, it might be that the controller hangs due to a too high Averaging value.

- *VoltProt_level* and *CurrProt_Level*: Defines the current- and voltage protection limit of the controller. For micro four-point probes, the maximum current should not exceed 500 µA and a voltage of 1 V is normally used as protection limit. If a higher voltage wants to be used, be aware that the multiplexer board can handle a maximum voltage of 4.5 V. Everything above 4.5 V will break through the board and the MAX4679 chips instead of the sample will be measured.

Once the right conditions have been set up, go to the *File* tab and define directory, filename, give a description of the sample and press *Create the file*. After the button *Sweep* can be pressed that starts the source sweeping. The filenames etc. do not have to be changed every time before a measurement will be performed; the software will check if the filename already exists and will enumerate it if it is already taken. This way, no data will be overwritten and lost.

Under the *Measurements* Tab, the progress of the sweep can be observed in real-time. If no

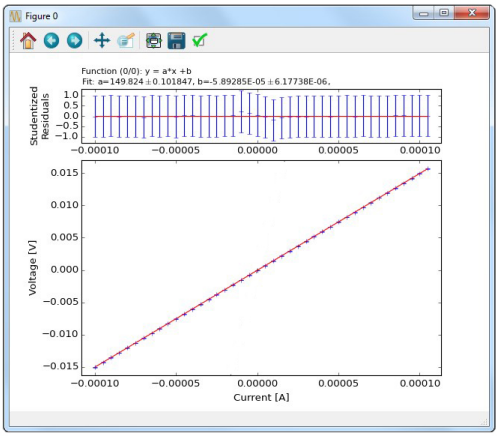

Figure 76: Automated fitting curve generated after every measurement.

live-stream appears, press *Show Script* and make sure that the input field shows the same entry as shown in figure 73.

Once the measurement will be done, a ready-to-publish graph will be generated similar to figure 76. In case the measurement is not good, use the multiplexer board to check if every

probe is in contact and sweep the source. If the measurement is still not good, make sure that the current is not too low (check what the voltage reading tells) and play around with the *Start-* and *StopValues*.

E.4. UHV Suitcase PiezoStage - Quick Guide

This is a quick startup and operation guide for the home-built UHV PiezoStage in the suitcase. It summarizes how to properly install and use it.

E.4.1. Components

In this section, all components needed are listed. When I did my military service, I once had a checklist where I had to mark if a Leopard II tank is present or not. So, although it seems obvious, all components are included for full completeness. It might be forgotten or lost, right?

- UHV Suitcase with the PiezoStage and the 19-pin electrical feed-through
- Electronics rack with a $\pm 12\,\mathrm{Vdc}$ power supply, high-voltage tank, controller board and the RaspberryPi board
- Power plug cord for the $\pm 12\,\mathrm{Vdc}$ power supply
- For RaspberryPi: 1x USB to Bluetooth adapter, 1x USB to Speaker sound adapter, 26-pin GPIO ribbon cable and a $5.1\,\mathrm{V}$ micro USB charger.
- 4x BNC cable (2x short for connection between controller board and HV tank, 2x long for connection to Suitcase)
- BNC to crimp style pin adapter (connection from BNC to feed-through)
- Nintendo Wiimote controller
- Standard AA batteries to power the Wiimote controller

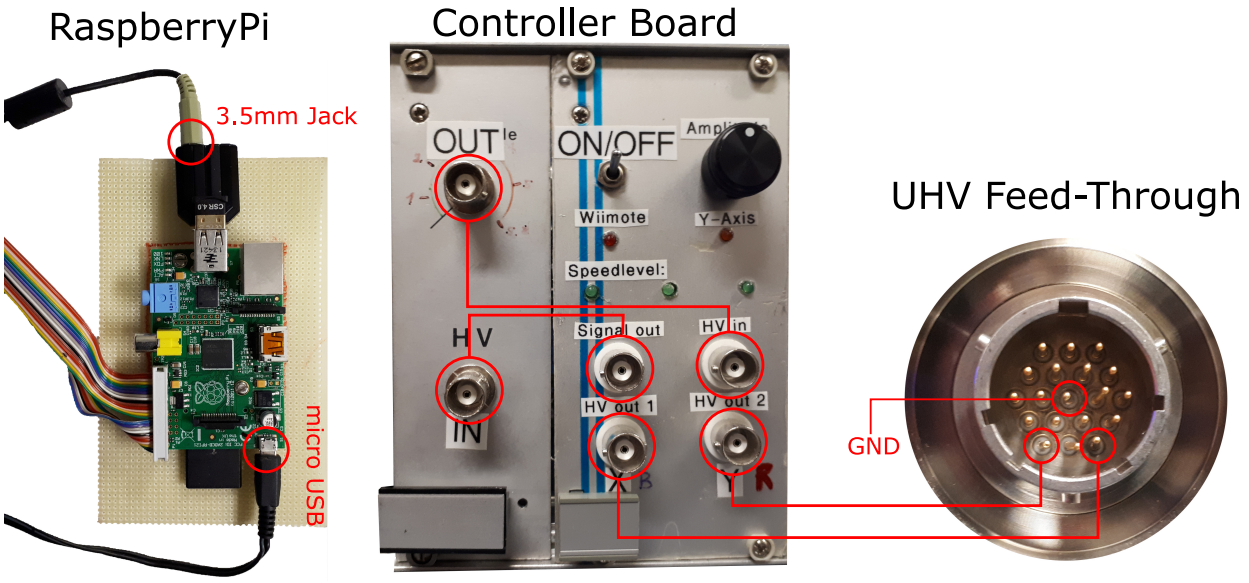

E.4.2. Connection and Operation

Most components listed above are normally already connected. Thus only check the following connections:

- The 3.5 mm stereo cable from the controller board is connected to the headphone output of the USB sound adapter.
- The micro USB charger is connected to the RaspberryPi and powered.
- The ±12 Vdc power supply is powered (I/O switch on the back side of the rack)
- BNC cables: connect *Signal Out* of the controller board with *IN* of the high-voltage tank. Connect *OUT* of the high-voltage tank with *HV in* of the controller board. Connect the *HV out 1* and *HV out 2* with the two long BNC cables to the BNC to crimp style pin adapter

To operate the PiezoStage, the following steps are necessary:

1) To start or reboot the RaspberryPi, switch the toggle switch from *OFF* to *ON* on the Controller Board. The RaspberryPi will start up.

2) Wait 1 min until the Wiimote LED on the Controller Board will light up (orange). When it's orange, connect the Wiimote controller by pressing the buttons *(1)+(2)* together at the same time. The Wiimote should connect within seconds. The orange LED will turn off and a green Speedlevel LED on the Controller Board will light up.

3) To change the position of the sample, press the buttons *up/down* and *left/right*. To increase the speed level, press the buttons *(+)* or *(-)*. There are 4 speed levels; the LEDs on the Controller Board indicate what level has been selected.

E.4.3. Problem Solving

In case the PiezoStage does not move, here are some ideas to solve it:

- The Wiimote normally disconnects after a 15 min when not used. Press *(+)*, *(-)*, *up/down*, *left/right* to see if the LEDs on the Controller Board indicate the change. If not, reconnect the Wiimote by switching the toggle switch to *OFF* and *ON* again. Wait until the Wiimote LED lights up orange and press *(1)+(2)* again to connect the Wiimote.

- **No movement in one or both directions:** Increase the amplitude of the signal (Potentiometer on the Controller Board). Make sure the ±12 Vdc power supply is powered (I/O switch on the back side of the rack). **If it still doesn't move:** when you switch the axis of movement from x to y, you should hear a click from the relay in the Controller Board. If you can't hear it, the relay might need to be replaced. **If you hear the click but still doesn't work:** Hold your ear against the suitcase and move the axis. When you move the piezo, you should hear a very high frequency from

the piezos. If you hear it, the piezo might be stuck. Gently lift the suitcase on one side and move the piezo until you can see a movement again. If you did not hear the high frequency, check the connections, hook up an oscilloscope and check *Signal out* if a signal is outputted, and use a *1:10* voltage divider to check the output from the high-voltage amplifier (*HV out*) with the oscilloscope.

E.5. Granville Phillips 835 Vacuum Quality Monitor - Quick Guide

This is a quick installation and startup guide for the Granville Phillips 835 Vacuum Quality Monitor System. It only summarizes how to set it up and how the initial Startup and Setup Sequence of the RGA works. It is recommended to also read the manual as this monitor does much more than what has been summarized here (e.g. can be used as a He leak detector!).

E.5.1. Important Notes

- Read the Instruction Manual provided by Granville-Phillips if you run the Mass Spectrometer the first time (p/n 835000).
- For safety reasons and proper operation, make sure that both the UHV chamber and the Series 835 VQM Controller are grounded (green Earth cable). Also, the Ground Pin of the AC to 24 Vdc Power Supply of the Controller must be connected to a Known Earth Ground.
- Do not connect a ground wire directly between the Controller and the vacuum chamber.
- To operate the Mass Spectrometer, a pressure of below 10^{-5} Torr is necessary. The MS Gauge filament may be damaged at system pressures higher than 10^{-5} Torr.
- Both Filament outgassing and Electron Multiplier Preconditioning are recommended before you run the Mass Spectrometer (see Initial Startup).
- Preparing a measurement with the Mass Spectrometer takes time! Important to mention: Outgassing the MS Gauge filament takes at least two hours, and you need to operate the gauge for another two hours to operate the system at optimum performance. Be aware of this 4 hours preconditioning time when you are about to use it for

an experiment. Plan ahead!

- For some reasons, the software provided by Granville-Phillips did not work on every computer (especially Windows 10, in the Cooke Lab). Make sure beforehand that you can connect the controller to the computer properly! Install the software, only connect the controller by USB and see if the software properly recognizes the controller.
- To assure maximum gauge lifetime, turn the gauge always Off or to Standby when not in use.
- Once the Gauge has been initialized, the 835 VQM system is ready to operate. To start scanning again, the scan function can directly be initialized.

E.5.2. Components

The following Components are needed

- 835 Vacuum Controller
- Interconnect Cable (VQM Controller to Gauge)
- Mass Spectrometer Gauge
- Ground Wire
- USB Cable
- AC to 24 Vdc Power Supply

E.5.3. Initial Startup

a) Pump the chamber to a pressure below 10^{-5} Torr. Do not turn on the VQM controller if pressure is higher, because the filament might be damaged.

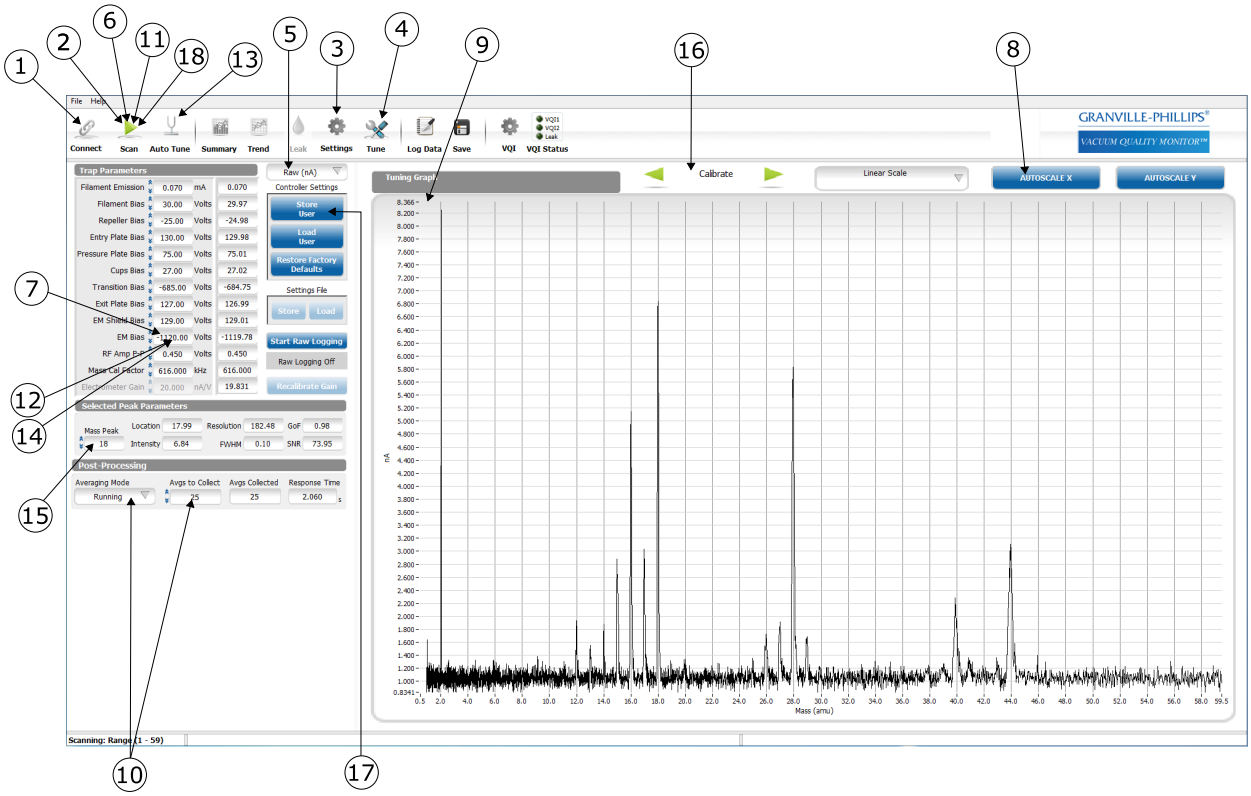

b) Press the power button on the front of the controller. The power LED button will change to a solid green indicating the power is on.

c) Open the 835 VQM Viewer application. Follow the steps, together with the illustration to setup the MS Gauge:

1) Click on the Connect icon and activate the connect the gauge to the computer.

2) Change gauge mode to Standby. The Standby Mode applies a default emission current with a reduced electron multiplier bias (500 V). The purpose of it is to outgas the filament. **Allow the system to run under this condition for two hours**.

3) If you have a Total Pressure Source, open the Settings screen and select the source. This is normally not the case (unless you bought one from MKS), so just skip this.

4) Open the Tune Screen.

5) Click on the Display Mode button (above Controller Settings) and select Raw (nA).

6) Change the Scan function from Standby to Off.

7) Set the EM bias to −750 V.

8) Click Autoscale Y button to set display of the mass spectra.

9) Set Y Axis to 30.

10) Set Averaging Mode to Running, and Avgs to Collect to 25.

11) Change the Scan function from Off to Scan. This turns on the Gauge to the preconditions of the Electron Multiplier.

12) Click to the right of the 10 s digit of the EM Bias setting, then use the down arrows on to decrease the voltage by −10 V every 30 seconds until the EM bias is at −900 V. **Allow the system to operate under these conditions for two hours**.

13) Click Auto Tune to automatically set the gauge parameters to perform at optimal conditions. If there is a problem with Auto Tune, there might be a problem with the gauge. **If Auto Tune fails, get in contact with Costumer Support.**

14) Click the arrows (either up or down) for the EM Bias to get the maximum peak of the MS scan display to be approximately 20 nA.

15) Select a known Mass Peak to calibrate the system. Any gas can be used but the easiest is to use the water peak (amu 18).

16) Calibrate the Mass Axis display. Use the Left and Right arrows (top of tuning spectrum) to shift the peak until the location value indicates the correct amu

(18.01 for water).

17) Click Store User to save these settings of this setup procedure. After the settings are stored, the MS gauge will turn automatically off.

18) The 835 VQM system is now ready to operate. To start scanning again, set the Scan function from off to Scan.